Graphene Transparent Conductors for Tandem Photovoltaic Cells

John O'Sullivan
Mansfield College
Department of Materials
University of Oxford

A thesis submitted for the degree of
Doctor of Philosophy

Under the supervision of Professor Ruy Sebastian Bonilla

Hilary Term 2025

Acknowledgements

Ar scáth a chéile a mhaireann na daoine.

This thesis would never have been written if not for the invaluable support I received throughout my DPhil. To Sebastian, your excellent supervision has enabled me to mature and grow as a scientist over the last four years. I appreciate that you always had the confidence in me to work with independence, but knew when to step in when I was getting carried away. I look forward to continuing many exciting research collaborations for years to come. To Peter, thank you for providing pressure and optimism in equal measure: without *VETS*, some of the most rewarding moments of my DPhil would never have materialised. I want to extend a special mention to Matthew Wright for his strong support of my academic writing and career development over the last few years, and for his extraordinary ability to find an appropriate "Simpsons" clip to fit any circumstance. I would also like to thank Radka Chakalova for her constant patience in the cleanroom, without which, no graphene layers would have been transferred. I am in great debt to the EPSRC for their generous DPhil studentship, and their willingness to support me on my next academic journey.

I want to also thank all group members who have supported me over the years. Anastasia, for your sage counsel and career advice. Mohsen, Tarek and Theo, thank you for your incisive feedback in group meetings and camaraderie in the lab on early mornings. Tarek, thank you for supporting me reach the final stages of my DPhil. To past DPhil students: Isabel Al-Dhahir, Eleanor Shaw, Shona McNab, Avery Yu and Donghao Liu, thank you for being invaluable peers and mentors. To current DPhils: Yifu, Xinya, Erica, Soumya, Yan, Yuelin, Darshit, Boom, Paul and James, savour your DPhil while you can – it goes by quickly. Xinya, my fellow 2D materials researcher – without you, I'm sure my FETs would never work, and the lab would be significantly less entertaining. Erica, thank you for encouraging me to "go home" and

recharge when I was stuck in a rut. Yifu and Yan, without you both I would still be wandering around Shenzhen trying to find my hotel. Soumya, you deserve credit for keeping me sane during my lengthy vacuum system repair in the electrochemical lab with late night conversations and entertaining chemical reactions.

I am also indebted to my friends in Ireland and around the world who supported me through lengthy phone calls with advice and humorous anecdotes – especially Cian, Briain and Billy. **Dr** Rafael Hunt-Stokes – thank you for being a loyal friend over the last 9 (!?) years, and providing me a safe haven in times of turbulence. Hope to have many Binsey-Ranch exchanges over the next year and beyond. Francesca, for being my rock, keeping me sane, reminding me of the importance of a Marston weekender, and the grand beauty of small things. I cannot wait for our next phase. In 2025, we will thrive…

Thank you to my family for supporting me over the last few years, especially Abbey, without whom I would have had nowhere to live during my third-year undergrad exams. Perhaps most of all, I want to thank my parents for their unwavering support of my education in the UK, despite not really knowing what I am doing. Thank you for your patience as I came home on the holidays, only to hide away with my laptop. From driving me to Cork on Saturdays for "extra school", to allowing me to use the car to do my MSci exams with the Cappabue Wifi, this DPhil is as much your achievement as it is mine.

"Between my finger and my thumb

The squat pen rests

I'll dig with it."

Seamus Heaney – Digging.

Abstract

Transparent conducting electrodes (TCEs) are a major source of efficiency loss in perovskite/silicon tandem solar cells. With the best-performing TCEs containing indium, they also compromise the sustainability of this promising renewable energy technology. Graphene, owing to its broadband transmittance and high mobility, offers great potential as an alternative TCE. However, its sheet resistance remains too high to be competitive against conventional TCE materials. Despite low sheet resistance being attainable via chemical doping, such techniques have poor stability and reduce transmittance, limiting their applicability in optoelectronic devices. This thesis explores how ion-charged dielectrics (ICDs) can be used to modulate the conductivity of graphene to achieve sufficiently low R_{sheet} to make it competitive with state-of-the-art TCOs in tandem solar cells.

In this thesis, a proof-of-concept for the ICD doping of graphene is first developed. The impact of a corona-charged dielectric on the properties of a graphene layer interfaced with it is characterised, demonstrating a graphene sheet resistance reduction of >75% to ~400 Ω/□. This is expanded upon by investigating the impact of migrated potassium ions in SiO_2/Si on graphene sheet resistance. A record 117.9 Ω/□ sheet resistance is achieved – among the lowest reported in the literature for CVD monolayer graphene wet transferred to SiO_2. Field-effect transistor characterisation indicates a charge concentration $>6\times10^{12}$ /cm^2 was generated on the graphene. The ability and stability of ionic charge in glass to dope graphene are also investigated, with sheet resistance <300 Ω/□ observed in vacuum after Na^+ migration to the graphene/glass interface. This is contrasted with graphene encapsulation with corona-charged PMMA and AlO_x. Although they can dope graphene, they have poor stability over time. Finally, the suitability of ICD-doped graphene for perovskite/silicon tandem cells is assessed via modelling. It is calculated that an efficiency gain of $>1\%_{abs}$ may be achieved if ICD-doped graphene is used instead of state-of-the-art indium-based TCOs.

Preface

This thesis is an account of the work I have carried out as a doctoral student at the Department of Materials, University of Oxford. I have not previously submitted any part of this thesis for another degree at this University or elsewhere. I hereby confirm that the work presented is my own, unless otherwise stated and duly acknowledged in the text as well as appropriately reference.

During this DPhil, I have written and contributed towards the following publications:

J. O'Sullivan, M. Wright, X. Niu, P. Miller, P.R. Wilshaw, R.S. Bonilla "Towards a graphene transparent conducting electrode for perovskite/silicon tandem solar cells". *Progress in Photovoltaics: Research and Applications.* 31 (12), 1478-1492. 2023. *Invited Contribution.*

B.C. Sheath, X. Xu, P. Manuel, J. Hadermann, M. Batuk, **J. O'Sullivan**, R.S. Bonilla, S. J. Clarke. "Structures and Magnetic Ordering in Layered Cr Oxide Arsenides $Sr_2CrO_2Cr_2OAs_2$ and Sr_2CrO_3CrAs". *Inorganic Chemistry* 61 (31), 12373-12385. 2020.

Y. Xiong, R. Zhou, A. H. Soeriyadi, Z. Liu, S. Maitra, Y. Shi, J. Chen, **J. O'Sullivan**, M. Wright, P. P. Altermatt, R. S. Bonilla. "Self-aligned laser opening and stencil metallization for silver-free contacts in silicon solar cells". *APL Electronic Devices.* 1, 026109. 2025.

Y. Wang, T. D. C. Hobson, J. E. N. Swallow, S. McNab, **J. O'Sullivan**, A. H. Soeriyadi, X. Niu, R. C. Fraser, A. Dasgupta, S. Maitra, P. P. Altermatt, R. S. Weatherup, M. Wright, R. S. Bonilla. "Impact of precursor dosing on the surface passivation of AZO/AlO_x stacks formed using atomic layer deposition". Energy Advances. 4, 553-564. 2025.

Contents

List of Figures

List of Tables

List of Abbreviations

AgNWs	Silver nanowires
ALD	Atomic Layer Deposition
AM1.5G	Air-Mass 1.5 Global
APS	Ammonium Persulfate
ARC	Anti-Reflection Coating
AZO	Aluminium-doped Zinc Oxide
BSG	Borosilicate Glass
CA	Corona Anneal
CMOS	Complementary Metal Oxide Semiconductor
CPD	Contact Potential Difference
CV	Capacitance-Voltage
CVD	Chemical Vapour Deposition
ETL	Electron Transport Layer
FCA	Free-Carrier Absorption

FOM	Figure Of Merit
FTO	Fluorine-doped Tin Oxide
GFET	Graphene Field Effect Transistor
HBC	Heterojunction Back Contact
HMDS	Hexamethyldisilazane
hBN	Hexagonal Boron Nitride
HTL	Hole Transport Layer
ICD	Ion-Charged Dielectric
IO:H	Hydrogen-doped Indium Oxide
IPA	Isopropyl Alcohol
ITO	Indium-doped Tin Oxide
IWO	Tungsten-doped Indium Oxide
IZO	Zinc-doped Indium Oxide
IZrO	Zirconium-Doped Indium Oxide
J_{SC}	Short-Circuit Current Density
KP	Kelvin Probe
LCOE	Levelised Cost of Electricity
MOS	Metal Oxide Semiconductor
P3HT	Poly(3-hexylthiophene)
PECVD	Plasma Enhanced Chemical Vapour Deposition
PEDOT:PSS	Poly(2,3-dihydrothieno-1,4-dioxin)-poly(styrenesulfonate)
PERC	Passivated Emitter and Rear Contact
PMMA	Polymethyl methacrylate

PV	Photovoltaic
RIE	Reactive Ion Etching
SEM	Scanning Electron Microscopy
SHJ	Silicon Heterojunction
$SOCl_2$	Thionyl Chloride
Spiro-OMeTAD	2,2',7,7'-Tetrakis[N,N-di(4-methoxyphenyl)amino]-9,9'-spirobifluorene
TCE	Transparent Conducting Electrode
TCO	Transparent Conducting Oxide
TOPCon	Tunnelling Oxide Passivating Contact
TSIC	Thermally Stimulated Ionic Conductivity
V_{DS}	Drain-Source Voltage
V_{GD}	Gate-Drain Voltage
V_{OC}	Open Circuit Voltage
WAT	Weighted Average Transmittance

Chapter 1

Introduction

1.1 **Achieving Multi-Terawatt Scale Solar Photovoltaics**

In the summer of 2024, global atmospheric carbon dioxide concentration reached a record 426 ppm, following an unprecedented increase since the dawn of the Industrial Revolution in the 1760s [1], [2], [3], [4]. CO_2 has a stronger tendency to absorb infrared radiation relative to other atmospheric gases, such as nitrogen and oxygen [5], [6], [7]. This "greenhouse effect" has driven a rapid increase in global surface air temperature since industrialisation, with temperatures reaching 1.5 ℃ above the pre-industrial average in 2024 [8], [9]. Figure 1.1 illustrates how the temperature rise measured in recent decades corresponds sharply with global atmospheric carbon dioxide increases. This temperature rise has been linked to an increase in extreme weather events, sea-level rises, and threats to global food and water security [6], [7]. To limit the increase in global average temperatures to well below 2 ℃ and mitigate the worst effects of climate change, we must achieve net-zero CO_2 emissions by 2050 [7]. This goal requires a significant increase in the proportion of the global energy mix generated through low-carbon sources, such as wind, solar, hydroelectric, and nuclear energy [6], [7].

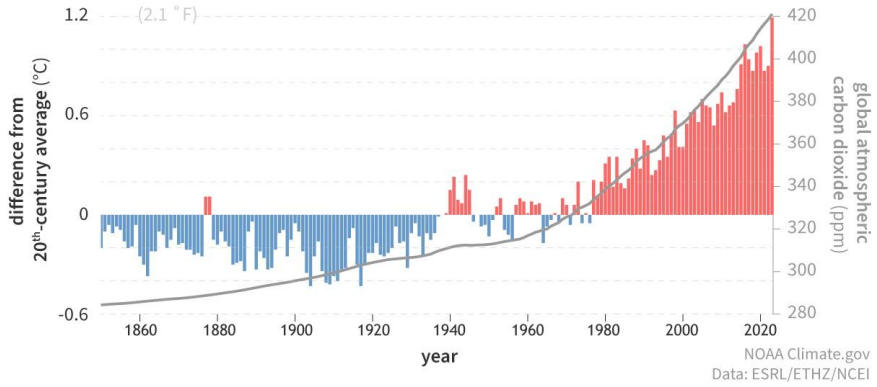

Figure 1.1: Yearly temperature compared to the twentieth-century average from 1850–2023 (left y-axis). Red bars correspond to warmer-than-average years; blue bars correspond to colder-than-average years. The grey line corresponds to the atmospheric carbon dioxide amounts (right y-axis): 1850-1958 from IAC, 1959-2023 from NOAA Global Monitoring Lab. Adapted from ref. [4], [10].

To reach net-zero, an estimated global solar photovoltaic (PV) capacity of 75 TW is needed by 2050 [11], [12]. In 2023, just ≈0.4 TW PV was added to the global energy mix, bringing the global PV capacity to ≈1.4 TW [13]. To reach 75 TW by 2050, we will need approximately 3-4 TW of new installations per year from 2030, a tenfold increase in the current deployment rate [11], [12]. Increasing capacity can be achieved by reducing the levelised cost of electricity (LCOE) of solar power, incentivising further production.

The LCOE of solar PV consists of two components: the PV modules themselves, and the balance of system (BOS), which includes wiring, installation, location and mounting costs [14]. Since 2010, the price of PV modules has decreased by 93%, while BOS costs have decreased much slower [14]. In 2023, BOS costs accounted for 61% of utility-scale PV electricity installation costs [14]. Increasing solar cell efficiency allows for a reduction in BOS costs, as less area is required to generate equivalent electricity, thereby necessitating fewer BOS components [14], [15], [16]. It is therefore clear that increasing solar cell efficiency can lower the LCOE of solar electricity and provide a strong impetus to increase PV capacity.

In standard single-junction solar cells, an electron-hole pair is generated at a p-n junction when a photon of energy higher than the band gap of the active material is absorbed [17]. The electron and hole then travel to the semiconductor-metal contacts at opposite ends of the p-n junction to generate electricity. The power conversion efficiency (η) of a solar cell can be defined as the efficiency with which the energy of photons is converted into usable electrical power. The power conversion efficiency of industry-standard single-junction silicon cells is limited to a practically achievable value of ≈29.4%, a limit that we are rapidly approaching [18]. Figure 1.2 illustrates the development of silicon PV towards this practically achievable value, with comparison to perovskite and perovskite/silicon-based cell technology. Lin et al achieved an efficiency of 26.81% in silicon heterojunction (SHJ) cells of industrial size using optimised nanocrystalline-silicon hole contacts at the back junction [19], and LONGi Solar have

demonstrated efficiencies up to 27.3% for heterojunction back contact (HBC) cells under laboratory conditions [20], [21]. This progress towards the practical limit has been made possible through improved surface passivation and optimised passivating contacts. However, further improvements are expected to yield diminishing returns as we approach 29.4%. For efficiencies greater than 30%, an alternative technology will be required to capture additional photons not absorbed by silicon.

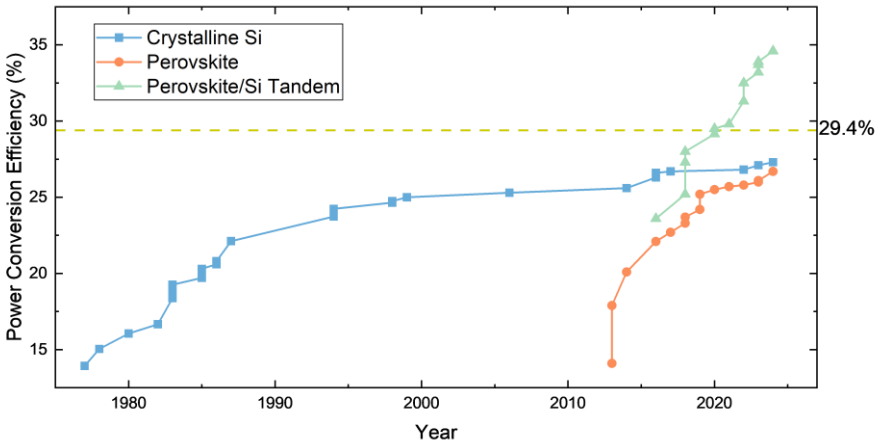

Figure 1.2: Research-scale power-conversion efficiency records of crystalline silicon, perovskite, and perovskite/silicon solar photovoltaic technologies with respect to time. The horizontal line at 29.4% indicates the practically achievable limit for single-junction silicon photovoltaics. Data extracted from National Renewable Energy Laboratory (NREL) "Best Research-Cell Efficiency Chart", ref. [22].

1.2 **Tandem Photovoltaics**

In single-junction cells, photons with energy below the band gap (1.1 eV in Si) cannot excite electrons from the valence band to the conduction band, preventing the generation of electron-hole pairs, and limiting potential efficiencies [17]. Similarly, when incident photons have energy significantly above the band gap, the excess energy of the photogenerated "hot carriers" is lost as heat during thermalisation [17]. Figure 1.3 depicts how a multi-junction, or "tandem" solar cell, uses multiple solar absorber materials of differing band gaps stacked together to mitigate these losses and make better use of the full solar spectrum. Photons with energy below or significantly above the band gap of a single junction cell can be more effectively absorbed by the additional solar absorber materials [17], [23], [24], [25]. This configuration increases

the maximum theoretical efficiency potential for a tandem cell to ≈45% for two absorbers, or >60% when using seven or more absorbers [26]. Using III-V solar cells, an efficiency of 39.2% has been achieved with six cells of differing band gap stacked on top on one another, and 47.1% under 143 suns illumination [27]. However, the high fabrication cost of III/V solar cells limits their utility in large-scale commercial applications [28]. To achieve widespread mainstream adoption, tandem solar cells must utilise semiconductor materials with appropriate band gaps that are both inexpensive and abundant.

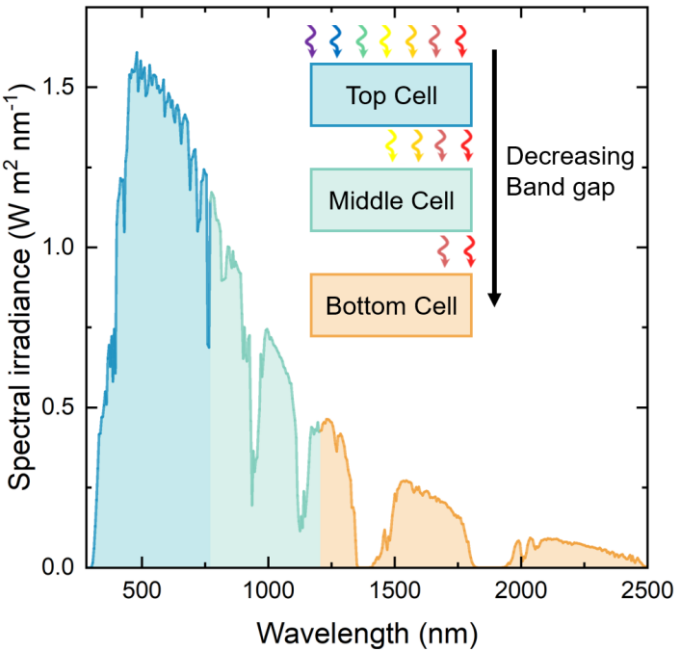

Figure 1.3: Spectral irradiance with respect to wavelength, corresponding to the reference Air-Mass 1.5 Global spectrum. The schematic depicts a multi-junction solar cell structure, where each cell captures a different region of the spectrum. Such multi-junction solar cells can absorb more incident light than single-junction cells by using separate semiconductor absorbers tailored to different parts of the electromagnetic spectrum. The AM1.5G data was extracted from ref. [29].

A promising combination of tandem sub-cells for widespread terrestrial application involves using a wide band gap perovskite top cell and a lower band gap silicon bottom cell. At laboratory scales, LONGi Solar has already developed perovskite/silicon tandems with efficiencies of 34.85%, yet there is significant potential for further efficiency improvements [30], [31], [32]. An efficiency of 45.1% is achievable using this material combination when connected in the two-terminal configuration, or 45.3% in a four-terminal configuration [33], [34], [35]. Perovskites are particularly promising as the top cell in a tandem due to their high

absorption coefficient [36] and large open-circuit voltage (V_{OC}) potential [37]. By varying the perovskite composition, its band gap can be readily tuned from ≈1.3 to 2.0 eV, providing excellent complementarity with silicon's 1.1 eV band gap [38], [39], [40], [41]. Among the available single-junction silicon cell architectures, the SHJ design is particularly advantageous as it has the highest efficiency potential compared with other designs. Additionally, the amorphous silicon (a-Si) passivating layers at the surface of a SHJ cell are conductive, which enables facile interconnection to the perovskite cell [21], [42], [43], [44]. However, both perovskite and a-Si have poor lateral conductivity; thus, they require additional layers with high lateral conductivity for efficient charge carrier collection to the metal fingers [45]. Such layers must also have high transmittance to minimise parasitic absorption losses. Photocurrent losses in these 'transparent conducting electrodes' (TCEs) can represent a major efficiency loss, contributing to a reduction of single-junction module efficiency by 10–25%$_{rel}$ [46]. Improving the trade-off between light absorption and conductivity in TCEs has been the subject of decades of research [47], [48], [49]. To improve the efficiency of tandem solar cells, materials which overcome the performance limitations of TCEs must be developed. To understand these limitations, a detailed examination of the materials properties of TCEs, and their role in tandem solar cells, as well as photovoltaics in general, is required.

1.3 Materials Properties of Transparent Conducting Electrodes

1.3.1 Optical Properties

Compared with single-junction cells, TCEs in tandem cells can have more stringent optical property requirements, depending on their position within a tandem solar cell stack [50]. Figure 1.4 depicts the positions of transparent conducting oxides (TCOs) typically used as TCEs in two-terminal and four-terminal perovskite/silicon tandem cell structures. All perovskite/silicon tandem configurations require a front TCE. This TCE must have high broadband transmittance to light from ≈280 to 1100 nm to maximise light absorption across the air-mass 1.5 global

(AM1.5G) spectrum in both perovskite and silicon sub-cells. This requirement contrasts with single-junction cells, where TCEs only need high transmittance to part of the spectrum. The front TCE in a two-terminal monolithic perovskite/silicon tandem, can contribute >1 mA/cm^2 loss in short-circuit current density (J_{SC}) through parasitic absorption, resulting in ≈1%$_{abs}$ loss in efficiency [51], [52]. The two- and four-terminal mechanically-stacked, and three-terminal monolithic tandem configurations typically require one or two additional TCEs between the sub-cells, which can contribute towards an additional ≈3–4 mA/cm^2 loss in J_{SC} [50], [51], [53]. This places significant pressure on TCE performance in tandems, compared with their single-junction counterparts. As TCEs tend to be one of the most expensive components in solar cell fabrication, as well as multiple-terminals increasing BOS costs, the single-TCE two-terminal monolithic configuration is preferable for large-scale commercial applications [50]. However, the series connection of monolithic two-terminal cells requires current matching between cells, constraining the bandgaps that can be used, and thus restricting potential perovskite compositions [38]. An extra TCE with high infrared (IR) transmittance and efficient light coupling is often needed at the rear to incorporate bifaciality [44]. Solar cell manufacturers must balance a trade-off between the high efficiencies of SHJ cells versus the high cost of requiring additional TCEs. The development of low-cost TCEs with broadband transmittance would eliminate this trade-off and enable higher efficiencies in tandem cells.

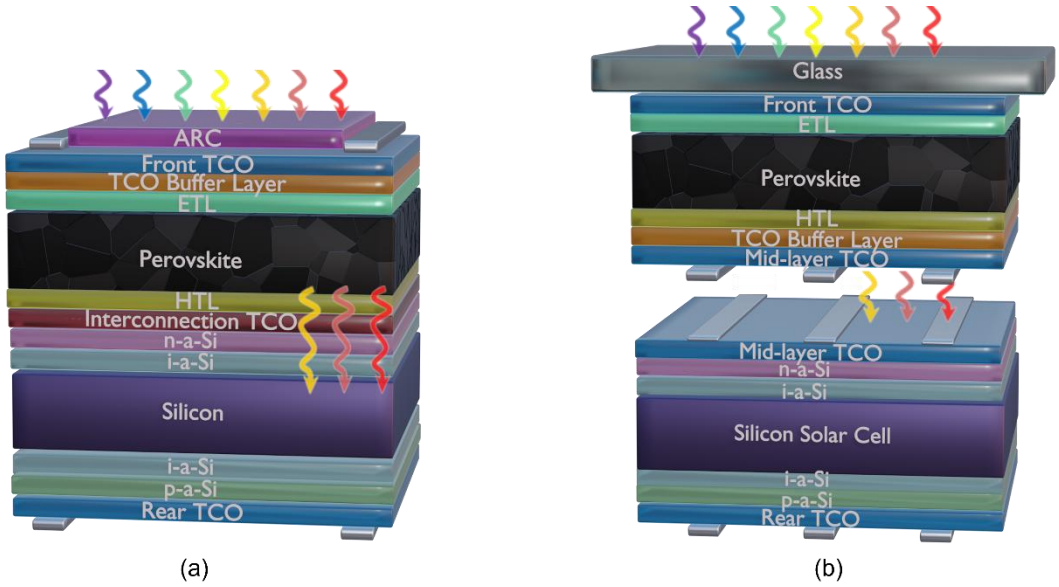

Figure 1.4: Transparent conducting oxide (TCO) positions in perovskite/silicon tandem solar cells in either (a) two terminal monolithic or (b) four-terminal mechanically stacked configuration.

To determine the materials properties required to achieve a high transmittance, consider the equation for TCE transmittance at given wavelength, following the Beer-Lambert Law:

$$T\% = (1 - R)^2 \cdot e^{-\alpha \cdot t} \; (1.1)$$

where R is the reflectance, α is the absorption coefficient, t is the TCE thickness [17], [48]. From this approximation, it is evident that TCEs have a combination of low thickness, and low absorption coefficient α. The absorption coefficient α, approximated following the Drude model [45], [48], [54], can be defined as:

$$\alpha = \frac{\lambda^2 q^3 N}{4\pi^2 \varepsilon_0 c^3 n (m^*)^2 \mu_{opt}} \; (1.2)$$

where λ is the wavelength of incident light, q is the charge of the majority carrier, N is the carrier concentration of the majority carrier, ε_0 is the permittivity of free space, c is the speed of light in vacuum, n is the refractive index, and m^* and μ_{opt} are the effective mass and optical mobility (excluding scattering between grains) of the majority charge carrier, respectively. To keep free carrier absorption (FCA) low, it is therefore critical to minimise the carrier concentration N. As the transmittance for a tandem must be broadband, it is essential that a low

absorption is maintained across a range of wavelengths. Figure 1.5 shows the dependence of absorptance on light for a range of different TCEs, where many TCEs have particularly increased absorption in the blue-violet and near-IR regions. In considering TCEs for tandems, further investigation of the mechanism behind this absorption is necessary.

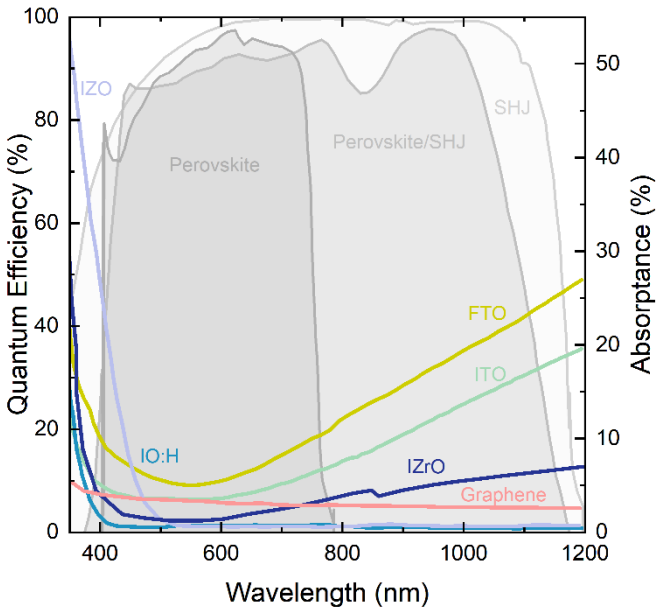

Figure 1.5: Dependence of absorptance on wavelength for a selection of transparent conducting electrodes. The left y-axis indicates the corresponding quantum efficiency of difference solar cell architectures. Based on Figure 2.b, ref. [45], replotted for the addition of more recent IZrO data from [55].

Infrared photons have lower energy compared with visible photons, and therefore can be more easily absorbed by free carriers and cause intra-band transitions, reducing the transmittance of the film for wavelengths in the near-IR and IR [56]. The effect of FCA is not as critical in wide band gap single-junction perovskite cells, where such low energy photons cannot be absorbed. But in a silicon, or perovskite/silicon tandem cell, the inability to absorb such IR photons is a significant source of efficiency loss [57], [58], [59], [60]. The range of wavelengths to which a TCE will be transparent is determined by its plasma frequency, ω_p [61]. The plasma frequency of a TCE can be defined as the natural frequency of oscillation of the free electron gas in the material, and is expressed as:

$$\omega_p = \sqrt{\frac{N\,q^2}{m^*\varepsilon_{TCE}}} \quad (1.3)$$

For a TCE with incident photons of energy greater than its ω_p, free electrons in the TCE cannot respond fast enough to the oscillating electric field of the incident photons, allowing photons to pass through [54], [61]. For incident photons with energy lower than the TCE's ω_p, they are either reflected or absorbed by the TCE [54], [61]. In many TCEs, the plasma frequency falls within the near-IR range. While high-energy visible and ultraviolet (UV) light can pass through, near-IR and IR light is absorbed. To minimise IR absorption loss in perovskite/silicon tandems, it is essential to use a TCE material with a low ω_p across all layers of the device stack. This can be achieved by reducing *N,* and increasing m* and ε_{TCE}. However, optimising these properties for improved transmittance may impact the electrical properties of the film.

1.3.2 Electrical Properties

TCEs in a tandem cell must contribute minimally to the series resistance (R_S) of the cell. To achieve this, TCEs must have a low sheet resistance (R_{sheet}), and a low contact resistance to the metal fingers. The R_{sheet} in units of Ω/□ can be approximated, assuming uniform carrier generation, by Equation 1.4:

$$R_{sheet} = \frac{1}{q \cdot \mu \cdot N \cdot t} \quad (1.4)$$

where μ and N are majority carrier mobility and concentration respectively, q is the charge of the majority carrier, and t is the thickness of the film [48], [62]. Equation 1.4 illustrates that to minimise $R_{sheet,}$ one must choose a TCE with large μ, N and t. However, as previously discussed, increasing t and N can lead to reduced film transmittance, necessitating a trade-off between properties [45], [55]. Figure 1.6 illustrates this trade off, showing the dependence of thickness on T% and R_{sheet}. It is therefore clear that a good balance of R_{sheet} to transmittance requires

TCEs with a very high carrier mobility. This would ensure a low R_{sheet} despite low carrier concentration and thickness, thus enabling high transmittance and low plasma frequency.

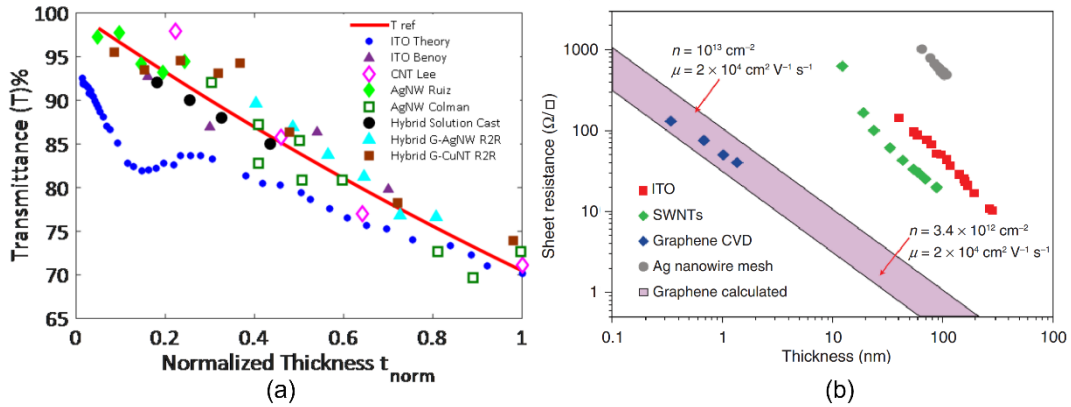

Figure 1.6: Dependence of sheet resistance and transmittance on thickness. (a) Increased thickness leads to reduced transmittance. Reprinted with permission from Figure 2, ref. [63]. Licensed by CC BY-NC-ND 4.0. (b) Increased thickness leads to reduced sheet resistance. Reprinted with permission from Figure 7, ref. [64]. Licensed by CC BY-NC-ND 3.0.

The carrier mobility μ can be expressed as:

$$\mu = \frac{q\tau}{m^*} \quad (1.5)$$

where τ is the carrier relaxation time (the average scattering time between two events). The mobility of the film, and therefore the sheet resistance, can be improved by minimising sources of scattering, and selecting materials such that the effective mass of the majority charge carrier is minimised. The effective mass represents the mass that the charge carriers appear to have when moving through a crystal, where they are subject to local forces within the material [65]. Inconveniently, reducing the effective mass can also increase the absorption coefficient and the plasma frequency, following Equations (1.2) and (1.3). Therefore, a suitable balance between effective mass and mobility must be considered. Scattering can be minimised by reducing impurities such as dopant atoms (especially if non-uniform), reducing defects, and increasing grain size to reduce scattering contributions at grain boundaries [45], [65], [66]

To improve TCE performance, the most practical and intuitive approaches include improving film quality to minimise scattering sources, moderately increasing carrier concentration *N* via

doping for a low sheet resistance, and reducing the film thickness as much as possible for a good balance between transmittance and R_{sheet} [67]. Precise control over these properties is crucial for optimum performance. To tailor these properties more effectively, a deeper understanding of existing TCEs used for tandem solar cells is necessary.

1.4 State-of-the Art TCE Materials for Tandem Solar Cells

1.4.1 Transparent Conducting Oxides (TCOs)

The most frequently used TCEs in optoelectronics are transparent conducting oxides (TCOs) [45]. TCOs are semiconductors that achieve high transmittance by utilising a wide band gap (>3 eV) and a low absorption coefficient [45], [48]. This wide bandgap results from their electronic structure, composed of oxides of post-transition metals, typically in the $(n - 1)d^{10}ns^2$ configuration [68]. Interactions between the metal s-orbitals and the oxygen p-orbitals (Ms-Op interactions) give rise to the wide band gap of TCOs: the conduction band is formed by the antibonding Ms–Op interactions, while the valance band is formed by the bonding and nonbonding O 2p states [45], [68]. There may seem to be an inherent contradiction in this definition, where typical conductors such as metals have zero bandgaps, where the bands instead overlap, providing many charge carriers available for conduction. In a TCO, a semiconductor with an ultrawide bandgap is degenerately doped, raising its Fermi energy into the conduction or valence band. This phenomenon, known as the Moss-Burnstein effect, results in increased conductivity and a widening of the optical band gap, helping to reduce FCA [65]. Figure 1.7 depicts the changes in band structure in a TCO experiencing degenerate doping, such that its Fermi level shifts above the conduction band minimum (CBM) and the Moss-Burnstein effect occurs. However, the doping level must not exceed a critical level, where many-body interactions such as electron-electron and electron-ion interactions may cause band gap renormalisation, reduce the band gap, and the reduce the overall transmittance of the TCO [69]. Due to their relatively high carrier concentration, TCOs tend to have a high plasma

frequency, leading to significant FCA in the IR. Additionally, TCOs experience considerable parasitic absorption of photons with energy greater than their band gap (>3 eV, corresponding to $\lambda \approx <410$ nm). For this reason, it is desirable to choose a TCO with the highest possible band gap, ideally greater than ≈3.5 eV, to maximise the blue to near-UV photons absorbed in the perovskite cell [70]. However, achieving such a band gap in a material that maintains sufficiently low sheet resistance remains challenging.

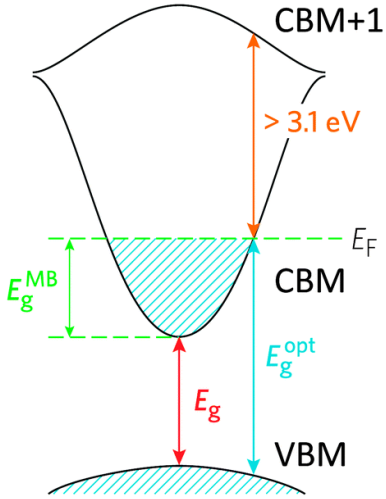

Figure 1.7: Band structure schematic of transparent metal-oxide with wide band gap (E_g). When degenerately doped, the Fermi level shifts above the conduction band minimum (CBM), in a process known as the "Moss-Burnstein Shift". This shift increases the apparent optical band gap E_g^{opt} due to the filling of low-energy conduction band states, which blocks certain optical transitions. This can enable simultaneous high conductivity and high optical transmittance in certain metal oxides. Reprinted from ref. [65]. Licensed by CC BY 3.0.

Like most TCOs, its high carrier concentration causes high parasitic FCA [45], [55], [71]. While ITO is widely used TCE in perovskite/silicon tandems, zinc-doped indium oxide (IZO) has recently become the most frequently used due to its high mobility ≈60 cm^2/Vs and thus reduced FCA in the NIR, as well as its ability to achieve high mobility without requiring high-temperature annealing [45]. However, it suffers from reduced transmittance in the ultraviolet–visible (UV–Vis) range compared to ITO due to its narrower band gap of ≈3 eV [45], [72]. Zirconium-oxide doped indium oxide (IZrO) is a promising TCO for tandems, demonstrating high mobility ≈77 cm^2/Vs and wide band gap ≈3.75 eV, keeping its parasitic absorption low [55], [73]. Replacing the conventional IZO with IZrO can increase perovskite/silicon tandem

efficiency by 2.3%$_{abs}$ [55]. Hydrogen-doped indium oxide (IO:H) also offers high transmittance at low Rsheet due to its exceptional mobility ≈100 cm^2/Vs and wide band gap, but suffers from poor stability due to hydrogen migration, which increases contact resistance at Ag fingers [45]. Other indium-based TCOs such as cerium/hydrogen and tungsten/hydrogen co-doped indium oxide can have high mobility, albeit achieving this requires a high-temperature anneal, limiting their suitability in tandems [45], [55], [74]. Most crucially, there are insufficient global indium reserves to meet the demand for TW photovoltaic capacity targets of 3-4 TW/yr [75]. Zhang et al. calculated that the annual manufacturing capacity for SHJ cells using ITO is only 37 GW/yr [75]. Due to their increased efficiency, perovskite/silicon tandems offer reduced indium consumption per W generated, yet they are still limited to an annual manufacturing capacity of just 29–177 GW/year, indicating that indium cannot be used in any significant PV manufacturing capacity [75], [76]. Figure 1.8 reveals the limitations in sustainable manufacturing capacity in tandem cells using ITO TCEs. The scarcity of indium causes high and fluctuating costs, hindering broader uptake. Additionally, the demand for ITO-based TCEs is rapidly increasing in the consumer electronics industry, where it is used in touch screens, LEDs and sensors. A high mobility indium-free TCE is hence a critical requirement to facilitate the future deployment of tandem PV cells as part of efforts to reduce global carbon emissions and mitigate anthropogenic climate change.

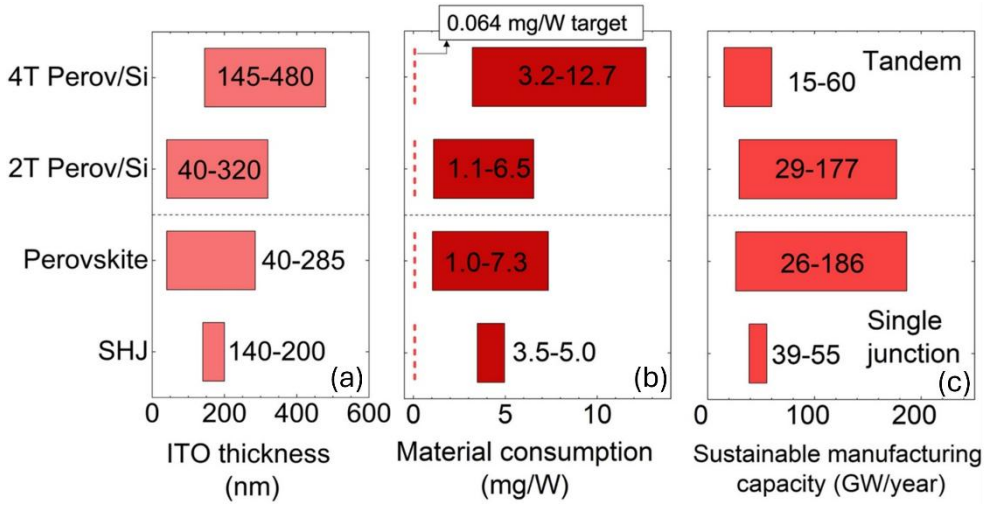

Figure 1.8: Assessment of tin-doped indium oxide (ITO) and indium consumption in perovskite/silicon, perovskite, and silicon heterojunction solar cell designs. (a) Current ITO thickness used, (b) calculated consumption ranges and (c) sustainable manufacturing capacity of different PV architectures. Adapted with permission from ref. [76], © 2023, John Wiley and Sons Ltd.

Indium-free TCOs such as fluorine-doped tin oxide (FTO) and aluminium-doped ZnO (AZO) show some promise for indium-free tandems. But these materials are beset by challenges: both exhibit high FCA due to low mobility, with AZO also suffering from instability, which hinders their implementation in high-efficiency tandems [45], [77]. Moreover, even if high-performing indium-free TCOs can be achieved, the sputter deposition process of TCOs tends to damage the underlying perovskite layers [67], [78]. This necessitates an additional buffer layer such as MoO_x or SnO_2 increasing processing time and costs, and often reducing stability and transmittance [67], [78]. While reducing sputter power can enable direct TCO-deposition on perovskite cells with low damage, this tends to produce low-mobility TCOs, which contribute to resistive and optical losses, and restricts options for charge transport layers [79], [80], [81], [82]. Additionally, most TCOs require a high temperature deposition or post-deposition anneal >200℃ to improve crystallinity and achieve high mobility and transmittance [45], [54], [83], [84], [85]. These high-temperature steps can damage delicate perovskite and a-Si layers. The stability of perovskite solar cells to TCO deposition and post-anneal temperatures depends on perovskite composition. Methylammonium lead iodide ($MAPbI_3$) based cells can undergo deleterious structural transformations at temperatures as low as ~85℃ [86], [87], while

formamidinium (FA) and FA/Cs mixed cation formations have been shown to withstand temperatures up to 150-200℃ [88], [89]. Although all-inorganic perovskite cells can exhibit stability >200℃, they suffer from moisture phase instability issues, and have a relatively low efficiency compared to mixed cation-based perovskites [90], [91]. This limits TCO annealing to <200℃ for deposition on most high-efficiency perovskite cells. Similarly, annealing TCOs deposited on a-Si in a SHJ cell over ≈200℃ for prolonged periods can increase contact resistance between the cell layers, and reduce passivation by hydrogen effusion [92], [93]. To maximise potential efficiency in future tandem cells, a high-performance indium-free TCE that can be deposited via a gentle, low-temperature process is necessary. Given these inherent limitations in TCOs, it is essential to explore alternative TCE materials to meet this goal.

1.4.2 Nanomaterial TCEs

Silver nanowires (AgNWs) can be deposited gently at room temperature as a dense conductive mesh, facilitating carrier transport to metal fingers while leaving voids for light transmission. By tuning the concentration and aspect ratio of AgNWs, a TCE film with properties comparable with ITO can be achieved [45], [94]. However, AgNWs are highly vulnerable to oxidation, which significantly reduces conductivity [95]. Additionally, migrating iodide ions in many perovskite cell compositions can react with the silver in AgNWs and form silver iodide, degrading the AgNWs and deforming the perovskite phase [96], [97]. Silver iodide formation can be reduced using protective buffer layers, albeit at the cost of increasing parasitic absorption as well as introducing an additional processing step [96], [97]. Even if these stability issues can be mitigated, increasing silver use in solar cells raises both cost and sustainability concerns [67], [75]. Alternatives such as copper nanowires and carbon nanotubes also exhibit poor stability, high contact resistance and poor substrate adhesion [45], [94]. A viable indium-free TCE must overcome these issues to achieve success in tandem solar cells.

Graphene shows great promise as a TCE for high-efficiency PV. Its broadband transmittance exceeds that of even the most transparent TCOs such as IO:H and IZrO, giving it unique benefits in a tandem device [98], [99], [100], [101]. In recent years, graphene has become increasingly low-cost to produce in large areas [102], [103]. It can be deposited gently on delicate perovskite layers at room temperature without sputtering [104], [105], [106]. Critically, it can be produced entirely using sustainable materials, giving it potential to enable multi-TW scale PV [107]. However, the use of graphene as a TCE in PV has been limited due to its relatively high R_{sheet}, owing to its very low carrier concentration [104], [106]. An understanding of methods to introduce additional carriers in graphene offers potential to unlock graphene as a TCE for high-efficiency tandem photovoltaics.

Chapter 2

Graphene as a Transparent Conducting Electrode for Perovskite/Silicon Tandem Photovoltaics

2.1 **Graphene Structure and Properties**

Graphene is a promising TCE owing to its properties including high T%, relatively low R_{sheet}, and strong chemical and mechanical robustness [101], [108]. These characteristics arise from its unique physical and chemical structure. Graphene consists of a single atomic layer composed entirely of carbon atoms arranged in a two-dimensional lattice [109], [110]. Unlike typical materials, carbon atoms can form a thermodynamically stable two-dimensional monolayer due to the tight in-plane covalent bonds which facilitate its strong hexagonal honeycomb lattice structure [109], [111]. Figure 2.1 (a) and (b) illustrate this lattice structure and bonding. Each carbon atom forms three σ-bonds with neighbouring carbon atoms with s, p_x, and p_y sp^2 hybrid orbitals. With four valence electrons, this lattice structure leaves one free electron in the p_z orbital to contribute to the conduction [112]. Adjacent p_z orbitals can overlap to form delocalised π-bonds, where the π-band is filled and the π∗-band is empty [112].

Figure 2.1 (c) and (d) illustrate how the π electrons in graphene follow a linear energy-momentum relationship, with the conduction and valence band edges meeting at Van Hove singularities known as “Dirac points” at each atom, forming the characteristic “Dirac Cones”. Is also clear from Figure 2.1 (c) and (d) that graphene does not have a band gap, despite the zero density of states at the Dirac point. This unique electronic structure allows graphene’s electrons to travel at a constant velocity, as if they are massless Dirac fermions [110], [113].

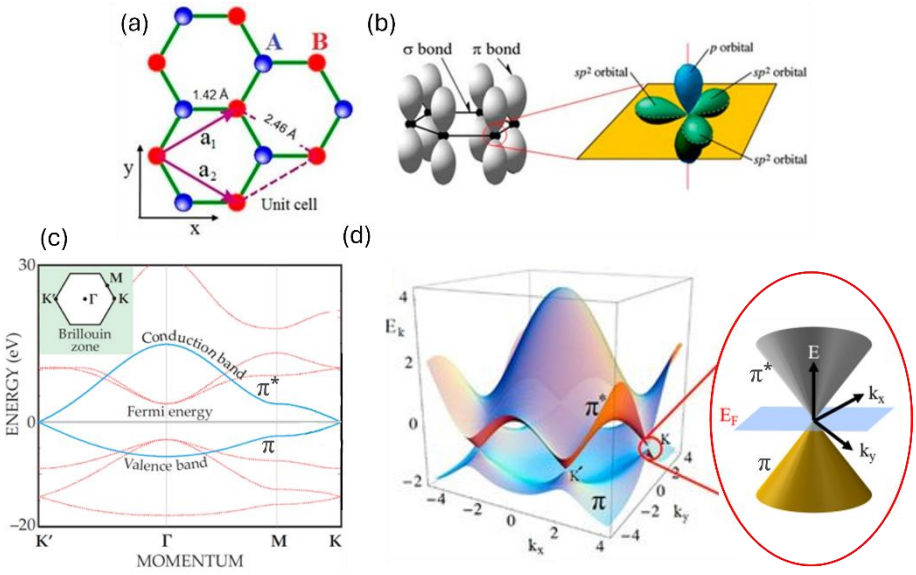

Figure 2.1: Bonding and band structure in graphene. (a) Unit cell from which the honeycomb lattice structure arises, consisting of two carbon atoms A, and B. (b) σ and π bonding of carbon atoms in graphene's honeycomb lattice, forming sp^2 and p_z orbitals. (c) Energy-momentum relationship in undoped graphene, with filled π and empty π∗ band. Inset, graphene Brillouin Zone, with the K point corresponding to the position of graphene's "Dirac cone". (d) "Dirac cone" in undoped graphene, with zero density of states at the Fermi energy E_F. Components adapted from ref. [114], [115].

The low carrier concentration of graphene arises from its structure. The overlap of p_z orbitals leads to the formation of delocalised π-bonds, resulting in graphene having an average of one free charge carrier to contribute to conduction per atom. This gives "undoped" monolayer graphene its low carrier concentration $\approx 10^{10}$–10^{12} /cm^2 at room temperature, often orders of magnitude below that of TCOs [111], [116], [117].

Despite its low carrier concentration and thickness, graphene's R_{sheet} remains relatively low due to its exceptionally high mobility. Graphene's delocalised charge carriers behaving as massless Dirac Fermions enable its carrier mobility to be among the highest of any material, and can be as high as 2×10^5 cm^2 /V s at room temperature, if freestanding in single-crystal form [111], [118], [119]. This gives undoped, freestanding graphene an intrinsic R_{sheet} limit of ≈30 Ω/□, assuming a typical carrier concentration of 10^{12} /cm^2 [111]. However, freestanding graphene of multiple cm^2 are unstable, as their high phonon density forces them to fold [113]. Transferring graphene to a substrate mitigates this folding, but limits its mobility to 4×10^4 cm^2 /V s. This reduction is attributed to carrier scattering by charged impurities on the substrate

[111], [120]. This gives undoped graphene a minimum sheet resistance of ≈160 Ω/□. Due to additional scattering processes which depend on the synthesis technique, typical values for graphene sheet resistance are 500−1500 Ω/□ in air [121]. The sheet resistance of undoped graphene therefore cannot compete with indium-based TCOs, and is usually deemed too high for most applications.

As a single atomic layer, the effective thickness of graphene corresponds to the spread of delocalised electrons above and below the atomic plane, equivalent to the inter-plane spacing of graphite, ≈0.335 nm [122]. However, its measured thickness may range from 0.4 and 1.7 nm depending on fabrication method, surface chemistry and substrate adhesion [122]. Even with this variation, graphene's thickness is approximately two orders of magnitude less than the 40-100 nm typical of TCOs used in PV, and this enables it to have an ultrahigh transmittance despite having zero band gap [98], [99], [108].

The main source of transmittance loss in graphene arises from the interband transitions of massless Dirac fermions within the material [123]. These transitions result in a constant absorption of light which is limited by two factors: the fine structure constant $\frac{e^2}{\hbar c}$ and the number of layers m. The average absorption per layer can be calculated as $A\% = 100 - m\pi\frac{e^2}{\hbar c} = 2.3m\%$ [110], [123]. Monolayer (T% = 97.7%), bilayer (T% = 95.4%) and trilayer (T% = 93.1%) graphene therefore have a superior T% to that of TCOs with thickness sufficient for low R_{sheet} [99], [124], [125]. Graphene, lacking a band gap, does not contribute bandgap induced losses in the blue-violet region. While graphene has a small absorption peak ≈250−270 nm due to π−π* transition of electrons, this is not relevant to PV devices as it falls outside the useful solar spectrum under AM1.5G conditions [126]. Additionally, due to graphene having low free carrier concentration and plasma frequency, it does not contribute substantially to NIR FCA [101], [108], [127].

Graphene TCEs could also help reduce reflection in perovskite/silicon tandems. TCOs provide an antireflective benefit, with $n \approx 1.8–2.0$, an appropriate intermediary between air and either perovskite ≈2.7 or silicon ≈3.9 [128]. TCO thickness can be tuned to minimise interfacial reflection, constraining the thicknesses that can be used. Although graphene has $n \approx 2.4\text{-}3.1$, as it is only 0.335 nm thick, it does not significantly impact reflection at interfaces [118], [129], [130], [131], [132], [133]. This might necessitate the deposition of an additional antireflective coating (ARC) such as SiN_x or SiO_x. While this adds an additional processing step, it allows the ARC thickness to be varied independently of a TCO layer. Additionally, graphene's tight lattice makes it impermeable to water and gas, conferring additional stability, as well as limiting the diffusion of perovskite halide ions to the metal fingers [134], [135].

Graphene has strong potential for TCE applications, provided its properties can be maintained when fabricated in large areas. The next section will review methods to deposit graphene and discuss their suitable for device compatibility.

2.2 Graphene Fabrication

2.2.1 Exfoliation

The layers between graphene sheets in graphite are held together by relatively weak Van Der Waals forces. Mechanical exfoliation overcomes these forces using normal or shear forces, or by exploiting graphene's self-lubricating ability to produce graphene sheets. For example, adhesive tape can be used to exfoliate graphite, producing graphene flakes [109], [116]. Mechanically exfoliated graphene is monocrystalline, giving it the lowest number of defects compared to other synthesis techniques [118]. Consequently, its carrier mobility is high, ≈ 1.50×10^4 cm^2 /V s [109]. However, this technique is limited to sheets of several hundred μm across, limiting scalability for use in large-area TCEs [136], [137]. Ball-milling can be used to produce mechanically exfoliated graphene powders for scalable film fabrication [138], [139].

However, the flakes produced are typically <5 μm laterally, rarely uniformly monolayer and have a high defect density, significantly limiting the conductivity and transmittance of such layers in a potential TCE film [139], [140], [141], [142], [143].

Graphene can also be produced at a low cost and on a large scale using chemical exfoliation [144], [145], [146]. In liquid-phase exfoliation, graphene flakes are produced from graphite dispersed in specific solvents, usually when subject to shear stress and sonication [145]. The Van der Waals attraction can also be overcome using chemical intercalants to separate the layers. However, this method produces small, non-uniform flakes with poor conductivity, and so is not suitable for TCE fabrication [146], [147].

2.2.2 Chemical Vapour Deposition

Chemical Vapour Deposition (CVD) enables the scalable production of high-quality graphene. Typically, a growth substrate, such as copper [121], [125], [148], [149] or nickel [150] is placed in a high-vacuum furnace. Hydrocarbons such as methane or ethylene are then catalysed on the metal substrates at a temperature ≈ 300−1000 ℃ and pressures ≈ 0.1−100 torr [94], [124], [149]. After catalysis, the temperature is lowered, reducing carbon atom solubility, causing atoms to precipitate and form a monolayer on the surface. This process produces polycrystalline graphene with small, randomly oriented grains. CVD graphene has a modest level of impurities such as point defects, voids, microcracks and high-resistance grain boundaries, which degrade mobility [118], [124], [151], [152]. While adjusting the gas flow and substrate selection can improve film quality, eliminating defects entirely is challenging [151], [152], [153]. Additionally, mismatches between the thermal expansion coefficients of graphene and the substrate can cause residual strain during cooling, leading to wrinkles and ripples [154], [155]. These impurities, along with substrate interactions, result in a carrier mobility in CVD-graphene ≈1−4×10^3 cm^2/V s – an order of magnitude below mechanically exfoliated graphene [148]. However, CVD enables the production of sheets that span tens of

cm, making it highly suitable for large-area TCEs [156]. Despite the high cost of generating high temperatures and low pressures, the precursor gases required are inexpensive [124]. Therefore, although CVD-graphene is lower in quality than mechanically-exfoliated graphene, and more expensive than chemically-exfoliated graphene, it remains the most practical option for TCE applications.

2.2.3 Graphene Transfer

A disadvantage of CVD-grown graphene is that it requires a complex transfer process from the metal to the target substrate [156]. This increases manufacturing costs, and introduces additional impurities such as wrinkles, and polymer residues. The most widely used technique is wet transfer [156]. Silicon with ~300 nm SiO_2 is often used as a target substrate as it enables the visualisation of graphene with the naked-eye through interference [148], [153], [157]. A polymer such as polymethyl methacrylate (PMMA) is spin-coated onto the graphene/copper surface to protect it during the transfer process [124], [153], after which low-quality graphene on the rear of the metal substrate is removed via oxygen plasma treatment [156]. The metal substrate is removed using an etchant such as $Fe(NO_3)_3$, sodium persulfate, or ammonium persulfate [124], [125], [153], [158], [159]. Next, the PMMA/graphene is rinsed in deionised water, and lifted from the water using the target substrate [158]. When the sample is heated above the glass transition temperature of PMMA, the PMMA softens and moulds to fit the substrate conformation, increasing contact and Van der Waal adhesion between the graphene and the substrate [153], [158], [160]. The PMMA is later removed using hot acetone [160]. This technique is low cost, which has led to its widespread use on laboratory scales. Moreover, the metal substrate can be reused, with the entire process consuming less energy and fewer carbon emissions compared to ITO [107]. The wet transfer process has several limitations. Principally, the PMMA is very difficult to remove completely, and its residues degrade graphene's carrier mobility and transparency [99], [125], [161], [162]. The polymer residues

also introduce an undesirable p-doping effect that is difficult to control [161], [162]. Moreover, the metal etchants used are environmentally hazardous, requiring expensive disposal [163]. The complexity and poor repeatability of wet transfers may also limit their ability to scale [147].

For successful implementation of graphene as a TCE, a scalable, contaminant-free, environmentally transfer technique is desired to replace the standard wet transfer. Yet, wet transfer remains suitable for material characterisation and assessing its suitability as a TCE for perovskite/silicon tandem cells under laboratory conditions.

2.3 Graphene for Perovskite/Silicon Tandems

To integrate CVD-graphene in tandems, its deposition must be compatible with the delicate layers involved. CVD-graphene has been successfully transferred to perovskite cells without damaging the absorber or typical hole-transport layers (HTLs), such as 2,2',7,7'-Tetrakis[N,N-di(4-methoxyphenyl)amino]-9,9'-spirobifluorene (spiro-OMeTAD), poly(3-hexylthiophene) (P3HT), Poly(2,3-dihydrothieno-1,4-dioxin)-poly(styrenesulfonate) (PEDOT:PSS) and NiO_x, maintaining good, defect-free interfaces [104], [105], [106], [164], [165], [166], [167], [168]. Graphene has also been implemented in SHJ cells without damaging the a-Si surface [169], [170], [171]. However, its R_{sheet} was too high to match the performance of TCOs [106]. To achieve its full potential in tandems, a suitable graphene doping technique compatible with the perovskite/silicon tandem device structure is essential.

2.4 Chemical Doping of Graphene

Doping can be used to increase the carrier concentration of graphene, in the same manner as bulk semiconductors. When dopants are introduced to graphene, they contribute localised energy states in its band structure; the Fermi level moves away from the Dirac point, providing extra charge carriers to improve electrical conductivity [98], [121], [172]. With additional

charge carriers, scattering increases, reducing the overall mobility of the device. Therefore, any doping process should be precisely controlled for a good balance between scattering losses and carrier concentration.

Chemical doping involves the addition of impurity atoms into a material, where these impurities should have more charge carriers than the intrinsic material. Chemical doping typically refers to substitution or surface-adsorbed doping [121]. Substitutional doping of graphene involves increasing carrier concentration by replacing a number of sp^2 carbon atoms with atoms of similar size, with fewer electrons such as boron for p-doping, or with more electron such as nitrogen for n-doping [121], [173], [174], [175]. However, substitutional doping techniques reduce carrier mobility of graphene by breaking the C-sp^2 -π bond conjugation so that the dopant species can covalently bond with the surrounding carbon atoms in the graphene lattice [121]. The balance between increasing carrier concentration and reducing carrier mobility is difficult to achieve, often leading to sheet resistances too high for TCEs, or poor dopant stability [173], [176]. Graphene can also be doped through the adsorption of electron-accepting or electron-donating species onto its surface. Charge is transferred with low lattice disruption via the formation of "charge-transfer complexes" [121]. Bianco et al. have used this technique to produce large-area monolayer graphene sheets with R_{sheet} comparable to that of many TCOs, reaching ≈120 Ω/□ [121], [125]. In that case, the thionyl chloride ($SOCl_2$) dopant species was also covalently bonded to a carbon in the graphene lattice to increase stability. However, as such a covalent bond involves disrupting the lattice, it likely reduces the carrier mobility through the introduction of localised scattering centres, but data on mobility was not provided by the authors.

Increasing the charge carrier concentration will inevitably reduce the mobility by increasing electron-impurity and electron-phonon interactions. However, with chemical doping, the doping is not fully uniformly distributed and introduces lattice disruption. This creates local

disorder and thus more pronounced scattering at charged scattering centres, further limiting mobility. To minimise mobility degradation, a uniform doping technique which can be precisely controlled must be developed.

2.4.1 Chemical Doping for Graphene TCEs in Perovskite/Silicon Tandems

Graphene can be doped using perovskite HTL materials MoO_3, P3HT and PEDOT:PSS in a perovskite cell, with compatibility in perovskite/silicon tandems [104], [164], [165], [167]. In these cases, the doping involves weak and often unstable p-type surface charge transfer from the HTLs. For thermally evaporated MoO_3, it usually exists as several intermediate oxidation states of MoO_x ($2<x<3$) [177]. This non-stoichiometric nature allows for positive charge to be transferred from the MoO_x to the graphene, inducing a weak, metastable p-type doping [167], [177], [178], [179]. The p-type nature of PH3T was ascribed to induce a p-doping effect in an adjacent graphene layer [164]. The authors did not explore the mechanism, but it is likely a limited surface charge transfer due to the relatively close work function between graphene and P3HT. Similarly, PEDOT:PSS doping likely occurs due to the transfer of holes from PEDOT to the graphene. Graphene doping was also achieved in perovskite cells by sandwiching graphene between a spiro-OMeTAD HTL and transparent polymer cap [105]. This enabled the stabilisation of atmospheric adsorbents close to the graphene surface to provide additional positive charge carriers for p-doping [105]. Yet, in these examples, the doping did not generate sufficient carrier concentrations, leading to low perovskite cell efficiencies relative to cells with indium-based TCEs [104], [164], [165], [167].

Doping graphene with $AuCl_3$ in a perovskite cell can reduce its R_{sheet} significantly, offering performance rivalling ITO [168], [180]. However, aggregated Au particles increase light scattering, minimising the maximum efficiency potential, particularly deleterious if incorporated in a tandem cell stack [168], [180]. 'Transfer-free' graphene for flexible substrates was doped using NiO_x, enabling R_{sheet} <150 Ω/□, while preserving high transmittance [166].

But this approach is limited to flexible substrates and specifically focuses on hole transport, limiting applicability. Therefore, it is critical to develop alternative approaches that can uniformly dope graphene TCEs throughout different regions of a tandem, ensuring that the desired R_{sheet} can be attained without impacting transmittance or stability.

2.5 Graphene Doping Using Ion-Charged Dielectrics

An alternative approach to dope graphene is using the electrostatic field effect. By establishing an electrostatic field in near graphene using a gate bias, a mirror charge is induced within it, increasing *N* [116]. This is typically achieved using a graphene field-effect transistor (FET). Figure 2.2 (a) depicts a typical graphene FET (GFET) on SiO_2/Si, with source, drain and gate terminals. For GFET characterisation, the drain-source bias (V_{DS}) can be fixed while the drain-source current (I_{DS}) is measured at varying gate-drain bias (V_{GD}); alternatively, the V_{DS} swept as V_{GD} remains constant. Figure 2.2 (b) shows a typical GFET curve at fixed $V_{DS,}$ in terms of R_{sheet}. At $V_{GD} = 0$, the charge carrier concentration is at its lowest and the R_{sheet} is at its highest. Varying this potential modulates the current flowing from S to D by changing the size and shape of the active channel, permitting carriers to flow. Figure 2.2 (c) illustrates the impact on the Fermi level of graphene as the V_{GD} is varied. When a negative V_{GD} is applied, the lower Dirac cone is filled, and the hole concentration is increased, inducing p-doping [109], [116]. N-doping can be achieved by applying a positive V_{GD} to increase the electron concentration [109], [116]. This technique allows for the reversible control of graphene's charge concentration up to $\approx 10^{13}$ q/cm^2 using a SiO_2 dielectric, limited only by its breakdown strength [116]. In field-effect doping, the mobility is reduced to a less significant extent than chemical doping, as the applied electrostatic field is relatively uniform, limiting impurities and lattice disruption. This method can reduce R_{sheet} to values <100 Ω/□ [116]. However, this R_{sheet} is only achieved when the power supply is switched on. This precludes it from use for graphene doping for TCEs and limits it as a characterisation technique.

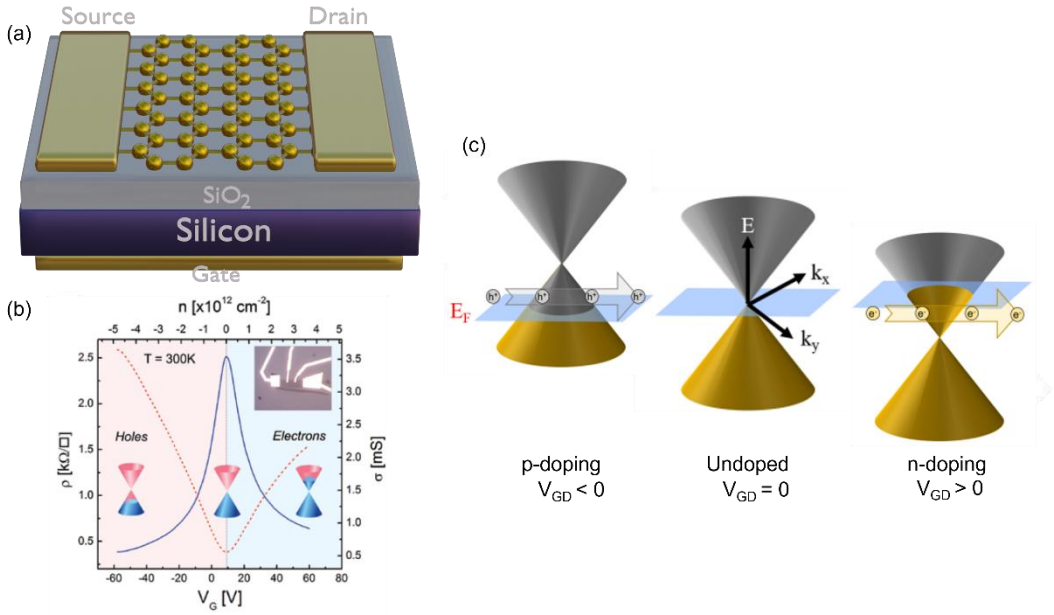

Figure 2.2: (a) Graphene Field-Effect Transistor structure. (b) Graphene FET drain-source current gate-drain voltage (I_{DS}-V_{GD}) type characteristics in terms of R_{sheet} and conductivity. Reprinted from ref. [181], with permission. © 2013 The Electrochemical Society. (c) Changes in position of the Fermi level under p-type, undoped and n-type doping conditions induced by varied V_{GD}.

A promising technique to electrostatically dope graphene without an opaque metal gate involves using charge stored in the substrate to generate the electric field. Paradisi et al. demonstrated that under applied bias and high temperature, Na^+ ions can be migrated within a thick soda-lime glass film to electrostatically dope graphene, enabling significant carrier concentration modulation $>10^{14}$ /cm^2 [182]. However, this requires an opaque metal electrode, is restricted to thick soda-lime glass, and the doping effect diminishes outside-of-vacuum, hindering its applicability for perovskite/silicon tandem cells. Additionally, its stability is unclear, given the high mobility of Na^+ ions at room temperature, which may lead to unintended changes in carrier concentration over time.

Bonilla et al. demonstrated that using corona charge and solid-state alkali ions, it is possible to permanently drive-in high charge concentrations in thin films of SiO_2 on Si [183], [184], [185] This establishes a quasi-permanent electrostatic field in the thin dielectric film that is expected to remain stable over commercial timescales [184]. In an "ion-charged dielectric" (ICD), ions are prevented from crossing from dielectric to silicon as no energy states are available for free

carriers in the silicon [184], [186], [187]. This technique has been used for effective surface passivation of silicon, but it has yet to be shown to increase the carrier concentration in graphene [183], [184].

Figure 2.3 is a schematic of how an ICD might be used to modulate the conductivity of graphene. Similar to a GFET, the electric field generated from a positively-charged ICD could be used to induce n-doping. As the mobility of electrons and holes in graphene is equal [64], this technique also gives the potential to p-type graphene with low R_{sheet}, if negatively-charged ICDs can be achieved. This could enable novel device functionality, as high-performance p-type TCOs are not yet available [188]. As graphene is extremely sensitive to substrate charge, ICDs bring the potential to dope graphene without disrupting the lattice for the minimum reduction in mobility, with stable, tuneable, and reversible charge control uniformly over large areas [184], [189]. Moreover, as this technique does not block light transmission, it is applicable to graphene doping for TCE applications. Additionally, other devices utilising TCEs such as touchscreen displays, LEDs and electrochromic displays could benefit from this technique.

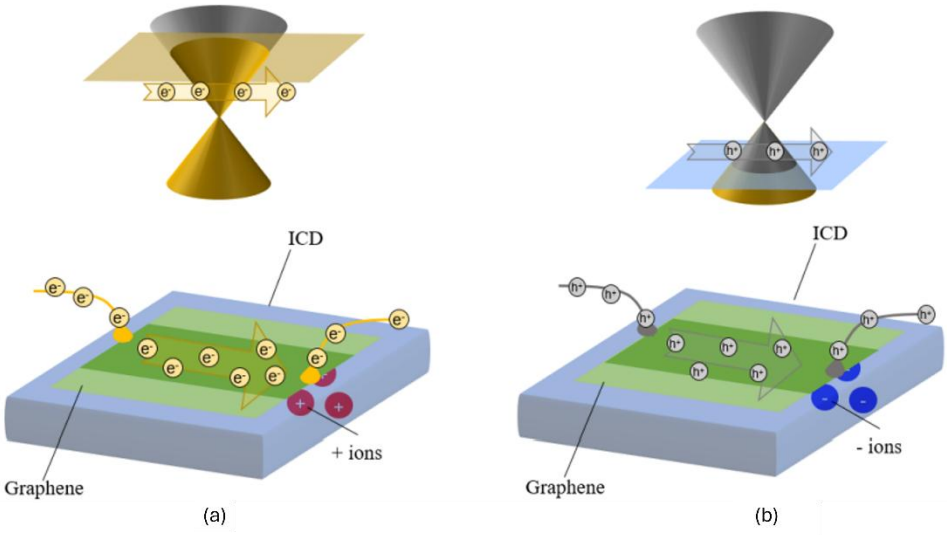

Figure 2.3: Using an Ion-Charged Dielectric to induce field-effect doping to produce n-type and p-type graphene. (a) Positive ions in the dielectric induce n-type doping. (b) Negative ions induce p-type doping in graphene.

2.6 **Aims and Objectives**

This thesis develops novel graphene doping techniques using ion-charged dielectrics and evaluates their suitability for integration in perovskite/silicon tandem photovoltaic cells. Methods to introduce ionic charge to a variety of different dielectric materials, including SiO_x, SiN_x, PMMA, AlO_x ,and their combinations, are developed and characterised, and their stability is investigated. These charged dielectric films are placed at close interface with graphene, and the impact on graphene's electrical, optical and structural properties are systematically studied.

Finally, the viability of these ICD-based doping techniques is modelled for integration in tandem photovoltaic cells. Such a highly-doped, high-transmittance graphene layer could circumvent the issues with conventional TCEs that are currently limiting perovskite/silicon tandem uptake and limit efficiency.

2.7 Structure of this Thesis

- **Chapter 3** provides a detailed description of the experimental procedures to fabricate and characterise the graphene and charged dielectric films
- **Chapter 4** shows the first proof-of-concept of ICD-doping of graphene, where the electrical and optical properties of graphene are recorded when interfaced to corona-charged dielectric membranes.
- **Chapter 5** demonstrates that the migration of charged alkali ions dielectric in can be used to strongly n-type doping in graphene. The migration of these ions under different conditions of temperature, applied bias, and their stability to the graphene transfer process is studied. The electrical properties of graphene are evaluated in these conditions.
- **Chapter 6** investigates the use of ions in glass to provide n- and p-type doping in graphene. The charge storage in SiO_x/SiN_x nanolayers interfaced with quartz is compared with the intrinsic ionic charge in borosilicate glass for graphene doping.
- **Chapter 7** demonstrates that polymer-based dielectrics such as a thin spin-coated PMMA layer can also hold sufficient charge to induce high charge concentration in graphene, offering scope for a wide range of device needs. The direct growth of a thin AlO_x layer on graphene using thermal evaporation is developed, and charged using corona ions for tailorable p- and n-type graphene.
- **Chapter 8** explores the impact of using an ICD-graphene TCE in a perovskite/silicon tandem device. The device performance is assessed using computational modelling, and compared with state-of-the-art TCEs.
- **Chapter 9** summarises the findings of this thesis, and discusses future research directions arising from this work.

Chapter 3

Methods

3.1 Sample Fabrication

3.1.1 Device Substrates

Table 3.1 summarises the main substrates used in this work. The p-type Czochralski (CZ) Si/SiO_2 substrates used in Chapters 5-7 were cleaved into squares ≈1.2 × 1.2 cm^2 using a diamond scribe, while the other substrates were used as supplied.

Table 3.1: Substrates used in this work

Chapter	Material	Total Area	Nominal dielectric thickness	Supplier
4	0.5 × 0.5 mm^2 SiO_2 membrane	0.5 × 0.5 cm^2	300 nm	EM Resolutions
4	1 × 1 mm^2 SiN_x membrane	1 × 1 cm^2	100 nm	EM Resolutions
5	p-type CZ Si/SiO_2	1.2 × 1.2 cm^2	300 nm	UniversityWafer Inc.
6	Borosilicate glass	1 cm^2	1.1 mm	UCQ Optics [190]
6	Quartz	2 × 2 cm^2	1 mm	UCQ Optics [191]

3.1.2 Plasma Enhanced Chemical Vapour Deposition

Plasma Enhanced Chemical Vapour Deposition (PECVD) allows for the growth of high-quality dielectric films within minutes, at relatively low temperatures [192]. PECVD was used

to deposit SiN_x and SiO_x on silicon, glass and quartz substrates for devices characterised in Chapter 6. Table 3.2 lists the deposition parameters used with an Oxford Instruments PlasmaLab 80+ PECVD. In the case of the 50 nm SiO_x layer, argon was used as the purge gas due to an equipment upgrade.

Table 3.2: Plasma Enhanced Chemical Vapour Deposition Dielectric Fabrication Conditions.

Deposition Parameter	**50 nm SiO_x**	**60 nm SiN_x**	**5 nm SiN_x**	**5 nm SiO_x**
Power (W)	20	20	20	20
Plate Temperature (℃)	350	350	350	350
Pressure (mTorr)	800	650	650	800
Time (s)	50 s	3 min 12 s	16 s	5 s
Ammonia (sccm)	—	40	40	—
Silane (sccm)	200	380	380	200
Nitrogen (sccm)	600	600	600	600
Nitrous Oxide (sccm)	680	—	—	680
Argon (sccm)	1000	—	—	—
Measured Thickness	57.0±0.1 nm	66.7 nm	4.8±0.1 nm	3.9±0.1 nm

3.1.3 Graphene Transfer

Monolayer CVD graphene on copper substrates was obtained from *Graphenea S. A.*, in 4 × 6 cm^2 sheets [193]. As supplied, the films were coated in a 60-80 nm poly-methyl methacrylate (PMMA) film, forming a PMMA/graphene/Cu/graphene stack, ≈18 μm thick [193]. Noting this PMMA thickness is insufficient for reliable graphene wet transfer due to its mechanical instability, an additional 500 nm PMMA was spin-coated on the film. The PMMA spin-coating process is described in Section 3.1.4.

Graphene was transferred in a cleanroom following the standard wet transfer process as described in ref. [156], with adaptions developed for reduced $R_{sheet,}$ minimal PMMA residues, and reduced processing time. Figure 3.1 depicts the graphene transfer workflow. Figure 3.1 (a) depicts how, following PMMA-coating, the low quality, air-exposed graphene on the rear was removed by reactive-ion etching (RIE) using an oxygen plasma source to expose the copper substrate for uniform etching. The oxygen plasma was generated for 1 minute, with oxygen flow of 80 sccm and forward power 25 W, under a chamber at 100 mTorr. The PMMA/graphene/copper stack was then cut to areas from 0.4 × 0.4 cm^2 to 1.5 × 1.5 cm^2 using a circular blade. Figure 3.1 (b) depicts how the copper layer was removed by floating the stack on 0.32 M ammonium persulfate $(NH_4)_2S_2O_8$ (APS) solution for 2-5 hours at room temperature, with etching time varying by graphene area; larger pieces require more time. Complete copper etching, indicated by the absence of visible copper, was confirmed by energy-dispersive X-ray spectroscopy (EDS).

Figure 3.1 (d) depicts how the remaining PMMA/graphene stack was rinsed by transferring it three times to fresh beakers of deionised water with a glass slide. Standard substrate cleaning involved rinsing in acetone and isopropanol alcohol (IPA) for 30 seconds each, followed by nitrogen spray drying until solvents were no longer visible under 50× magnification. For experimental workflows where extrinsic ions were not to be added, the substrates were further cleaned by annealing at 350℃ with 300 sccm nitrogen at 650 mTorr for 5 mins. Substrates were subsequently made hydrophilic using an oxygen plasma cleaning process, involving a 5-minute oxygen flow of 25 sccm and forward power 200 W, in a chamber at 100 mTorr. This final process helps to improve graphene adhesion to the substrate, as water at the graphene/substrate interface can weaken graphene/substrate adhesion, and result in hole formation and additional defects if it rapidly evaporates through the graphene at high temperatures.

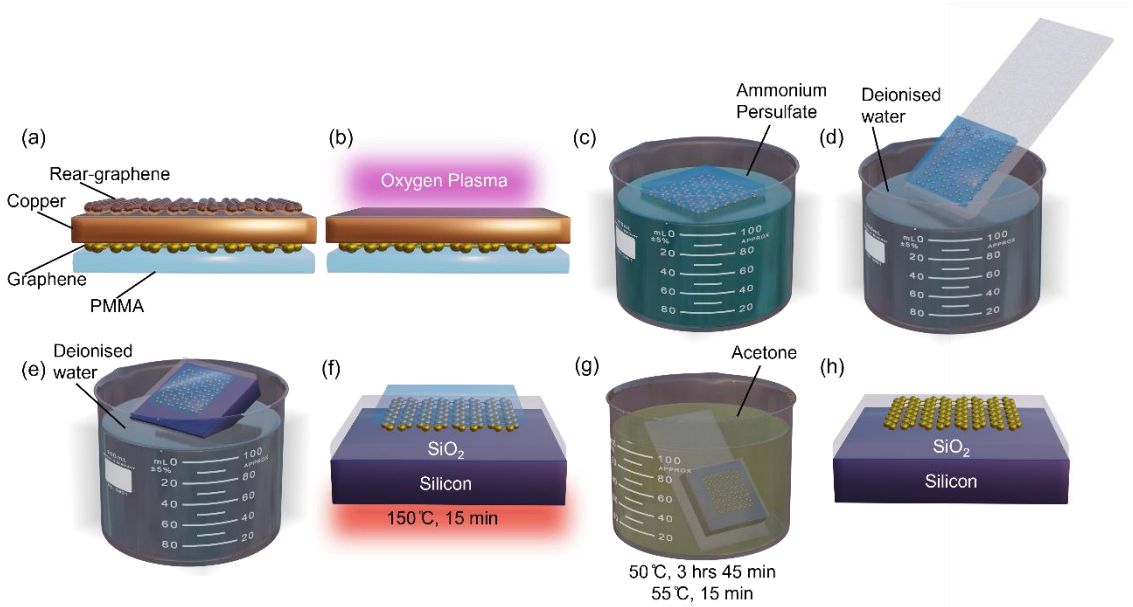

Figure 3.1: Graphene Transfer Workflow. (a) As purchased graphene stack consisting of PMMA/graphene/ccopper/rear-graphene. (b) Rear-graphene removal using oxygen plasma. (c) Copper substrate removal in ammonium persulfate. (d) Rinsing in deionised water. (e) Substrate fishing of graphene layer from deionised water. (f) Annealing on a hotplate. (g) PMMA removal in hot acetone. (h) Completed graphene transfer.

Figure 3.1 (e) depicts how the cleaned substrates were used to "fish" the graphene from the deionised water. After allowing residual water to evaporate over 1-2 minutes, the samples were dipped by each corner in a beaker of fresh IPA, ensuring that the entire graphene layer was exposed to the IPA. When IPA contacts the water near the graphene, it reduces the surface tension of the water, allowing it to flow away more easily. Dipping the corners, helps to gently displace excess water molecules at the graphene/substrate. Figure 3.1 (f) depicts how after drying in air at room temperature for 24 hours for further water evaporation, the samples were annealed on a hot plate at 180 ℃ for 15 mins, slowly ramping to the set temperature over an additional 15 minutes to prevent rapid moisture evaporation, which may cause defect formation. This anneal ensures strong graphene/substrate adhesion. Following this, the samples underwent a 10-hour bake at 150 ℃ in a nitrogen furnace to remove any residual moisture. Figure 3.1 (g) depicts how the PMMA layer was removed by immersing the samples in acetone for 3 hours and 45 mins at 50 ℃, with a final 15 mins at 55 ℃. It was observed that warmer temperatures facilitated more complete and rapid PMMA removal. These temperatures were

chosen to ensure the acetone remains as hot as possible without reaching its boiling point of 56.2 ℃, at which the graphene might be damaged by agitation. To maintain uniform elevated temperatures, a water bath was used, and the beaker was covered with aluminium foil to limit acetone evaporation. To remove any residual PMMA or acetone, the samples were dipped in acetone and IPA for 30 s each, followed by a gentle nitrogen spray after each solvent dip. This completes the transfer process. Samples were stored in a low-pressure chamber purged with nitrogen to minimise moisture-induced degradation and were only removed to carry out further processing and characterisation. Table 3.3 provides a list of the graphene dimensions transferred in this work.

Table 3.3: Summary of the transferred graphene areas used in this thesis.

Chapter	Material	Substrate Area	Graphene Area
4	0.5 × 0.5 mm^2 SiO_2 membrane	0.5 × 0.5 cm^2	0.4 × 0.4 cm^2
4	1 × 1 mm^2 SiN_x membrane	1 × 1 cm^2	0.4 × 0.4 cm^2
5, 7	p-type CZ Si/SiO_2	1.2 × 1.2 cm^2	1 cm^2; 1.5 × 1.5 cm^2
6	Borosilicate glass	2 cm^2	1 cm^2; 1.5 × 1.5 cm^2
6	Quartz	1 cm^2	1 cm^2; 1.5 × 1.5 cm^2

3.1.4 PMMA Spin Coating

Spin-coating is a well-established technique for rapidly depositing uniform thin films such as polymers and nanoparticle suspensions and is used widely in microelectronic device fabrication [194], [195], [196]. To deposit a thick PMMA support layer for graphene transfer, a PMMA/graphene/copper/graphene sheet with 60-80 nm PMMA, of area ~4 cm^2 was attached to a dummy silicon wafer or glass slide using Kapton^{TM} tape, and placed on a vacuum chuck

in a Laurell WS-650Mz-23NPPB spin coater. The substrate was gently cleaned with a nitrogen gun to remove any dust particles. For the case of Chapter 7, fully-metallised graphene/SiO_2/Si devices were first rinsed with acetone and IPA, then dried with a nitrogen gun before spin coating, to ensure uniform coating. In this case, the Kapton tape was placed over the edges of the metal contact to prevent PMMA deposition on the electrical contact. Details of device metallisation are provided in Section 3.1.6.

PMMA is a single co-polymer commonly used as a high-resolution positive resist in photolithography for microelectronics patterning, as well as a protective layer [195]. In this work, PMMA with molecular weight 495,000 (495K) diluted a concentration of 8% in anisole (A8) sourced from *Kayaku Advanced Materials* was used. Figure 3.2 presents the relationship between spin speed and PMMA concentration in anisole, with data extracted from the supplier [197]. There is clearly strong proportionality between film thickness and PMMA concentration, with A8 PMMA saturating at thickness 520 nm at 4000 RPM. Table 3.4 presents the PMMA deposition processing steps used. In all cases, the solution was deposited dropwise with a pipette, with ≈2 ml sufficient to cover the surface of the substrate. Care was taken to avoid shaking the solution, or otherwise introducing air bubbles with the pipette. The solution was dropped at 500 RPM, and then spun at 4000 RPM for improved uniformity. After coating, the sample was annealed on a hot plate in air at 180 ˚C for 90 s for good adhesion between the PMMA and PMMA/graphene or graphene surface. PMMA thickness was determined using a Dektak Pro stylus profilometer.

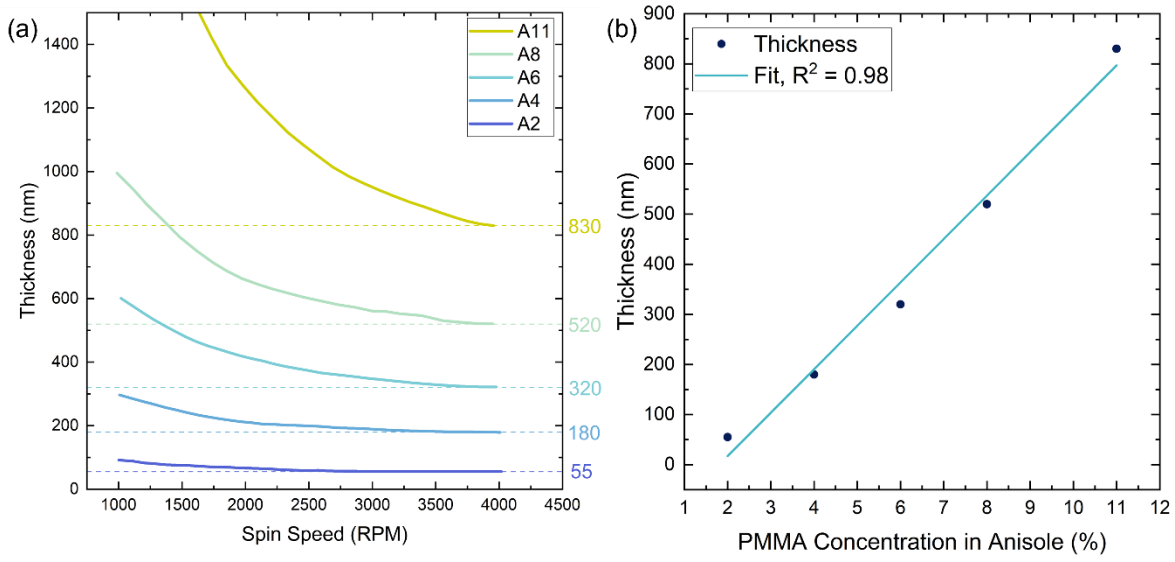

Figure 3.2: Relationship between the concentration of 495K PMMA in anisole, spin speed, and thickness. (a) Spin speed vs PMMA thickness. (b) PMMA concentration in anisole vs thickness. Data extracted from ref. [197].

Table 3.4: Processing parameters for PMMA spin-coating used in this work.

Step	Speed (RPM)	Time	Action
1	500	5 s	Solution pipetted on substrate surface
2	4000	50 s	—
3	500	5 s	—
4	—	—	Sample removed, and baked at 180 ˚C for 90 s

3.1.5 Graphene Laser Ablation

After transfer, a subset of samples underwent graphene patterning using a 5 W Linxuan LX-C1 UV nanosecond (ns) laser. An in-house process was developed for this work. Conventional patterning techniques, such as UV photolithography, e-beam lithography are widely established, achieving micron-scale or sub-10 nm resolution [198], [199], [200], [201]. However, such techniques often introduce chemical residues that can be difficult to be remove and thus contribute towards scattering [161], [202], [203], [204]. These chemicals may also compromise the stability of any extrinsic charge added. Additionally, such patterning

techniques typically require photoresist spin-coating, and use high-pressure vacuum chucks for mask alignment, processes that can destroy the delicate membrane substrates used in this work.

The laser graphene ablation process was developed following similar ablation protocols using ns and femtosecond lasers as in ref. [201], [205], [206], [207]. The Linxuan LX-C1 uses a crystal that when electrically excited, emits a coherent beam of UV photons at 355 nm. A Q-switch is used to limit the pulse release times to the ns range. The total fluence at a specific area is controlled by adjusting the laser power, frequency, speed, and number of loops. The fluence is maximised, and ablation width minimised at the focal point. The sample-lens distance was varied from the focal point to reduce fluence and prevent substrate damage. Table 3.5 presents the graphene ablation laser parameters used in this work. Patterns were designed in *EzCAD2.8*, and the sample positioned with a purpose-built stage allowing micron-scale XYZ manipulation. This enabled the patterning as low as ≈10 μm graphene channels.

Table 3.5: Laser parameters for graphene ablation.

Laser Parameter	Setting
Power	40%
Number of loops	12
Frequency	150 kHz
Speed	750 mm/s
Q-pulse width	5
Distance from focal length	5.7 mm

3.1.6 Thermal Evaporation

Thermal evaporation is a well-established physical vapour deposition technique for semiconductor device metallisation [17]. A high current is applied to a metal (Al, Au, Cr) under low vacuum, heating it until it melts and subsequently evaporates in all directions. To prevent

oxidation, a vacuum <4×10^{-6} mbar was maintained. Bespoke brass stencil masks for custom contact structures in standard devices were fabricated in-house using a Linxuan LX-A1 20 W ns 1064 nm fibre laser. The mask fabrication process for FET devices is described in Section 3.1.7.

For standard devices, ≈100 nm Al was deposited. Precise thickness control was achieved using a calibrated quartz crystal monitor. For high-temperature measurements in air, a 5 nm/50 nm Cr/Au contact was used to mitigate oxidation risks. The thin Cr layer was used as Au alone has poor adhesion to oxides and glass [208]. To protect contacts from probe damage during repeat measurements, a silver electrodag was painted over the evaporated metal. This was allowed to dry for 30 minutes before measurement to ensure good contact with the evaporated metal.

3.1.7 Stencil Fabrication and Metallisation of Field-Effect Transistor Devices

A specialised stencil mask fabrication process was developed for FETs, as these require micron-scale mask alignment with 10-15 μm graphene channels. Group member Xinya Niu developed the mask fabrication protocol for MoS_2, which was adapted in this work for graphene FETs. A copper transmission electron microscopy grid with metal line width ≈15 μm to set the FET channel length, was attached to a 3-mm diameter ferromagnetic washer using paraffin wax. A 355 nm Inngu UV-picosecond laser was used to selectively ablate the copper grid, allowing for a larger area can be electrically connected. This mask was then attached to sample using a magnetic stage and aligned to the graphene channel for thermal evaporation using an optical microscope and in-house mask alignment stage.

3.2 Charge Deposition and Drive-In

3.2.1 Corona Charge Deposition

The corona discharge method was used to deposit positive or negative ions on the surface of a material. Corona charges arise from the ionisation of air molecules. Figure 3.3 depicts the

standard “point to plane” corona-charging setup used in this work. Samples are positioned with the rear side in contact with a ground electrode, while the dielectric to be charged faces up towards a point discharge electrode at a known distance. When a high voltage is applied between the electrodes, the air molecules near the discharge electrode become ionised, accelerating electrostatic charge towards the ground electrode, where the sample lies. Positive applied voltage deposits positively charged corona ions (mostly $(H_2O)_nH^+$) on the sample, while a negative applied voltage deposits negatively charged corona ions (mostly CO_3^-) [209], [210].

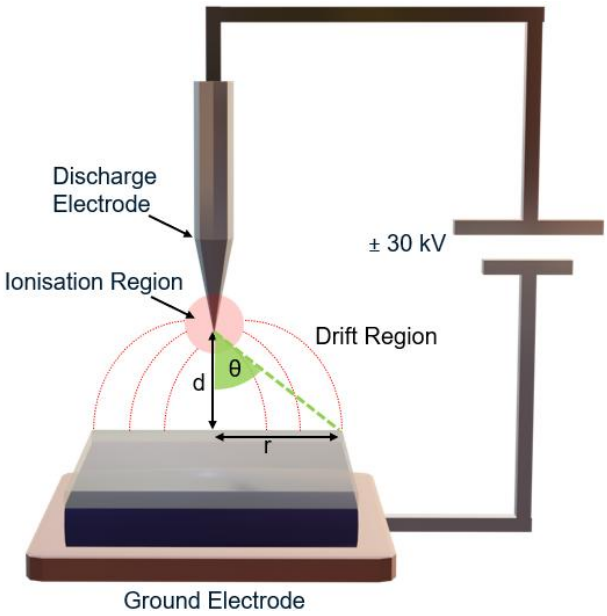

Figure 3.3: Standard point-to-plane corona charging setup used in this work.

The quantity of charge deposited was controlled by varying the duration the samples were held under the biased discharge electrode. The uniformity of the charge distribution follows Warburg’s law, which describes current density (j) of corona charges deposited these conditions [211], [212]:

$$j(r,d) = j_0 cos^5\theta \quad (3.1)$$

$$\theta = tan^{-1}\left(\frac{r}{d}\right) \quad (3.2)$$

$$j_0 \approx \frac{I}{2d^2} (3.3)$$

where j_0 is the peak current density, *I,* the total corona current, *d*, the distance from the discharge to the ground electrode, and θ the angle between the point discharge and the sample edge, as shown in Figure 3.3. Increasing *d* improves charge uniformity across the plane by reducing θ displacement, albeit reducing the deposition rate, necessitating an increase in applied voltage to maintain deposition. Typically, samples were placed at *d* = 20 cm below the discharge electrode, with an applied potential of ±30 kV, generating a corona current of I ≈ ±0.015-0.02 mA. With samples in this work having area 0.25 cm^2 to 2.25 cm^2, *r* = 0.25-0.75 cm. Under these conditions, the variation of deposited charge across the surface is <0.5%.

To further probe charge storage in suspended SiO_2 membranes with lateral dimension ~500 μm, I constructed a bespoke micro-corona charger to allow for direct deposition of corona charge on the dielectric with simultaneous electrical measurement. The set-up and calibration of this apparatus is described in Section 4.8, and is illustrated in Figure 4.14.

3.2.2 K^+ Ion Deposition and Drive-In

An alkali ion source can be deposited using thermal evaporation, spray coating or spin coating, with ions driven into dielectric/semiconductor interfaces by applying an electric field at elevated temperatures [183], [184], [213], [214], [215]. Here, spin-coating was used due to its rapidity and uniformity. The spin coating process is described in Section 3.1.4. Following the method of Yu et al, a KCl salt was dissolved in a solution of deionised water and IPA (30:70) at a concentration of 0.01 M [215]. Table 3.6 lists the KCl film spin-coating parameters used.

Table 3.6: Spin-coating parameters for KCl film deposition.

Step	Speed (RPM)	Time	Action
1	500	10 s	Solution pipetted on substrate surface
2	3000	30 s	—
3	500	5 s	—

After spin-coating, ions were typically driven to the interface by charging the surface with positive corona ions for 30 seconds, and immediately placing the sample on a 420℃ hotplate for 10 seconds. Figure 3.4 depicts this processing step [215]. The high-temperature anneal provides sufficient energy for ion injection. By corona charging, a positive surface electric field is generated, promoting ion drift across the dielectric, such as toward the Si/SiO_2 interface. This process of corona charging with annealing was repeated for eight cycles to maximise the charge delivered [215], [216].

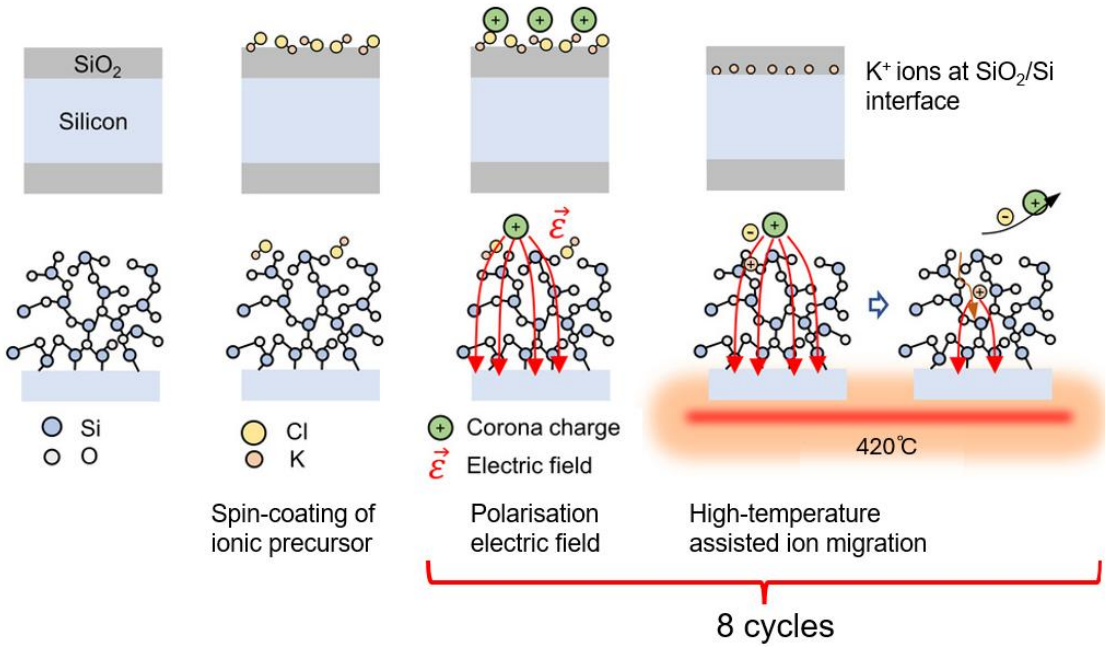

Figure 3.4: Primary method for ion delivery to dielectric interfaces used in this work, adapted from ref. [215]. Licensed by CC BY.

3.3 Electrical Characterisation

3.3.1 The van der Pauw and Hall Method

The van der Pauw (vdP) method can be used to measure the electrical resistivity of thin films, such as graphene [217]. In 1958, Leonard J. van der Pauw derived a relation for the resistivity of flat samples with arbitrary geometries and point contacts (A, B, C, D) [218], [219]. Figure 3.5 (a) depicts such a sample. Its R_{sheet} can be approximated by:

$$e^{\frac{-\pi R_{AB,CD}}{R_{sheet}}} + e^{\frac{-\pi R_{BC,DA}}{R_{sheet}}} = 1 \quad (3.4)$$

where $R_{AB,CD}$ and $R_{BC,DA}$ are the horizontal and vertical resistances, V_{DC}/I_{AB} and V_{AD}/I_{BC}, measured at 90° with respect to each other [218], [219]. "V_{12}" is the DC voltage measured between the contacts "1" and "2", while "I_{12}" is the DC current I injected into contact "1" and extracted from contact "2". However, Equation (3.4) applies directly only when $R_{AB,CD} = R_{BC,DA}$, simplifying to $R_{sheet} = \frac{\pi R}{\ln(2)}$, for a given resistance R. In the general case, where $R_{AB,CD} \neq R_{BC,DA}$, we need multiply R_{sheet} by a correction factor f where:

$$\frac{R_{AB,CD} - R_{BC,DA}}{R_{AB,CD} + R_{BC,DA}} = f \cdot \operatorname{arccosh}\left(\frac{e^{\frac{ln(2)}{f}}}{2}\right) (3.5)$$

where if $R_{AB,CD}$ and $R_{BC,DA}$ are almost equal, f can be approximated by:

$$= f \approx 1 - \left(\frac{R_{AB,CD} - R_{BC,DA}}{R_{AB,CD} + R_{BC,DA}}\right)^2 \frac{\ln(2)}{2} - \left(\frac{R_{AB,CD} - R_{BC,DA}}{R_{AB,CD} + R_{BC,DA}}\right)^4 \left(\frac{(\ln(2))^2}{2} - \frac{(\ln(2))^3}{12}\right) (3.6)$$

where $f \rightarrow 1$ as $R_{AB,CD} \rightarrow R_{BC,DA}$. This leads to the general equation for R_{sheet} in (Ω/□):

$$R_{sheet} = \frac{\pi}{\ln(2)} \cdot \left(\frac{R_{AB,CD} + R_{BC,DA}}{2}\right) \cdot f (3.7)$$

A typical square graphene measurement configuration is given in Figure 3.5 (b). This symmetrical structure ensures that $R_{AB,CD}$ and $R_{BC,DA}$ are similar, allowing the approximation for f to be valid.

The Van der Pauw method requires contacts be infinitesimally small to minimise errors from non-uniform current flow [218], [219], [220]. As this is not practically feasible, a contact correction factor can be applied [221], [222]. Figure 3.5 (c) depicts this correction factor, which is dependent on the ratio between contact width (δ) and sample width (*l*). Fine alignment of the metallisation mask ensured that the contacts were positioned at the edges, with triangles protruding onto the graphene layer such that δ <500 μm. With device width l = 0.4-1 cm, this ensures that δ/l = 0.05-0.125, for a correction factor of 1.01-1.001. This factor was applied to Equation (3.7) to give a corrected R_{sheet}. To validate this basic structure, it was compared to a more optimal cloverleaf structure, which minimises errors due to non-uniformities and suboptimal contact size and positioning [220]. Graphene cloverleaf structures were fabricated using UV laser patterning following the dimension guidelines from ref. [220]. Measurements indicated no significant deviations from the rectangular structure, indicating that the correction factors applied were sufficient.

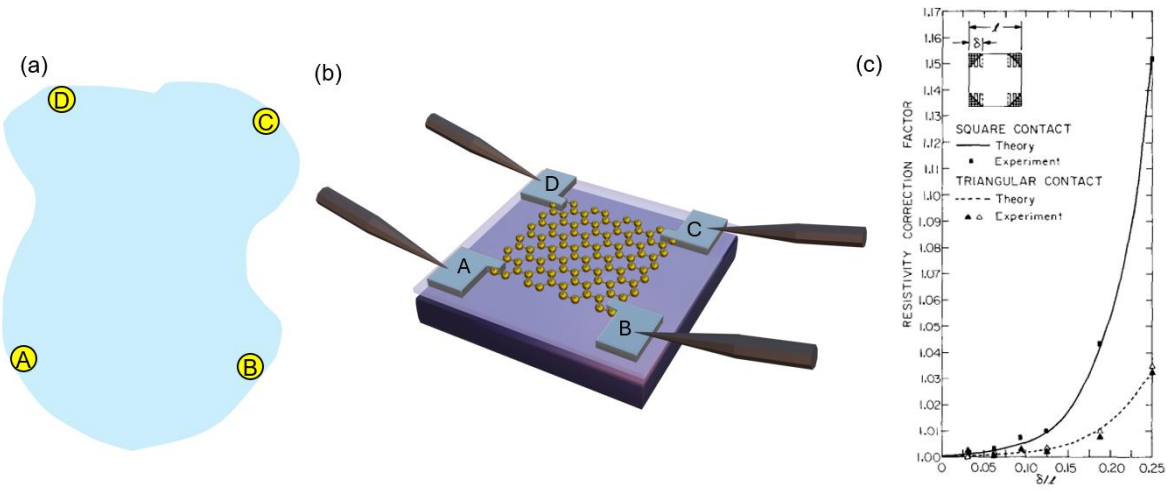

Figure 3.5: Van der Pauw measurement configuration. (a) Arbitrary-geometry sample with four-point contacts A-D. (b) Standard graphene vdP measurement geometry. (c) Contact size correction factor for vdP measurements, adapted from ref. [221]. The parameter l represents the length of the sample, while δ represents the width of the metal contact.

For the vdP relation to be valid, samples must be flat, homogeneous, have uniform thickness, have no isolated holes, and have a thickness much less than its width. Samples were visualised using optical microscopy to confirm compliance with these conditions.

The vdP method can be extended to measure carrier properties [218], [219]. By placing a strong permanent magnet with constant and uniform magnetic field B perpendicular to the sample, a potential difference known as the Hall voltage (V_H) is generated due to the Hall Effect [218]. The Hall effect refers to the deflection of charge carriers by the Lorentz force induced by the magnetic field. A positive V_H indicates p-type conduction, and a negative V_H indicates n-type conduction. The magnitude of this voltage can be used to calculate the sheet carrier concentration N (/cm^2), following:

$$N = \frac{IB}{q|V_H|} \quad (3.8)$$

where I is the current passing through the material. Using the same configuration as in Figure 3.5, V_H can be measured under applied magnetic field by injecting a current between diagonally opposite contacts, and measuring the voltage between the remaining two contacts, e.g. applying I_{BD} and measuring V_{AC}.. The difference in voltage measured under positive and negative B is

recorded. To minimise misalignment and thermoelectric voltage contributions, measurements under ±B are also taken with reversed current and opposite contacts (applying I_{AC} and measuring V_{BD}). The overall Hall voltage V_H is calculated as the mean of these measured voltages, and is used to calculate *N* following Equation (3.8). As $\mu = \frac{1}{N \cdot q \cdot t \cdot R_{sheet}}$ following Equation (1.1), we can rewrite Equation (3.8) to calculate Hall mobility (cm^2/Vs) as:

$$\mu = \frac{|V_H|}{I \cdot B \cdot R_{sheet}} \quad (3.9)$$

A magnet with magnetic field B = 0.165124 T was used, calibrated against a float zone silicon sample with known carrier concentration. Identical wires and probes were used to minimise errors associated with the thermoelectric effect.

For vdP and Hall measurement, I constructed two bespoke measurement apparatuses: one for small and large area samples for measurement ambient conditions. I also constructed a bespoke vdP apparatus for simultaneous electrical measurement and corona charge deposition in ambient conditions using the micro-corona charger described in Section 4.8. For these apparatuses, signal generation and measurement were conducted using a high-impedance Keysight B2901A source-measuring unit, controlled virtually in a bespoke LabVIEW program.

Finally, I constructed an additional VdP stage for high temperature measurements in vacuum. In these cases, a Keithley 2611A source-measurement unit with Thurlby Thandar TSX3510P DC power supply was used. The high temperature vacuum stage is described in further detail in Section 3.3.6.

3.3.2 Four-Point Probe Method

The four-point probe (4PP) method can also be used to characterise graphene's sheet resistance [223], [224], [225], [226], [227]. Four sharp metal probes of equal diameter and spacing are placed in contact with a material's surface. A current is injected through the outer two probes,

while the inner two probes measure the voltage drop generated by the current flow through the material. This technique assumes a homogeneous and uniform film, with sample area significantly larger than the probe spacing, and thickness much smaller than the probe spacing [223]. Under these assumptions, the sheet resistance can be calculated as [227]:

$$R_{sheet} = \frac{\pi \cdot V}{ln\,(2) \cdot I} \quad (3.10)$$

Measurements were taken at a minimum of 5 points and the mean calculated, to minimise error. Unlike vdP, the probes can be positioned anywhere on a sample, excluding edge areas where edge effects may distort current distribution. In this work, 4PP was used to measure graphene R_{sheet} differences on different substrate areas with varying charge concentrations. An Ossila Four Point Probe with 1.27 mm probe spacing, and 0.48 mm diameter probes was used.

3.3.3 Field Effect Transistor Characterisation

Field-effect transistor (FET) characterisation provides alternative technique to measure the carrier concentration, type and mobility of graphene [228]. The principles of this technique were explained in Section 2.7. The carrier concentration of a graphene channel can be determined using Equation (3.11):

$$n = \frac{\varepsilon_0 \varepsilon_r \cdot V_{Dirac}}{d \cdot q} \quad (3.11)$$

where V_{Dirac} is the voltage at the Dirac point, ϵ_0 is the vacuum permittivity 8.85×10^{-14} F cm^{-1} , ϵ_r is the dielectric permittivity, and d is its thickness [116].

Field-effect mobility of electrons and holes can be derived from the transconductance $\frac{\partial I_{DS}}{\partial V_{GD}}$ at constant drain-source voltage V_{ds}, the slope of the linear regime on either side of the Dirac point [228]. This slope relates to mobility as:

$$\mu = \frac{L}{W} \cdot \frac{d}{\varepsilon_0 \varepsilon_r \cdot V_{ds}} \cdot \frac{\partial I_{DS}}{\partial V_{GD}} \quad (3.12)$$

where L and W are the channel length and width.

In fabricated devices, V_{ds} was varied from 1-500 mV, with channel dimensions L ≈ 15 µm and W = 5-30 µm. Channels >50 µm were not achievable, as increased channel size increases the risk of encountering inhomogeneities such as defects, wrinkles, folds, and grain boundaries. Moreover, larger channels suffer from high current leakage and may lead to dielectric breakdown during high voltage sweeps, often necessary to reach the Dirac point. Signal generation and measurement were performed using Keithley 2401 and 487 source-measuring units controlled via a bespoke LabVIEW programme.

3.3.4 Capacitance-Voltage

The capacitance-voltage (CV) technique was used to measure the K^+ density at the SiO_2/Si interface. In a metal-oxide-semiconductor (MOS) capacitor structure, changes in gate voltage change its capacitance, modifying the band structure and carrier concentration at the SiO_2/Si interface. CV is widely used in semiconductor characterisation, with detailed descriptions available in refs. [17], [229], [230], [231], [232]. Figure 3.6 (a) depicts a typical CV curve of a p-type MOS, showing its three distinct regions representing the accumulation, depletion, and inversion of majority carriers at the SiO_2/Si interface. The flatband voltage (V_{FB}) is the voltage required to bring carrier concentrations at the silicon surface to the same amounts as in the bulk, making the surface potential zero. This is indicated in Figure 3.6 (a) as the transition from accumulation to depletion. The position and shape of the CV curve are influenced by interface charges, such as fixed charges in the oxide, and traps at the SiO_2/Si interface. When additional charges such as K^+ are introduced at the interface, the position of V_{FB} shifts as the voltage required to flatten the energy bands in silicon is increased in the presence of this charge. By

quantifying the ΔV_{FB}, we can calculate the charge at the Si/SiO_2 interface, and infer whether this charge has migrated toward a graphene layer at the front surface.

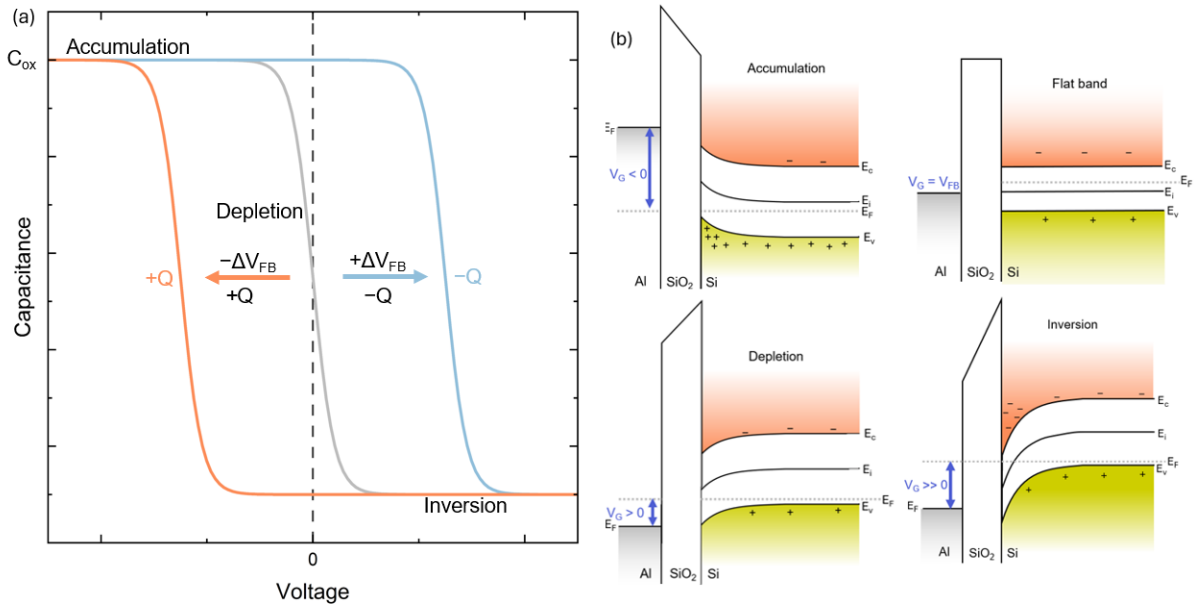

Figure 3.6: (a) Capacitance-voltage characteristics in a metal-oxide-semiconductor, showing accumulation, depletion and inversion. With increasing positive or negative charge at the oxide-semiconductor interface, the curve shifts left or right respectively. (b) Energy band diagrams during different periods of capacitance-voltage measurement.

Since the exact charge distribution within the dielectric is unknown, we can assume an effective sheet of charge with centroid x_c at the SiO_2/Si interface, at position $x = d$. The V_{FB} can be related to the effective total charge concentration Q_{eff} at the Si/SiO_2 interface following:

$$Q_{eff} = \frac{\varepsilon_r}{d - x_c}\left(\frac{\Phi_M - \Phi_{Si}}{q} - V_{FB} - \frac{Q_{it} d}{\varepsilon_r}\right) \quad (3.13)$$

where Q_{it} is the interface trapped charge, assumed to be very low ~10^9-10^{10} q/cm^2 in the samples used in this work.

MOS structures were fabricated by evaporating a 100 nm Al dot contact of diameter 0.5-1 mm on a SiO_2/Si surface. The rear of the Si was scratched using a diamond scriber to expose the Si for metallisation using a 100 nm thermally-evaporated Al. CV measurements were performed at 0.1-1 MHz using a Boonton 7200 LCR meter.

To provide a more complete understanding of ion migration kinetics, the thermally stimulated ionic conductivity (TSIC) method was used to determine the temperatures and bias required for ionic drift across the 300 nm SiO_2 interface towards graphene. TSIC measures the <1 nA current fluctuations as ions drift across a dielectric at elevated temperature and applied bias [233]. The TSIC technique will be described further in Chapter 5.

3.3.5 Kelvin Probe

Kelvin Probe (KP) is a contactless method to measure the work function difference between metals and semiconductors, as well as characterising the surface potential of dielectric films [234], [235], [236], [237]. To measure work function difference, a gold probe of known work function (Φ_{tip}) is electrically connected to the sample rear. Figure 3.7 (a) and (b) depict the resulting band alignment of a silicon sample and gold probe upon connection. In this case the electrons travel from the lower work function silicon (Φ_{Si}) to the gold (Φ_{tip}), their Fermi levels equalise, and a contact potential difference V_{CPD}, equal to the work function difference between the silicon and the gold is generated. The probe tip is brought close to the silicon surface, forming a capacitor between them. The tip is then sinusoidally oscillated, generating a corresponding capacitance oscillation between sample and tip. This capacitance oscillation generates an AC backing current i_b, following $i_b = \frac{dQ}{dt}V$.

A counter potential is applied to the probe, and is increased until i_b is zero [237]. The nullification of i_b corresponds to the voltage at which the contact potential between tip and sample is cancelled. The voltage required to nullify i_b is known as the "backing voltage" (V_b) and is equal to the negative of the contact potential difference (V_{CPD}) as illustrated in Figure 3.7 (c), and is equivalent to the work function difference between tip and sample, i.e. $V_b = -V_{CPD} = \frac{\Phi_{Si} - \Phi_{tip}}{q}$ [237].

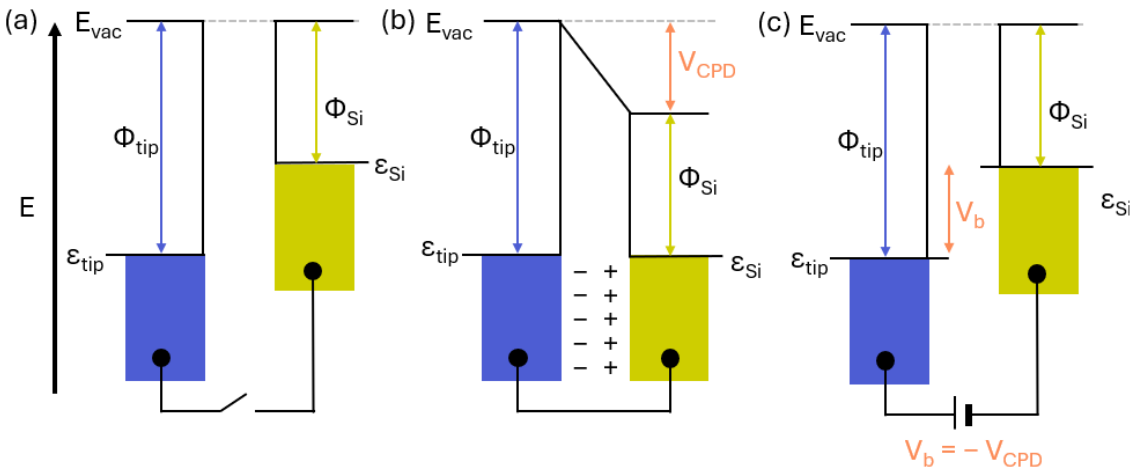

Figure 3.7: (a) Kelvin Probe tip and silicon disconnected. (b) Tip and silicon electrically connected. (c) Backing voltage applied to the gold tip.

In this work, a KP Technology Scanning Kelvin Probe SKP5050 with a 50 µm or 2 mm gold tip was used to measure the surface potential of charged dielectrics on silicon, rather than work function differences. In this case, the measured V_{CPD} also includes contributions from the dielectric, and is highly dependent on surface charge.

Assuming the potential contribution from air is negligible, V_{CPD} in a silicon/dielectric system can be expressed as:

$$V_{CPD} = -\left(\frac{\Phi_M - \Phi_{Si}}{q} + \phi_{SCR} + V_{dielectric}\right) \quad (3.14)$$

where ϕ_{SCR} is the surface potential due to the space-charge region in the silicon, and $V_{dielectric}$ is the potential drop across the dielectric [235], [238]. Like in CV, the exact charge distribution in the dielectric is unknown, and is instead represented as a fixed sheet of charge density Q_f with centroid at distance x_c from the SiO_2/Si interface. Using Q = CV we can the rewrite Equation (3.14):

$$V_{CPD} = -\left(\frac{\Phi_M - \Phi_{Si}}{q} + \phi_{SCR} + \frac{x_c \cdot Q_f}{\varepsilon_0 \varepsilon_{dielectric}}\right) \quad (3.15)$$

By rearranging in terms of Q_f we can calculate the surface charge density:

$$Q_f = -\frac{\varepsilon_0 \varepsilon_{dielectric}}{x_c}\left(V_{CPD} + \frac{\Phi_M - \Phi_{Si}}{q} + \phi_{SCR}\right) \quad (3.16)$$

In this work, the space-charge region is expected to be negligible compared to the dielectric charge. Previous work demonstrates that the space-charge region contribution is negligible except in the case of very thin dielectrics with charge $>10^{13}$ q/cm^2 at the Si/SiO_2 interface, conditions which are not explored using KP in this work [235], [238], [239]. Therefore Equation (3.16) can be rewritten as:

$$Q_f = -\frac{\varepsilon_0 \varepsilon_{dielectric}}{x_c}\left(V_{CPD} + \frac{\Phi_M - \Phi_{Si}}{q}\right) \quad (3.17)$$

Figure 3.8 depicts a schematic of the measurement configuration for a typical sample used in this work, illustrating the position of the gold tip with respect to the SiO_2/Si sample. An aluminium contact is evaporated on the rear of the silicon to allow for good electrical connection to circuit, and is positioned such that the SiO_2 surface is close to the gold tip. The V_{CPD} is measured by nullifying the AC backing current i_b generated between tip and sample. Equation (3.17) is then used to calculate the charge density Q_f on the dielectric surface, where x_c is the dielectric thickness.

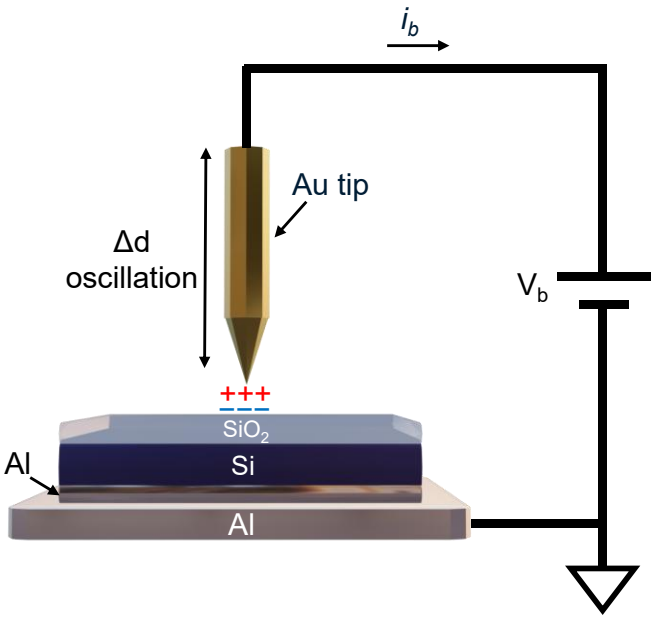

Figure 3.8: Schematic of setup of the scanning Kelvin Probe measurements for a standard SiO_2/Si sample used in this work. The tip and rear of the sample are electrically connected. The tip is then oscillated close to the sample, generating an AC backing current i_b. This backing current is nullified by applying a backing voltage V_b which is used to calculate the surface charge density.

3.3.6 Vacuum Electronics Testing Station for High-Temperature, Low-Noise Measurements

In Chapters 5 and 6, it became apparent that electrical measurements in vacuum were necessary to eliminate the effects of atmospheric contamination, and ensure reproducibility. To achieve this in a short timeframe, I retrofitted an out-of-use Edwards E306 Thermal Evaporator and adapted it specifically for this work, constructing a bespoke "vacuum electronics testing station" (VETS) for vdP, CV, FET and low-noise thermally stimulated ionic conductivity (TSIC) measurements. This involved removing the components relating to evaporation such as the piezoelectric crystal monitor, shutter and evaporation stage from the system, and cleaning the diffusion pump to ensure vacuum $<4\times10^{-7}$ mbar could be achieved in a short timeframe and remain in place at high temperatures. I then fabricated and installed a low-noise electrical measurement stage in the chamber. Figure 3.9 depicts the fabricated stage, in this case with probes in place for high-temperature FET measurement. Source and drain electrodes are contacted to metal electrodes on the sample surface, while the gate electrode is contacted to an aluminium plate in contact with the rear of the sample. To reduce electrical noise sufficiently

to carry out TSIC measurements, the Al plate was electrically isolated by placing an insulating mica sheet under the Al stage, and grounding an Al electrode under the mica. The entire vacuum chamber was electromagnetically shielded using a purpose-built, grounded Faraday cage, which was placed over the chamber during operation. These modifications to the chamber and stage ensured sources of current noise >1 pA were eliminated for TSIC measurements.

The heating elements consist of six cartridge heaters, placed under the grounded Al. These elements were calibrated and controlled using a thermocouple secured near the sample area to stably achieve 350 ℃ in vacuum. Temperature control calibration was carried out using a proportional–integral–derivative controller programmed in LabVIEW. The plastic coating of the thermocouple and cartridge heaters were removed to minimise outgassing at high temperature, which can increase chamber pressure and damage the diffusion pump during operation. To prevent the chamber base heating and so damaging the Viton vacuum seal, the entire measurement stage was secured 10 cm from the base using a stainless-steel plate and stainless-steel screws. This distance was deemed suitable based on an estimate of heat transfer from the stage to the base of the vacuum chamber accounting for the thermal conductivity and the area of the air, the stainless-steel plate, and the screws. During operation at high temperatures over several hours, the chamber base remained <50 ℃, and the vacuum remained at least $<10^{-6}$ mbar at all times.

For CV and TSIC measurements the source and gate probe were used to apply a bias across the device stack. FET used a probe for source, drain and gate electrodes, as depicted in Figure 3.9. For vdP measurement, four probes were used for signal generation and measurement. For TSIC, FET and vdP measurements, a Keithley 2611A source-measurement unit with Thurlby Thandar TSX3510P DC power supply was used, while CV measurements used a Boonton 7200

LCR meter. All source-measurement units and power supply were controlled remotely using LabVIEW.

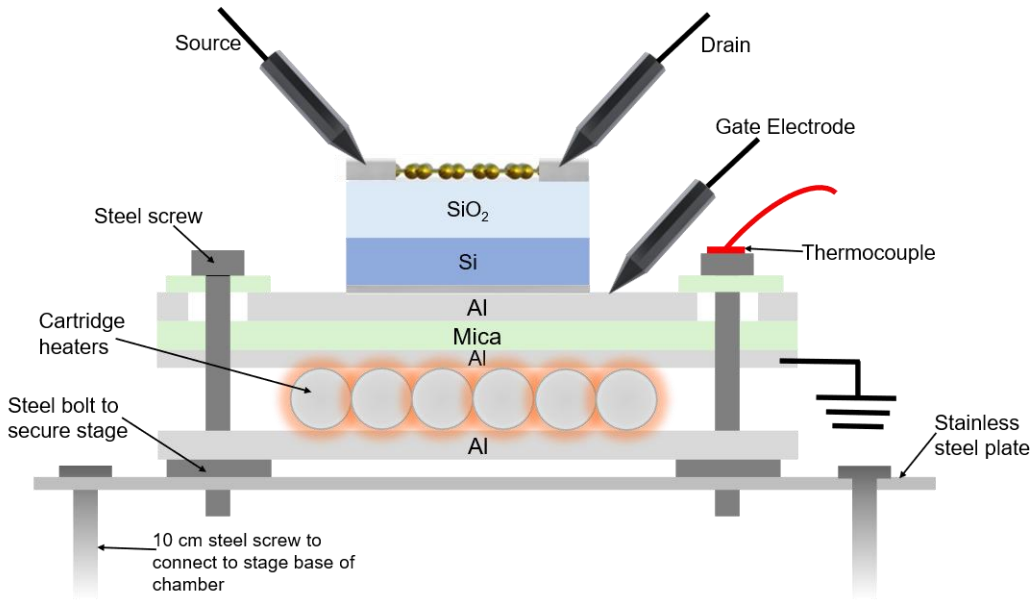

Figure 3.9: Vacuum Electronics Testing Station (VETS) stage and sample measurement configuration for high-temperature vacuum measurements. In this case, it is configured for Field-Effect Transistor measurements, with source, drain and gate electrodes labelled.

3.4 Optical & Structural Characterisation

3.4.1 Raman Spectroscopy

Raman spectroscopy enables the measurement of the molecular vibrations of particular chemical bonds and lattice arrangements when illuminated with a monochromatic laser [240], [241]. When a laser of known wavelength $\lambda_{incident}$ is directed at a material, most photons are scattered elastically by Rayleigh scattering, where $\lambda_{scatter} = \lambda_{incident}$ [242]. A small fraction of these photons undergoes inelastic scattering, gaining or losing energy by exciting or absorbing quasiparticles in the material such as phonons or magnons [242], [243]. This process is known as Raman scattering, and results in photon emission with wavelength $\lambda_{scatter} \neq \lambda_{incident}$. This difference between $\lambda_{scatter}$ and $\lambda_{incident}$, known as the "Raman shift", corresponds to the specific vibrational modes of the material's molecular or crystal lattice structure [244]. Raman spectroscopy measures the Raman shift to provide detailed information about the material's

composition and structure [244]. In this work, Raman spectroscopy was used to determine the quality, defect density, doping levels, and layer thickness of graphene.

To understand the physical origin of graphene's Raman spectra, a discussion of its phonon dispersion is necessary. The unit cell of monolayer graphene consists of two carbon atoms, and each atom can vibrate in three directions. Therefore, there are six distinct phonon dispersion bands in graphene at the Brillouin Zone (BZ) centre (Γ), consisting of three optical (O) and three acoustic (A) modes [244], [245]. Figure 3.10 (a) depicts the electronic BZ of graphene, overlayed with a schematic of the electronic dispersion at the K point, while Figure 3.10 (b) depicts the calculated phonon dispersion relation of graphene [245], [246]. In Figure 3.10 (b), the six phonon dispersion bands are illustrated: the longitudinal optical (LO), longitudinal acoustic (LA), in-plane transverse optical (iTO), in-plane transverse acoustic (iTA), out-of-plane transverse optical (oTO), and out-of-plane transverse acoustic (oTA). The optical phonons at Γ and at the K points are accessible by Raman spectroscopy, and so is relevant to graphene characterisation.

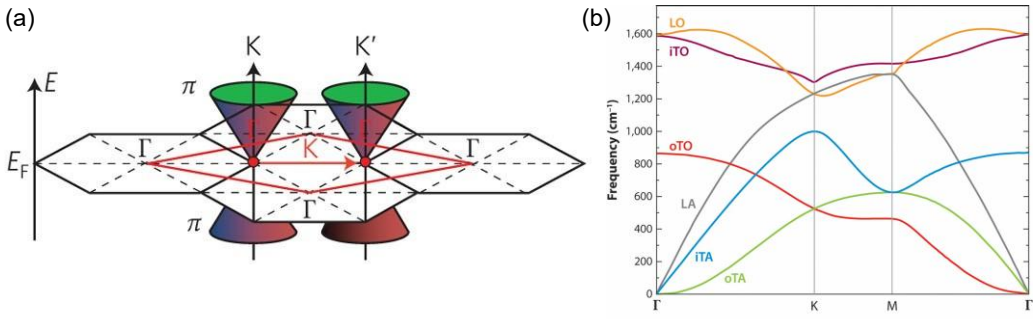

Figure 3.10: (a) Electronic Brillouin Zone (BZ) of graphene (black hexagons) and the first-phonon BZ (red rhombus) with schematic of graphene's Dirac cones at the BZ edges. Adapted with permission from ref. [246], Copyright © 2013, Springer Nature. (b) Calculated phonon dispersion of graphene, showing the LO, LA, iTO, iTA, oTO and oTA branches. Adapted with permission from ref. [245]. Copyright © Annual Reviews.

The Raman spectrum of pristine graphene features two prominent peaks: the G band at ≈1580 cm^{-1}, and the 2D band, at ≈2690 cm^{-1}. The G band peak arises from the in-plane vibrational mode of sp^2-bonded carbon atoms in the lattice, as the C-C bond stretches and contracts [126], [246], [247]. This peak involves the LO and iTO phonons at the BZ centre Γ,

represented in Figure 3.10 (b) [244], [246]. The 2D peak does not correspond to a fundamental phonon mode at the BZ centre. Instead, the 2D peak results from a second-order scattering process involving two iTO phonons near the K point, and is indicative of the long-range order in the graphene lattice [121], [244], [247]. In monolayer graphene, this peak is sharp and symmetrical, with higher intensity than the G peak. With increasing layers, the 2D becomes more asymmetric, allowing for the determination of graphene layer number [244]. A third peak, "D", also corresponds to a second-order scattering process, and typically appears around $\approx$1350 cm^{-1} [121], [247]. In this case, the scattering process involves one iTO phonon and one lattice defect in the sp^2 network [244]. As the D band requires a lattice defect for activation, its presence or absence is a good indicator of the degree of defects in the graphene film [244], [246], [247], [248]. The intensity ratio between the D and the G peak is therefore commonly used to indicate the density of defects in graphene [246].

The relative shifts of the G and 2D peak can indicate the degree and polarity of doping in graphene [132], [249], [250], [251]. The G peak shifts blue with doping of either p- or n-type. The origin of this shift relates to the Kohn anomaly at the Γ point. The Kohn anomaly is a discontinuity in the phonon dispersion arising from strong electron-phonon coupling near the Fermi level [244], [250]. When additional carriers are present during doping, the Fermi level shifts, and the electron-phonon interaction is relatively suppressed. This removes the Kohn anomaly non-adiabatically, and in turn increases the frequency of phonons contributing to the G band [250], [252]. This manifests as a blueshift in the G peak of graphene's Raman spectra.

The 2D peak shift direction indicates the type: a redshift suggests n-doping, and a blueshift suggests p-doping [253]. The physical mechanism for these shifts relates to the electronic band structure and electron-phonon coupling in graphene. The 2D peak arises due to a double-resonant scattering process. The conditions for this resonant scattering are determined by the available electronic states, which depend on the Fermi level. As the Fermi level shifts due to

doping, the momentum and energy of the phonons involved are changed [250], [253]. In n-doping, the Fermi level is raised, and the conduction band fills, supressing the energy of the phonons contributing to the 2D peak [250], [251], [252]. In contrast, as the Fermi-level is lowered in p-doping, the energy of the phonons contributing to the 2D peak can increase [250], [251], [252]. However, G and 2D peak shifts can also occur due to other factors including compressive strain due to wrinkling, oxidation, or changes in layer number so care must be taken in interpretation of the data [244], [246], [247].

A LabRam Aramis HORIBA Jobin Yvon Raman spectrometer with a 532 nm monochromatic laser and charge-coupled device (CCD) detector was used. LabSpec 6 software was used for measurement acquisition and calibration. Figure 3.11 depicts a simplified schematic of the measurement set-up for Raman spectroscopy used in this work. An optical microscope is built into the LabRam Aramis so that area of interest on the sample can be identified and brought into view. An objective lens with 50× magnification was used, with measurement spot size 1-2 μm. Once the area to be characterised is identified and brought into focus with the objective lens, the laser is turned on. The laser is directed through a series of filters to optimise the beam. A wavelength-selective dichroic mirror then reflects the laser light toward the objective lens where it is focused on the sample. Photons interact with the sample, and a small fraction experience a shift in energy via the Raman effect. Reflected photons are then directed back through the objective lens and through the dichroic mirror toward the detection system. The light first passes through an edge filter, which filters out low energy photons close to the Rayleigh line. Photons are then directed through a pinhole. This pinhole is part of a confocal system, which rejects out-of-focus light and enhances spatial resolution and contrast. A diffraction grating with 1800 lines/mm was used to disperse the light by wavelength. Photons are finally directed to the CCD detector, which captures the intensity of scattered photons as a function of Raman shift in wavenumbers.

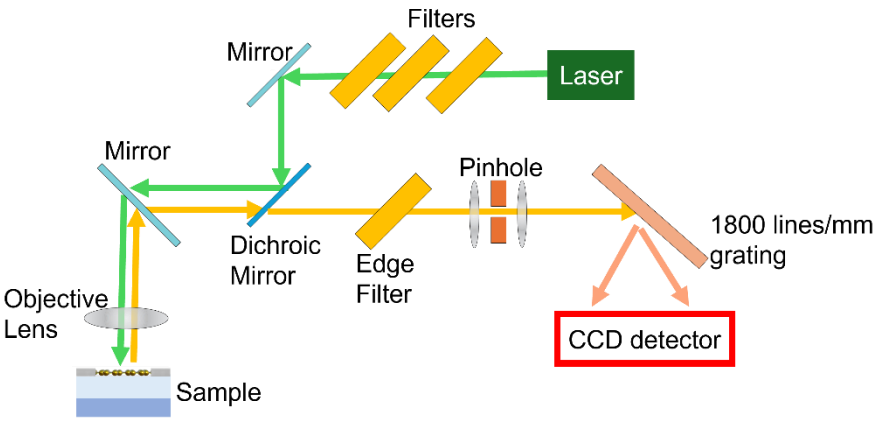

Figure 3.11: Simplified schematic of the measurement set-up using the Raman spectrometer and charged-couple device (CCD) detector.

Before performing measurements, the laser is calibrated LabSpec by focusing it on a reference silicon sample with known Raman peak. Laser power, acquisition time and number of acquisitions were adjusted to maintain a high-resolution measurement without damaging the sample. All measurements carried out at room temperature and pressure.

3.4.2 Spectrophotometry

The transmittance of the graphene film before and after doping processes was measured using an Ocean Optics FLAME-T-XR1-ES spectrophotometer. A DH-2000-BAL light source was used, with deuterium and tungsten-halogen bulbs for 210-370 nm and 320-1100 nm emission respectively. Figure 3.12 depicts the measurement set-up. Light is directed perpendicularly incident on a sample, passing from the light source to the sample through an optical fibre cable. An optical fibre was also positioned at the rear of the sample to direct the transmittance light to the spectrophotometer, to compare transmitted to incident light. In the spectrophotometer, a blaze-grating separates the light into individual wavelengths, with the separated components selected for using a wavelength slit. The selected wavelengths are then directed into a photodiode detector, which converts the light to an electrical signal.

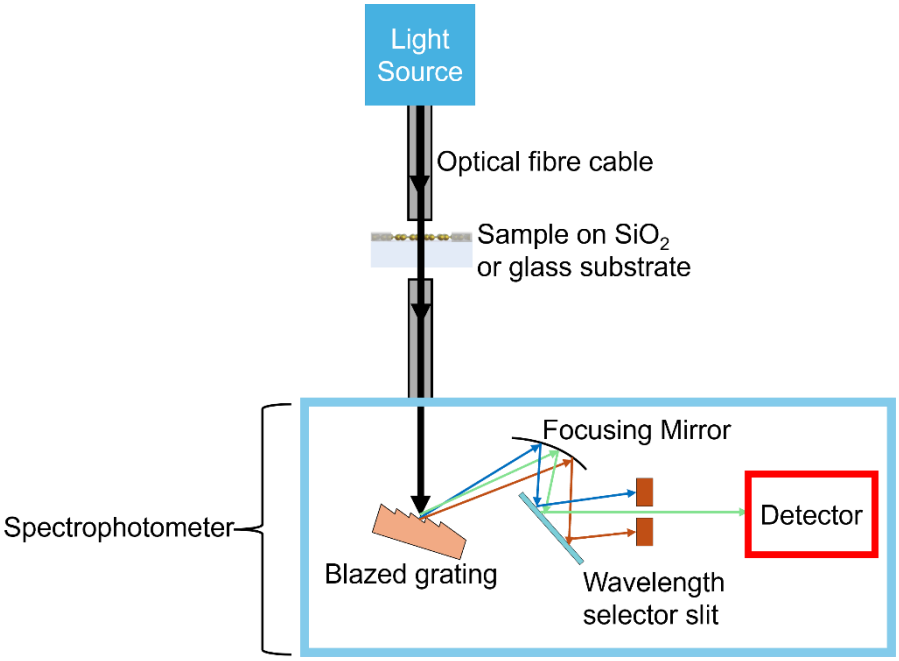

Figure 3.12: Spectrophotometry set-up for transmittance measurements used in this work. Light is directed through a sample on a SiO_2 or glass substrate, and then directed to a spectrophotometer where the wavelengths are separated for detection.

To calibrate the set-up for measurements, a value of 0% and 100% transmittance was defined. The value of 0% transmittance was obtained by closing the light source shutter. The value of 100% transmittance was obtained using different methods depending on the purpose of the measurement. For measurements of the graphene on a transparent substrate, the 100% transmittance background reference was obtained by measuring the total transmittance light when no sample was positioned between the source and the detector. For measurements comparing the transmittance of graphene only, an equivalent transparent substrate without graphene was used as the 100% transmittance value for calibration. For improved signal-noise ratio, the boxcar averaging method was used. Strong noise for $350 < \lambda < 1000$ nm was observed, limiting measurements to the visible and near-IR. All measurements were carried out in the dark.

3.4.3 Ellipsometry

A FilmSense FS-1 multi-wavelength ellipsometer was used to measure dielectric film thickness. Linearly polarised light is incident on a dielectric surface. The interaction between

the light and the film modifies the polarisation state, the phase (Δ), and the amplitude (Ψ) of the reflected light [254], [255]. The reflection coefficients r_p and r_s for p- and s-polarised light can be determined via:

$$\frac{r_p}{r_s} = \tan(\Psi) \cdot e^{i\Delta} \quad (3.17)$$

Fitting algorithms based on the Cauchy, Palik and McGraw-Hill models were used to extract thickness from the outputted data for the SiO_2, SiN_x and AlO_x films studied [254], [255], [256], [257], [258].

3.4.4 Optical and Electron Microscopy

An Olympus BH-2 optical microscope was used to visualise the transferred graphene, ensuring polymers residues were removed, and stencil masks aligned adequately for thermal evaporation. In the Olympus BH-2, a white lamp directs light towards a sample. The light reflects off the sample surface and magnified through an objective lens and is directed to a camera to produce high resolution images that can be viewed on a computer. Optical microscopy allows for easy graphene visualisation on substrates with ≈300 nm SiO_2 due to the interference effect [153], [156], [157].

A Carl Zeiss Merlin Scanning Electron Microscope (SEM) was used to visualise the surface of the transferred graphene under high magnification. In SEM, a focused beam of electrons is scanned over the sample surface. When these electrons interact with the sample surface, secondary and backscattered electrons are generated. These electrons are collected by detectors in the SEM chamber and are used to generate a high-resolution image of the surface. As SEM it only used briefly for initial characterisation of transferred films, it is not described in detail here. A detailed description of SEM for graphene characterisation can be found in ref. [153], [259], [260], [261].

Chapter 4

Corona-Charged Dielectric Membranes: A Proof of Concept for Graphene Doping with Ion-Charged Dielectrics

4.1 **Introduction**

The deposition of corona charge on dielectric thin films on silicon is a widely studied technique for silicon solar cell surface passivation [183], [184], [214], [262]. When charge is driven toward the Si/SiO_2 interface, the field-effect repels charge carriers of the same polarity away from the silicon surface, reducing the surface recombination rate, and thus increasing the overall efficiency of a silicon solar cell. A central question in this thesis is whether the charge in such a dielectric is sufficient to increase the carrier concentration in an adjacent graphene layer, and how this might impact carrier concentration, mobility, and transmittance. However, when corona charge is deposited on dielectrics such as SiO_2, it exhibits poor stability during chemical processing. Polar molecules such as water, as well as solvents such as IPA and acetone introduce neutralising charges that cancel out the field-effect mechanism [185], [263]. For this reason, this technique poses challenges for the CVD-graphene system, which requires water, IPA and acetone during the transfer process.

A stabilising layer, such as hexamethyldisilazane (HMDS) can improve the stability of corona charge against moisture. However, this layer is liable to decomposition during the PMMA removal step, which involves immersing the samples in hot acetone. Moreover, both corona charge and HMDS molecules have poor stability at elevated temperature, with the 180℃ anneal required to adhere the graphene to the substrate likely to remove the corona ions [185]. Although alkali ions can be used to drive corona charge into the Si/SiO_2 interface, this process

is complex and may not withstand the chemical and thermal stresses involved during graphene transfer. This is explored in depth in Chapter 5.

In this chapter, the disadvantages of the corona-charged SiO_2 substrate system are deferred in favour of designing a proof-of-concept for the ion-charged dielectric doping of a 2D semiconductor. Figure 4.1 depicts the steps involved in the sample fabrication and charging process. A simplified system is used where graphene is transferred directly onto SiO_2 membranes, which are suspended on a Si support layer. The graphene is laser etched so that it only remains over the membrane, and metallised with Al for vdP measurement. Corona charge is then deposited on the rear side of the dielectric at varying intervals. In this way, as the corona charge is deposited after graphene transfer and device fabrication, ensuring graphene processing will not impact the stability of the deposited charge. The magnitude and stability of corona charge on SiO_2 and SiN_x membranes are measured using the Kelvin probe. The electrical and optical properties of the graphene are also measured before and after corona treatment, as well as the impact on its Raman spectra. This proof of concept is used to develop an understanding of the relationship between the properties of graphene and the charge in a dielectric adjacent to it. After examining this relationship in detail, the use of ionic charge to dope graphene in stable configurations, including those with direct relevance to tandem devices, will be explored in Chapters 5, 6, and 7.

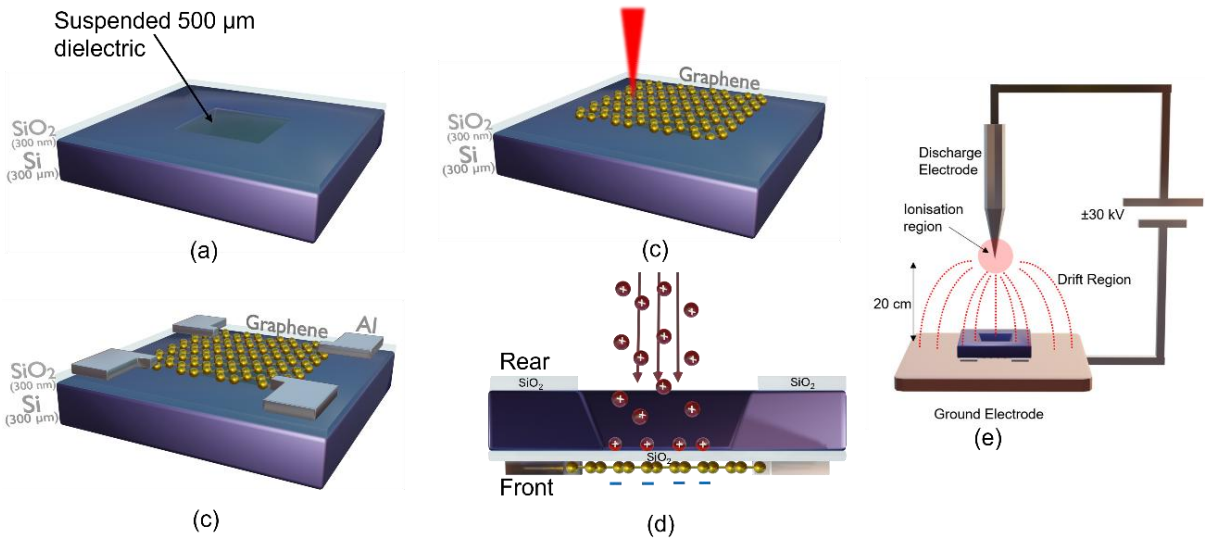

Figure 4.1: Sample fabrication for corona charging of dielectric membranes for graphene doping. (a) Initial substrate, with 300 nm SiO_2 dielectric, with suspended dielectric layer of width 500 µm in the centre. (b) Graphene is transferred to the substrate, and laser etched such that the graphene only covers the suspended layer. (c) Device metallisation with Al. (d) Device is rotated, for corona charge deposition on the rear. (d) Corona charging apparatus for device charging.

4.2 Characterisation of Transferred and Laser Patterned Graphene

Fabrication of 2D nanomaterial devices had not been attempted in the Bonilla group. This project initiated the method development for systematic graphene transfer, and hence attention was placed in the techniques, charactering and ensuring high quality and reproducibility. Figure 4.2 (a) depicts an optical microscopy image of graphene transferred to a SiO_2/Si, where the uniform purple colour of the graphene indicates low PMMA residues and minimal wrinkles or tears, with defects primarily located at the film edge. Figure 4.2 (b) presents an SEM image of a typical layer of transferred graphene on SiO_2/Si at 2,000× magnification, showing a modest number of wrinkles and point defects. Its grain size is ~10 µm, consistent with typical values reported in the literature [264]. The measured sheet resistance, mobility and carrier concentration of typical "undoped" square and cloverleaf devices in air was ~500-1000 Ω/□, 500-1000 cm^2/Vs and (3-6)×10^{12} $/cm^2$ respectively, values which closely align to those reported in the literature for undoped graphene in air [101], [169], [249]. This validates the reproducibility of the graphene transfer technique. For a more

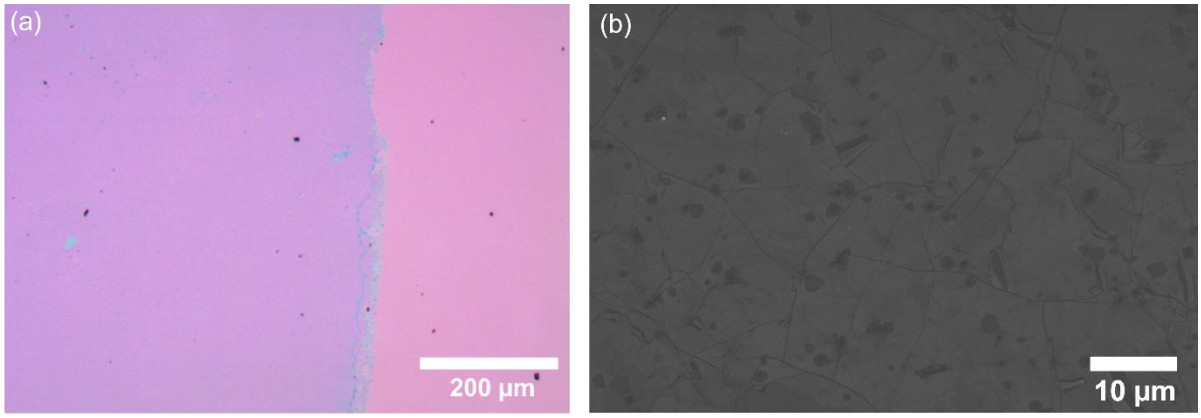

Figure 4.2: (a) Optical micrograph of graphene (purple) on a 300 nm SiO_2 layer on silicon.(b) Scanning electron micrograph of graphene transferred onto a 300 nm SiO_2 layer on silicon.

Optical microscopy and Raman spectroscopy were used to verify that the etched graphene was fully ablated without damaging the substrate. Figure 4.3 (a) depicts an optical microscopy image of a region of graphene, with a 20 µm wide line laser ablated across the width of the image. There is a clear absence of graphene in the channel labelled "2", with no visible oxide damage compared to the unablated oxide. Figure 4.3 (b) compares the Raman spectra of the region before and after ablation. The Raman spectrum of the unablated region "1" includes graphene's characteristic G and 2D peaks, with a low-intensity D peak indicating low defect density. The 2D peak is sharp and symmetrical, with an intensity twice as that of the G peak, providing evidence that the transferred graphene is a monolayer [244], [247]. More comprehensive measurement of surface morphology could be obtained using high resolution atomic force microscopy, but this technique was not used in this work. Conversely, the Raman spectrum at the ablated region exhibits no Raman peaks, indicating that the graphene layer has been removed.

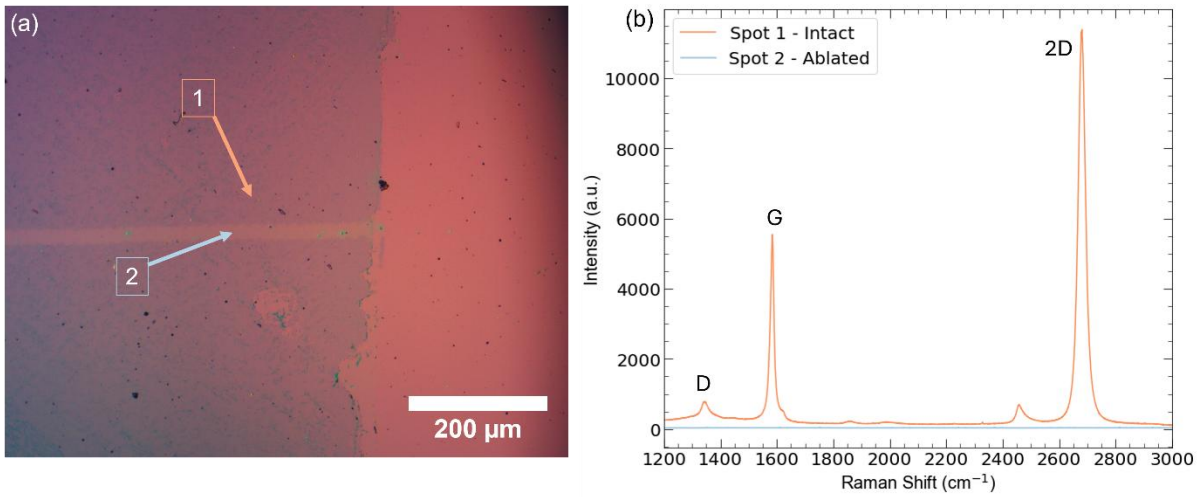

Figure 4.3: Characterisation of ablated graphene. (a) Optical Microscopy image of graphene on Si/SiO_2 substrate, with a 20 µm wide ablated across the width of the image. (b) Raman counts versus wavenumber for intact and ablated graphene.

4.3 Characterisation of Surface Charge on Dielectric Membranes

Before transfer of the graphene to the SiO_2 membrane for corona charging, it was first necessary to measure the concentration of static charge could be built and maintained on the membrane. For surface charge measurement, an Al layer was deposited on the front of the dielectric to provide electrical connection to a Kelvin Probe (KP). Figure 4.4 (a) depicts the KP contact potential difference (CPD) of the rear of the SiO_2 membrane, and the inset illustrates the sample architecture. The device was held under an applied corona voltage of ±30 kV over 16 min of total charging time. As the charging time increases, the CPD of opposite polarity increases. The magnitude of the CPD is proportional to the amount of corona charge deposited on the surface of the SiO_2 membrane. After 6 min at +30 kV, the CPD saturates at circa −12 V, while after 8 min at −30 kV, the CPD saturates at circa +20 V. At this point, no additional charge can be deposited on the film, and the electric field generated is likely to be at its maximum. Using Equation (3.17), the CPD on such a film can be converted to surface charge in q/cm^2, with positive corona deposition saturating at ~9×10^{11} q/cm^2, and negative corona deposition saturating at 1.6×10^{12} q/cm^2. Figure 4.4 (b) depicts the variation in CPD as the charge decayed over time. The sample was left in air directly under the KP instrument for up to 10 hours, after

either positive or negative charging. The measured CPD decayed by 2.80% after positive charging, and 7.82% after negative charging. This stability after several hours enabled R_{sheet} measurements to be taken minutes after each charging interval, with confidence that the charge deposited on the film had not substantially decreased.

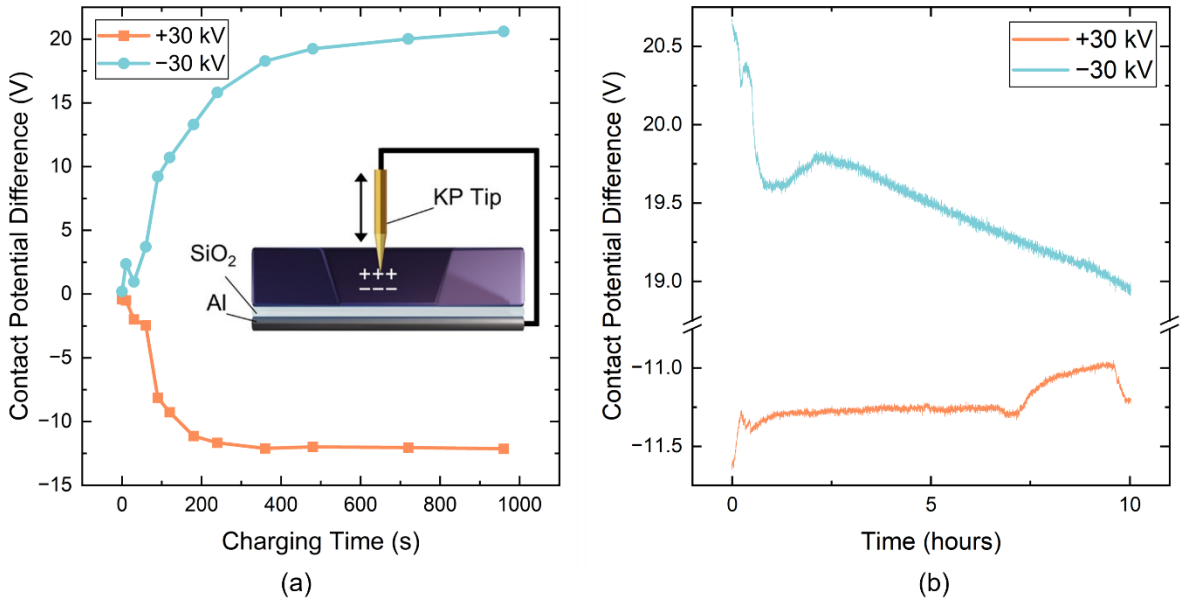

Figure 4.4: (a) Change in contact potential difference over time while held under constant ±30 kV voltage, for a SiO_2 membrane measured by Kelvin probe microscopy. At each charging interval, 100 measurements were taken, and the mean value is recorded in the plot. Inset: Kelvin probe microscopy measurement configuration. (b) Contact potential difference versus decay time for positively and negatively charged SiO_2 membranes. In this case, 6000 measurements were taken and recorded continuously over 10 hours.

4.4 Electrical properties of graphene interfaced with charged SiO_2 membranes

Graphene was transferred to dielectric membrane substrates, and then laser etched such that the graphene covered only the freestanding membrane. After metallisation with Al to form a vdP device, the device was charged with corona ions by placing it face down on the ground electrode in a corona discharge apparatus. Figure 4.5 (a) shows how the R_{sheet} of graphene varied as the dielectric membrane was charged under either +30 kV or −30 kV over time. The initial R_{sheet} of ≈1.7 kΩ/□ to 3.3 kΩ/□ is high for undoped CVD-graphene. This is attributed to the difficulty of wet-transferring the graphene to substrates <1 cm^2, resulting in an increased number of wrinkles, cracks and defects in the film relative to those deposited on larger-area substrates. The red line in Figure 4.5 (a) shows how increasing the quantity of positive charge

deposited on the membrane decreased the sheet resistance. In the case of positive charging, it is assumed that the reduction of R_{sheet} observed is due to n-type electrostatic doping by the positively charged dielectric substrate. In under 3 min, the R_{sheet} of graphene was reduced by ≈60% from 1810 to ≈759 Ω/□. The reduction in R_{sheet} occurs over the same timescales as the charge was measured to increase in equivalent charging conditions, shown in Figure 4.4 (a). After storing this sample in a low-pressure, nitrogenated chamber for 2 months, its sheet resistance decreased further, to ≈607 Ω/□. This is comparable to the behaviour observed by Yu et al when investigating R_{sheet} reductions in charged dielectric nanolayers in inversion layer solar cells [215]. It is likely that the field established causes further reductions of graphene's R_{sheet} over time. A potential mechanism for this process is discussed in Section 4.11. A device charged equivalently, then stored in a well-ventilated fume hood at room temperature and pressure for two months (here referred to as "standard laboratory conditions" for device storage), experienced a 2% (1910–1881 Ω/□) reduction in R_{sheet}. For comparison, a set of uncharged devices experienced a 10%–15% increase R_{sheet} when held in "standard laboratory conditions" during the same period, likely due to atmospheric contamination, which reduces mobility [161], [265], [266]. This could indicate that the electric field induced in the graphene may counteract the effect of atmospheric contamination from increasing R_{sheet}. However, the doping induced by the atmosphere can be highly variable and is dependent on changes in relative humidity, so a firm conclusion cannot be drawn based on these data alone [267], [268]. When subjected to further positive charge, the sheet resistance of the sample decreased further from 607 to ≈573 Ω/□, saturating after 30 s, and reducing further to 506 Ω/□ over another 30 days in an air-free environment. This is a combined reduction of R_{sheet} by >70% in the positively charged sample from the initial R_{sheet}. The relative change of R_{sheet} demonstrated in this novel doping technique is already approaching that of chemical doping, which typically

reduces the R_{sheet} by 70%–80%, even without optimisations of the charge deposition process for increased charge concentration [121], [269].

The blue line in Figure 4.5 (a) shows how the R_{sheet} of graphene varied as the dielectric membrane was charged under −30 kV corona voltage over 16 min. The R_{sheet} decreases from 3.5 to 2.4 k Ω/□ after 3 min of negative charging time. Similar to the effect of a positively-charged substrate, the reduction in R_{sheet} is assumed to occur due to p-type doping effect of the negatively-charged substrate. The high initial R_{sheet} is due to processing difficulties resulting from using small substrates, as was the case in the positively charged sample. Due to the equal electron and hole mobilities in graphene, both p- and n-type graphene TCEs can be developed using this technique [270]. Figure 4.5 (b) depicts the change in R_{sheet} of a graphene device subject to +30 kV for 2 min, followed by −30 kV for 2 min. The addition of negative electrostatic charge counteracted the n-type doping provided by initially deposited positive charges, demonstrating the reversibility of this technique. This showcases that precise conductivity tailoring for specific device applications is achievable, where both n- and p-type doping are required for better interconnection to active semiconductors.

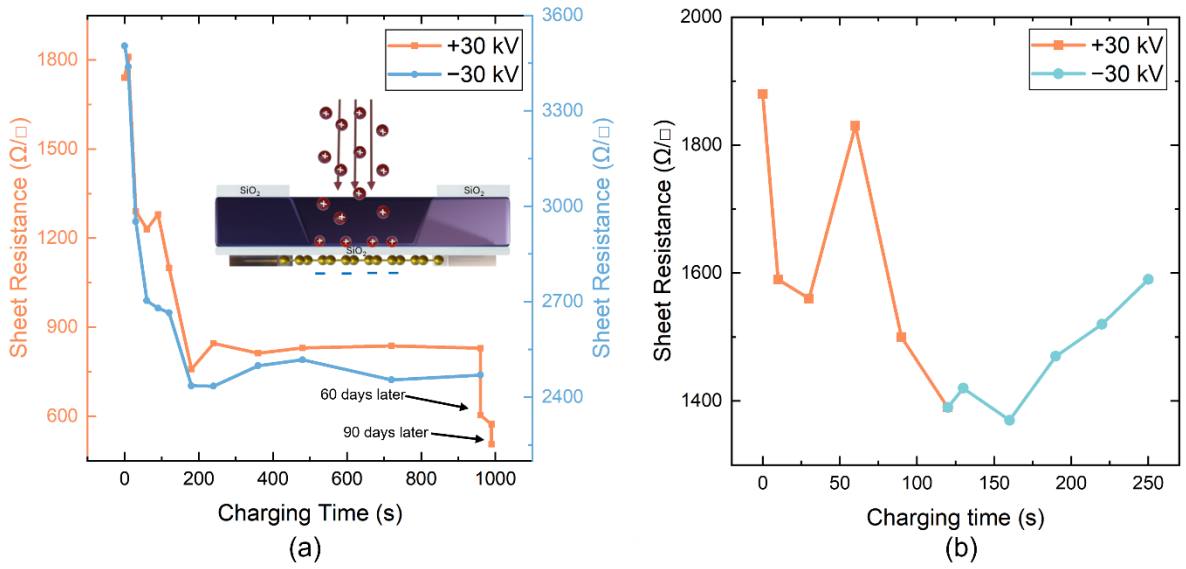

Figure 4.5: (a) Graphene sheet resistance over time held under constant ±30 kV voltage. Inset: Schematic of a graphene device on a freestanding SiO_2 layer charged using corona ions incident on its substrate. (b) Graphene sheet resistance as a function of time held under positive (red) and negative (blue) charge at ±30 kV.

Figure 4.6 (a) depicts the variation in Hall carrier concentration and mobility of a graphene sheet as the membrane is charged with positive electrostatic charge over time. The initial charge carrier concentration of the graphene is high, at 1.56×10^{13} /cm^2, attributed to doping induced by remaining polymer residues, as well as increased contamination incurred from suboptimal graphene transfer [161], [271]. The Hall coefficient was positive, indicating intrinsic p-doping. The initial mobility was relatively low at ≈213 cm^2/Vs. This relatively low mobility can be attributed to the high density of defects, wrinkles and cracks induced by the graphene wet transfer onto such small films, as well as scattering by polymer residues [161], [265], [266]. The charge carrier concentration increases by nearly a factor of 3 after just 2 min of positive charge deposition, from 1.56×10^{13} to 4.35×10^{13} /cm^2. Moreover, on deposition of positive charge the polarity of the Hall coefficient switches to negative, indicating n-type doping. This indicates that deposition of positive charge on the dielectric film induces additional negative charge carriers in the graphene film. The carrier mobility decreases by just a factor of 2, from ≈213 to ≈104 cm^2/Vs. As the increase in N is greater than the decrease in μ, this results in a net decrease in R_{sheet}. It is noted, however, that the initially low mobility in the wet transferred

films accounts for the high resistances initially observed, and it should be tackled to achieve competitive graphene TCEs. Unlike chemical doping, in ICD doping of graphene, the lattice is undisturbed and no additional scattering centres are induced from dopant atoms. This ensures that the mobility does not decrease significantly.

Figure 4.6 (b) depicts the variation in Hall carrier concentration and mobility of graphene as an initially positively charged membrane is charged with negative electrostatic charge. The carrier concentration initially decreases with applied negative charge concentration, indicating that this specific graphene film, presented an initial level of n-type doping, which was compensated by the p-doping produced by negative charge on the SiO_2 membrane. Furthermore, the Hall coefficient switched from negative to positive as p-type behaviour was achieved. Further negative charging increased the carrier concentration by close to a factor of four from 1.04×10^{13} to 4.2×10^{13} /cm^2. The carrier mobility was observed to decrease by a factor of three from ≈172 to ≈60 cm^2/Vs after a complete 3 min of charge exposure, resulting in a net R_{sheet} reduction. During the initial 30 s of charging, the carrier mobility increases significantly from 172 to >2000 cm^2/Vs, whereas the carrier concentration decreased to ≈10^{12} /cm^2, indicative of a near "undoped" film with few charge carriers available for conduction. This sharp increase in mobility and reduction in carrier concentration is indicative that the deposition of negative charge not only neutralised the initial n-type doping, but likely have led to a temporary reduction in charged impurity scattering. This reduction in scattering may have arisen due to neutralisation of surface adsorbates introduced during fabrication or from the environment. Additionally, local electric fields due to trapped charges could modulate potential fluctuations across the graphene. The mobility jump may therefore reflect a flattening of potential inhomogeneities in the graphene microstructure, which would otherwise hinder carrier transport. However, measuring these changes in microstructural charge likely requires another technique such as high-resolution atomic force microscopy-based technique, such as

kelvin probe force microscopy, which was not explored in this work. Overall, the variation of graphene carrier properties and polarity using corona charge deposition on the dielectric substrate indicates the possibility for precise tailoring and reversibility of R_{sheet}, carrier concentration and mobility.

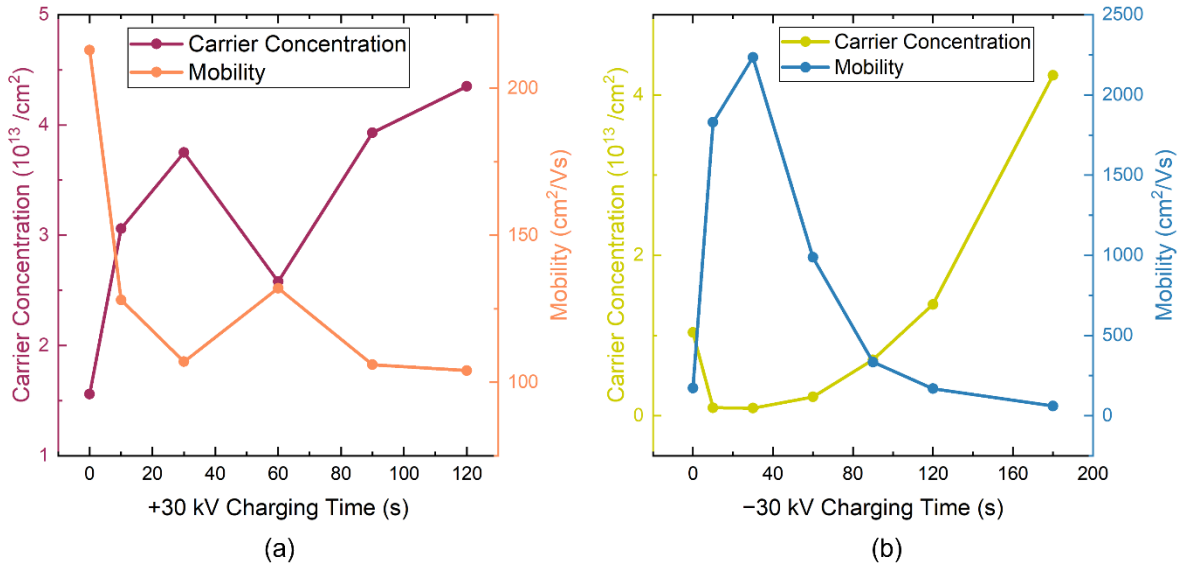

Figure 4.6: (a) Variation in graphene sheet carrier concentration and mobility as the SiO_2 membrane substrate is subjected to positive charge for 2 min. (b) Variation in graphene sheet carrier concentration and mobility as an initially positively charged SiO_2 membrane is subjected to negative charge for 3 min. Statistical analysis is not presented for these samples due to the limited number of devices fabricated under identical conditions; the focus here is on representative behaviour to illustrate the qualitative trends in carrier modulation.

4.5 Raman spectroscopy of graphene interfaced with charged SiO_2 membranes

Figure 4.7 (a) depicts the Raman spectrum of a device before and after positive electrostatic charging of the SiO_2 layer. The relatively high D peak in the uncharged device indicates that the initial high sheet resistance of 1740 Ω/□ was due to a high density of defects, reducing mobility. When charged, the D/G intensity ratio did not increase, indicating that no additional defects were induced by the electrostatic doping process. This contrasts with chemical doping techniques, which often induce additional defects in the graphene film because of lattice disruptions by dopant atoms [62], [64], [272]. Figure 4.7 (b) and (c) highlight the G and 2D peaks. The slightly blue-shifted G peak and decrease in full-width half maximum indicate that moderate doping has occurred [249], [250]. The redshift of the 2D peak indicates that the

doping is n-type [249], [250]. Figure 4.8 (a) and (b) depict the G and 2D Raman shift of a device before and after negative electrostatic charging of the SiO_2 layer. There is a clear and distinct blueshift of the G and 2D peaks, indicative of p-doping. These findings are in line with those reported by Fates et al and Das et al where field effect modulation of the carrier concentration produces such changes to the G and 2D Raman spectrum peaks [249], [250].

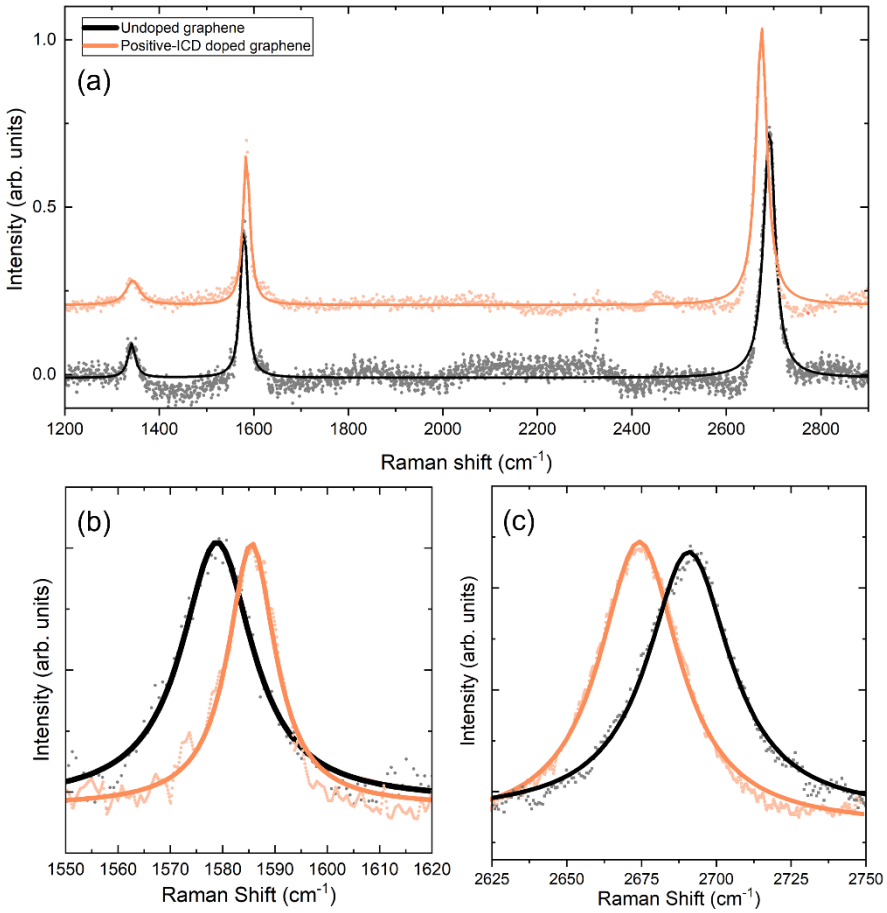

Figure 4.7: (a) Raman intensity versus wavenumber for a graphene device with a positively charged SiO_2 substrate and an uncharged control. Data fit to a Lorentzian function. The displayed data consists of the mean curve from 5 distinct points measured at different areas on the graphene deposited on the SiO_2, before and after charging. (b) G peak Raman shift. (c) 2D peak Raman shift.

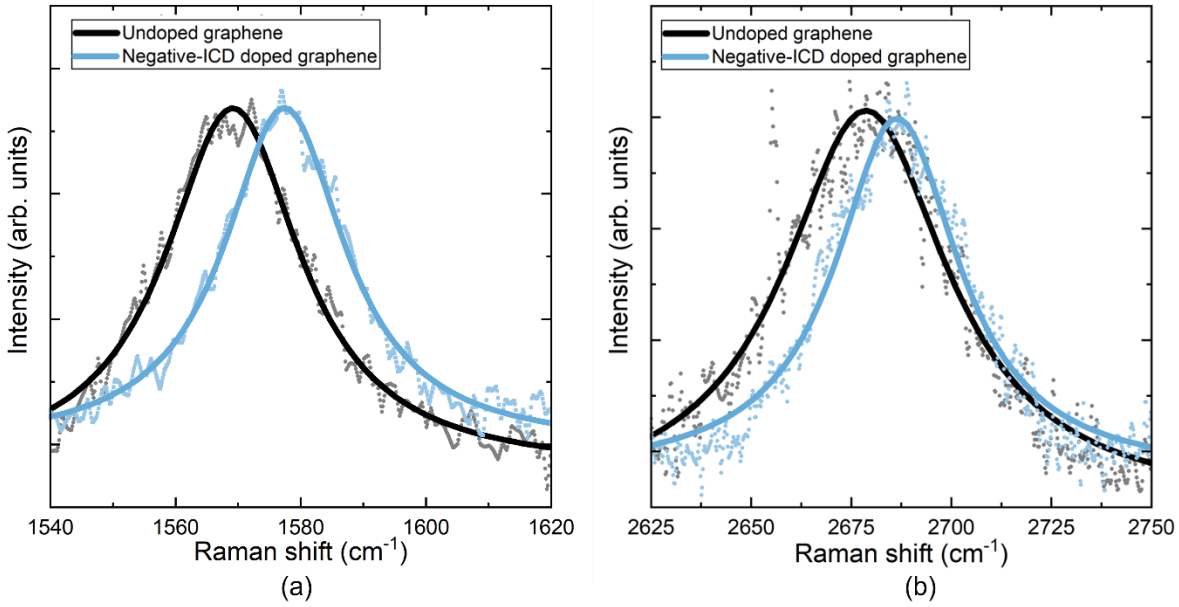

Figure 4.8: Raman intensity versus wavenumber for a graphene device with a negatively charged SiO_2 substrate and an uncharged control. The displayed data consists of the mean curve from 5 distinct points measured at different areas on the graphene deposited on the SiO_2, before and after charging. (a) G peak Raman shift. (b) 2D peak Raman shift.

4.6 Optical characterisation of graphene interfaced with charged SiO_2 membranes

Figure 4.9 (a) compares the transmittance of 350–800 nm light through an undoped graphene film, a graphene film doped with a corona-charged SiO_2. In this case, the optical transmittance loss through an uncharged SiO_2 was used as the background, and so the presented data is given to represent the change in transmittance in the graphene or by the generation of a large electric field on the dielectric film. Graphene's characteristic high transmittance >95% is clear, as is the result that the doping by corona-charged SiO_2 did not reduce its transmittance significantly. This contrasts with most doping techniques that tend to cause transmissivity reductions because of the addition of dopant atoms [62], [64], [272]. The ability to alter the R_{sheet} of graphene rapidly and reversibly without impacting transmittance is significant, as it offers the potential to eliminate the challenging requirement to balance a trade-off between R_{sheet} and transmittance in TCEs. The TCE layer in thin film solar cells will normally be deposited on glass, while commercial solar modules usually involve glass encapsulation. Therefore, it is important to consider the effect of a glass substrate losses if these TCEs would be considered for such

applications. Figure 4.9 (b) presents the ICD-doped graphene transmittance data in the context of glass and graphene/glass transmittance loss, as well as 100 nm ITO and IZO films from the literature for comparison [72], [80]. It is clear ~10% transmittance is lost due to the glass layer alone, with mean transmittance from 400-800 nm calculated to be 89.8%. When graphene is deposited on such a layer, the transmittance drops further, with a mean from 400-800 nm calculated to be 87.0%. As the doping process did not substantially reduce graphene transmittance when measured in isolation, it is expected that the "Graphene on 1 mm glass" with a mean transmittance of 87.0% from 400-800 nm is broadly representative of the transmittance expected if ICD-doping could be replicated on large area glass substrates. In the case of these TCOs, the transmittance measured included the glass substrate. While the transmittance of graphene/glass across the spectrum is mostly greater than these TCO/glass layers from the literature, their R_{sheet} (60 Ω/□ and 45 Ω/□ for ITO and IZO respectively) values over an order of magnitude lower than the graphene layers demonstrated in this Chapter. It is likely that additional charge needs to be introduced into the dielectric to make graphene competitive with typical TCO materials in both optical and electrical properties.

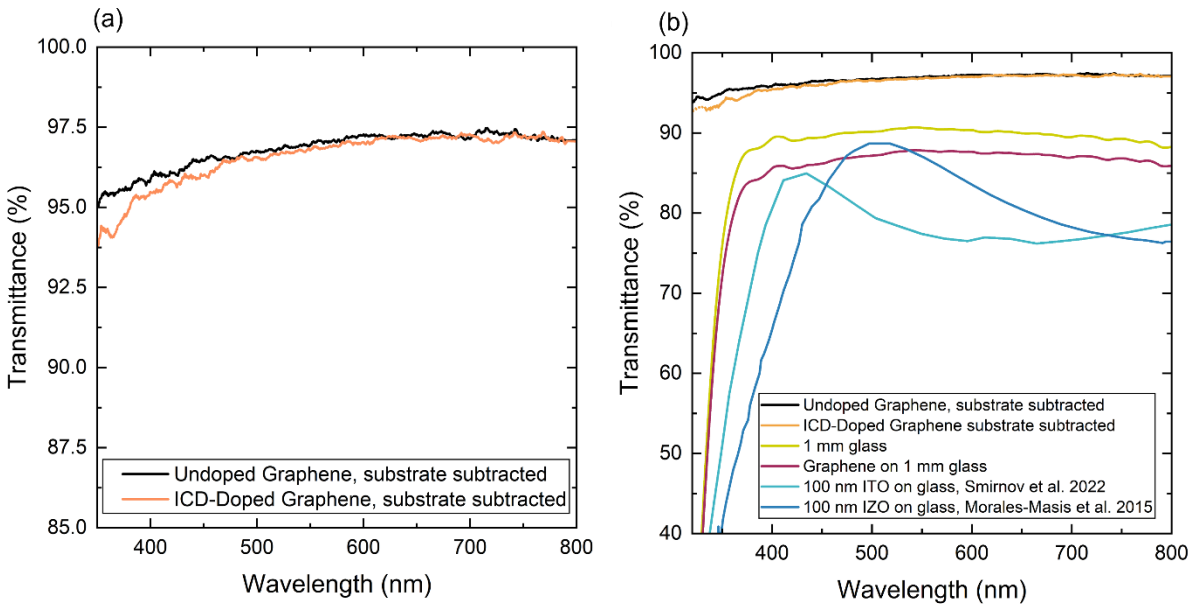

Figure 4.9: Transmittance with respect to wavelength for graphene samples fabricated in this Chapter, with literature values for comparison. (a) Undoped graphene compared with an ion-charge dielectric (ICD)-doped graphene. For these samples,

the transmittance through a 300 nm dielectric without graphene deposited was used as the background reference. This reference was subtracted from the graphene on the 300 nm dielectric, to determine the transmittance of the graphene only. (b) Comparison between graphene transmittance, glass transmittance, and the combined transmittance of graphene deposited on glass. Also included, are data from two commonly used TCOs from the literature. The TCO samples referenced were measured on glass, and so their transmittance includes optical losses from the glass substrate. The 100 nm indium tin oxide (ITO) film was deposited on glass, and had a sheet resistance of 60 Ω/□ [80]. The 100 nm indium zinc oxide (IZO) film was deposited on glass, and had a sheet resistance of 45 Ω/□ [72].

Due to the limitations of the in-house spectrophotometer, the transmittance outside of the 350–800 nm window was not measured. Further work should include transmittance measurements across the entire AM1.5G spectrum before and after doping, to enable more meaningful comparisons between the optical properties of TCOs and ICD-doped graphene for tandem applications. The transmittance of undoped graphene remains broadband from 200 to 3000 nm, encompassing all light absorption within the AM1.5G spectrum [273], [274]. If the ICD doping does not affect the transmittance of these regions, it opens the possibility for a highly transmissive TCE for tandem cell applications.

4.7 Limitations on Corona Charge Storage in SiO_2 Membranes

The measured CPD in this work, is significantly below that of what might be expected in a 300 nm SiO_2 layer. The maximum CPD attainable on a 300 nm SiO_2 membrane should exceed 100 V (>7×10^{12} /cm^2) and is only limited by its dielectric breakdown strength [275]. The reason the CPD measured is below what might be expected could relate to the charging configuration, or a particularly low breakdown strength of the SiO_2 membrane. Figure 4.10 (a) and (b) depict the standard charging configuration and Kelvin probe measurement set-up respectively. In this case, the corona charge is incident on the "rear" side of the SiO_2 membrane. The membrane is supported by 300 µm silicon, capped with a thin 100 nm SiO_2 layer. In this configuration the 100 nm SiO_2 on the support is closer to the discharge electrode than the SiO_2 membrane. When charge is incident on the rear of the sample, it is likely to build up on both the SiO_2 on the silicon support as well as the SiO_2 membrane. However, charge build-up on the support may cause some repulsion of charge from the membrane. This screening effect could have the consequence of reducing the total charge that can be deposited on the membrane, and reduce

the achievable doping effect when interfaced with graphene. To determine whether the charge was being screened, the charge build-up on the "front" side of the membrane was investigated. Figure 4.10 (c) and (d) depict a modified charging and KP measurement configuration for front side charging. In this case, the surface of the membrane is planar, so any charge screening effects should be eliminated.

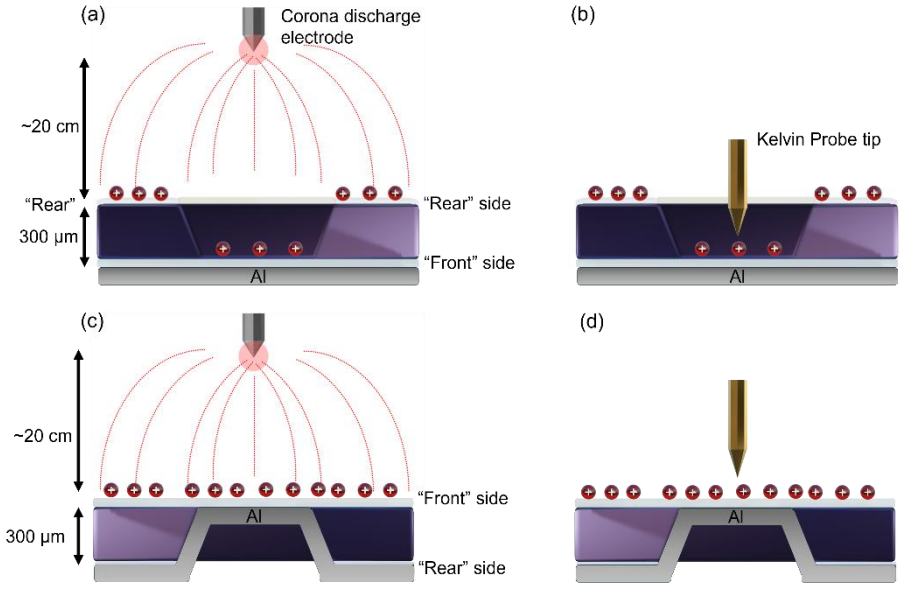

Figure 4.10: (a) Rear side charging with Al electrode. (b) Rear side contact potential difference measurement using scanning Kelvin Probe. (c) Front side charging. (d) Front side contact potential difference measurement.

Figure 4.11 (a) depicts the CPD versus positive charging time for two membranes, charged from the rear or front sides respectively. A greater magnitude CPD is reached when the device is charged from the front side, up to ca. –80 V after 3 minutes. For the rear, the maximum CPD of –12 V is equivalent to $\approx 8.3\times10^{11}$ q/cm^2 , while for the front side, the maximum CPD of –80 V is equivalent to $\approx 5.7\times10^{12}$ q/cm^2. This indicates that when the charge screening effect is not present, there is a near-sevenfold increase in the amount of corona charge that can be deposited on the SiO_2 membrane window, offering the potential for a significantly more dramatic reduction in graphene's R_{sheet}. Figure 4.11 (b) depicts the variation in CPD as the charge decayed over time, up to 10 hours, in the case of membranes positively charged from the rear side and front side respectively. It is clear from Figure 4.11 that decay occurs more rapidly

when the membrane is charged from the front side, indicating that the dielectric is relatively closer to its breakdown limit. To increase the charge deposited on the film and demonstrate the full potential of charged dielectrics for graphene doping, a method to eliminate this charge screening must be developed.

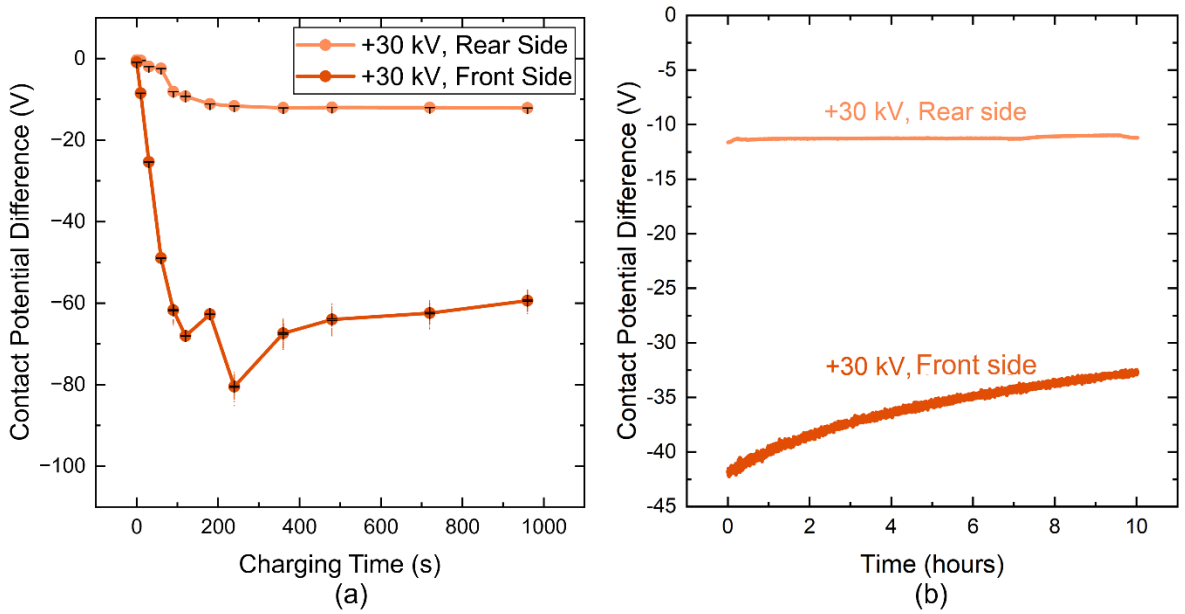

Figure 4.11: (a) Contact potential difference versus charging time of front and rear side of SiO_2 membrane over 16 minutes of total charging time. For each charging time interval, 100 data points were collected. The mean of these data points is presented at each point with a large, filled circle, and the black error bars indicate the standard error. In the case of the front side measurements, the measured contact potential difference decayed rapidly where the device was charged for 90 seconds or greater. This is apparent by the widening of the standard error. The 100 data points measured at the 90 to 960 charging intervals have been overlayed (small dots) over the large circles in this case, showing the spread in the data. (b) Contact potential difference versus decay time for positively charged SiO_2 membranes charged from the front or rear side over 10 hours. In this case, 6000 data points were measured over 10 hours, and every measured data point is presented to showcase the variations in charge on the surface over time.

4.8 **Micron-Scale Corona Deposition for Enhanced Charge Concentration**

To avoid the impact of charge screening at the dielectric, a bespoke corona discharge apparatus was manufactured such that the discharge electrode could be placed inside of the dielectric layer. Figure 4.12 (a) and (b) depict the differences between the standard corona apparatus used, and the micron-scale corona-charging apparatus developed for dielectric membrane samples. For deposition via "the micro-charger", the discharge electrode was positioned using a micron-scale x-y-z stage, such that the discharge tip is closer to the membrane than it is to the silicon support layer, preventing charge deposition on layers liable to cause screening.

However, at reduced tip-sample distance, a reduced applied bias is required to maximise charge deposition without generating arc discharge, which can lead to the destruction of the dielectric membrane, as well as damaging the tip itself. To improve deposition, it was necessary to develop an improved understanding of the relationship between corona-current and SiO_2 dielectric breakdown using this apparatus.

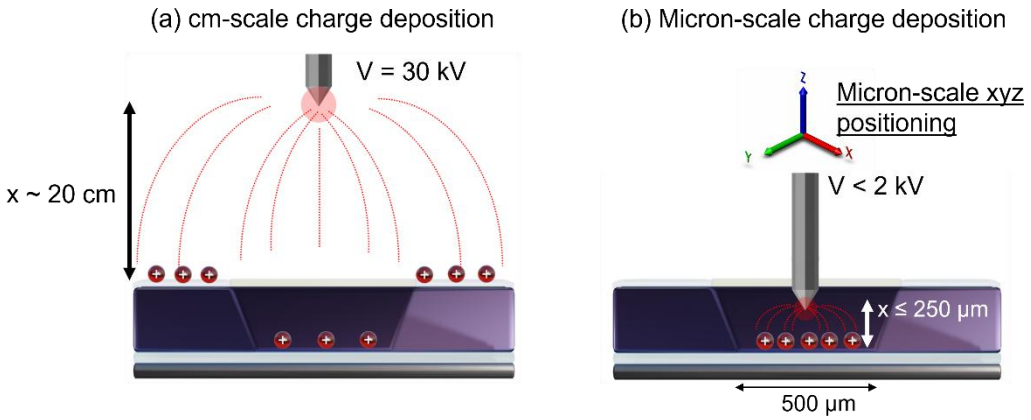

Figure 4.12: (a) Standard corona charging apparatus used in this work. (b) Purpose-built "micro-charger" for micron-scale charge deposition. With the micro-charger, the probe is positioned close to the dielectric membrane to minimise charge screening effects.

To determine an appropriate voltage to improve corona deposition, a planar SiO_2/Si sample was first used. The voltage gradually was increased until just before arc discharge occurred, and the contact potential difference recorded. This was repeated for a number of different sample-tip distances. Figure 4.13 (a) depicts the relationship between contact potential difference, tip-sample distance, and applied voltage, at a fixed deposition time of 20 minutes. This result indicates that is possible to achieve CPD of magnitude ~50 V on planar 300 nm SiO_2 on a silicon substrate using a corona charging apparatus with tip-sample distance x~300 µm. At closer tip-sample distances, such a high magnitude CPD was not achieved due to the insufficient corona current generated at low voltages without arc discharge occurring. Figure 4.13 (b) depicts a CPD map across an area of a SiO_2/Si substrate subject to 40 mins corona deposition at x=300 µm, and applied voltage +1.25 kV. The deposited charge is relatively

uniform within a 500 $\mu m^2 \times 500\ \mu m^2$ area under the KP tip, indicating its suitability for ion deposition on a dielectric membrane of such an area.

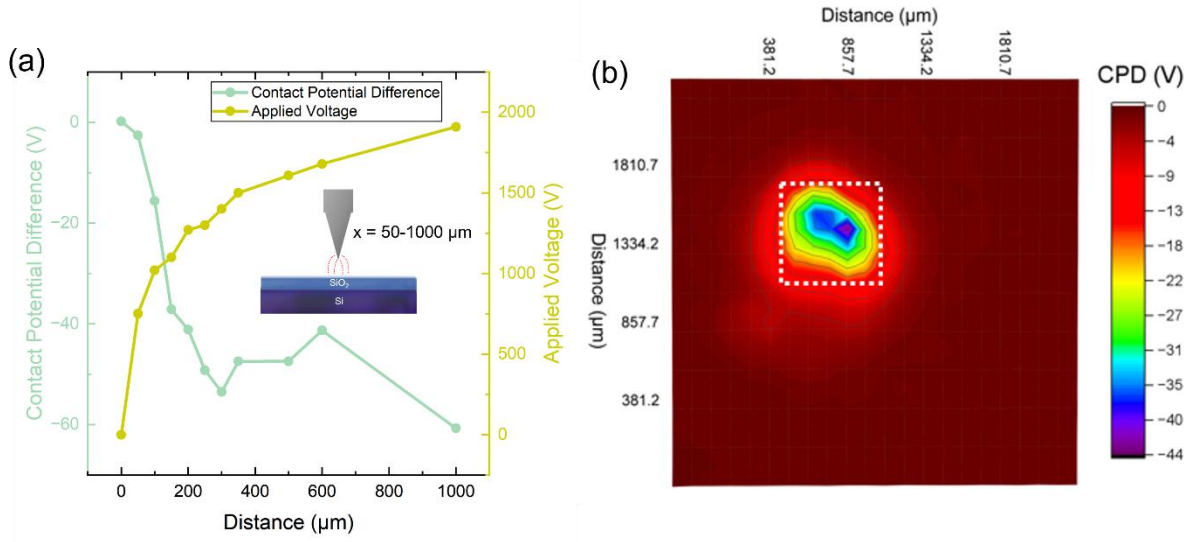

Figure 4.13: (a) Contact Potential Difference with varying corona plate-tip distance, with varied applied bias, for constant corona deposition time of 20 minutes on a planar SiO_2/Si sample with 300 nm oxide. (b) Contact potential difference map of area under micron-scale corona discharge tip on a planar SiO_2/Si sample with 300 nm oxide. The 500 $\mu m^2 \times 500\ \mu m^2$ charged area highlighted with a white dotted line.

The micro-charger was then applied to SiO_2 membrane samples. Figure 4.13 (a) depicts the discharge electrode positioning setup for dielectric membranes, where x indicates the tip-sample distance, and d the tip diameter. Figure 4.13 (b) depicts the variation of contact potential difference on a dielectric membrane over time held under applied bias in such a "micron-scale" corona discharge apparatus. The lime line indicates the contact potential difference measured on the top of the silicon support layer "position 1", while the green-yellow line indicates the contact potential difference measured at the membrane, "position 2". The largest CPD value of ~33 V is achieved at x = 250 µm, at an applied voltage of 1.35 kV, equivalent to 2.4×10^{12} /cm^2. This method to increase charge concentration on the dielectric was then used to facilitate an increased doping effect in a graphene layer interfaced with it.

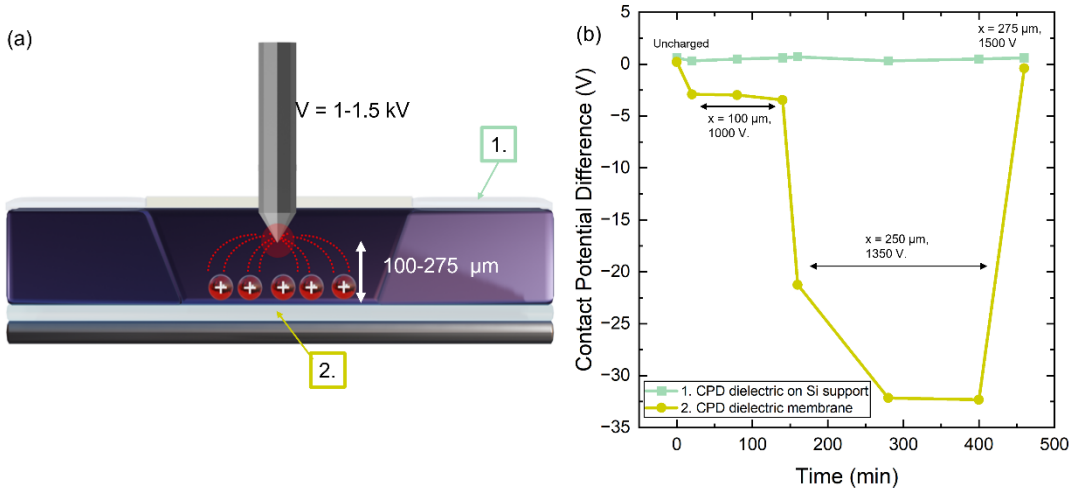

Figure 4.14:(a) Schematic of micron-scale positioning of the corona discharge electrode in membrane devices. (b) Contact potential difference over time at differing set tip-sample distances and applied voltages for SiO_2 membrane samples.

4.9 In-Situ Corona Deposition and Sheet Resistance Measurements

Following the investigation of enhanced corona ion deposition on dielectric membranes via the micro-charger, a graphene device was placed in this new micro-charger, and modifications made so that R_{sheet} could be measured during ion deposition. Figure 4.15 depicts the variation of sheet resistance of graphene on SiO_2 membrane held under such a micron-scale corona discharge apparatus, with R_{sheet} measured at 2-minute intervals. The initial R_{sheet} ~1.65 kΩ/□ drops precipitously as time held under corona charge is increased, reducing to ~400 Ω/□ after 25 mins of positive charging. This dramatic reduction of >75% demonstrates the viability of the ICD-doping technique, offering graphene R_{sheet} reduction comparable with the best chemical doping techniques [121], [272]. This increased reduction is deemed to be directly as a consequence of the increased charge deposited on the dielectric film. The plateau in R_{sheet} was likely due to an increased reduction in mobility as the charge concentration on the dielectric layer increased.

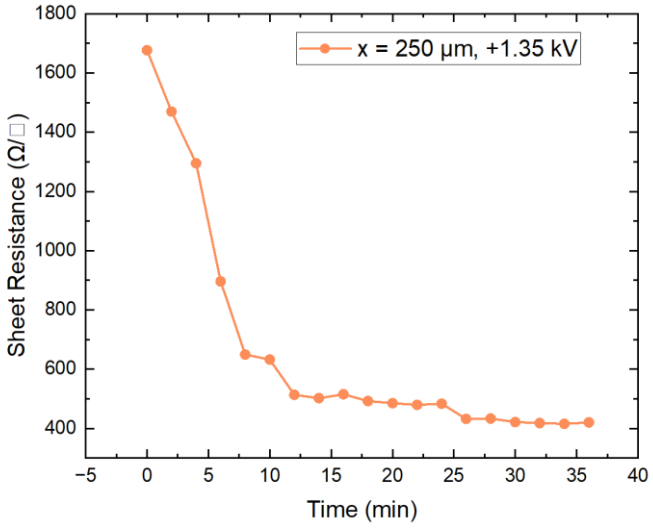

Figure 4.15: Sheet resistance of graphene over time held under corona charge with +1.35 V applied bias and sample-tip distance 250 µm.

4.10 Charge Deposition on SiN_x and Planar Silicon Structures for Graphene Doping

In an optoelectronic device such as a solar cell, the membrane is not likely suspended, but instead part of a layered device stack. When supported by a substrate, the ability of a dielectric film to hold corona dielectric charge may be improved due to reduced environmental exposure. Hence, measuring the CPD of the SiO_2 when supported by Si would provide a closer indication of the corona charging potential of such films, if applied in devices. Figure 4.16 (a) depicts a contact potential difference map of area 1000 × 800 µm^2 on the front side of a SiO_2 membrane, before charging. Figure 4.16 (b) depicts a contact potential difference map across the same area on the front side of the sample, after the front side was positively charged for 3 minutes. Data points first measured are displayed at the front-left side of the plots in Figure 4.16, with the final data points measured displayed at the rear-right side of each plot. The data acquisition times for such plots is ca. 1 hour. Therefore, the difference between the CPD data presented at the front-right and rear-right will indicate how much the charge concentration on this sample decayed over 1 hour. The area in which the 500 × 500 µm^2 membrane was mapped is identifiable in teal-green, at ~ −60 V in the charged sample. The reduced CPD over the membrane suggests that even in the absence of screening effects or current restrictions imposed

by the micron-scale corona deposition apparatus, the suspended SiO_2 does not reach as high a CPD as that of the Si-supported SiO_2. Immediately after charging, the Si-supported SiO_2 reaches a maximum of ca. –100 V, a near-order of magnitude increase in CPD compared to that used in the ICD-doping in this work. Such increases in CPD indicate a potential for much higher charge concentrations and thus further reductions in graphene's R_{sheet}, when using the ICD-doping technique.

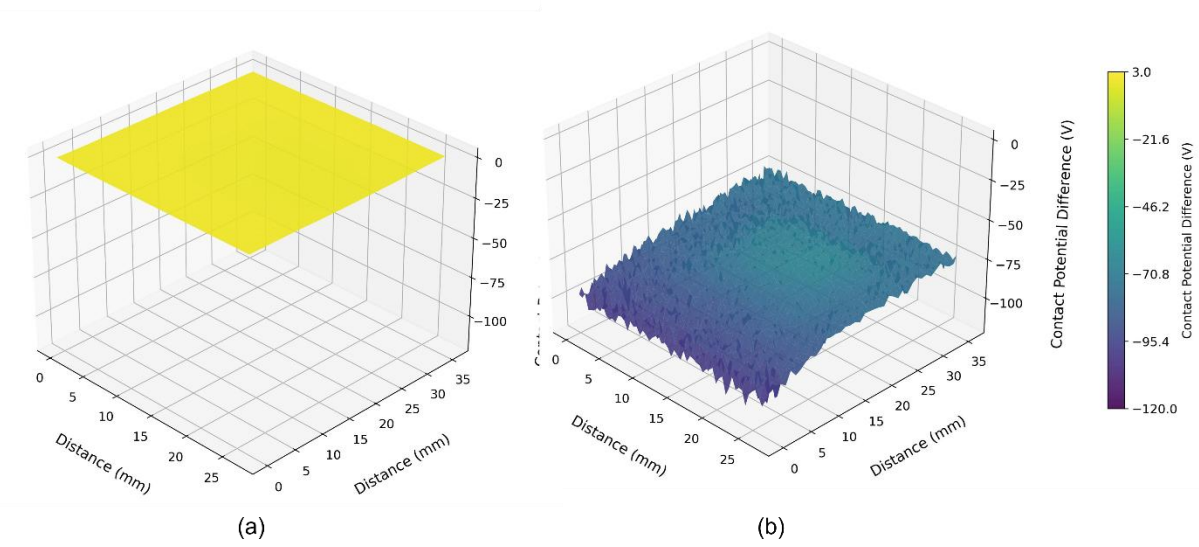

Figure 4.16: Kelvin probe mapping of contact potential difference versus distance on the front side of SiO_2 membrane windows. (a) Before charging. (b) 180 s positive charging, from the front side, with an applied voltage of +30 kV. The measurement was carried out by raster scanning the Kelvin Probe across the sample surface with step size 12.7 µm.

Electrostatic ICD doping of graphene also applies to other materials that can store corona charge. Figure 4.17 (a) depicts the contact potential difference (CPD) versus charging time for a 100 nm SiN_x membrane, positively the standard corona apparatus setup. After 8 minutes of total charging time, the CPD reached ca. –4 V. Using Equation (3.18), for d = 100 nm, and silicon nitride $\epsilon_r = 7.4$, this corresponds to a charge concentration of $\approx 1.4\times10^{12}$ q/cm^2 deposited on the surface of the dielectric film. If the same relationship between the magnitude of charge deposited on SiO_2 film and a change in graphene's R_{sheet} holds for SiNx, a graphene monolayer transferred to this SiN_x membrane could attain >50% reduction in R_{sheet} after membrane charging. The availability of charged SiN_x as a charged dielectric graphene dopant could

provide varied integration opportunities for ICD-doped graphene in devices. However, as is depicted in Figure 4.17 (b), the stability of corona charge in such a membrane appears reduced compared to SiO_2, which may limit its applicability.

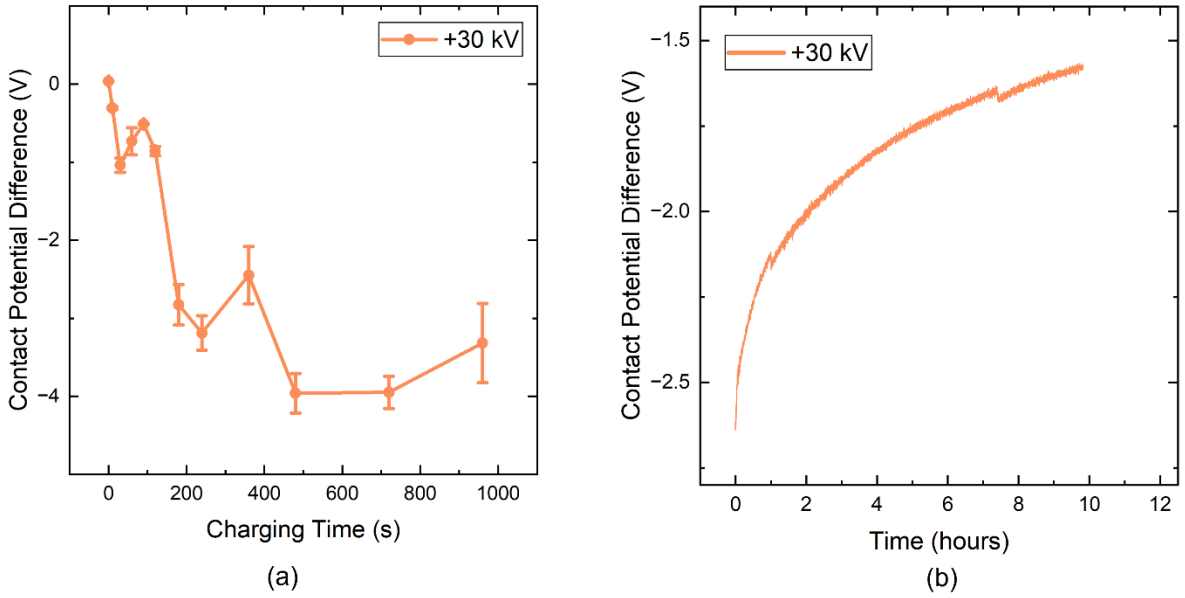

Figure 4.17: (a) Contact Potential Difference versus positive charging time for 100 nm SiN_x membrane. 100 points were measured at each charging interval, and the mean calculated. In this case, the error bars represent the range of data captured at each data point. (b) Contact potential difference versus time for positively charged SiO_2 membranes, as 6000 data points were captured over 10 hours.

4.11 **Discussion and Conclusions**

In this chapter, ion-charged dielectric doping of graphene was demonstrated for the first time. A sheet resistance reduction of >60% was attained when dielectrics were subjected to positive or negative charge, with doping verified by the G blueshift in its measured Raman spectra. Change in the polarity of the Hall coefficient, as well as the shift of 2D indicated that the deposition of positive and negative charge induced n- and p-type doping in the graphene respectively. Increases in carrier concentration $>4\times10^{13}/cm^2$ were achieved, with modest reduction in mobility, contributing towards the strong reduction in R_{sheet} observed. Crucially, such reductions in R_{sheet} were found not to have impacted the transmittance of the film, with both the doped and undoped film retaining high transmittance >95% across the spectrum. To improve the charge deposition, methods to deposit corona charge directly on the surface of the

membrane with no charge screening were developed. This allowed an increase in surface charge on the membrane, and a subsequent reduction of graphene's R_{sheet} by >75% to ~400 Ω/□. The stability of such charge on different dielectrics and their potential for improved charge storage in devices was also discussed, laying the groundwork for a novel approach to dope graphene for improved optoelectronic devices.

In this work, the ultimate achievable R_{sheet} was limited by the high defect density of the as-deposited films reducing mobility, as well as the poor charge storage in freestanding dielectrics as compared to the measured charge storage on the Si supported SiO_2. With improved dielectric synthesis techniques, the amount of charge deposited on the film can be increased. Such improvements could allow for R_{sheet} <100 Ω/□ in high-mobility graphene layers.

To accommodate varying device requirements, the thickness of the dielectric can be reduced without reducing the amount of charge that can be deposited on the film. Reducing thickness to 10s of nm for improved optics should not impact amount of charge that can be deposited on the dielectric, as a stable inorganic dielectric typically only depends on the dielectric constant and dielectric strength of the material. Consider the relation for dielectric strength, $E_{bd} = V_{bd}/d$, where V_{bd} is the dielectric breakdown voltage, and d is the dielectric thickness. If one assumes that the dielectric in a device behaves as a parallel-plate capacitor, one can calculate the approximate charge concentration, per area, that can be deposited on the dielectric surface as: $q = E_{bd}\epsilon_0\epsilon_r$. In this case, the charge concentration per area deposited on the surface is a product of the dielectric strength and the permittivity, being independent of dielectric thickness. If the dielectric quality is high, the thickness of the dielectric can be, in principle, reduced to <20 nm without compromising the charge storage. This provides opportunities for varied device requirements and potential combination of ICD-doped TCEs with anti-reflection layers. For example, a charged SiN_x layer of 75 nm thickness could be used as an anti-reflection layer,

while also electrostatically doping the graphene which is interfaced with the perovskite HTL or ETL at the front of a perovskite/silicon tandem structure.

ICD-doping of graphene using charged dielectric membranes is not applicable to optoelectronic devices such as tandem solar cells. The poor stability of corona charge to elevated temperatures, moisture, as well as its limitation to fragile dielectric membranes, limits this configuration to a proof-of-concept study. Chapter 5 will go beyond this proof of concept, investigating alkali ion migration in dielectrics for stable graphene doping that can be applied uniformly across large area optoelectronic devices.

Chapter 5

Permanent Electrostatic Doping of Graphene via K^+-ions inside SiO_2 Thin Films

5.1 Introduction

In Chapter 4, it was demonstrated that corona-charged dielectrics can provide sufficient charge to dope graphene, establishing the “proof-of-principle" of ICD-doping of 2D materials. Specifically, corona charge, when deposited on SiO_2 or SiN_x dielectrics, was shown to increase the carrier concentration of an adjacent graphene layer by >4×, demonstrating a direct relationship between dielectric charge and graphene doping. This chapter builds upon this principle, investigating migrated alkali cations as the charge source to achieve strong electrostatic doping of graphene with long-term stability. Alkali ions can be migrated from a SiO_2 surface to the Si/SiO_2 interface, where they remain stable over commercial timelines [183], [184], [214], [262]. This technique, originally developed for field-effect passivation in silicon solar cells, follows decades of study of silicon MOSFETs, where such ions were considered undesirable contaminants [276], [277], [278]. While promising for passivation, this approach has not yet been explored for 2D materials doping.

A range of alkali ions can migrate within SiO_2, but not all are suitable graphene dopants. Heavy ions with large ionic radii such as Rb^+ and Cs^+ have low mobility in SiO_2, and so require very high temperatures of >450-550 ℃ to drift through it [214]. Such high temperatures may compromise the graphene quality, and are unsuitable for delicate tandem layers such as perovskite and amorphous silicon. The high-temperature stress may also reduce the breakdown strength of the dielectric, limiting its charge storage potential. Lighter ions such as Na^+ and Li^+ drift at lower temperatures, ~50-150 ℃, but due to their smaller ionic radii and high mobility, they are expected to have poor stability as dopants [279], [280], [281], [282]. In this chapter,

K^+ ions are selected as the candidate dopant due to their balance of stability and relatively low migration temperatures.

A KCl precursor solution is deposited on the front side of a SiO_2 thin film grown on Si, and a high-temperature electric field is used to drive the K^+ ions to the Si/SiO_2 interface. After ion migration to the Si/SiO_2 interface, a graphene layer is deposited on the surface of the SiO_2. Due to the screening of the alkali ions by the charge carriers in silicon, graphene will not experience any discernible doping effect compared to a control sample with no ions deposited. A reverse bias is then applied to migrate the K^+ ions close to the graphene. It is expected that the ions will then provide additional charge carriers to induce doping in graphene via the field effect. This chapter investigates the migration of K^+ ions in SiO_2, and correlates their position and magnitude in the SiO_2 film with a corresponding doping effect in graphene interfaced with it. The feasibility of this technique for application in tandem cells and other optoelectronics devices is discussed.

5.2 Characterisation of K^+ Charge Concentration in SiO_2/Si

5.2.1 Capacitance-Voltage of K^+ Migration in SiO_2 with Al Electrode

Capacitance-voltage (CV) measurements of SiO_2/Si were used to determine the concentration and position of ions in the SiO_2. Due to the processing complexity of using CVD graphene, the conditions necessary to effectively migrate K^+ in SiO_2 were first validated using a simplified configuration with an Al electrode. Subsequently, the ion stability when undergoing the graphene transfer process and the conditions required to migrate the ions to a graphene electrode are investigated. Initial substrates were p-type silicon with a 300 nm thermally grown SiO_2. A KCl precursor solution was spin-coated on the surface, and an Al metal contact of diameter 0.5-1 mm was deposited by thermal evaporation. A ±5 V bias, a temperature of 350 ℃, and 20-minute dwell time were chosen as initial conditions. A simulated CV curve was

used to determine the position of the V_{FB}, which was then used to calculate the SiO_2/Si interfacial charge. The movement of ions between the SiO_2/Si and the Al/SiO_2 interface can be used to infer the charge concentration that can be migrated to the Al, hence determining the number of additional carriers available for graphene doping.

Figure 5.1 (a) and (b) depict the capacitance-voltage characteristics of a device with 300 nm oxide, with and without a KCl solution spin-coated on the SiO_2 surface. In both control and KCl-treated samples, the initial V_{FB} is close to 0 V. This indicates a low initial charge concentration at the SiO_2/Si interface. Figure 5.1 (c) shows the calculated charge concentration at the SiO_2/Si interface before and after high-temperature bias stress. The median ion concentration at the SiO_2/Si interface before high-temperature bias stress for the control and treated samples was $(3.7\pm0.6)\times10^{11}$ q/cm^2 and $(4.2\pm0.6)\times10^{11}$ q/cm^2, respectively. Since both values are within the margin of error of each other, it can be assumed that the deposition of ions at the surface did not contribute to a significant increase in charge at the SiO_2/Si interface.

In the control group, after applying +5 V at 350 ℃ for 20 minutes, the V_{FB} shifted positively slightly. The ΔV_{FB} corresponded to a slight reduction in charge at the SiO_2/Si interface, from $(3.7\pm0.6)\times10^{11}$ q/cm^2 to $(1.5\pm0.2)\times10^{11}$ q/cm^2. By applying a reverse bias, the charge concentration at the SiO_2/Si interface increased to $(3.0\pm0.2)\times10^{11}$ q/cm^2. This implies that a mobile charge concentration of $\sim1.5\times10^{11}$ q/cm^2 can be migrated between the SiO_2/Si and the Al, independent of extrinsically added K^+ ions. This change in charge concentration could be due to residual trapped charges or impurities being released due to the bias-temperature stress, or impurities introduced at the surface that neutralise positive interface charge. Such charges are unlikely to contribute to noticeable doping in graphene, as their magnitude is too low to significantly shift its Dirac point.

In the KCl-treated sample (s1), after +5 V at 350 ℃ for 20 minutes, the V_{FB} shifts negatively beyond the −60 V limit of the source-measuring unit, demonstrating a significant increase in charge concentration at the SiO_2/Si interface. This corresponds to a charge carrier concentration at the interface of > 4.2×10^{12} q/cm^2. This suggests a K^+ concentration at the interface of ≳4.05×10^{12} q/cm^2, accounting for mobile charges observed in the control sample, assuming all introduced positive charges are K^+ ions. If we assume a realistic dielectric breakdown strength of thermally-grown SiO_2 on Si of 9-10 MV/cm, films are limited to ~2×10^{13} q/cm^2 before dielectric breakdown [283], [284], [285], [286]. Therefore, the charge concentration at the SiO_2/Si interface can be assumed to be ~0.4-2×10^{13} q/cm^2. When a reverse bias is applied to the KCl-treated sample, the SiO_2/Si interface ionic concentration returns to $(4.6\pm0.8)\times10^{11}$ q/cm^2 as the ions migrate back to the Al contact. This is within the margin of error of the initial concentration at the SiO_2/Si interface, indicating that all K^+ ions introduced at the SiO_2/Si interface can be migrated back to the Al/SiO_2 interface under this treatment. In contrast, at a metal pad (s2) 10 mm away from the biased electrode (s1), the charge concentration did not change significantly. This indicates that a good electrical connection to the biased electrode is required for the ions at the Al/SiO_2 interface to achieve sufficient activation energy to migrate to the SiO_2/Si. Such findings provide scope for a highly tailorable platform for doping highly conductive 2D materials to ~10^{13} q/cm^2 when using KCl-treated substrates.

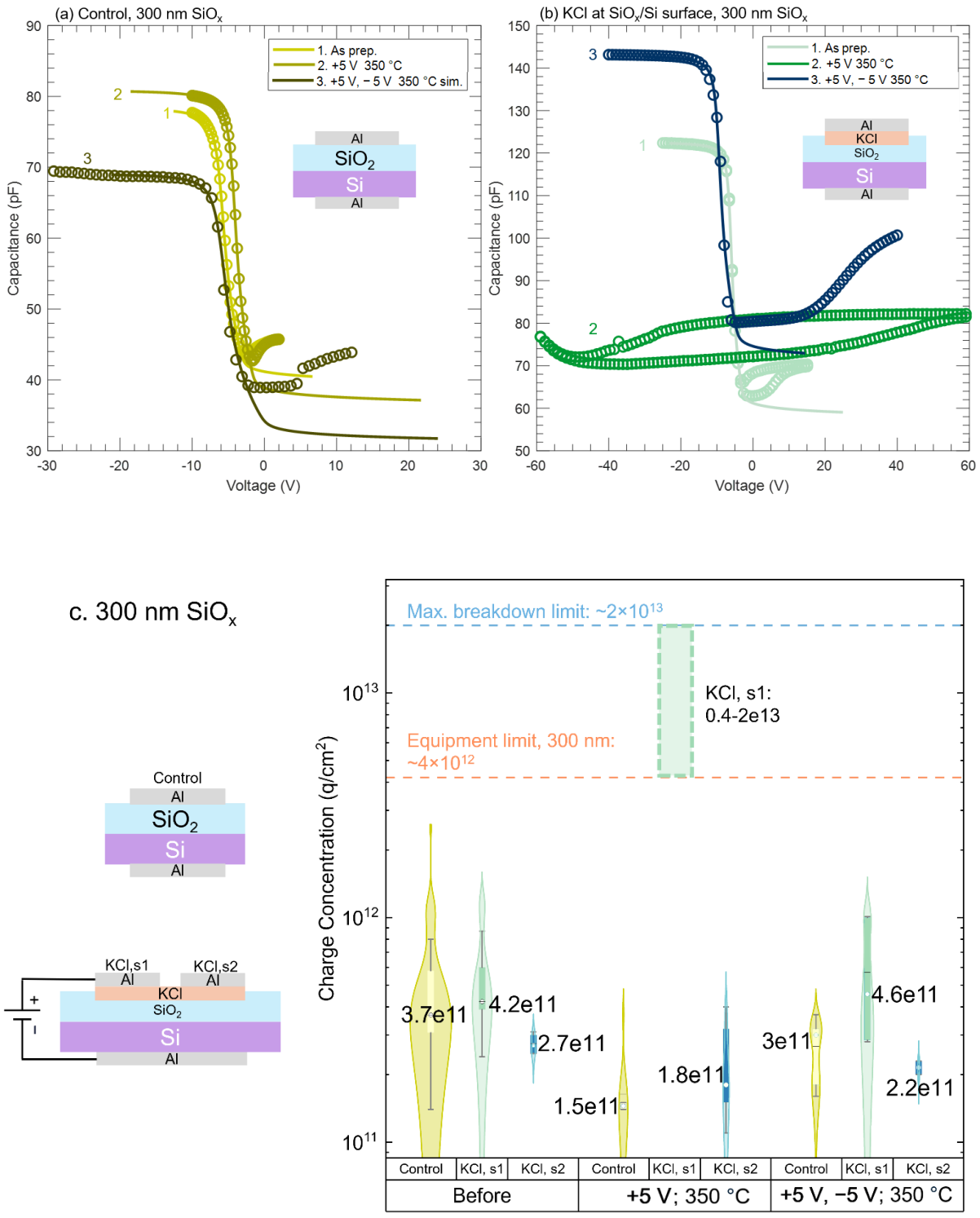

Figure 5.1: (a), (b) Capacitance-voltage characteristics of a SiO_2/Si sample subjected to bias-temperature stress, without and with KCl spin-coated on the surface respectively. Circle markers indicate data points, while solid lines indicate simulated capacitance-voltage curves used for charge calculation. (c) Charge Concentration at SiO_2/Si interface for KCl-treated, and control samples with 300 nm SiO_2, before and after various temperature-bias stress conditions. The median is labelled, with the box corresponding to the range within 25%-75% percentiles, and the error bars indicating the range within 1.5 times the interquartile range.

As the equipment used was limited to ±60 V, the charge measured was limited to ~4.2×10^{12} q/cm^2 for a 300 nm oxide. Figure 5.2 (a) depicts the charge concentration at the SiO_2/Si

interface for samples with 100 nm SiO_2, subjected to the same process as in Figure 5.1(a)-(c). For a 100 nm SiO_2, the V_{FB} also shifts from close to 0 V to beyond the measurement range of the equipment at ±60 V. For a 100 SiO_2, a ΔV_{FB} of >60 V corresponds to Si/SiO_2 charge $>10^{13}$ q/cm^2. This was used as the basis of an assumption that at least 10^{13} q/cm^2 K^+ ions also migrated between the Al and the silicon in the case of the 300 nm oxide. However, it is not clear whether this assumption applies to a thicker 300 nm layer, as it requires that ions to drift three times further. This can be probed by reducing the applied bias. Figure 5.2 (b) depicts the CV characteristics of a K^+ treated SiO_2/Si sample with 300 nm oxide, subjected to a ±1 V bias-temperature stress for 20 mins at 350 ℃. The energy from +1 V at 350 ℃ is sufficient to migrate $<4.2 \times 10^{12}$ q/cm^2 to the Si/SiO_2 interface, but −1 V is insufficient to migrate these ions back to the metal. Even after three cycles at approximately −1 V, there remains $\sim 1.25 \times 10^{12}$ q/cm^2 at the SiO_2/Si interface. This indicates a greater energy barrier for ion de-trapping from the SiO_2/Si interface, than for drift through the dielectric. Therefore, the energy required to cross a 100 nm SiO_2 layer should be similar to that of a 300 nm SiO_2. It is therefore likely that $>10^{13}$ q/cm^2 is present at the SiO_2/Si interface in samples with 300 nm SiO_2, assuming similar breakdown strengths of the thermally-grown oxide. This is sufficient to provide strong graphene doping if the ions can be effectively migrated to the graphene/SiO_2 interface. The ability to finely vary applied voltage ~1 V offers the potential for a wide range of charge concentrations, and thus finely tailorable 2D material sheet resistance.

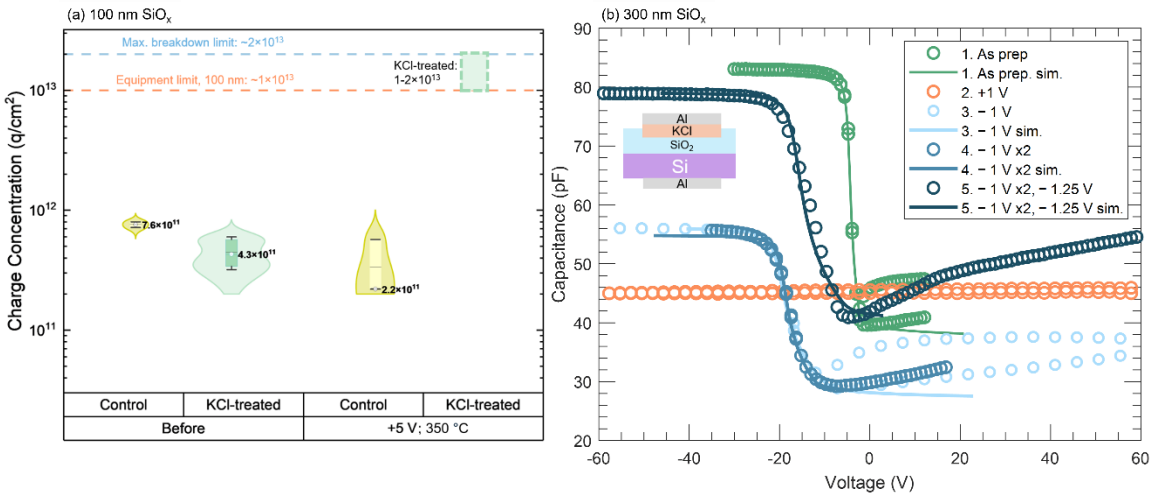

Figure 5.2: (a) Charge concentration at SiO_2/Si interface for KCl-treated, and untreated samples with 100 nm SiO_2, before and after various temperature-bias stress. (b) Capacitance-voltage characteristics of a KCl-treated SiO_2/Si sample subjected to 1-1.25 V bias-temperature stress.

5.2.2 Thermally Stimulated Ionic Conductivity of K^+ ions in SiO_2

To confirm ion migration to the metal and quantify the charge drift across the dielectric, the current between the silicon and the Al contact can be measured during bias-temperature stress. This process is known as "thermally stimulated ionic conductivity" or "thermally stimulated ionic current" (TSIC) [233], [282]. While the ions are transient, a corresponding increase in current (<1 nA) can be measured. This allows ionic drift temperatures to be determined and provides corroborating quantification of the ion concentration driven to and from the Si/SiO_2 interface. By integrating the area under the current peak vs time $\int I\ dt$, the ion concentration in q/cm^2 can be determined, following the equation $q = \frac{\int I\ dt}{e \cdot A}$, where e is the electron charge and A is the metal contact area. The metal contact area was calculated to be 0.0082 cm^2 after measuring the metal diameter using an optical microscope at room temperature. However the effective area of the metal contact can change during measurement due to thermal expansion as well as probe-sample scratching, making precise area measurement during ion migration difficult to determine.

Equipment to minimise current noise was constructed in-house, with radiative components electromagnetically shielded and grounded. Figure 5.3 (a) depicts the current across a KCl-

treated SiO_2/Si sample with respect to temperature as it is held under positive and negative bias. The peak current at ~300 ℃ and 325 ℃ correspond to the peak in ion drift from the Al/SiO_2 and Si/SiO_2 interface respectively, indicating that higher energy is required to overcome the barrier to migration of ions from the Si than from the metal, as supported by the CV measurements in Figure 5.2 (b). There is a small additional peak on the +5 V curve at ~130 ℃, likely due to contamination from Na^+ introduced during processing [282]. Figure 5.3 (b) depicts the calculated transient charge after the +5 V and −5 V processes. The calculated median transient charge of ~1.74×10^{13} q/cm^2 and 1.25×10^{13} q/cm^2 also corroborates well with CV measurements. However, the difficulty in precisely determining the metal contact area due to thermal expansion and scratching during measurement, and appropriately integrating the curve area may contribute towards some variation in these calculated results. Nevertheless, it is clear that a high charge concentration can be migrated across the interface towards a metal during a bias-stress process, with potential for >10^{13} q/cm^2 to contribute towards graphene doping.

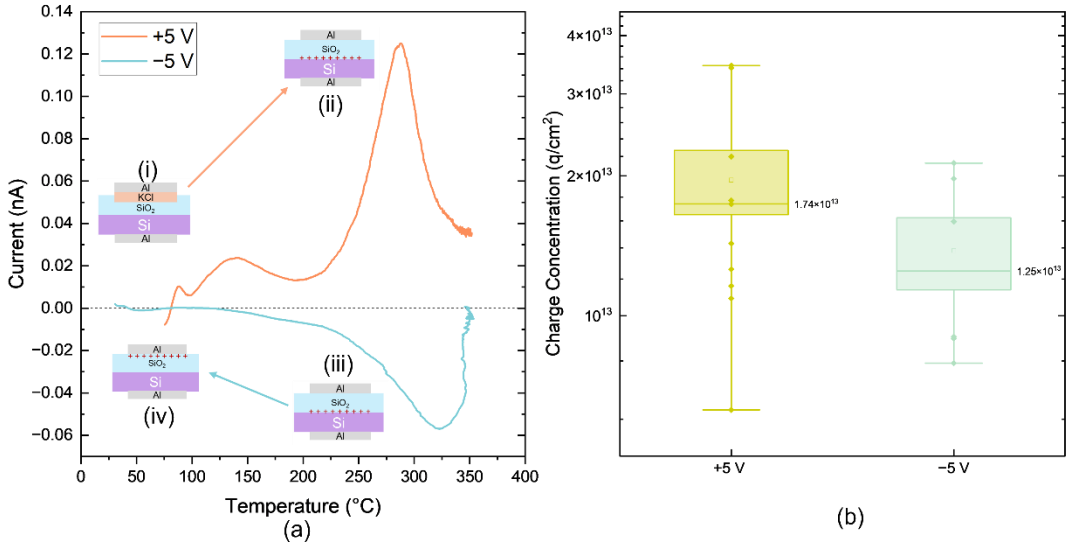

Figure 5.3: (a) Current vs temperature for a SiO_2/Si sample with Al contact of 0.5 mm diameter, with KCl spin-coated on the SiO_2 surface, then subjected to bias-temperature stress. (b) Calculated transient charge concentration obtained using the TSIC technique, for positive ions migrating from the metal to the SiO_2/Si interface (+5 V), and from the SiO_2/Si interface to the metal (−5 V) respectively.

5.3 Stability of K^+ in SiO_2/Si with Graphene Electrode

To migrate ions to a graphene layer, the graphene must be transferred to the SiO_2 surface. However, water and solvents introduced during the transfer process remove the deposited KCl solution from the SiO_2 surface. To prevent KCl from being washed away, the K^+ ions are first driven to the SiO_2/Si interface using the corona anneal (CA) process described in Section 3.2.2. In this case, K^+ ions are driven to the SiO_2/Si interface using the field generated by the corona charge, rather than by an externally applied bias [215]. An external reverse bias can be subsequently applied to migrate the ions to the graphene or metal at the surface. Ionic drift to the SiO_2/Si interface was first verified via CV with a 1 mm Al front electrode. Figure 5.4. (a) depicts the capacitance-voltage characteristics of an Al/SiO_2/Si device subjected to CA prior to metallisation, and Figure 5.4. (b) depicts the calculated charge concentration compared with control samples with no extrinsically added ions. The initial CV characteristics indicate a charge concentration >4.2×10^{12} q/cm^2 at the SiO_2/Si interface due to the negatively shifted V_{FB} beyond the scope of the source-measuring unit, indicating that the CA provided sufficient energy for the ions to migrate to the SiO_2/Si interface. By subsequently applying a bias of −5V at 350 ℃, the V_{FB} shifts positively as ions migrate to the metal surface. This leaves a calculated $(5.8\pm0.5)\times10^{11}$ q/cm^2 K^+ ions at the SiO_2 interface. This implies a concentration >10^{13} q/cm^2 has been migrated to the Al/SiO_2 interface, assuming a similar concentration of ions is introduced to the oxide via corona charging as when using an external field. At a second Al pad (s2) on the treated sample 10 mm away from the biased Al electrode (s1), the charge concentration at the Si/SiO_2 interface remains high, indicating that ions migrate only underneath the biased electrode, as there is insufficient energy to activate ion migration at adjacent contacts. Ions can subsequently be moved back to the SiO_2/Si interface by applying a +5 V bias at high temperature. This demonstrates precise control of ionic position laterally and at dielectric interfaces, offering the potential for patterned doping.

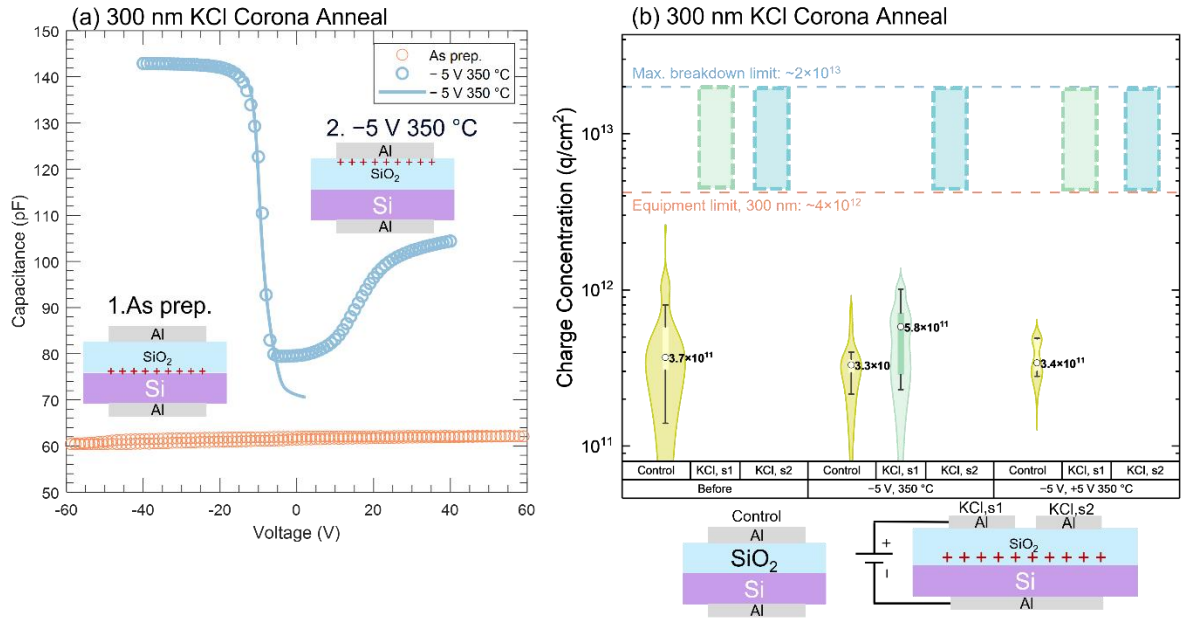

Figure 5.4: (a) Capacitance-voltage characteristics of a SiO_2/Si sample subjected to KCl corona anneal, and bias-temperature stress. Circle markers indicate data points, while straight lines indicate simulated capacitance-voltage curves used for charge calculation. (b) Charge Concentration at SiO_2/Si interface for KCl corona annealed, and untreated samples with 300 nm SiO_2, before and after various temperature-bias stress. The median charge is labelled, with the box corresponding to the range within 25%-75% percentiles, and the error bars indicating the range within 1.5 times the interquartile range.

To determine K^+ ion stability to the graphene transfer, the charge at the Si/SiO_2 interface was measured before and after samples were subjected to various processing conditions to mimic the graphene transfer process. Figure 5.5 depicts the CV characteristics of various SiO_2/Si samples after undergoing a K^+-CA, then subjected to different treatments. The inversion capacitance of 10-20 pF is within the expected range for a ~0.5 mm diameter Al contact, with area variation ±150 µm due to processing damage between measurements. A high charge concentration appears to remain at the SiO_2/Si interface after respective samples are subjected to IPA, acetone, oxygen plasma and water. Subsequently, devices were annealed at 180℃ for 15 minutes in air, and at 150℃ for 10 hours in a nitrogen furnace, and immersed in 50℃ acetone for four hours. The resulting CV characteristics indicate the stability of a high charge concentration at the SiO_2/Si interface. It is plausible that graphene laser patterning could contribute towards high localised heating and risk ion de-trapping, so this was also included as a comparative processing step. The laser patterning might also cause impurity or localised pinhole formation, compromising ion stability and migration kinetics. However, after this step,

the V_{FB} remained outside the range of the CV meter, indicating a high charge stability at the SiO_2/Si interface. The charge concentration of 6.65×10^{11} q/cm^2 at the Si/SiO_2 interface after reverse biasing indicates that the graphene transfer process does not substantially impact the stability or concentration of the charge in the dielectric, nor its ability to be migrated through the dielectric after processing.

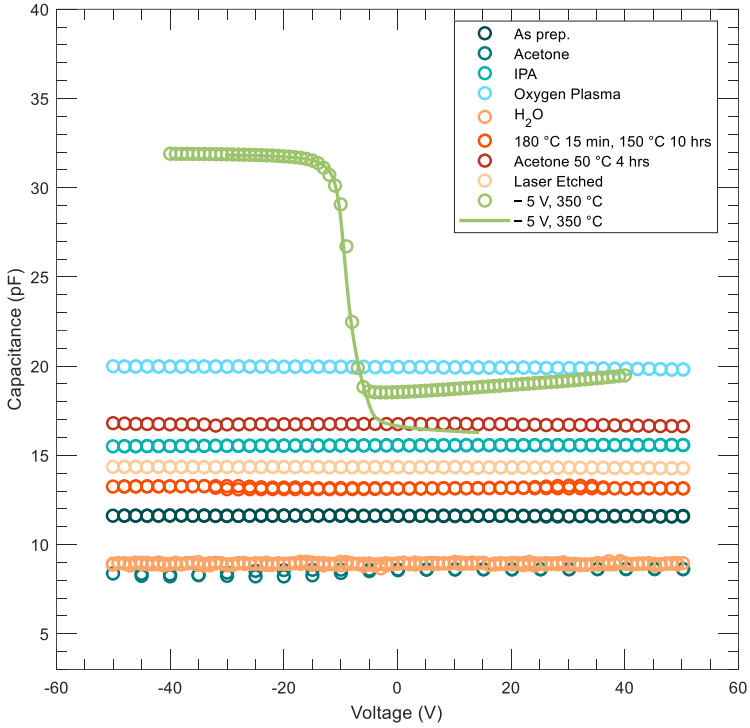

Figure 5.5: Capacitance-voltage characteristics of Al/SiO_2/Si sample subjected to a KCl corona anneal, then various processing conditions to mimic the conditions of a graphene transfer process.

5.4 Migration of K^+ in SiO_2/Si with Graphene Electrode

The next step was to determine whether graphene could act as an electrode for ion migration. CV measurements of graphene/SiO_2/Si devices were carried out to measure ion migration to the graphene. However, graphene's non-uniform resistance introduces a distributed resistor-capacitor effect, making capacitance-voltage behaviour difficult to measure, as multiple capacitors will be measured in series. Consequently, expected CV behaviour was not observed, with films instead exhibiting a peak in capacitance at 0 V, with declining capacitance at

increased ±V. Moreover, the peak capacitance measured in the graphene device was far below the expected capacitance for this area and thickness. Leakage effects when using a large-area graphene electrode also prevented reliable TSIC charge measurement. To determine ion migration to a graphene electrode, the graphene was laser etched after bias-temperature stress, and an Al electrode deposited in the etched area.

A graphene vdP device with Al contacts was fabricated on a SiO_2:K^+/Si substrate, and subjected to a bias-temperature stress, with an Al contact serving as the biased electrode. Figure 5.6 depicts the CV characteristics measured at the graphene area after etching, at the biased Al electrode, and at an area electrically disconnected from the graphene device. The CV characteristics of the dot outside the graphene device before bias-temperature stress indicate $>10^{13}$ q/cm^2 charge at the SiO_2/Si interface, confirming that the graphene transfer did not impede the interface charge stability. After a −5 V bias stress at 350 ℃ for 20 minutes at the Al vdP contact, the V_{FB} shifted positively, such that ~3.5×10^{11} q/cm^2 remained at the SiO_2/Si interface. However, at the etched area, a charge concentration >4.2×10^{12} q/cm^2 remained at the Si/SiO_2 interface. Assuming ~10^{13} q/cm^2 was introduced to the Si/SiO_2 interface by the CA, it is possible that up to ~5×10^{12} q/cm^2 ions were migrated to the graphene/SiO_2 interface, but this speculation requires further data to be confirmed. However, it is clear that –5 V is sufficient for substantial ion migration to a 0.5-1 mm Al contact, but is insufficient in large-area graphene devices. Increased bias is likely required to generate sufficient energy to migrate the ions to the graphene electrode.

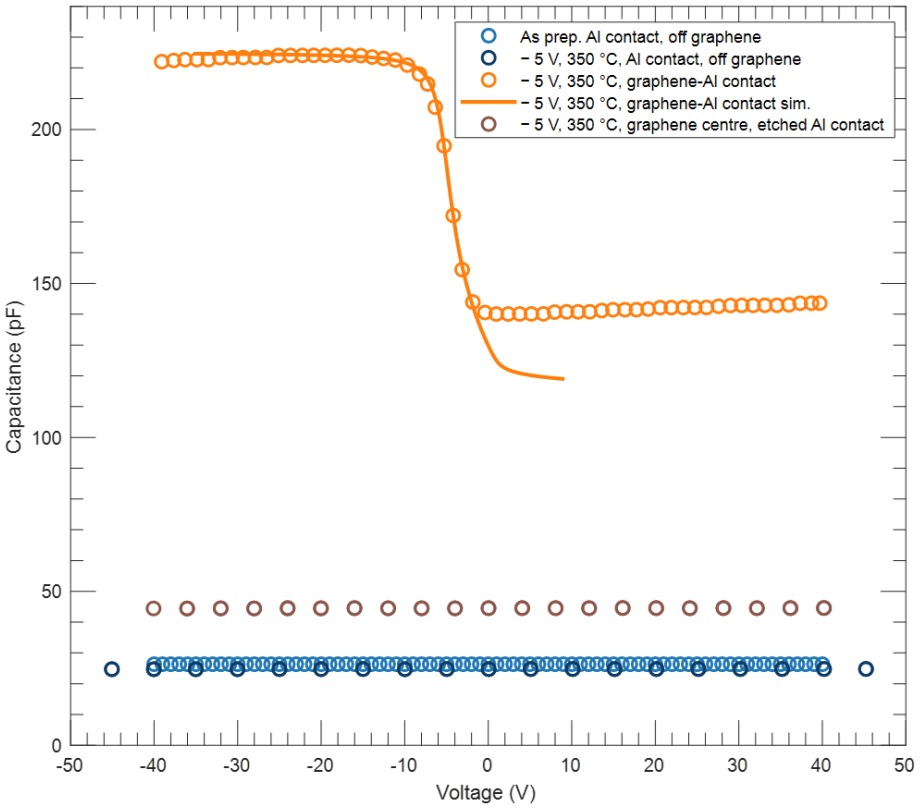

Figure 5.6: Capacitance-voltage characteristics of a Graphene/SiO_2/Si sample subject to KCl corona anneal, before and after bias-temperature stress. Circle markers indicate data points, while lines indicate simulated capacitance-voltage curves.

The reduction in ion migration to graphene may be due to a drop in the total effective voltage across the dielectric, V_{eff} [229], [287]. The effective voltage across the dielectric V_{eff} with metal-semiconductor work function difference φ_{MS} and dipole length d_{dipole} can be given by:

$$V_{eff} = V_{bias} - \varphi_{MS} - \frac{eC_{ox}d_{dipole}}{\varepsilon_0\varepsilon_r} \quad (5.1)$$

Equation (5.1) illustrates that a larger φ_{MS} can contribute towards a reduction in V_{eff} [229], [287]. In this work, the p-type silicon substrates were measured to have a resistivity 13.25±0.78 Ω cm, corresponding to a calculated dopant concentration of (1.02±0.04)×10^{15} /cm^3 (PV Lighthouse Resistivity Calculator). Using the standard equation approximating Fermi level shift as $k_BT \ln\left(\frac{N_A}{n_i}\right)$ [229], [288], the calculated work function of this silicon is 4.88 eV at room temperature. Assuming that the work function of thermally-evaporated Al is ~4.5 eV, based on

literature values [289], $\varphi_{Al,Si}$ is approximately −0.38 eV. This provides an in-built forward potential, which promotes ion migration to the SiO_2/Si. The work function of CVD graphene on SiO_2 is ~4.6-4.8 eV, with variations dependent on surface dopants and processing conditions such that $\varphi_{Gph,Si}$ is approximately −0.3 to −0.1 eV [290], [291]. These conditions imply a similar, or possibly increased V_{eff} promoting ion migration towards a graphene electrode relative to an Al electrode. It is therefore likely that the ion migration toward the graphene was not reduced due to work function difference.

Equation (5.1) also indicates that an increased d_{dipole} can reduce V_{eff}. A longer d_{dipole} increases the electric field at the metal-oxide interface that opposes further addition of ions to the interface. It may be that an increased d_{dipole} at the graphene-SiO_2 interface relative to the Al-SiO_2. The Al-SiO_2 d_{dipole} is on the order of 1-10 nm [292], but the dipole length for a graphene-SiO_2 is unclear. Graphene's high carrier mobility may contribute significant charge redistribution, modulating the local electric field and increasing d_{dipole} as ions migrate to the graphene/SiO_2 interface.

Reduced migration to the graphene relative to Al could also be due to its structural characteristics. Inhomogeneities, such as isolated holes, wrinkles, or defects may contribute toward a non-uniform electric field. Additionally, the higher resistivity of a 1 cm^2 graphene sheet relative to a 1-0.5 mm diameter Al dot of thickness 100 nm, could lead to a significant voltage drop across the dielectric. This could result in limited or localised ion migration to the graphene surface, and reduce the driving force for ion migration, requiring an increased bias or time for complete ionic drift.

The applied bias can be increased to compensate for V_{eff}, but this risks dielectric breakdown, especially over a large-area graphene device, where there is an increased chance of encountering a pinhole or defect. This risk is greater at high temperatures, where mobility and

thermal stresses are increased. Such pinholes and defects could also cause a voltage drop across the dielectric, reducing ion migration. To determine whether pinholes might be present, and their density, an electrochemical pinhole test was carried out. Figure 5.7 (a) depicts the measurement setup, which was constructed in-house for this experiment. Silicon with thermally grown SiO_2 of differing thickness were metallised at the rear and placed such that ~1 cm^2 SiO_2 layer is in contact with a 0.1 M copper sulphate solution, with an ethyl acetate coating over the sample edges. When a bias is applied between the silicon and a copper rod in the copper sulphate solution, a thin copper layer will build up at pinhole sites. The presence of pinholes will increase current flow through the device, and so cause a voltage drop across the dielectric. Figure 5.7 (b) presents the leakage current through different samples of different dielectric thicknesses at an applied voltage of +5 V at room temperature, as measured in the TSIC configuration, and in the electrochemical rig. The typical current flow through a 1 cm^2 SiO_2 is ~0.1 mA, with a slight increase after graphene processing and removal. This contrasts with the 0.5 mm Al contacts measured via TSIC in Figure 5.3, where the background current remained <10 pA. This increased current flow likely necessitates increased bias application to move ions to compensate for the voltage drop across the dielectric. However, this may risk dielectric breakdown. Alternate structures, including an added 20 nm ALD AlO_x capping layer on 300 nm SiO_2, were also explored to minimise current leakage, however, this did not yield improvements, with current leakage still around ~1 mA.

Figure 5.7 (c) depicts optical micrographs of SiO_2 surfaces after 3 hours under +5 V at room temperature. Copper deposition occurred on the SiO_2 surface, appearing as dots at a density of ~5 dots/cm^2. This density of pinholes made it difficult to increase the applied bias without causing current leakage through the oxide for large-area graphene films. Leakage through these pinholes may have contributed to a voltage drop across the dielectric such that an equivalent bias applied to a 1 cm^2 graphene device was insufficient to migrate ions to the surface compared

to a 1 mm diameter Al contact. These factors were considered to inform the quantification of graphene resistivity changes during ion migration. Higher biases are likely necessary to activate ion migration, albeit at the risk of increasing current leakage which might also limit the total migration of ions drifting across the dielectric.

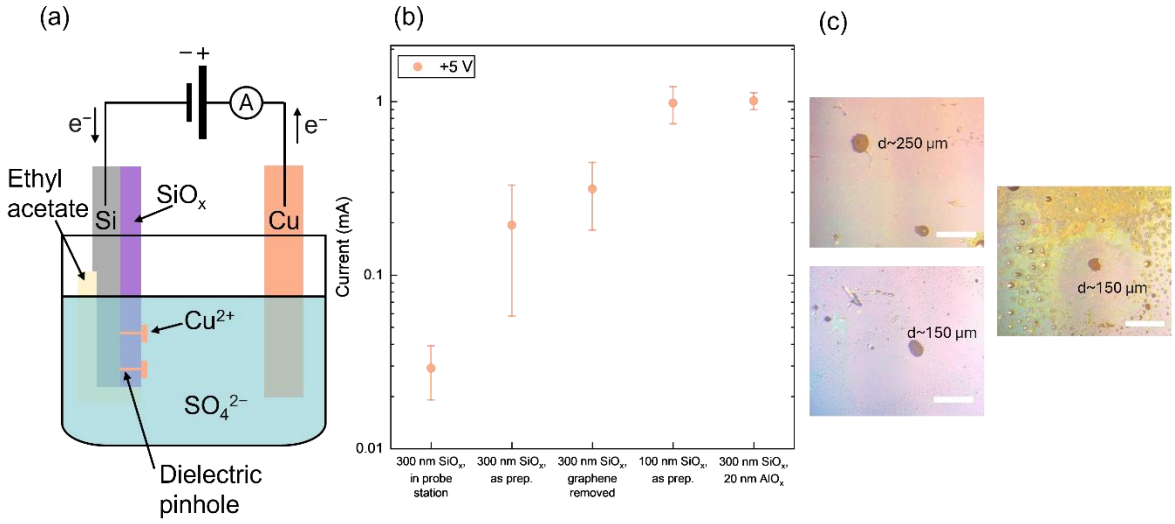

Figure 5.7: (a) Electrochemical pinhole detection test rig.(b). Current flow measured through the device, measured in the TSIC setup (data point 1), else using the electrochemical rig. (c) Optical microscopy images of samples surface after 3 hours at +5 V, scalebar: 0.5 mm.

5.5 Sheet Resistance of Graphene on K^+ ion charged SiO_2

To determine whether migrating the ions toward graphene can contribute to doping, its R_{sheet} before and after bias-temperature stress was measured via the vdP method. However, when graphene is exposed to temperatures ~350℃ in air, it was found that its sheet resistance can vary significantly. This has been attributed to the desorption and reabsorption of atmospheric contaminants at elevated temperatures, as well as the formation of hydroxyl groups at graphene edges and reaction with metal contacts increasing contact resistance [204], [293], [294], [295], [296]. These reactions can contribute to variations in atmospheric p-doping, and the formation of deleterious scattering centres and defects that reduce its mobility. This makes it difficult to decouple whether changes in R_{sheet} are observed due to doping from migrated ions, or changing conditions of the graphene at elevated temperatures. To eliminate this uncertainty, a vacuum

electronics testing station was developed for this work. This involved the retrofitting of an Edwards E306 Thermal Evaporator for high-temperature vdP and FET measurement in vacuum $<4\times10^{-7}$ mbar.

Figure 5.8 (a) depicts the sheet resistance of graphene on SiO_2/Si over time, with different conditions indicated by colour variation. A control sample with no extrinsically added ions is indicated by a dotted line, while the KCl-treated sample is indicated by a solid line. The initial sheet resistance in air is ~1.6-1.9 kΩ/□ in the control and treated sample, respectively. The increase in R_{sheet} as the chamber is evacuated to $<4\times10^{-7}$ mbar is likely due to the desorption of atmospheric contaminants. Devices were annealed at 350℃ until the R_{sheet} reduced and then plateaued to ~600 Ω/□, which occurred in both control and treated samples after ~30 minutes. This reduction likely occurred due to an increase in mobility as further atmospheric contaminants and PMMA residues were removed [204]. With the R_{sheet} of the control and treated sample reaching similar values before reverse biasing, the introduction of ions to the Si/SiO_2 interface did not have a discernible doping effect on the graphene, as they are shielded by the electrons in silicon. It is also not expected that this annealing at 0 V will result in ion migration away from the Si/SiO_2 interface as the work function difference $\varphi_{Gph,Si}$ is expected to promote ion migration toward that interface with no applied bias.

Figure 5.8 (a) shows the variation in R_{sheet} after varying intervals of reverse biasing at 350℃. At –5 V, the R_{sheet} appears to reduce slightly in the treated sample, to ~570 Ω/□, plateauing after ~15 minutes. This indicates a modest introduction of K^+ ions to the graphene/SiO_2 interface, contributing to doping. As the bias was increased to –10 V, and subsequently –20 V and –50 V, the R_{sheet} reduced to 490 Ω/□, 410 Ω/□, and 129 Ω/□, respectively. No substantial change was measured in the control sample, where CV indicated only 3×10^{11} q/cm^2 could contribute towards doping, insufficient to shift graphene's Dirac point. It is likely that the reduced R_{sheet} in the treated sample occurred due to increasing K^+ ions at the graphene/SiO_2

interface as increased energy is applied, compensating for any inhomogeneities, current leakage or dipole effects, which reduce ion migration. Figure 5.8 (b) depicts the R_{sheet} variation over time in the champion sample, where an R_{sheet} of 117.9 Ω/□ was achieved. This value is among the lowest reported R_{sheet} values of monolayer CVD graphene on SiO_2 with an area ≥1 cm^2, at room temperature [121], [297], [298]. Repeat measurements on other samples achieved R_{sheet} values including 125.9, 134.5, and 145.0 Ω/□, indicating the reliability of this technique to reproducibly achieve low R_{sheet} approaching 100 Ω/□. Figure 5.8 (c) illustrates the expected ionic drift behaviour demonstrated to induce these reductions in R_{sheet}.

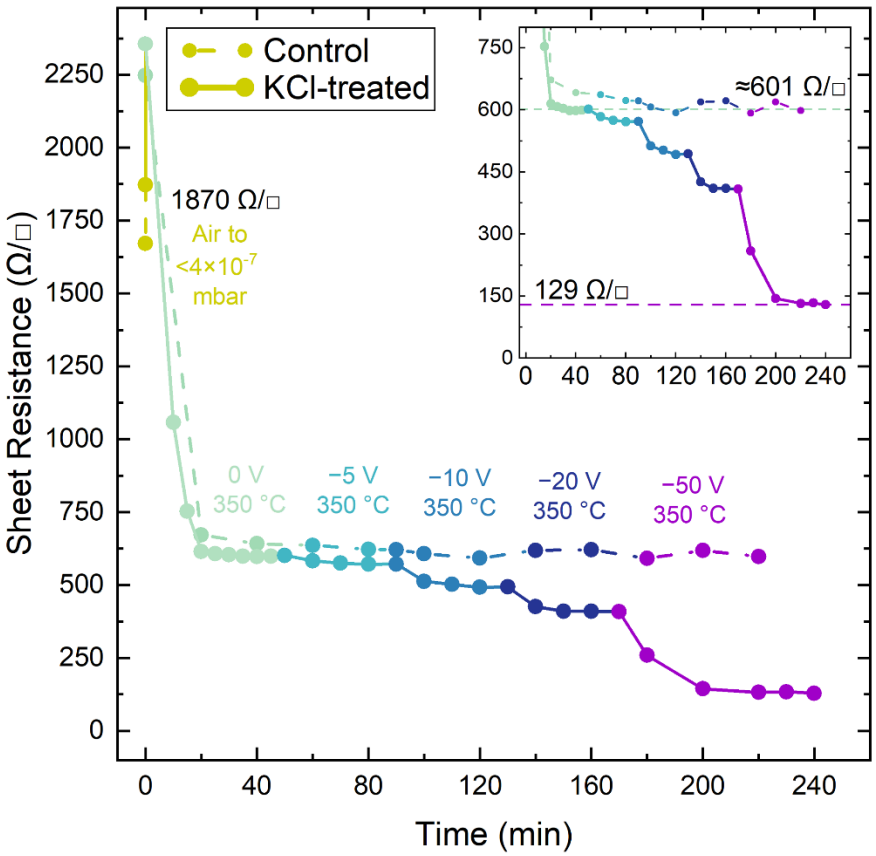
Control
KCl-treated
1870 Ω/□
Air to
<4×10-7
mbar
0 V
350 °C
−5 V
350 °C
−10 V
350 °C
−20 V
350 °C
−50 V
350 °C
≈601 Ω/□
129 Ω/□
Sheet Resistance (Ω/□)
Time (min)

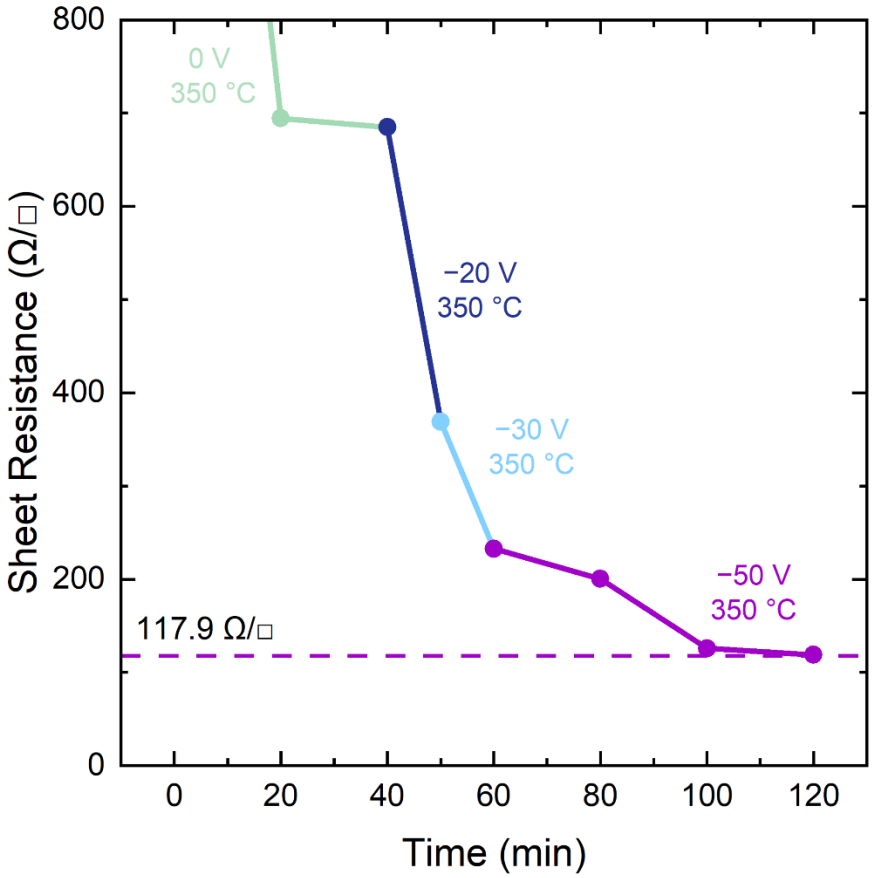
0 V
350 °C
−20 V
350 °C
−30 V
350 °C
−50 V
350 °C
117.9 Ω/□
Sheet Resistance (Ω/□)
Time (min)

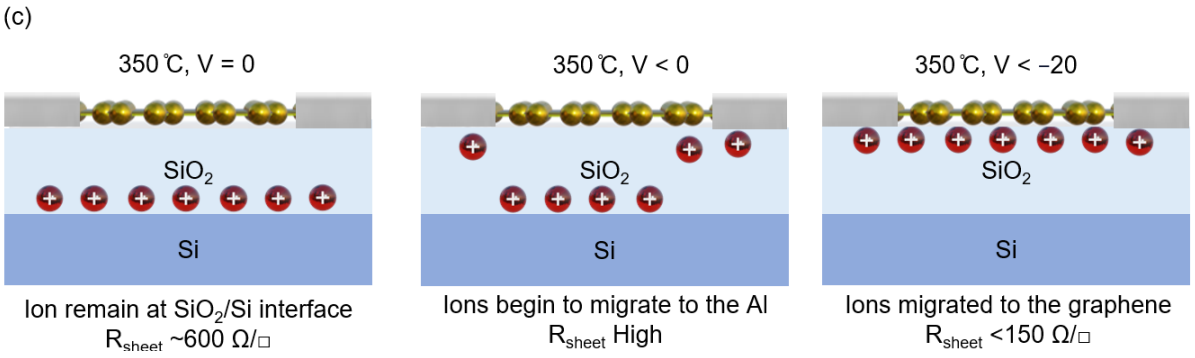

Figure 5.8: (a) Sheet resistance of graphene/SiO_2:K^+/Si samples over time, subject to high-temperature biased annealing. The dotted data line indicates a control sample, with no extrinsically added ions, while the solid line indicates KCl-treated samples. Inset: Sheet resistance over time (focused range). The green and purple horizontal lines indicate the sheet resistance of the experimental group after annealing, and after annealing under reverse bias, respectively. (b) Champion sample, where graphene sheet resistance reached a record ~118 Ω/□ after bias-temperature stress. (c) Expected positions of the K^+ ions with respect to the graphene under differing applied bias at high temperature.

Figure 5.9 depicts the relationship between applied bias and R_{sheet} for the two KCl-treated samples in Figure 5.8. For both samples there is a clear linear relationship, where increasing applied bias reduces R_{sheet}. Assuming this ΔR_{sheet} is dominated by linearly increasing carrier concentration with increasing K^+ at the graphene/SiO_2 interface, it may be that the system is dipole-limited. This implies that the graphene-SiO_2 d_{dipole} is larger than that of Al-SiO_2, and this may be a major contributor towards reduced ion migration using graphene rather than an Al electrode.

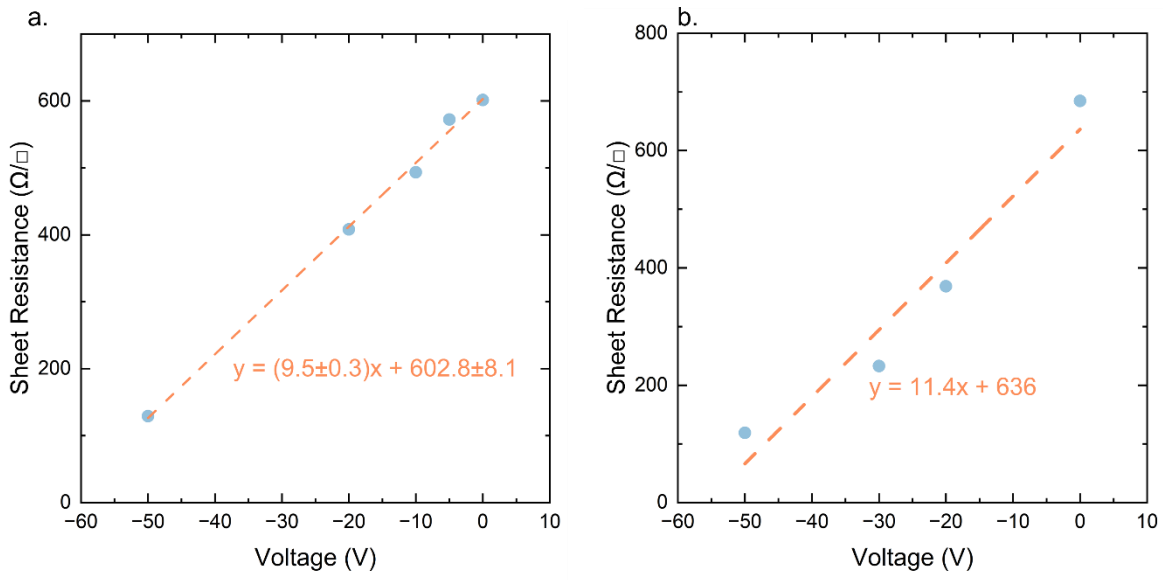

Figure 5.9: (a), (b) Applied bias versus sheet resistance for graphene/SiO_2:K^+/Si samples held at 350 ℃. The dotted lines correspond to linear fits with R^2 coefficients 0.99 and 0.94 respectively.

If we assume that the graphene-SiO_2 d_{dipole} is larger than that of Al, it may generate a strong electric field that repels ions from the graphene. This could result in electrostatic instability, and an unstable doping effect. To investigate the stability of the K^+ ions at the graphene/SiO_2 interface, the R_{sheet} of samples was compared over time. Figure 5.10 (a) depicts how the sheet resistance of a KCl-treated sample reaches a steady value of ~745 Ω/□ after annealing at 0 V. This reduces to ~427 Ω/□ after 60 mins at −5 V. After cooling under bias, the sample is returned to room pressure. Figure 5.10 (b) shows its R_{sheet} 1 day later, where it has increased to ~920 Ω/□, due to the adsorption of atmospheric moisture. However, when annealed in vacuum, it returns to ~440 Ω/□, indicating that the doping effect induced by the ions remains intact. Even when subject to 350℃ for 30 minutes, the R_{sheet} remains stable, suggesting that ions are stably localised at the graphene-SiO_2 interface. This stability suggests strong electrostatic interactions between the graphene and the ions, generating a stable energy minimum once ions reach the graphene. When cooled to room temperature, the R_{sheet} remains low, decreasing to ~340 Ω/□, as expected due to reduced phonon scattering, which increases mobility [299]. The R_{sheet} is only returned to its initial state of ~745 Ω/□ after ~1 hour at +5 V, indicating the presence of a substantial energy barrier at the graphene-SiO_2 interface. These results demonstrate the potential for tailored, stable doping configurations for a range of optoelectronic device requirements.

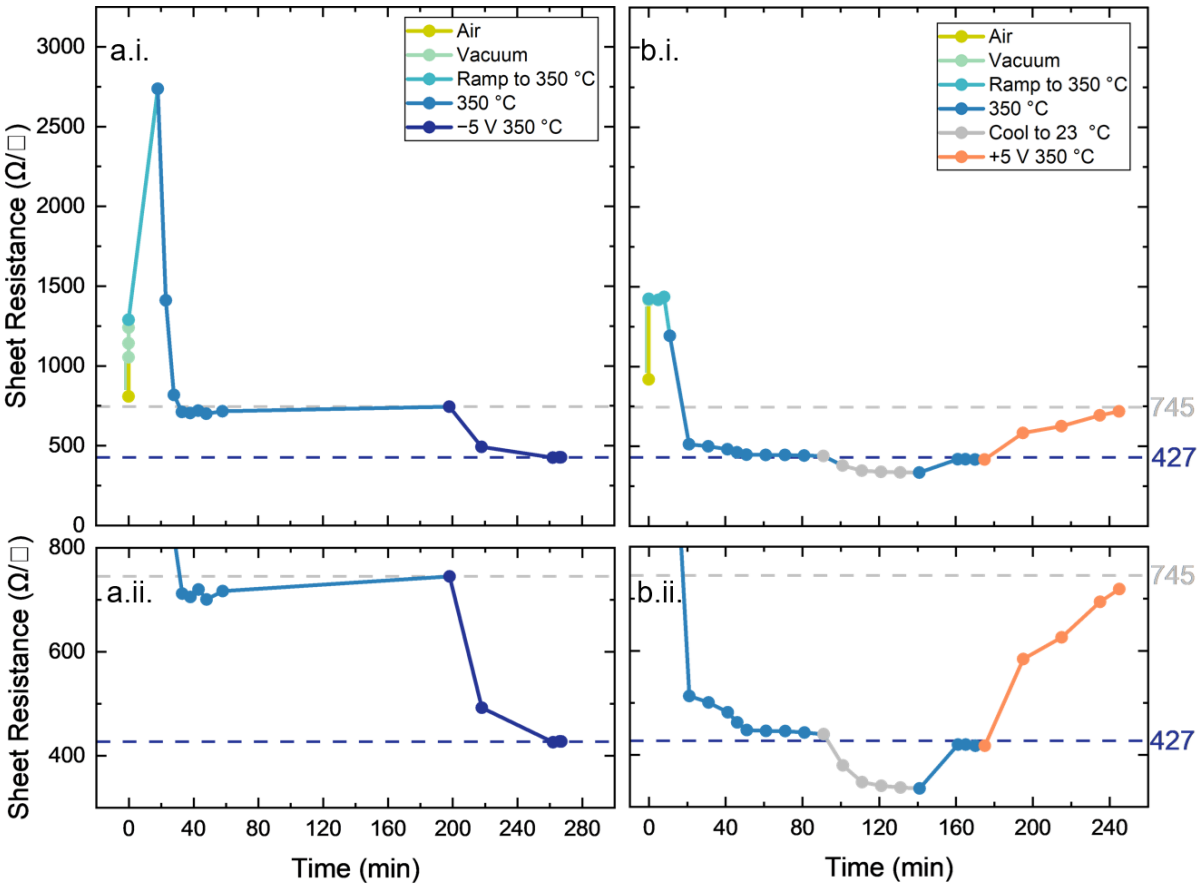

Figure 5.10: Graphene sheet resistance over time subjected to various bias-temperature annealing conditions. (a) Initial measurement. (b) 1 day later.

Figure 5.11 compares the R_{sheet} variations over time on three KCl-treated samples, S1, S2, and S3. After 1 day, the R_{sheet} increases by ~32 Ω/□, while after 2 months, an increase of ~92 Ω/□ is measured, indicating a gradual release of the ions from the graphene-SiO_2 interface. However, these relatively small fluctuations may also arise from degradation over time due to thermal stresses, contact degradation or surface damage when exposed to the atmosphere

between measurements. Nevertheless, it is clear that strong doping can be preserved over timescales >2 months.

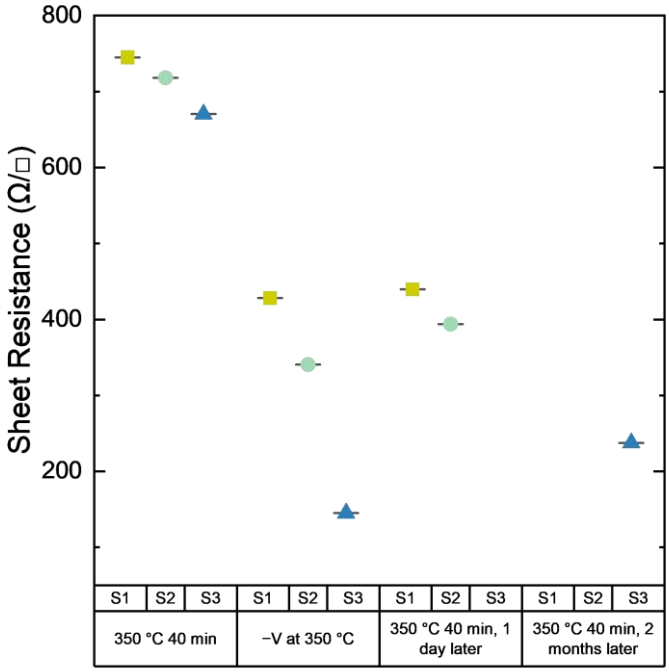

Figure 5.11: Graphene sheet resistance on KCl-treated SiO_2/Si substrates, over time after bias-temperature stress.

5.6 Investigating the Carrier Properties of Graphene on SiO_2:K^+/Si in Air

Due to the high temperatures required for ion migration, Hall effect measurements were not performed in vacuum as doing so would damage the magnets required. Instead, the device was returned to the air for Hall effect measurement. When samples are exposed to air, the low R_{sheet} is not preserved. Figure 5.12 (a), (b) and (c) depict the variation in carrier concentration, mobility, and R_{sheet} in air, before and after annealing or bias-temperature stress. For comparison, data from samples where bias-temperature stress was attempted in air is also included. It is clear from Figure 5.12 (a) and (b) that annealing in air resulted in a significant reduction in mobility, masking the effect of migrated ions on its R_{sheet}. The vacuum-annealed samples, while achieving low R_{sheet} in vacuum, R_{sheet} increases dramatically in air due to rapid adsorption of atmospheric molecules. It is expected that the K^+ ions at the graphene/SiO_2 interface induce negative charges in the graphene. It is possible that this negatively-charged

surface attracts further p-type atmospheric ions, resulting in a compensating effect that neutralises the doping observed in vacuum, as was observed in n-doped graphene in ref. [300]. This highlights the need for a suitable encapsulation layer for application in optoelectronic devices such as tandem cells.

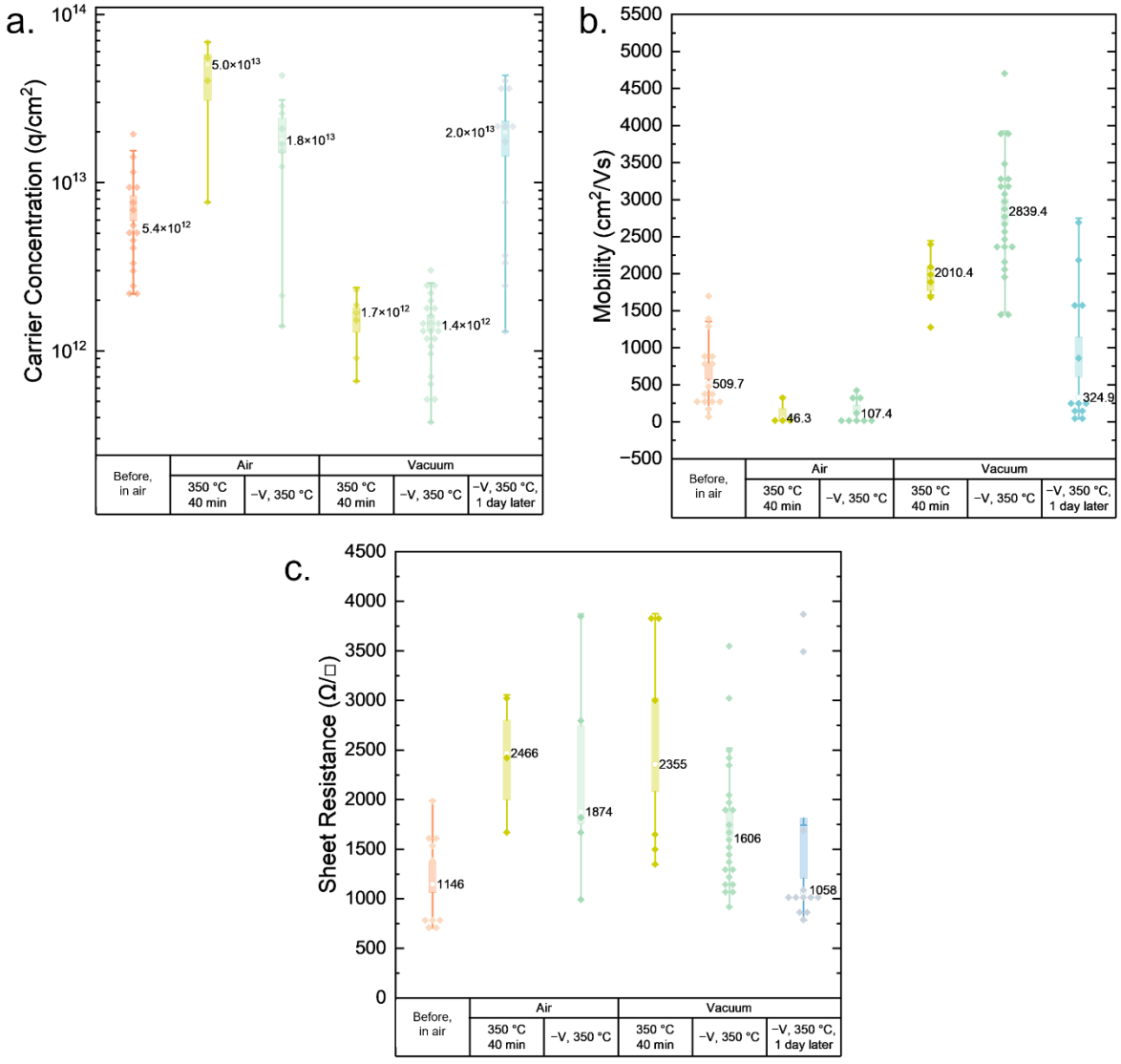

Figure 5.12: (a) Carrier concentration, (b) mobility, and (c) sheet resistance of graphene on KCl-treated SiO_2/Si substrates measured in air; before and after air- or vacuum bias-temperature stress.

To provide further corroborating evidence of the doping effect, Raman spectroscopy was carried out in air before and after the reverse-bias anneal. Figure 5.13 (a) and (b) depict the change in the graphene G and 2D Raman peak positions respectively. After reverse-bias anneal, there is a substantial blueshift from ~1589 cm^{-1} to 1603 cm^{-1}, indicating that doping has

occurred. However, the blueshift in 2D peak indicates that this doping is p-type [301]. However, as these measurements are taken in air, it must be considered that this p-doping effect may have arisen due to other factors, including the increase in atmospheric adsorption after devices are returned to air after vacuum annealing. For precise quantification of the doping effect, its carrier properties must be probed in vacuum.

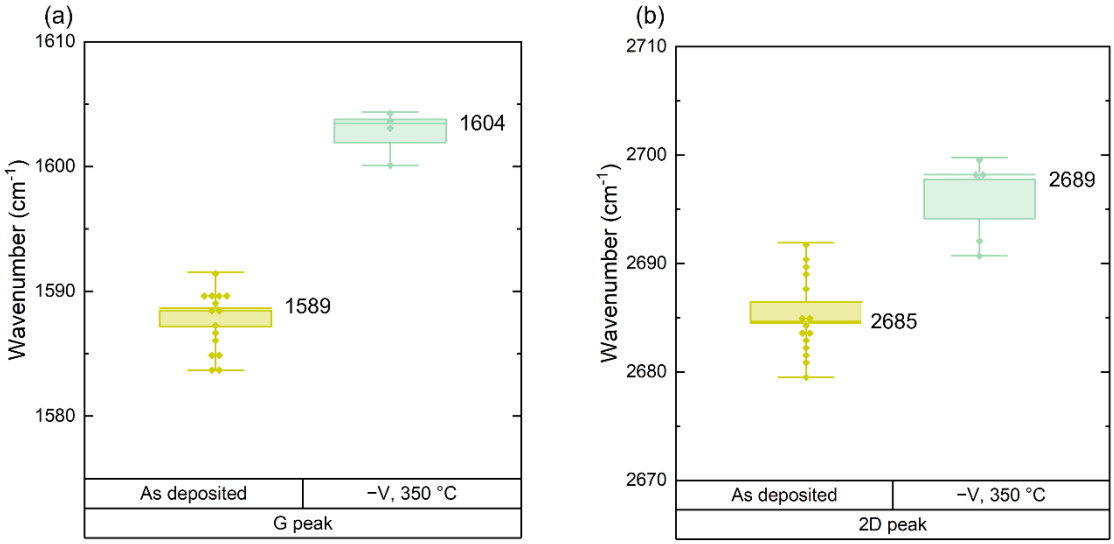

Figure 5.13: Variation in graphene (a) G peak and (b) 2D peak position before and after bias-temperature stress.

5.7 Vacuum Field Effect Transistor Measurement of Graphene on SiO_2:K^+/Si

To measure graphene's carrier properties in vacuum, FET devices were fabricated by UV laser etching. Figure 5.14 (a) illustrates a schematic of the fabricated devices, with channel length of 16 µm and a width of 17 µm, while Figure 5.14 (b) presents an optical micrograph of this device. Figure 5.14.c depicts the relationship between I_{DS} and V_{GD} for a graphene FET device on SiO_2:K^+ substrates. In air, the Dirac point is at 60.8±6.4 V, indicating p-type doping. Some hysteresis is present, likely due to the adsorption/desorption of atmospheric molecules or the filling and emptying of trapped charges during the high-voltage bias sweep. After the device is annealed at 350℃ for 40 mins in vacuum, then cooled to room temperature, the Dirac point shifts to 2±2 V. The Dirac point close to 0 V, and the reduced hysteresis indicate the removal of atmospheric dopants. After the device is held at 350℃ for an additional 40 minutes, with

−50 V applied between the source and gate contacts, then cooled, there is a notable negative V_{Dirac} shift to −88.16 V. This negative V_{Dirac} shift indicates strong n-type doping as the K^+ migrated to the graphene.

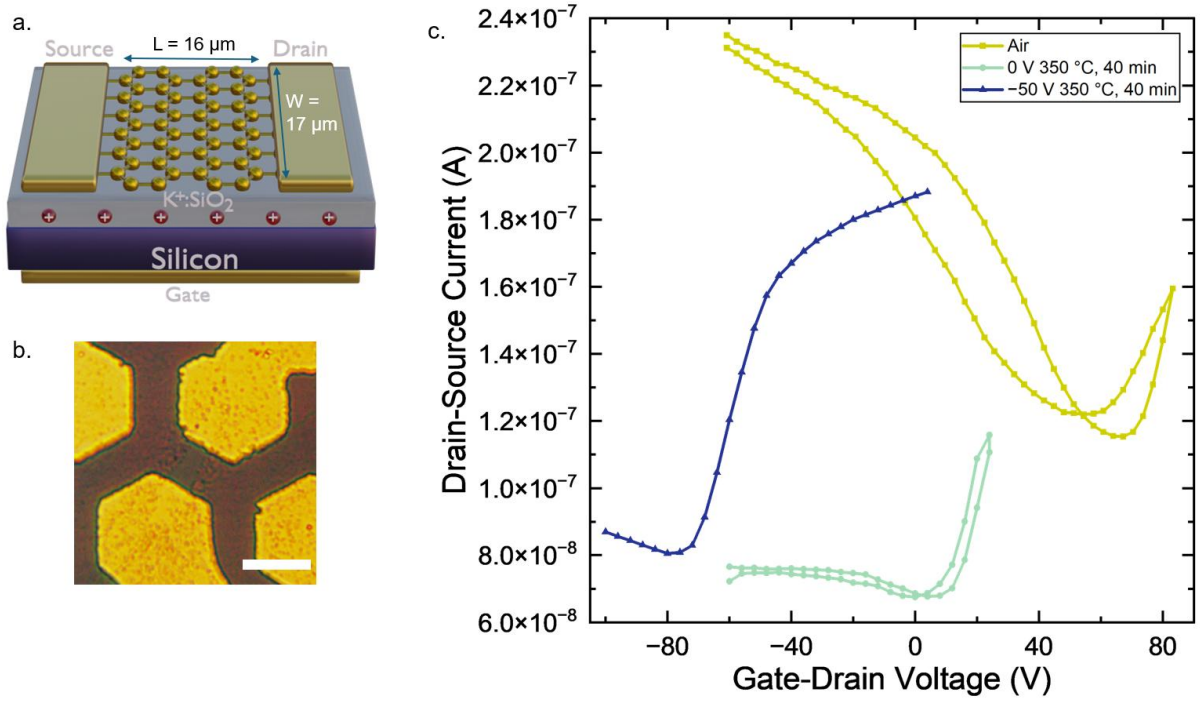

Figure 5.14: (a) Graphene field effect transistor device structure. (b) Optical micrograph of FET device, with 20 µm scalebar. (c) Drain-source current I_{DS} vs Gate-Drain Voltage V_{GD} characteristics in air, after vacuum annealing, and after reverse bias of −50 V for 40 mins at 350 ℃ in vacuum.

Figure 5.15 (a) and (b) depict the calculated carrier concentration and mobility from the FET curves in Figure 5.14 (c). It is clear from Figure 5.15 (a) that this K^+ migration doping technique has contributed to strong n-doping, achieving ~6.2 $\times 10^{12}$ q/cm^2. Assuming each K^+ ion contributes to one additional charge carrier in graphene, this value falls short of the 10^{13} q/cm^2 expected from TSIC measurements with Al electrodes, indicating incomplete ion migration. If so, there is potential for further reductions in graphene R_{sheet} with increased applied bias. Figure 5.15 (b) indicates a relatively low initial mobility of ~220 cm^2/Vs compared to the vdP structures, which may occur due to processing difficulties such as poor graphene-metal contact, or laser damage at the graphene edges. After vacuum annealing, the electron mobility modestly improved, albeit to only ~300 cm^2/Vs, suggesting that the graphene is relatively low-quality. However, after ion migration, the mobility dropped only slightly to ~290 cm^2/Vs, suggesting

that the presence of the K^+ ions does not contribute significantly to scattering. This low scattering may indicate that the distribution of K^+ is relatively uniform, and is not heavily perturbing the graphene lattice. This provides evidence that it is not the inhomogeneities in graphene that increase the driving force necessary for graphene doping, but likely its large dipole length at the SiO_2 relative to Al. Assuming a linear relationship between carrier concentration and bias as for R_{sheet} in Figure 5.9, we can use the slope $\frac{dq}{dV}$ and equation $d_{dipole} = \frac{\varepsilon_0 \varepsilon_r}{\left(\frac{dq}{dV}\right)}$ to estimate the d_{dipole} length of this system as ~120 nm, ~2 orders of magnitude greater than Al. This suggests that increasing the ion concentration at the graphene/SiO_2 interface with higher voltages facilitated by improved dielectric processing, may yield further reduced R_{sheet} in graphene without substantially impacting the mobility. This offers great potential for devices where minimal R_{sheet} is ideal to reduce losses, as in transparent conductors in tandem photovoltaic cells.

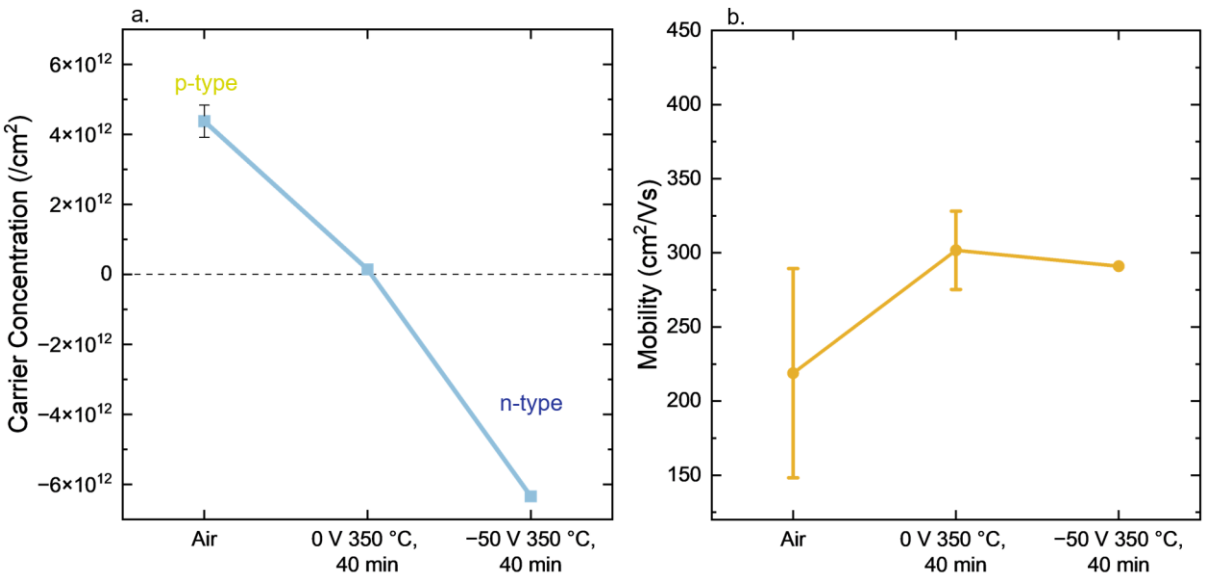

Figure 5.15: (a) Carrier Concentration and (b) electron mobility calculated from the FET data in Figure

5.8 **Discussion and Conclusions**

In this chapter, a novel graphene doping technique was investigated and developed, through the introduction of K^+ ions to a thermally-grown SiO_2 layer on silicon. CV and TSIC methods

using an Al/SiO_2/Si structure were used to determine that $>10^{13}$ q/cm^2 K^+ ions could be introduced to the SiO_2/Si interface, and remain stable to all steps of the graphene transfer process. However, it was observed that a greater bias was required to migrate ions to the graphene as compared to an Al electrode, despite graphene having a φ_{ms} more favourable for this process than Al. By applying a reverse bias up to −50 V, a graphene R_{sheet} as low as 117.9 Ω/□ was achieved, among the lowest reported for a large-area CVD graphene monolayer on SiO_2 at room temperature, indicating that the ion migration induced strong n-type doping [121], [298], [302]. It was noted that the R_{sheet} reduced linearly with applied bias, indicating dipole-limited ion migration when using a graphene electrode, with dipole length at the graphene-SiO_2 interface calculated to be ~2 orders of magnitude greater than the Al-SiO_2 interface. Moreover, the doping effect remained stable at high temperatures, and at room temperature over at least 2 months, indicating strong electrostatic interaction between the graphene and the dopant ions. The technique is reversible, where the application of a positive bias returned the R_{sheet} to close to that of its original value.

FET measurements confirmed that n-doping up to 6.2×10^{12} q/cm^2 was induced by reverse-bias annealing. This indicates that the K^+ ions induce doping when at the interface with graphene through the generation of negative mirror charges on the graphene surface. Notably, the mobility did not degrade substantially, indicating relatively uniform ion migration and minimised scattering. Figure 5.16 depicts a schematic of the impact of the vacuum annealing process and ion migration on graphene. The R_{sheet} of graphene is reduced as is it cleaned, and then subject to a field-effect induced negative mirror charge as the ions are migrated to the surface.

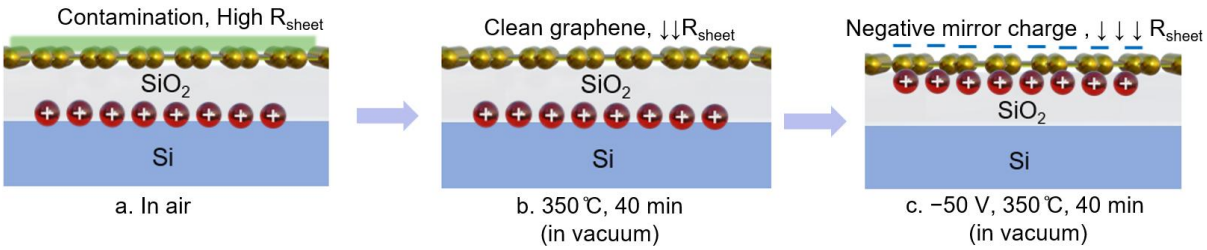

Figure 5.16: Schematic of ion position in SiO_2 and its impact on graphene R_{sheet}.

Increasing bias beyond –50 V was attempted to reduce R_{sheet} further, but this routinely resulted in dielectric breakdown or significant current leakage. Further reductions in R_{sheet} are likely achievable through improvements in dielectric quality such that a higher bias could be applied for increased ion migration without risking breakdown. Given this technique does not appear to substantially reduce mobility after doping, an R_{sheet} <100 Ω/□ is likely achievable through the doping of high-mobility graphene, and potentially <50 Ω/□ if the effect can be replicated using a dielectric of higher breakdown strength to increase ion concentration to contribute to doping.

The applicability of K^+:SiO_2 ICD doping offers great potential for optoelectronic devices where low R_{sheet} is desirable. This technique could also be used to fabricate memory devices, where the change in R_{sheet} induced by reversible ion migration could be used for information storage. However, this technique faces several challenges toward integration in tandem photovoltaics. The requirement for vacuum conditions or encapsulation to preserve the low R_{sheet} introduces processing complexity. Importantly, the high temperature required to migrate the K^+ is incompatible with the poor stability of amorphous silicon and perovskite layers. A Na^+ ion species might be better suited to such designs, given that Na^+ mobility is activated at temperatures <150 ℃. After confirming the K^+ ion is stable at the graphene/SiO_2 interface at high temperatures, it is possible that Na^+ ions might be similarly stable at the graphene/SiO_2 interface, but this is yet to be explored.

Crucially, in this technique, the ions are first stabilised at the Si/SiO_2 interface before graphene transfer, severely restricting the position of such a graphene layer in a tandem device stack. In an ideal case, owing to its high mobility, an ICD-doped graphene layer is best suited at the front interface with the glass/CTL on a 4T structure or at the front surface of the CTL at the top layer of a 2T device stack. Chapters 6 and 7 will explore methods to induce ICD-doping in graphene in such structures compatible with tandem cells.

Chapter 6

Ion-Charged Glasses for Graphene Doping

6.1 **Introduction**

Chapter 3 demonstrated ICD doping of graphene using a corona-charged, freestanding SiO_2 nanolayer. Chapter 4 built on this principle, showcasing stable graphene doping with record low R_{sheet} =117.9 Ω/□ on a K^+ charged SiO_2/Si substrate. However, these systems have limited applicability to tandem cells, where the TCE must be in contact with the charge transport layers of a perovskite top cell, or the amorphous silicon layer of a SHJ bottom cell [43]. To integrate ICD-doped graphene in a tandem cell, the ICD likely needs to be either directly deposited on the graphene layer, or incorporated as part of the perovskite cell TCO/glass substrate.

An ICD-doped graphene layer could be integrated into tandem cells by developing a charged dielectric on the surface of a glass substrate. A graphene electrode can be deposited on the ICD/glass layer, replacing the typical TCO/glass substrate for perovskite cell fabrication in four-terminal perovskite/silicon tandems. Figure 6.1 (a) depicts a conventional four-terminal perovskite/silicon tandem structure, while Figure 6.1 (b) presents the proposed method of graphene/ICD integration in such a cell. In this case, as with TCOs such as FTO, the ICD can be safely prepared at high-temperature, as the deposition of delicate CTL and perovskite layers occurs at a later processing step. This Chapter explores methods to generate charged dielectrics on the surface of glass, including using mobile ions, and through the deposition of charged PECVD SiO_2/SiN_x nanolayers on quartz. The charge concentration developed in the dielectric and the doping induced in graphene are investigated, and the suitability of each ICD/graphene layer for integration in tandem cells and other optoelectronic devices is discussed.

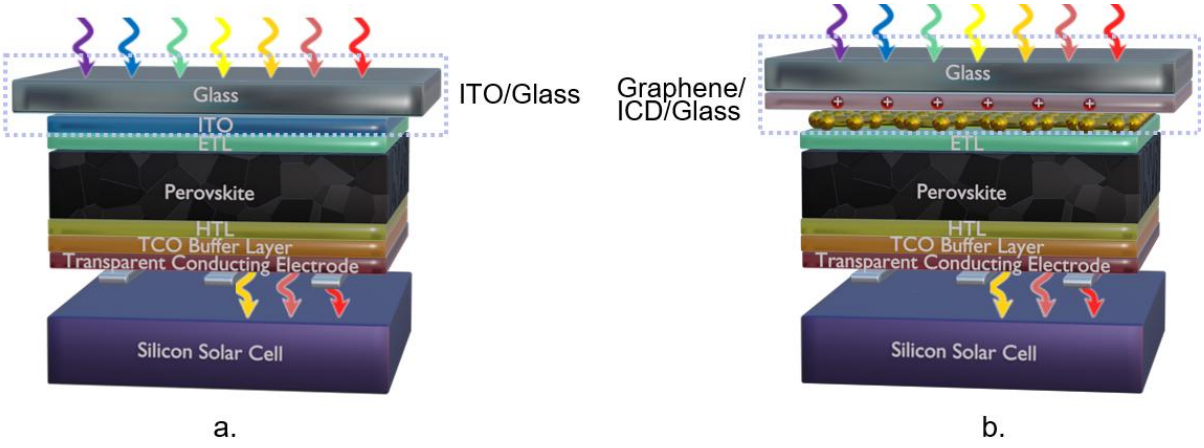

Figure 6.1: (a) Standard four-terminal perovskite/silicon tandem device architecture, with n-i-p perovskite top cell using an ITO/glass layer as a substrate and TCO. (b) Proposed four-terminal perovskite/silicon tandem structure with Graphene/ICD/Glass TCE substrate.

6.2 Ion-Charged Dielectric Generation using Alkali Ions in Glass

Conventional silica-based glass primarily consists of slightly distorted SiO_4 tetrahedra [303]. These SiO_4 tetrahedra form the glass network by covalent bonding at the edges, with the bonding oxygen referred to as a "bridging oxygen" [303]. Additional "network modifier" species are frequently added to lower its melting point for improved ductility, as well as to enhance properties such as optics, and thermal and chemical stability [303], [304]. In soda-lime glass, a large concentration of Na_2O and CaO species are introduced via the melting of silica with Na_2CO_3 and $CaCO_3$ at temperatures 1400-1500℃ [303]. Na^+ ions enter the glass as single-charged cations and occupy interstitial sites. This typically occurs via the breaking of SiO_4 tetrahedral bridging oxygen bonds through the formation of $Si\text{-}O^-\text{-}Na^+$ species by ionic bonding. The creation of a "non-bridging oxygen" reduces the connectivity of the network, and hence alters its viscosity and melting point [182], [303]. Na^+ can be exchanged for K^+ using a hot potassium-salt ion-exchange bath, improving shatter resistance for application in touch-screen displays and automobile windows [297], [305]. Borosilicate glass (BSG) incorporates B_2O_3 as well as SiO_4 network formers to improve chemical and thermal stability, with a small fraction of network modifier Na_2O added to maintain a low melting-temperature [304]. With

careful control of the distribution of ionic network modifier species, the properties of not just glass, but also materials interfacing with it, can be modified.

In principle, the network-modifier ions in glass are randomly distributed and thus contribute no electric field. However, at moderate temperatures, small alkali ions in glass can achieve sufficiently high mobility to drift through the glass [306]. This migration is often deleterious and can reduce mechanical strength and transmittance over time [306], [307]. However, ion migration can be exploited by directing it with an electric field. By intentionally migrating the ions, the original symmetry and neutrality of the glass is lost, generating a strong electric field within the material. This is a well-established technique in industry, and is used to strongly bond silicon wafers to glass through anodic bonding [308], [309] and to generate a permanent second-order non-linearity in optical fibres and modify their refractive index [310]. This electric field also impacts the properties of interfacing materials. Migration of Na^+ ions in soda-lime glass and BSG has been demonstrated to induce strong doping in an interfacing graphene layer [182]. The Shukla group has used this technique extensively to study 2D materials doping in high-vacuum environments, as in ref. [182], [311], [312], [313], [314], [315], while mobile Li^+ ions in glass have been used for electrostatic gating of few-layer WSe_2 flakes in high-vacuum [316]. K^+ ions concentrated at the surface of ion-exchanged glass have also been shown to dope graphene, albeit only exhibiting high carrier concentrations when encapsulated with an ALD-AlO_x layer [302]. These techniques demonstrate the potential of ion-charged glass for graphene doping for TCE applications in optoelectronics. However, the stability of these techniques, the relationship between applied bias and doping strength, and their suitability for tandem structures are unclear.

After observing the highly stable doping of graphene on K^+:SiO_2/Si substrates in Chapter 5, it was proposed that stability may also be achievable using Na^+ ions on glass, which might benefit from a similar electrostatic environment. Na^+-containing soda-lime glass is the usual glass

substrate for perovskite top cells in four-terminal tandems, owing to its good balance of cost with mechanical stability and transparency [303], [317], [318], [319], [320]. However, the high concentration of Na^+ ions in soda-lime glass can precipitate and form crystallites at the surface over time, reducing transmittance [306]. Additionally, migration of a high concentration of Na^+ ions from soda-lime glass has been linked to degradation in perovskite cells, while the use of borosilicate glass has been shown to reduce potential-induced degradation [319], [320], [321], [322]. Therefore, BSG was deemed a more suitable candidate substrate in this work due to its lower concentration of Na^+ ions. Figure 6.2 presents a proposed mechanism for graphene doping via ion migration in BSG. Initially, it is expected that the ions are distributed homogeneously through the SiO_2, and so do not contribute an electric field to induce graphene doping. On application of a reverse bias between the graphene and a rear metal electrode at elevated temperatures, mobile ions migrate to the graphene/BSG interface. As the ions aggregate at the graphene, it is expected that they will contribute towards doping via the electric field effect, in a similar mechanism to that described in Chapter 5. On application of a positive bias, the mobile ions move to the rear metal interface, leaving behind a negative space-charge region close to the graphene, which is expected to induce p-doping in graphene. The first half of this chapter will explore graphene conductivity modulation and stability using this technique.

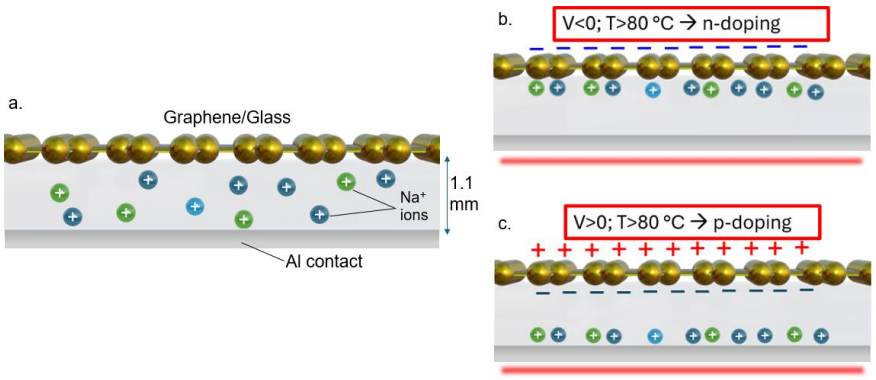

Figure 6.2: Mechanism for alkali ion migration to graphene electrodes on borosilicate glass. (a) Graphene on borosilicate glass, initial state. (b) Ion migration on application of a reverse bias at high temperature. (c) Ion migration on the application of a positive bias at high temperature.

6.3 Characterising Mobile Ion Concentration in Borosilicate Glass

To characterise the charge in glass that could contribute to graphene doping, the TSIC method was used to measure transient current across the dielectric under bias-temperature stress [233], [323]. Figure 6.3 depicts the variation of temperature and current over time for a 1.1 mm BPW-1010 BSG plate with 2 mm diameter Al contact [190], subject to −10 V, held at 150℃ for 40 minutes. The increase in current observed at ~86℃ is expected due to the activation of Na^+ mobility, commensurate with temperatures observed in the literature [182], [233], [324]. As sources of noise >1 pA were eliminated in the measurement setup, it was assumed that the increase in current observed could be primarily attributed to the migration of ions toward the Al contact. Using the equation $q = \frac{\int I\,dt}{e \cdot A}$, the migrated charge can be calculated as ~3.51 $\times 10^{14}$ q/cm^2. According to the manufacturer, the BPW-1010 glass plate is expected to have a Na_2O concentration of 4% [190], corresponding to a calculated Na^+ concentration of ~1.7×10^{21} q/cm^3. This implies a displacement of Na^+ ions by ~1.7 nm towards the metal surface due to the application of the bias at elevated temperatures. Given the similar work function of Al and graphene at ~4.5 and 4.5-4.7 eV respectively [289], [290], [291], it is reasonable to assume that these conditions can be conserved using a graphene electrode. Additionally, the use of a thick BSG dielectric of 1.1 mm offers the ability to increase the applied bias substantially to overcome dipole-limiting effects without risking dielectric breakdown. Assuming stability can

be conserved, this technique could enable graphene doping at very high carrier concentrations $>10^{14}$ /cm^2.

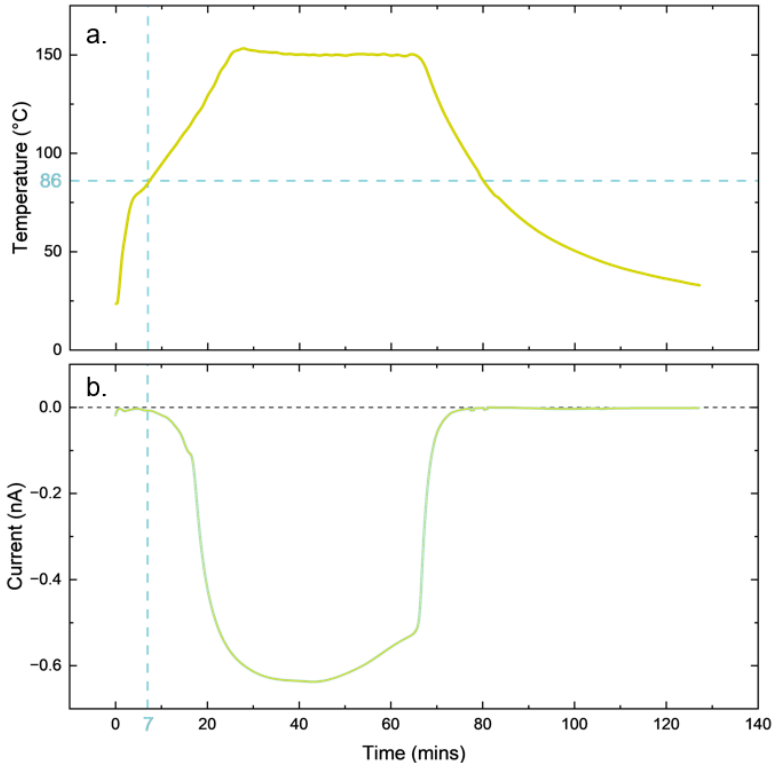

Figure 6.3: (a) Temperature vs time and (b) current vs time for a 1.1 mm thick borosilicate substrate with 2 mm diameter Al contact, subject to −10 V bias for the duration of the measurement.

6.4 Electrical Characterisation of Graphene on Borosilicate Glass under Bias-Temperature Stress

To evaluate the effect of migrated ions on the graphene's electrical properties, a graphene layer was transferred to the surface of a 1 cm^2 BPW-1010 BSG substrate, and fabricated into a vdP structure via UV laser etching. Al contact pads were deposited at the corners of the graphene layer and at the rear of the BSG metallised with thermally evaporated Al. In this work, charge stability to the graphene transfer process was not investigated explicitly, as it was assumed that the charge concentration, initially distributed randomly in the glassy matrix at a concentration $>10^{21}$ /cm^3, should remain high after transfer.

Figure 6.4 (a) depicts the R_{sheet} of graphene on 1.1 mm BSG substrates subject to bias-temperature stress, compared with that of graphene device deposited on a fused quartz

substrate, where it was assumed that no ions were present that could comparably contribute to doping. As in Chapter 5, devices were first measured in air, then annealed in vacuum at 350℃ for 40 minutes to remove atmospheric contamination. Measurements were carried out in a high-vacuum environment to control for atmospheric effects during annealing. The temperature was subsequently cooled to a stable 200℃ so that high Na^+ mobility in the glass could be maintained. At 200 ℃, the R_{sheet} stabilised at 620 Ω/□ and 600 Ω/□ for BSG and quartz, respectively. At this temperature, with no bias applied, it is assumed that the ionic species are homogeneously distributed through the BSG, so no doping from the Na^+ ion is expected. The quartz sample exhibits a slightly lower initial R_{sheet} after annealing, but within the normal range of typical undoped graphene samples.

After application of a −5 V bias, the R_{sheet} of the graphene/BSG sample reduces further to 465 Ω/□ at 200 ℃, while the graphene/quartz sample remains ~600 Ω/□, suggesting that the Na^+ moved toward the graphene to induce doping. As the bias was increased to –10 V, –20 V, and –50 V, the R_{sheet} of the graphene/BSG sample reduced further to 401 Ω/□, 360 Ω/□ and 350 Ω/□, respectively. At each bias step, the R_{sheet} is reduced, then plateaus toward a minimum. This suggests that an increased field is required to migrate more ions toward the graphene and induce carriers in it. At increased magnitude biases up to –200 V, the R_{sheet} appeared to plateau, suggesting saturation of ion migration had occurred. Figure 6.4 (b) depicts the relation between R_{sheet} and applied bias for the graphene/BSG sample, presenting an apparent exponential reduction in R_{sheet}, with plateaus after a predicted –20 V. At increased bias magnitude, it is expected that a dynamic equilibrium has occurred, where the ions have reached saturation concentration at the graphene/BSG interface. As the ion concentration in BSG is $>10^{21}$ /cm^3, it is not likely that ions have been depleted, but possible that a dipole layer has been formed which opposes further Na^+ migration. This technique has been used to repeatedly achieve R_{sheet} ~ 350 Ω/□ in various BSG samples, and as low as 299 Ω/□ in the champion sample. Typically,

the R_{sheet} is reduced by ~50% compared to its original value. Despite greater charge carrier concentrations available for conduction doping than SiO_2:K^+/Si substrates, the higher R_{sheet} demonstrated here could relate to the surface roughness of BSG compared to thermally grown SiO_2, which can contribute to additional scattering, and localised doping. With improved substrate flatness, it is expected that the potential charge carriers that contribute to doping without contributing towards significant additional scattering will increase, allowing for further reduced $R_{sheet.}$ It is also possible that the extremely high charge concentration close to the graphene/BSG interface negatively interferes with graphene's electronic structure, which could cause additional Coulomb scattering [325].

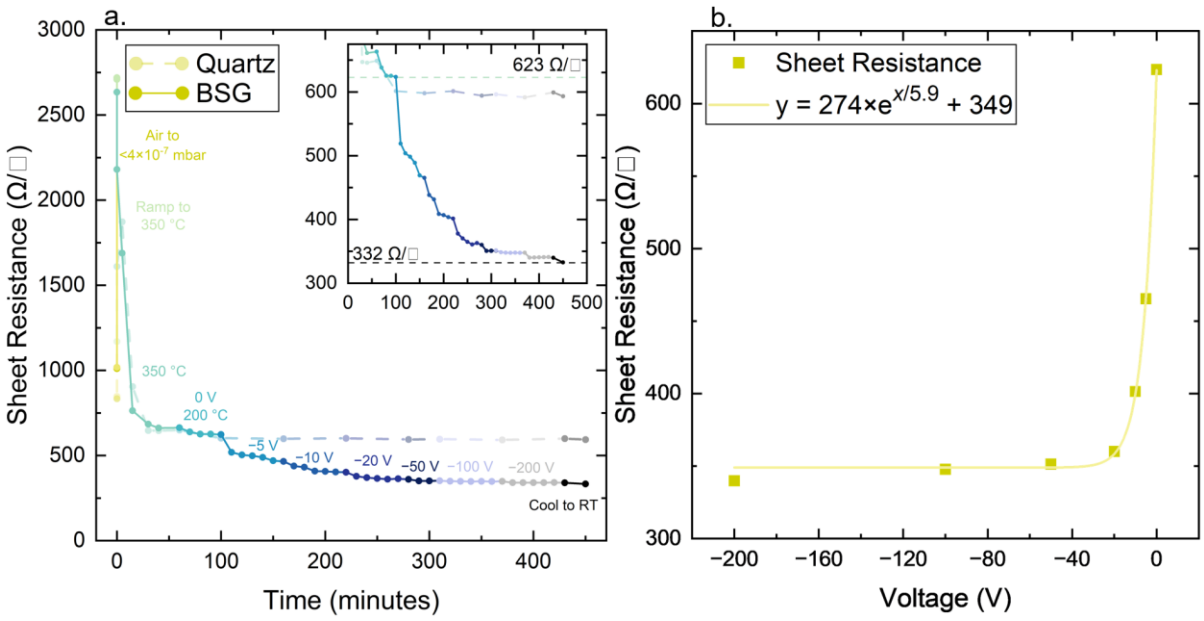

Figure 6.4: (a) Graphene sheet resistance on borosilicate glass over time under negative applied bias at elevated temperatures. (b) Relationship between applied voltage and minimum sheet resistance obtained.

To reduce potential scattering induced by the Na^+ ions, a 57±0.1 nm PECVD SiO_x layer was deposited on the surface of the BSG before graphene transfer. The layer was measured using ellipsometry and its deposition recipe is given in Table 3.2. With the SiO_x acting as a barrier layer, the ions are not expected to aggregate so closely to the graphene layer to cause significant scattering, but will be sufficiently close to induce a strong, uniform electric field. Figure 6.5 (a) depicts the variation in R_{sheet} as a graphene/SiO_x/BSG structure, subject to various reverse

bias stresses at high temperatures in vacuum. As in Figure 6.4 (a), the R_{sheet} reduces with increasing applied reverse bias, gradually plateauing at very high voltages. This relationship appears exponential with increasing voltage, as indicated by Figure 6.4 (b). In this case, the R_{sheet} reduces by >70% compared to the initial value after annealing. This more significant reduction compared with the graphene/BSG samples implies less pronounced scattering and hence improved mobility in this case. Characterisation of layer mobility and carrier properties in vacuum would provide sufficient evidence to verify this claim, and thus provide greater insight into the electrostatics of the doping mechanism.

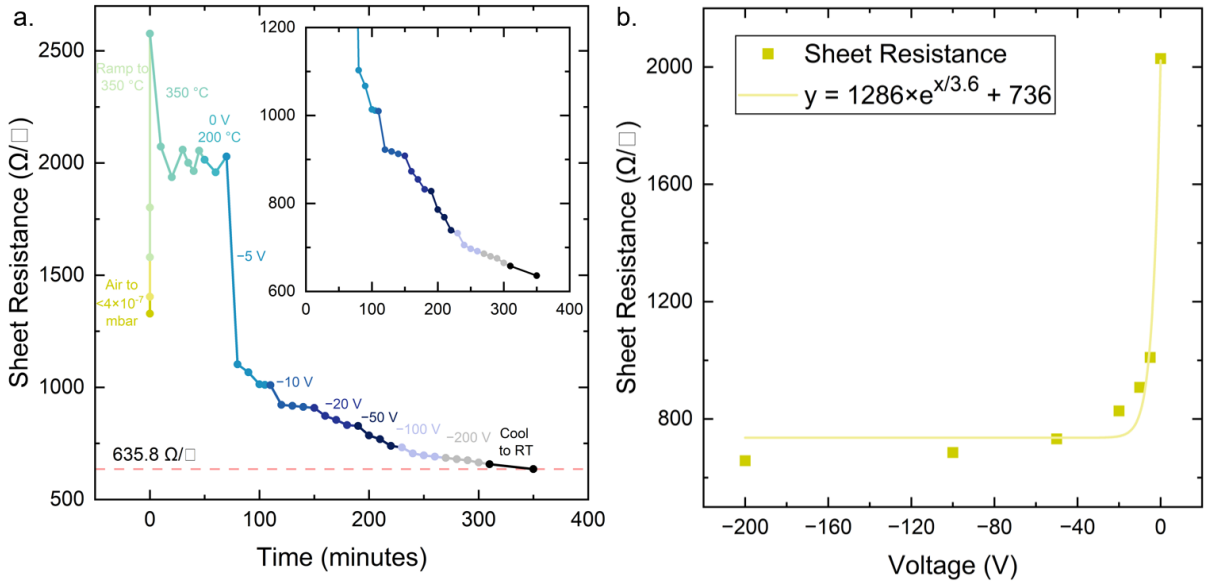

Figure 6.5: (a) Graphene on a SiO_x/BSG substrate, subject to bias-temperature stress under vacuum. (b) Relationship between bias applied to the graphene/BSG and the R_{sheet} of graphene.

Figure 6.6 (a) and (b) present a graphene/BSG sample subject to a similar high-temperature bias stress process in vacuum. In Figure 6.6 (a), after annealing at 350℃, then reduction to 200℃, the R_{sheet} stabilised at ~850 Ω/□. Subsequently, −200 V was applied at 200℃ for 40 minutes, reducing the R_{sheet} to 373.4 Ω/□. The device was allowed to cool under zero bias. Despite zero bias applied at a temperature sufficient for high Na^+ mobility, the R_{sheet} did not increase, but reduced further to ~340 Ω/□. Figure 6.6 (b) depicts the R_{sheet} of the device 12 hours later, in vacuum. After 12 hours, the R_{sheet} increased by just 12 Ω/□, to 354 Ω/□,

indicating strong stability at room temperature over time. The device was subsequently annealed at 200℃ for 40 minutes, and was then allowed to cool to room temperature under vacuum. It was noted that the R_{sheet} remained low after annealing, at ~360 Ω/□, within 20 Ω/□ of the lowest R_{sheet} achieved. This strong stability at high temperatures was also observed in the Graphene/K^+:SiO_2/Si system in Chapter 5, suggesting a similar electrostatic interaction between graphene and alkali ions at its interface. The same stable behaviour was also observed after Na^+ migration in the graphene/SiO_x/BSG system. This also implies that Na^+ ions migrated in thermally grown SiO_2 on Si should also demonstrate strong stability, offering the possibility of inducing migration at lower temperatures and energies for more varied device applications.

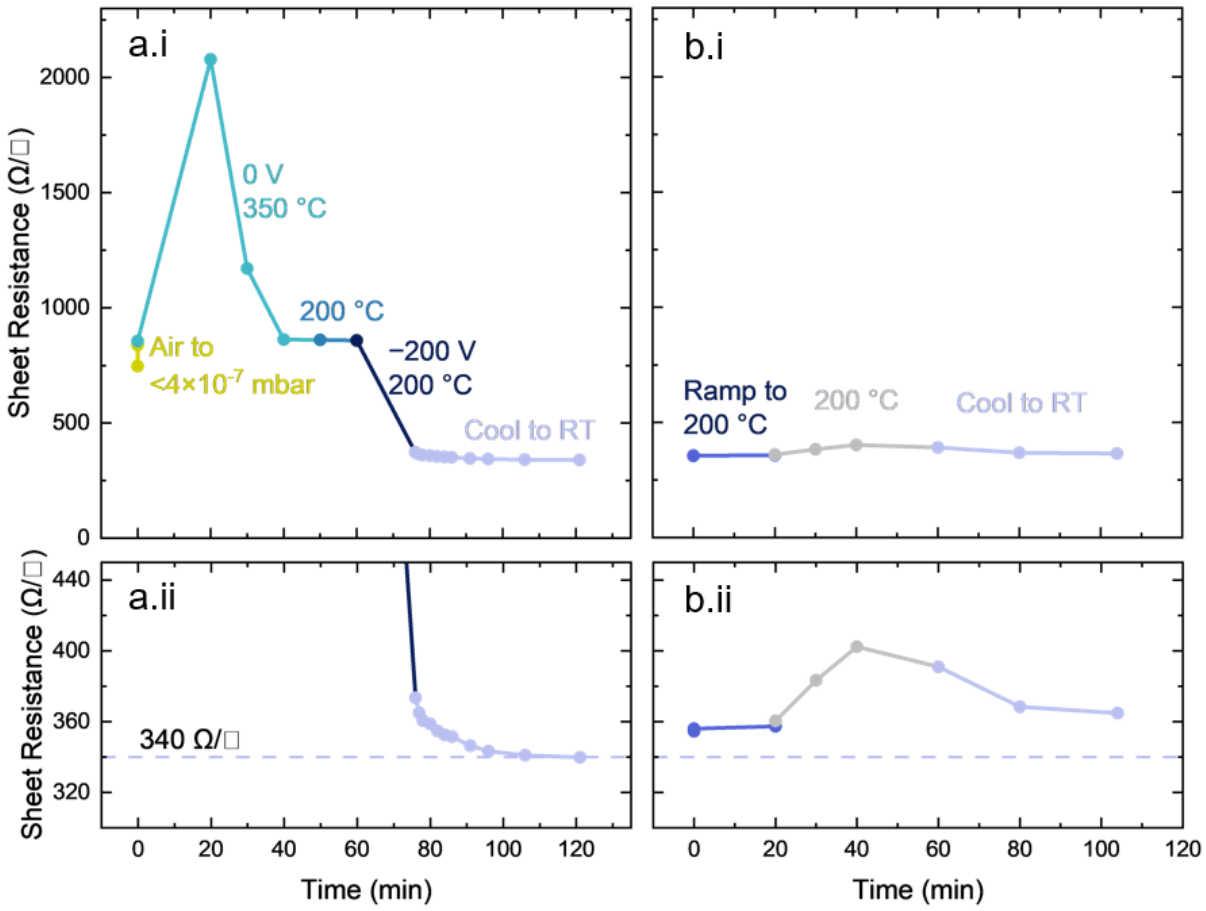

Figure 6.6: Sheet resistance of graphene/borosilicate glass subject to bias-temperature stress over time. (a) Initial measurement. (b) One day later, left overnight in vacuum.

The Na^+ ions can also be migrated away from the graphene to induce a negative space charge region near the graphene through the formation of O^{2-} interstitials. This negative space charge

region can p-dope 2D materials [182]. Figure 6.7 (a) depicts the variation of R_{sheet} over time in vacuum, held at high temperatures with a +V bias applied. After initial annealing at 350℃ and reduction to 200℃, the R_{sheet} stabilised at ~1400 Ω/□. The high R_{sheet} in this case is likely due to the relatively poor quality of the transferred graphene. On application of +200 V, the R_{sheet} reduced until it plateaued after ~60 mins to ~600 Ω/□. As in the case of migrating Na^+ ions toward the graphene, this reduces the R_{sheet} by >50%, albeit requiring more energy to achieve it. When the bias is removed, the R_{sheet} quickly returns to the initial value of ~1400 Ω/□, if held at high temperature. As Na^+ ions are the only mobile charged species at this temperature, this result indicates that the stability of the Na^+ at the rear Al electrode is relatively poor. It is apparent that at elevated temperatures, the Na^+ ions gradually return to equilibrium, reducing the doping effect.

Positive applied bias can also be used to reverse the n-doping effect. Figure 6.7 (b) depicts the R_{sheet} variation over time for a graphene/SiO_x/BSG device in vacuum, which was previously subject to a reverse bias at high temperatures. The dotted line indicates the initial R_{sheet} after annealing, ~2000 Ω/□, which was subsequently reduced to ~650 Ω/□ after reverse biasing. It is of note that significant energy was required to move the ions away from the graphene in this case, where over 40 minutes at an applied bias of +100 V was necessary to return the graphene to its initial state. This provides further evidence for the strong stability of the Na^+ ions when migrated close to the graphene layer.

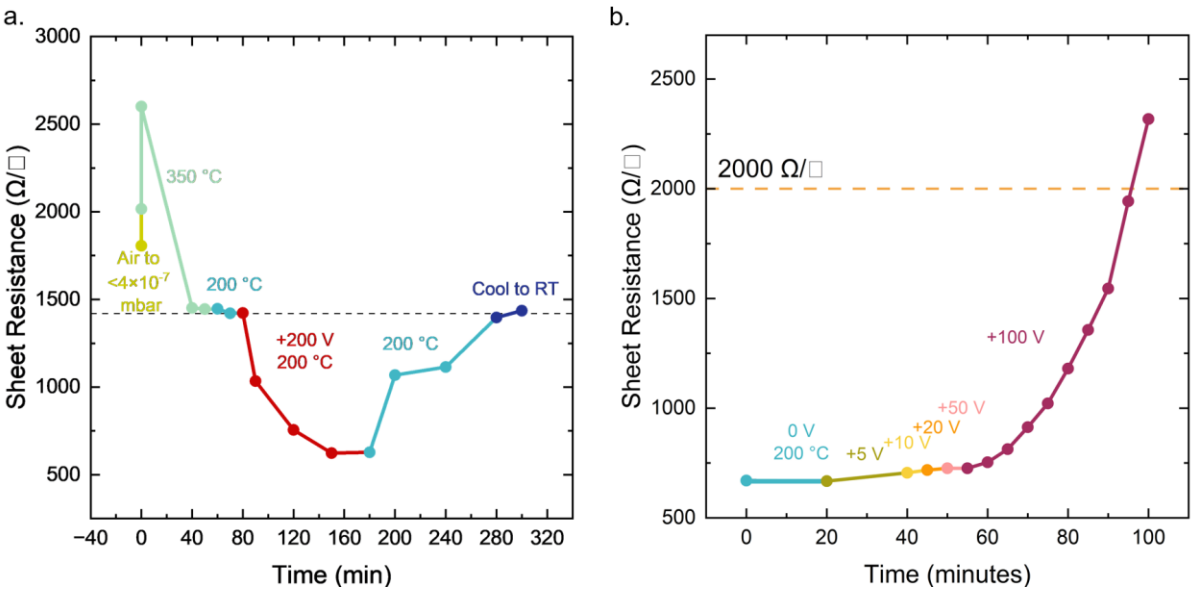

Figure 6.7: (a) Graphene sheet resistance on borosilicate glass over time held under positive applied bias at elevated temperatures. a. Initially undoped sample. (b) Sample previously n-doped, held stably at 200℃ before positive bias application.

As in the case of graphene/SiO_2K^+/Si in Chapter 5, on return to air, the low R_{sheet} achieved in vacuum increased due to the rapid adsorption of atmospheric contamination. However, when reannealed in vacuum, the low R_{sheet} achieved when using a negative bias can be recovered as the Na^+ ions remain stable at the graphene/BSG interface.

These new observations reveal that the stability of the graphene-alkali ion dipole ensures that n-doping remains in place after ion migration to the graphene layer. This stability is conserved even at high temperatures up to 200℃. In contrast, the relative instability of the Na^+ to the Al electrode requires a rapid quenching process to ensure that p-doping is maintained [182]. This p-doping is likely not stable over commercial timescales in an operational PV device in which it will be subject to potential stress at temperatures sufficient to activate Na^+ drift [319], [322], [326], [327]. Additionally, p-doping relies on Na^+ build-up at an opaque metal/BSG interface, preventing light transmission through the glass. It is unclear whether such doping could be preserved if the metal electrode were etched away to enable transmission. Depending on the length of the Na^+/Al dipole, after etching the opaque metal, migrated Na^+ ions may more easily reach equilibrium and reduce the graphene doping effect. This may limit the potential of p-

doped graphene/BSG for TCE applications. In contrast, as n-doping involves a strong electrostatic interaction at the graphene/BSG interface only, it is unlikely that etching the rear electrode will impact ionic stability. This insight into n-doping stability could allow for more varied applications of BSG-doped graphene in optoelectronic devices, with the stability of the Na^+-graphene interaction likely allaying concerns of Na^+ ion migration into a perovskite cell from a graphene/BSG TCE.

6.5 **Raman Spectroscopy of BSG-Doped Graphene**

Raman measurements were conducted after removing the graphene from vacuum and transporting samples to the Raman microscope for measurement within 1-2 hours of air exposure. Figure 6.8 (a) and (b) present the relative changes in Raman G and D peak position for graphene on BSG, before and after Na^+ ion migration towards the graphene layer. The observed G peak blueshift of ~4 cm^{-1} in Figure 6.8 (a) indicates that a moderate increase in doping has occurred [301]. However, the blueshift of the 2D peak indicates that this doping is p-type [301]. This suggests that the increased density of charge at the graphene surface attracted increased p-type contaminants from the atmosphere relative to the undoped layer. However, due to variability in air, it cannot be ruled out that such changes induced by doping are masked by the vacuum annealing process. For a more conclusive analysis of carrier properties, measurements in an inert atmosphere, or in encapsulated samples, might be necessary.

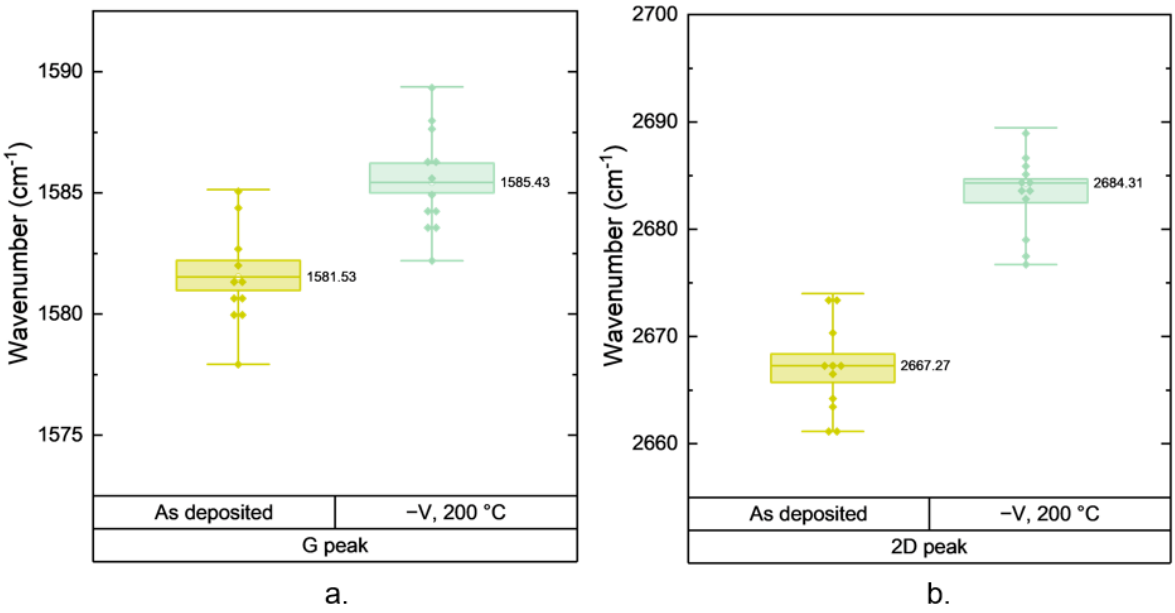

Figure 6.8. (a) G peak, and (b) 2D peak, for graphene on borosilicate glass substrates, before and after high temperature bias annealing.

6.6 Transmittance of BSG-Doped Graphene

After doping via reverse bias annealing, graphene/BSG samples were returned to air and the rear metal electrode was removed using an Al etchant consisting of 70% phosphoric acid, 5% nitric acid, 10% acetic acid, and 15% water. Figure 6.9 depicts the transmittance of the sample before and after reverse-bias annealing. It is clear that the transmittance has increased slightly, from ~95% to ~97%, but this can be attributed to the reduction in polymeric contaminants after undergoing a high-temperature vacuum anneal [204], [295], [328]. Before and after doping, the transmittance remains high at >95%, confirming that the presence of Na^+ ions at high concentration at the graphene/BSG interface did not impact the transmittance of the graphene, and indicating that Na-based precipitates did not form at high concentration using this technique.

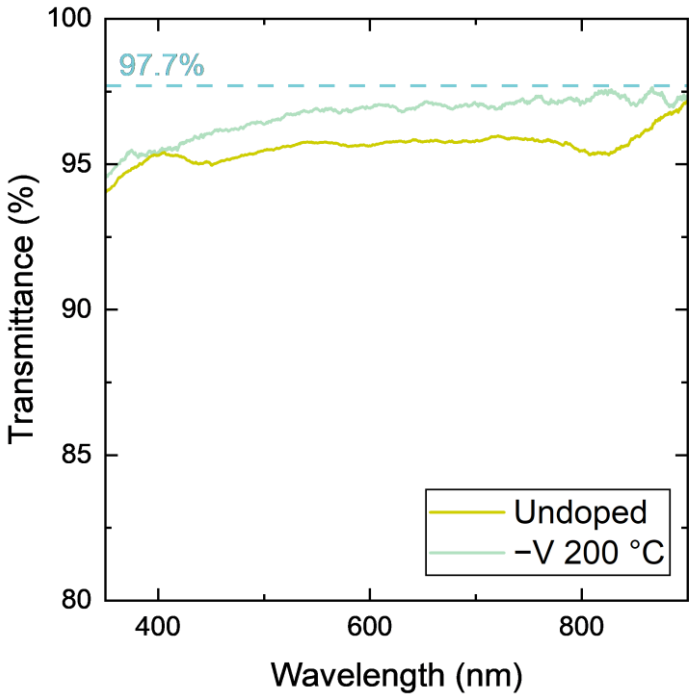

Figure 6.9: Transmittance of a graphene layer on borosilicate glass, before and after bias-temperature stress in vacuum. The dashed line indicates the theoretical maximum transmittance of graphene.

While the migration of Na^+ ions in BSG enables low R_{sheet} graphene with >95% transmittance, the process of ion migration is relatively time-consuming. To be used as a TCE in a device, the rear aluminium electrode must be deposited, graphene transferred, the front metal electrode deposited, and the graphene/BSG layer subsequently subjected to a high-temperature anneal under bias. The metal electrodes must then be removed via etching before device fabrication. Such requirements hinder its industrial applicability. Additionally, despite showing strong stability in this work, it is highly plausible that the mobile Na^+ would contribute towards the degradation of an adjacent perovskite cell over long-term device operation. While graphene should be impermeable to atoms as large as Na^+, it is possible that some ions may drift through defect sites and permeate to the perovskite layer. This may necessitate a dense capping layer such as IZO to prevent degradation, further contributing to processing time as well as parasitic absorption. From a device perspective, doping using charge in a borosilicate glass layer offers limited configuration possibilities, as the introduction of ions via rapid quenching is only

possible on thick films [303]. To fully exploit ICD-doping in devices, ICDs need to be ultrathin, rapidly fabricated, and ideally not rely on highly mobile alkali ions.

The remainder of this chapter explores the development of ultrathin corona-charged dielectric nanolayers to facilitate graphene doping on glass substrates. This approach offers the potential for an ICD-doping process that can be rapid, industrially scalable, and free from the deleterious device degradation associated with mobile ions.

6.7 Charged Dielectric Nanolayers for Graphene Doping

To demonstrate stable doping without using mobile alkali ions, an ICD was fabricated by corona charging dielectric nanolayers at high temperatures. Figure 6.10 (a) depicts the fabrication process. PECVD is used to deposit the dielectric layers, allowing for highly uniform deposition on glass in seconds. Fused silica quartz substrates were used to control for the impact of any additional mobile charges typically present in most glass materials. Charge is then introduced through an 8-cycle high-temperature corona anneal process. Finally, a graphene layer is transferred to the surface of the charged dielectric layer.

To facilitate a high, stable charge concentration in the dielectric layers, two candidate structures were prepared, and are depicted in Figure 6.10 (b) and (c). Structure 1 is of a ~60 nm PECVD SiN_x layer. The non-stoichiometric nature of SiN_x generates within it a high density of deep traps in the dielectric bulk, with a density ranging from 10^{18} to 1.7×10^{19} /cm^3 [329], [330], [331]. Defects sites, including nitrogen and silicon dangling bonds offer the potential to store high charge concentrations with low charge leakage [332], [333], [334]. When corona charge is deposited on the surface at high temperatures, the electric field induced drives the corona ions into the dielectric, where they can become trapped at such defect states [332]. For these samples, the corona charging protocol described in Figure 3.4 was modified, to include eight cycles of: 30 s corona deposition, and 5 min at 450 ℃, with no alkali ion precursor used. The

increased temperature and annealing time were used to encourage charge injection into deeper, more stable traps. The ~60 nm thickness was chosen as it offers an anti-reflective benefit in PV devices [335], [336].

Figure 6.10 (c) depicts Structure 2. In this case, multiple ~5 nm SiO_x and SiN_x layers are used. The additional interfaces between SiO_x and SiN_x provide additional sites for stable charge trapping [337], [338]. The layer thicknesses of ~5 nm should be sufficient to allow charge injection at high temperatures under an electric field, yet thick enough to prevent substantial charge leakage through tunnelling. The total thickness of the stack is ~60 nm, to preserve a similar anti-reflective benefit as in Structure 1.

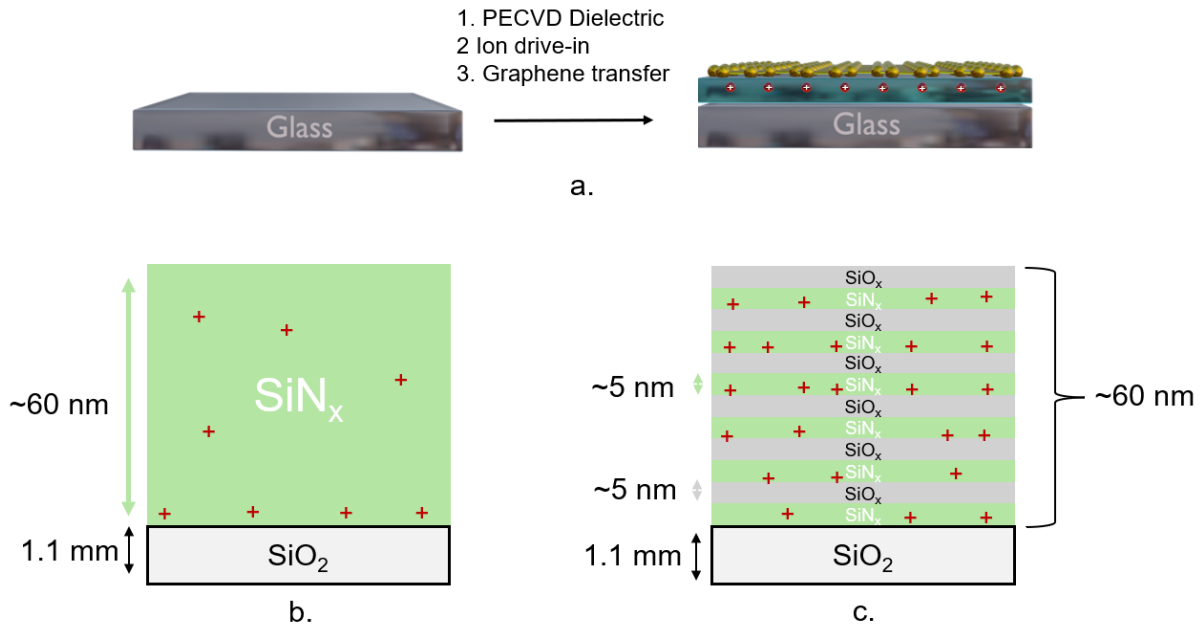

Figure 6.10: Fabrication process for graphene doped using an ion-charged dielectric nanolayer on a glass substrate. b. ICD Structure 1, thick PECVD SiN_x on glass. c. ICD Structure 2, SiO_x/SiN_x nanolayer on glass.

The thickness of the fabricated PECVD films was validated using ellipsometry. The recipes used are indicated in Table 3.2. Figure 6.11 (a) depicts the thickness of single SiO_x and SiN_x nanolayers, which were ~3.9±0.1 nm and 4.8±0.1 nm respectively. To account for the impact of varying substrate environments on the PECVD deposition rate, the total thickness of one "double" layer consisting of SiO_x/SiN_x or SiN_x/SiO_x was compared. Figure 6.11 (b) depicts

these results, illustrating that the SiO_x base layer sample is slightly thicker by ~ 3 nm, likely due to the more favourable deposition of a SiO_x layer on the substrate relative to SiO_x deposition on SiN_x. When this process is repeated 6 times, the deposited multilayer reaches a thickness of ~53.4±0.4 nm. This thickness appears plausible assuming a linear deposition-time relationship, however, it may differ slightly from the actual value due to the difficulty in accurately fitting the ellipsometry model to such a layer with multiple interfaces. Finally, Figure 6.11 (d) depicts a case where the basic SiN_x recipe is extended 12 times longer than the initial recipe, yielding a thickness of 66.7±0.6 nm. The 66.7 nm SiN_x and 53.4 nm multilayer structures provide the recipe for “Structure 1” and “Structure 2” respectively, for use for charging and graphene doping.

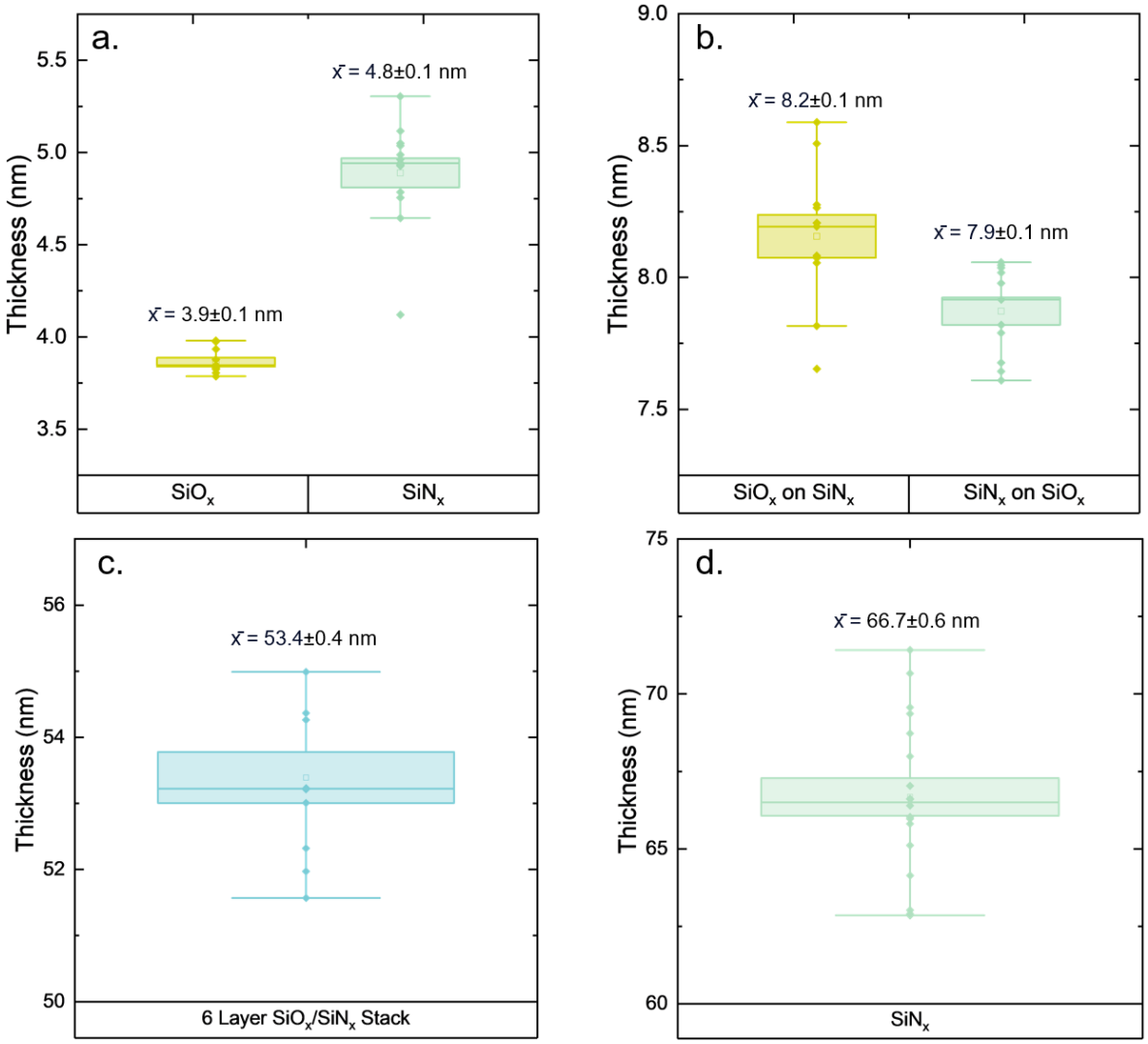

Figure 6.11: Thickness of PECVD fabricated SiN_x layers as measured using ellipsometry. (a) 1 cycle deposition of each layer on quartz. (b) 1 cycle deposition of a SiO_x/SiN_x or SiN_x/SiO_x layer. (c) 6-layer SiN_x/SiO_x stack on quartz. (d) Thick SiN_x layer on quartz.

6.8 Characterisation of Charge Concentration in Dielectric Nanolayers

The charge concentration in the charged dielectrics was measured using Kelvin probe. However, due to the 1 mm thickness of the quartz layer, measurements on these substrates proved challenging. The relative signal from the charge on a <100 nm layer on a 1 mm quartz substrate was determined to be too small to measure accurately using KP. For charge characterisation, the SiN_x/SiO_x multilayers were instead deposited on a silicon substrate, with native oxide removed using 1:7 concentration hydrofluoric acid. It is not expected that the corona charge stability of dielectrics on glass substrates should differ from that on silicon, as

the charge principally resides in the deposited layers themselves [339]. Figure 6.12 depicts the Kelvin probe map across an 8 × 8 mm^2 PECVD SiN_x layer of thickness 66.7±0.6 nm, with Figure 6.12 (a) depicting the measurement scan setup. Figure 6.12 (b.i) and (b.ii) depict the 3D and 2D surface plots of the CPD measured before charging. The mean CPD measured in the uncharged state was −0.54 V. Figure 6.12 (c).i and c.ii depict the CPD 3D map and 2D surface plot of the same layer after undergoing the 8-cycle corona anneal process. After charging, the CPD increases to a mean of −1.51 V, with a variation of just 3.7 mV across the surface. Assuming most charges reside in the bulk of the SiN_x [329], [330], [334], this corresponds to a positive charge of magnitude ~3.2×10^{13} q/cm^2. This is on the upper end of literature values for bulk charge in SiN_x, which typically reach ~ 10^{13} q/cm^2, indicating that the high-temperature corona anneal process efficiently introduced a high charge concentration to the dielectric [340]. This uniform, high charge concentration indicates the potential ICD-doping across large-area graphene samples interfacing with it, with limited impact on graphene mobility.

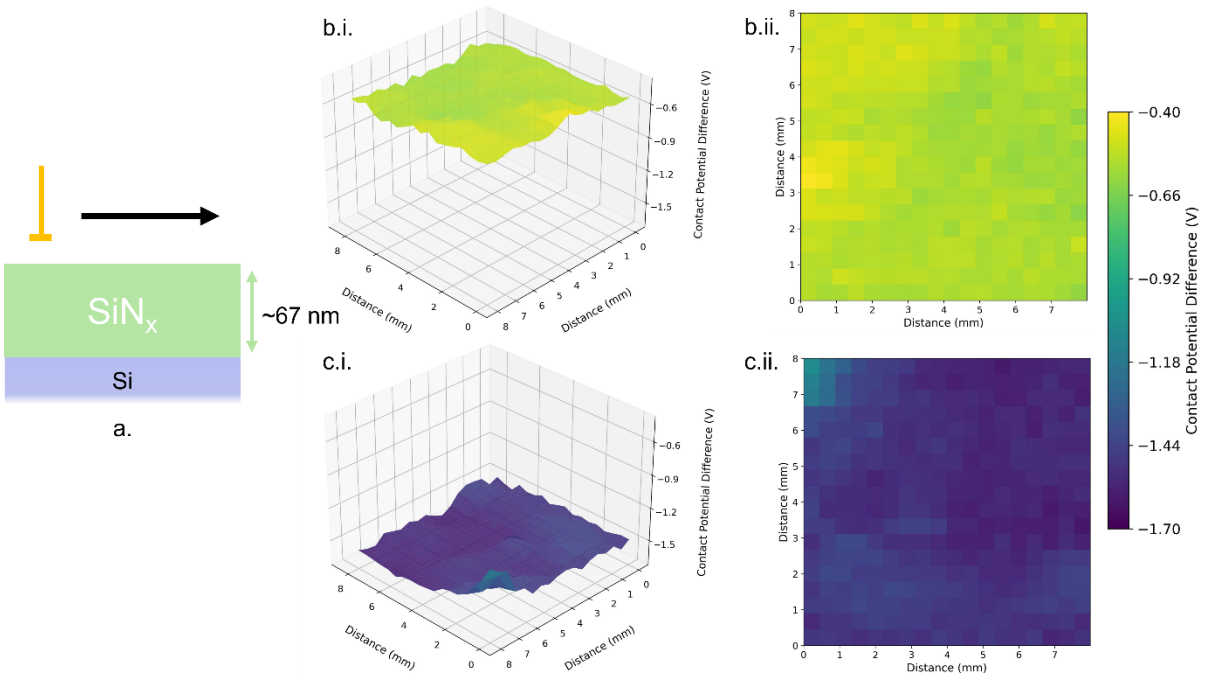

Figure 6.12: Kelvin Probe Mapping of the surface of a 60 nm SiN_x layer on silicon. (a) Measurement set up. (b.i) and (b.ii) Before corona anneal. c.i and c.ii. After corona anneal.

The charge storage in the SiO_x/SiN_x multilayer structure was then investigated in the same way as in the case of a ~67 nm SiN_x. Figure 6.13 (a) depicts the measurement set-up used for KP mapping of the surface. In this case, a mask was used to deposit ~53 nm multilayer stack on one side of an HF-cleaned silicon wafer only, enabling the variation in charge between the layers to be visualised. Figure 6.13 (b.i) and (b.ii) depict the 3D and 2D surface plots of the CPD measured before charging. The mean CPD on the uncharged multilayer surface was −0.34 V. Figure 6.13 (c.i) and (c.ii) depict the 3D and 2D surface plots of the CPD measured after charging. The CPD at the charged region now increases in magnitude to a mean of −2.67 V. To calculate the charge in the dielectric stack, we can assume an effective oxide thickness t_{eff}, following:

$$t_{eff} = t_{SiOx} + \left(t_{SiNx} \cdot \frac{\varepsilon_{SiOx}}{\varepsilon_{SiNx}}\right) \quad (6.1)$$

Using this effective thickness, and assuming the charge primarily resides in the bulk of the dielectric stack, the charge after corona annealing is calculated as 2.4×10^{13} q/cm^2. This should be a sufficiently high charge concentration to induce doping in an adjacent graphene layer.

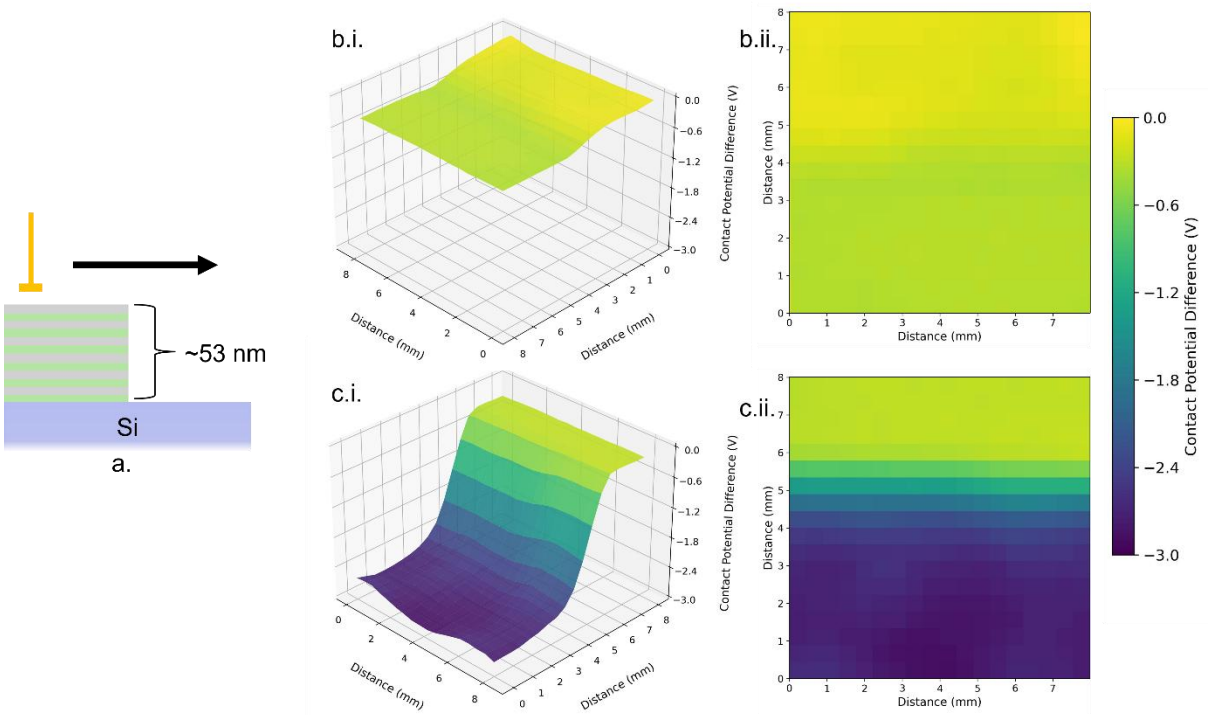

Figure 6.13: Kelvin Probe Mapping of the surface of charged SiO_x/SiN_x dielectric on silicon. (a) Measurement set up. (b.i) and (b.ii.) Before corona anneal. (c.i) and (c.ii) After corona anneal.

6.9 Characterisation of R_{sheet} Variation of Graphene Doping Using Dielectric Nanolayers

To characterise the variation in R_{sheet} in the charged dielectric nanolayers, substrates were fabricated such that one half is coated in a charged dielectric layer, with the other half in contact with the bare quartz substrate only. Due to the large thickness and lack of conductive pathways on the quartz substrate, the charge on the quartz will remain primarily on the surface during corona annealing, and so is likely to be removed by water and solvents during graphene transfer. The charged nanolayers are assumed to remain relatively stable to the graphene transfer. The solvents used will primarily interact with loosely trapped surface charge, while the 180℃ 15 min annealing process is likely too low to release the charge which is assumed to be held at high-energy deep bulk traps.

The graphene is transferred such that half is in contact with the charged layer, and half is in contact with the uncharged quartz layer. There is significant inter-sample variability in R_{sheet}

between CVD-grown graphene deposited via the wet transfer in this work, making it difficult to determine whether reductions in R_{sheet} measured in air were due to variations in processing conditions or due to doping. However, the R_{sheet} measured at different positions near the centre of the graphene layer are relatively uniform. Therefore, measuring the R_{sheet} of the same sample on a charged region and on the bare quartz provides a good indicator of whether the charged dielectric was sufficiently charged to contribute to doping.

Figure 6.14 (a) depicts the measurement process, where the 4PP method was used to measure the R_{sheet} at different positions on the surface of the graphene layer, in air. To minimise the impact of atmospheric contamination on measurement, devices were placed in a nitrogen-purged low-vacuum chamber immediately after PMMA removal, and measured using 4PP in air promptly after removal from inert conditions. Figure 6.14 (b) depicts the R_{sheet} measured across five samples with Structure 1, with ~67 nm SiN_x layer. The mean R_{sheet} of the graphene on the quartz was 497.6 Ω/□, while the R_{sheet} over the charged region was 452.4 Ω/□. The particularly careful control of atmospheric contamination in these samples likely contributed to their relatively low R_{sheet} in both cases. The slight reduction in R_{sheet} by ~50 Ω/□ on the SiN_x layer indicates that doping was induced by the charge concentration within it. Figure 6.14 (c) depicts the R_{sheet} measured for Structure 2, with a ~53 nm SiO_x/SiN_x multilayer. The R_{sheet} of the graphene on the quartz was 580.4 Ω/□, while the R_{sheet} over the charged multilayer was reduced by ~95 Ω/□ to 484.1 Ω/□. This larger reduction in R_{sheet} relative to the charged SiN_x could indicate more stable charge at the SiO_x/SiN_x interfaces. However, as these variations could also relate to variation in graphene quality or atmospheric contamination, a more detailed examination of charge decay in these layers is necessary to make firm conclusions about the mechanism at work.

The ultimate achievable R_{sheet} in both cases is likely limited due to atmospheric contamination. The behaviour observed here is similar to that demonstrated by Graham et al for graphene

transferred to ion-exchanged glass with a high charge concentration at the surface [302]. Graham et al. demonstrated a modest 70 Ω/□ shift in air from ~1.39 kΩ/□ to 1.32 kΩ/□ on charged substrates. However, charged samples encapsulated with a 40 nm thick ALD Al_2O_3 layer exhibited a ~5× reduced R_{sheet} compared to those on uncharged quartz, reducing from ~1.2 kΩ/□ to ~250 Ω/□ [302]. It is believed that the charged samples described here should behave similarly in vacuum, or if ALD-encapsulated, provided that atmospheric contamination before encapsulation can be limited.

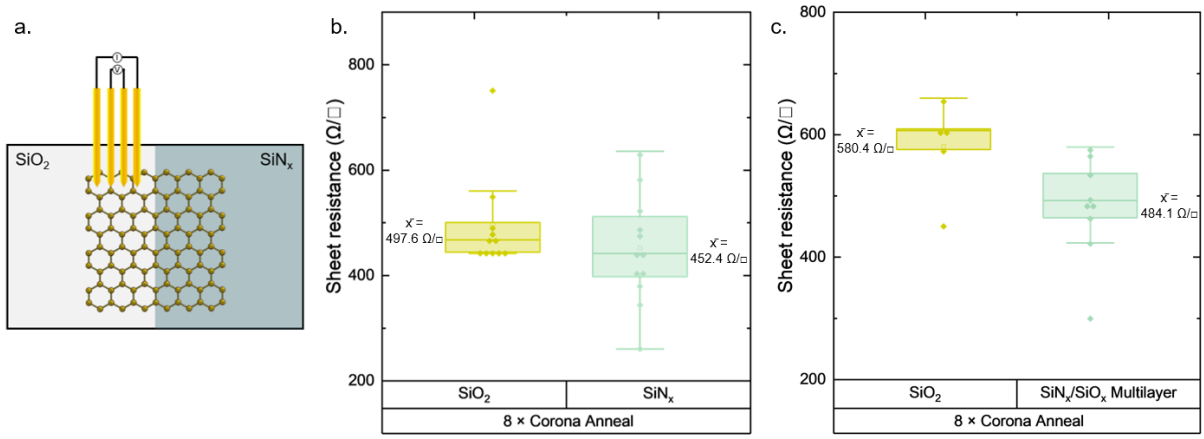

Figure 6.14.Four-point probe measurement of graphene on quartz, and charged dielectric nanolayers. (a) Four-point probe measurement set up. (b) Four-point probe R_{sheet} of graphene on SiO_2 quartz and charged SiN_x. (c) Four-point probe R_{sheet} of graphene on SiO_2 quartz and charged SiN_x/SiO_x multilayers.

6.10 **Raman Spectroscopy of Graphene on Charged Dielectric Nanolayers**

Raman spectroscopy was carried out on the fabricated devices in air, to determine whether the different charged substrates contributed to different doping environments. As in the R_{sheet} measurement, samples were kept in an air-free environment before measurement. Figure 6.15 (a) and (b) depict the G and 2D peak positions for graphene on the quartz layer and the charged SiN_x dielectric respectively. The positions of the G peaks at 1588.0 cm^{-1} and 1585.7 cm^{-1} indicate that the graphene is moderately doped on both substrates. However, the 2D peak of the graphene on the charged layer is notably redshifted by ~6 cm^{-1} compared to the graphene on SiO_2. This indicates that the introduction of positive charges to the substrate layer provided n-doping to the graphene [301].

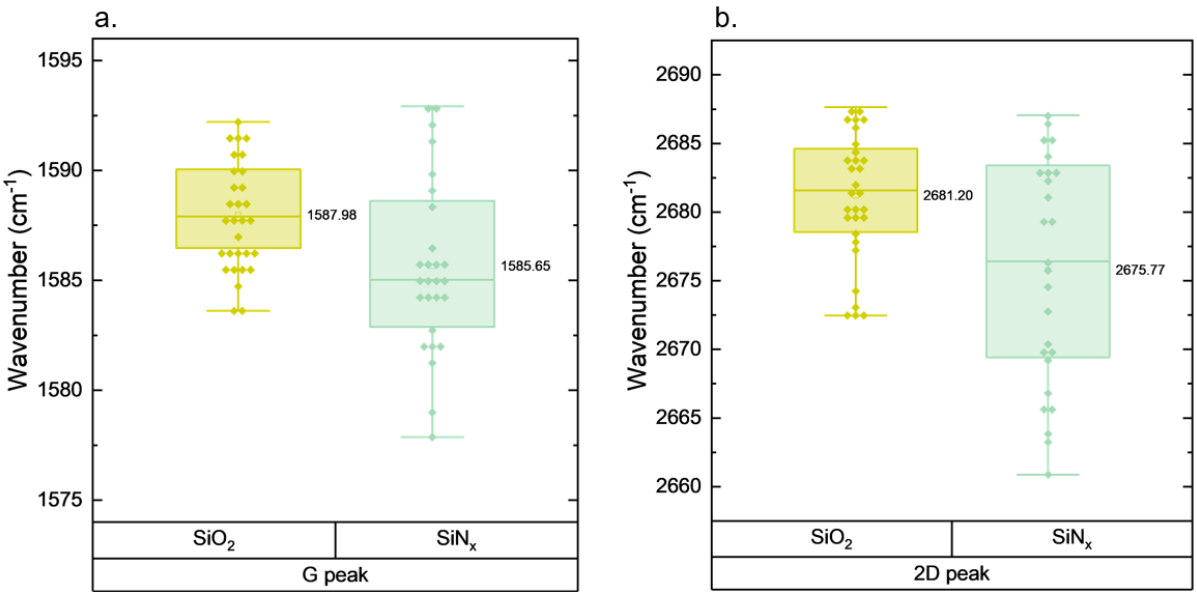

Figure 6.15: Raman (a) G and (b) 2D peaks of graphene doped using charged dielectric nanolayers.

6.11 **Transmittance of Graphene on Charged Dielectric Nanolayers**

Finally, the transmittance of the graphene on charged dielectric nanolayers was compared. Given the nature of the doping process, it was not expected to contribute substantially to any additional absorption or reflection. Figure 6.16 depicts the transmittance of graphene on an uncharged SiN_x layer, compared with graphene on a charged SiN_x layer, with the uncharged SiN_x substrate used as the background reference for the measurement. Both layers exhibit high transmittance >95%, indicating that the charging did not contribute substantially to light absorption or scattering. The charged layer has a slightly reduced transmittance at ~95% in the 450-800 nm range. This variation could be due to changes in SiN_x properties after annealing, but such effects are likely minimal. A 2% variation is within the range of absorption induced by polymeric contaminants from the transfer process, so this is assumed to be the dominant source of reduced transmittance in the charged sample. This result indicates that the charging process can dope graphene without impacting transmittance substantially.

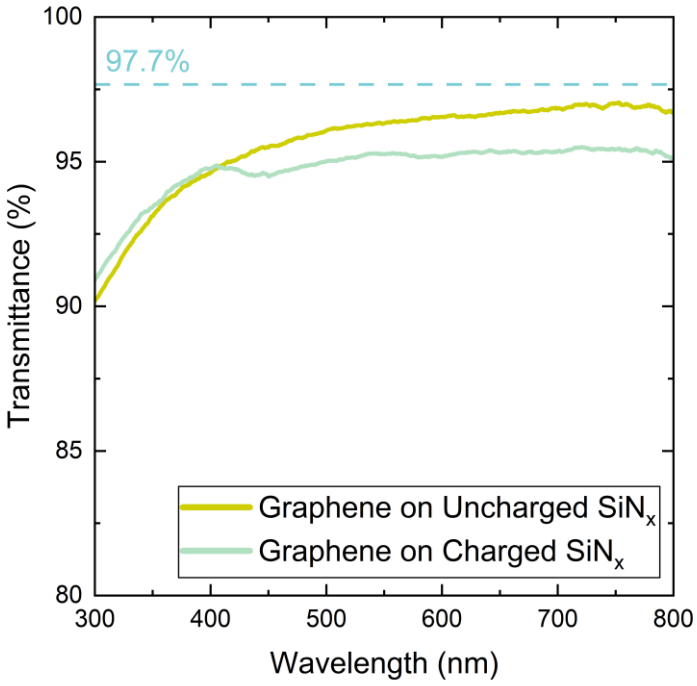

Figure 6.16: Transmittance of graphene on uncharged vs charged SiN_x. The dashed line indicated the maximum theoretical transmittance of graphene.

6.12 **Discussion and Conclusions**

In this Chapter, glass-based ion-charged dielectrics were developed and investigated, with the goal of demonstrating an ICD-doped graphene layer that could be feasibly integrated as the glass substrate in a 4-terminal tandem cell, or single-junction perovskite cell. It was confirmed that Na^+ ions, when migrated to the graphene/BSG interface provide strong n-doping for R_{sheet} <300 Ω/□, with strong stability to elevated temperatures and over time. The use of a SiO_x buffer layer was investigated, with evidence indicating that this additional interface reduces scattering at the graphene surface, enabling a >70% reduction in R_{sheet}. The space-charge doping induced by the net migration of Na^+ to the opposite end of the device for p-doping was also confirmed, except this process exhibited significantly reduced stability compared to the n-doped sample. The impact of the Na^+ doped layer on graphene's Raman peaks in air was also investigated, revealing that the high concentration of positive charge under the graphene layer likely induced increased atmospheric adsorption. As this process does not impact

transmittance, provided a suitable encapsulation process can be developed, BSG-doped graphene offers strong potential for TCE applications.

Doping using a dielectric nanolayer consisting of SiO_x/SiN_x was also investigated to facilitate ultrathin ICD-graphene layers. A strong charge concentration $>10^{13}$ /cm^2 was demonstrated in PECVD-grown SiN_x and SiO_x/SiN_x multilayers after a high-temperature corona anneal process. It was noted that graphene on the charged SiN_x and SiO_x/SiN_x multilayers exhibited a reduction of R_{sheet} of ~50 and ~90 Ω/□ compared to an uncharged quartz layer, suggesting moderate n-doping, confirmed via Raman spectroscopy. It was also evident from measurements that the charging process did not contribute substantially to transmittance losses. However, the relatively small shift in R_{sheet} indicates that air-free conditions are likely necessary to exploit the benefit of the high dielectric charge concentration for substantial graphene doping. If appropriate encapsulation can be achieved, it would offer the possibility of graphene-ICD integration in a wide array of device applications where low R_{sheet} is desirable. The development of encapsulation methods for ICD-doping will therefore be investigated in Chapter 7.

Chapter 7

ICD-Encapsulation of Graphene

7.1 **Introduction**

Atmospheric contamination is a critical challenge to ICD-graphene device integration. A recurring motif in Chapters 4-6 is that, even though very high charge concentrations are achieved in the substrate, the ultimate achievable R_{sheet} in graphene is limited by the adsorption of atmospheric contaminants. Samples annealed and then n-doped in a vacuum often became p-doped upon returning to air. This change is assumed to result from the pronounced adsorption of p-type atmospheric dopants induced by the charged substrate. Such unpredictable doping profiles in air limit the applicability of ICD-doped graphene in devices. As vacuum conditions are not practical for photovoltaic device applications, a suitable encapsulation technique is necessary.

For four-terminal tandem, or single-junction perovskite devices, graphene encapsulation can be comparatively straightforward. In these cases, the ICD/graphene layer is prepared where the protective layer used for transfer is removed in an inert/air-free environment. The graphene/ICD is then coated with a suitable perovskite charge transport layer in the same inert/air-free environment. In this way, the front surface of the graphene becomes encapsulated by the deposition of the perovskite cell materials. This approach could serve as a viable strategy to integrate ICD/graphene into PV cells, using the ICD structures developed in Chapter 6. However, these methods all rely on ICD fabrication on thick glass substrates and require high-temperature annealing. For two-terminal devices, such processing conditions and architecture are not usually compatible.

In a two-terminal structure, the graphene layer should be deposited directly on the charge transport layer at the front side of the cell, and the ICD layer deposited on the graphene

thereafter. In this configuration, the dielectric layer must serve both as an encapsulant and an ICD. Figure 7.1 (a) depicts a conventional two-terminal perovskite/silicon tandem cell, while Figure 7.1 (b) depicts a proposed two-terminal perovskite/silicon tandem structure incorporating an ICD/graphene layer at the front. In the proposed structure, the front TCO and buffer layer are replaced with a graphene layer encapsulated by an ICD. The TCO buffer is not necessary, as graphene deposition can be gentle, without causing perovskite or charge transport layer damage [104], [105], [106], [167], [341]. An anti-reflection coating is deposited on top of the ICD to improve light coupling, although the ICD itself could be adjusted to serve this purpose. However, this structure presents major processing challenges: ICD deposition must not damage the graphene, the ICD must be deposited at low temperatures, ideally < 100 ℃ to prevent damage to the perovskite cell layers [342], [343], [344], and the ICD must be suitable for deposition over large areas. The development of a highly-charged ICD encapsulant that can meet these limitations while doping graphene is critical to realise ICD/graphene integration in two-terminal tandem cells.

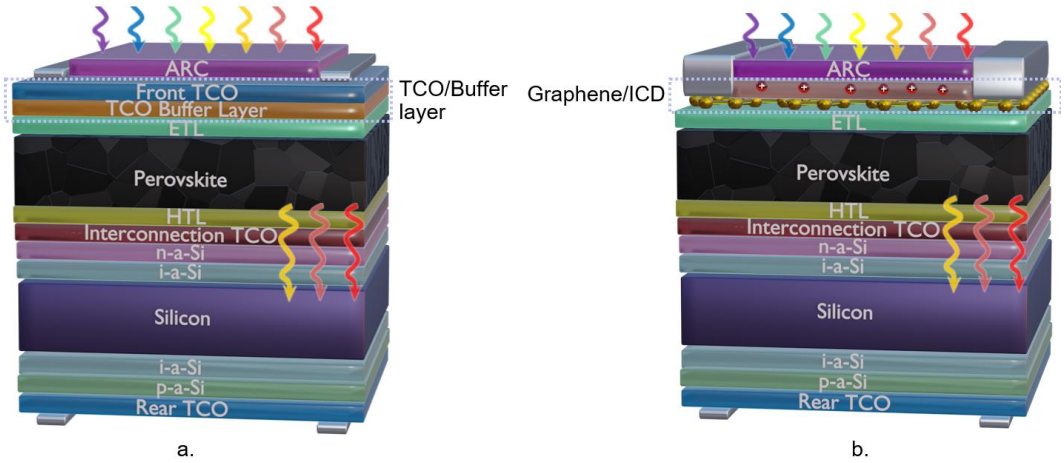

Figure 7.1: (a) Standard two-terminal perovskite/silicon tandem cell structure. (b) Two-terminal perovskite/silicon tandem cell incorporating an ICD/graphene front TCE.

This Chapter studies two approaches to developing such ICD encapsulation of graphene. These approaches will address the importance of encapsulation in preserving strong doping in air using ICD-doped graphene layers. With optimisation aimed at improved charged storage and

stability, these methods could enable ICD integration in tandem photovoltaic cells. Additionally, the development of ICD-substrates alongside ICD-encapsulants introduces a new profile for exploring 2D materials, where a potential dual-ICD-gated structure could provide stable charge concentrations approaching the theoretical limit for 2D materials of several 10^{14} /cm^2 without requiring an externally applied gate bias.

7.2 **Graphene Encapsulation**

Graphene encapsulation can improve charge carrier stability and reduce scattering by preventing the ingress of atmospheric contaminants [345], [346]. High-quality encapsulation methods, such as those using 2D hexagonal boron nitride (hBN), can enable ballistic carrier mobility >100,000 cm^2/Vs at room temperature [347], [348], [349]. However, despite recent progress in CVD-based hBN growth [350], high-quality 2D hBN fabrication is usually limited to micron scales, restricting such encapsulation to research-scale environments [347], [351]. A robust, large-area encapsulant is therefore essential to facilitate optimum graphene properties in practical solar devices.

A facile approach to encapsulate 2D materials over large areas is to coat them with polymers such as PMMA or PDMS [352], [353], [354], [355], [356]. These materials are simple to deposit at room temperature using spin- or spray-coating, allowing deposition without causing damage to 2D materials [195], [357], [358], [359]. PMMA is known to be a useful dielectric for gate tuning of graphene devices [354], [360], [361]. However, its relatively low dielectric constant (3-4) limits its utility in complementary metal-oxide semiconductor (CMOS) applications which require low-thickness, low-leakage dielectrics [354], [361], [362].

The need for high dielectric constant encapsulants for CMOS applications has motivated the development of atomic layer deposition (ALD) fabricated gate dielectrics on graphene [363], [364], [365]. The soft deposition of ALD layers at relatively low temperatures enables the

encapsulation of graphene with limited damage, with optimised layers only slightly reducing its mobility [365]. ALD has been used to deposit high-quality AlO_x and HfO_x layers on graphene at temperatures of <130℃, making it compatible with the temperature constraints of a tandem cell [365], [366], [367], [368]. ALD is a well-established technique in the fabrication of perovskite/silicon tandem cells, where it is typically used to deposit SnO_2 electron transport layers on perovskite absorbers [369]. This combination of high-quality and low-temperature dielectric deposition makes ALD-deposited dielectrics a promising approach to integrating ICD/graphene in tandem cells.

Independently, PMMA and AlO_x layers have been demonstrated to store high concentrations of ionic charge [370], [371], [372], [373]. Knowing that applying an external gate bias to these materials induces the field effect in graphene, it is reasonable to assume that building a high concentration of ionic charge in these polymer or ALD dielectric layers, could enable graphene doping via the field effect. This presents a method to achieve ICD-doping using encapsulating layers.

In this chapter, the ability of PMMA and AlO_x layers to store charge is explored. Charged PMMA and AlO_x layers are then used to demonstrate graphene doping using an encapsulating ICD. Such insights offer a roadmap for achieving low R_{sheet} ICD-doped graphene integration into optoelectronic devices with constrained fabrication requirements, such as tandem solar cells.

7.3 Charge Storage in PMMA for Graphene Doping

PMMA is a polymer of methyl methacrylate with a repeating structure of $–[CH_2 – C(CH_3)(COOCH_3)]_n–$ molecules [374]. The $COOCH_3$ groups in PMMA are polar and can create dipoles which interact with charge and readily accumulate charges incident upon them. A significant charge build-up on PMMA has been demonstrated by the deposition of positive

and negative corona charges on its surface [375], [376], [377]. Along with polar $COOCH_3$ dipoles, charge can also accumulate due to surface defects and impurities at the surface which can cause charge trapping. Variations in humidity, temperature and roughness have also been shown to impact the charge storage potential of PMMA [371], [375], [376]. Due to PMMA's widespread use in 2D materials processing, corona-charged PMMA is an ideal candidate to investigate ICD-encapsulation of graphene.

Corona charge deposition on PMMA has been used to induce an electric field to generate carriers in epitaxial graphene grown on silicon carbide substrates in previously published work [378]. However, this investigation was limited: characterisation was restricted solely to Hall bar measurements of mm and μm areas, details regarding the stability of the charge storage was not revealed in the data provided, and the corona deposition was poorly controlled using a commercial anti-static gun held at a distance from the sample. In the first half of this Chapter, this method will be examined further, revealing new insights into charge stability and the impact of different polarity charges on the doping of graphene.

7.4 Characterisation of Charge Storage in PMMA

To characterise charge storage on the PMMA layer, a silicon substrate was first prepared by etching in hydrofluoric acid at a concentration of 7:1 for ~30 seconds to remove surface oxides which can store charge. A PMMA layer was immediately spin-coated on the silicon surface, following the same recipe as used for the protection of graphene during transfer, described in Table 3.4. The thickness of the spin-coated PMMA was measured using a DekTak profilometer, with mean thickness found to be 251±21 nm.

Figure 7.2 (a) depicts the KP measurement setup. The CPD was measured at the PMMA surface, and the surface was then subject to negative or positive corona charge. Figure 7.2 (b) presents the CPD at the PMMA surface as the device is held under negative or positive corona

charge. In the case of the negative charge CPD increases rapidly with increasing charging time, saturating after ~60 seconds to around 80 V, indicating significant negative charge build-up on the surface of the PMMA layer. Charging beyond 60 seconds led to measurement difficulties due to strong static build-up, which often prevented price KP positioning close to the PMMA surface. The presented values from 60-240s are the CPD measured after a few minutes of charge dissipation. It is likely that the CPD is >100 V after charging, but stable measurements at this voltage were not possible.

When positive charge is deposited on the PMMA, the CPD increases gradually in magnitude from ~0 V to <80V over 4 minutes of total charging time, indicating a high concentration of positive charge at the film surface. In contrast to negative charge deposition, in this case, stable CPD measurements could be obtained each interval. This suggests the PMMA layer has the capacity to store significantly more negative than positive charge.

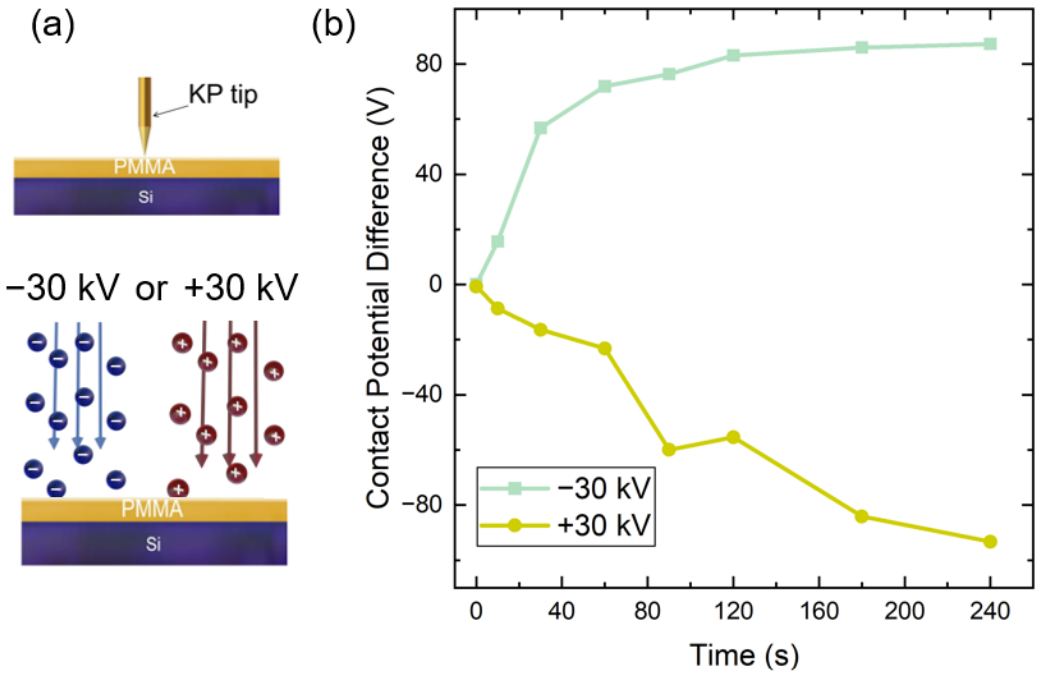

Figure 7.2: (a) Schematic of Kelvin probe CPD measurements and corona charging of PMMA layers on silicon. (b) Contact Potential Difference of a PMMA/Si sample as it is held under negative or positive corona charge.

To determine whether corona charge remains stable on PMMA over time, the CPD was measured as the device was held directly under the KP tip, in air, for an extended period. Figure

7.3 (a) depicts the variation in CPD on a negatively-charged PMMA/Si sample over 8 hours after charging. The initial points exceed 100 V, but this charge dissipates quickly. After 4 hours, the CPD decreases to ~30 V, eventually plateauing toward ~25 V after 8 hours. Figure 7.3 (b) depicts the variation in CPD on a positively-charge PMMA/Si sample over time. Here, the charge decay is significantly faster, with the CPD increasing to over – 25 V within 80 minutes. This demonstrates that a high concentration of negative charge remains stable on the PMMA surface on the timescales of hours, while positive charge stability on PMMA is limited to a few minutes.

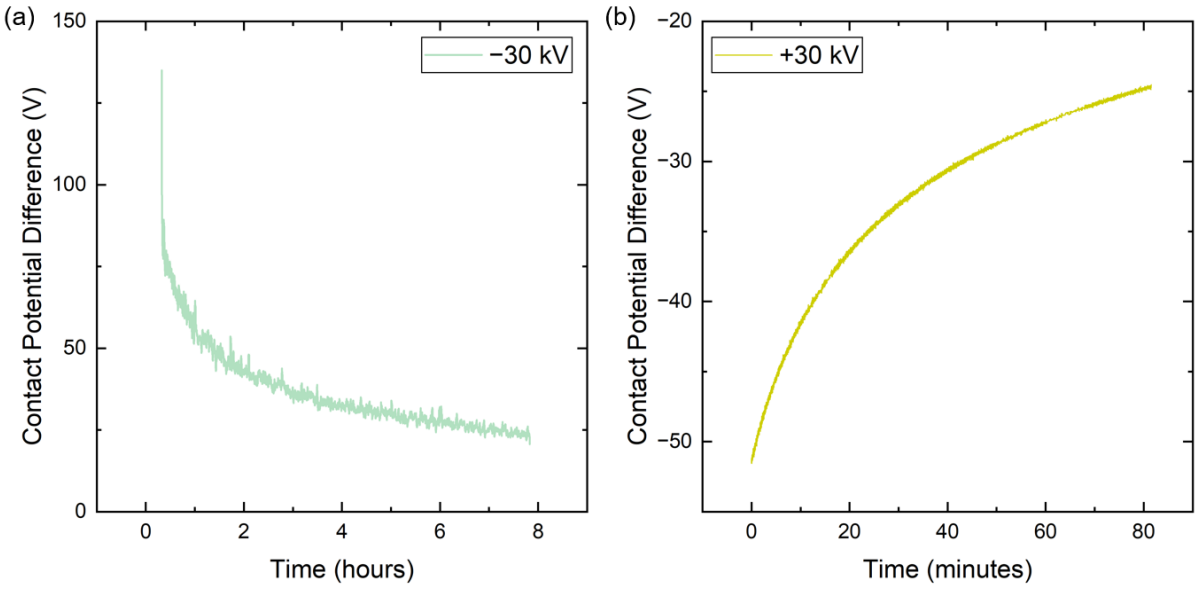

Figure 7.3: Decay in contact potential difference over time, as PMMA/Si samples are left in air after (a) negative corona charging, and (b) positive corona charging.

The higher stability of negative charge relative to positive charge on PMMA indicates a non-symmetrical charging mechanism. In a previous report, positive corona charge on PMMA was reported to be more stable in air than negative corona charge [371]. As negative charge stability was reduced in increased relative humidity environments, it was proposed that the absorption of H^+ from water at the surface caused increased neutralisation of the deposited negative charge [371]. However, it is postulated in this work that the higher electric field generated by the corona apparatus provided sufficient energy for charge trapping of deposited electrons near the

surface of the polymer matrix. This improved the stability of negative charge, which persisted for several hours. This is corroborated by previous work which reveals a ~2× greater density of electron traps in PMMA as compared with hole traps [376]. Further processing the PMMA layer through functionalisation or surface modification using oxygen plasma, could lead to increased charge concentration and improved stability.

Assuming a maximum CPD after negative charging of ~135 V as recorded in Figure 7.3 (b), the approximate charge concentration on the PMMA can be calculated using Equation (3.1). Taking the PMMA thickness to be ~250 nm and the dielectric constant to be ~3-4, the charge concentration on the dielectric after negative charging can be approximated as $8\text{-}12\times10^{12}$ /cm^2, likely sufficient to induce graphene doping. This calculation assumes the dielectric constant of the PMMA layer remains constant close to its literature values. However, PMMA has been shown to be degraded under high concentrations of corona charge, potentially causing molecular changes, modifying its dielectric constant and improving charged storage [371]. Moreover, the instability of CPD measurement for values >80 V suggests that a greater charge concentration charge on the surface, up to several 10^{13} /cm^2, but may be present but unmeasurable using KP. Additionally, it is possible that the polymer undergoes structural changes under long-term corona exposure at a high voltage, which allows charge to hop or to tunnel between localised states in the bulk of the material [376]. These bulk charges are not easily detectable using the KP, and their determination likely requires advanced characterisation of the electronic structure via methods such as x-ray photoelectron spectroscopy. It is therefore expected that the negative charge on the layer is likely greater than this approximate value calculated here of ~10^{13} /cm^2.

The poor stability of the positive corona ions could be related to the comparatively low hole trap density in PMMA [376], where they instead react with negative species in the ambient air

such as $OH^{-}\cdot(H_2O)_n$, reducing the overall charge on the surface. Therefore, negatively-charged PMMA appears to offer the most utility toward ICD-doping of graphene.

7.5 PMMA Encapsulation of Graphene

Figure 7.4 depicts the PMMA/graphene encapsulation process. Initially, graphene was transferred onto an insulating substrate and fabricated into a standard vdP structure with thermally-evaporated Al contacts. A silver electrodag contact was painted over the Al pads and allowed to dry. The Ag paint was then covered using Kapton tape. The PMMA layer was spin-coated on the surface of the graphene, and baked following the standard recipe described in Table 3.6. Profilometry was used to confirm that the PMMA thickness over the graphene layer was also ~250 nm, as in the silicon substrates. Removal of the Kapton tape facilitated electrical contact between deposited measurement probes and the graphene.

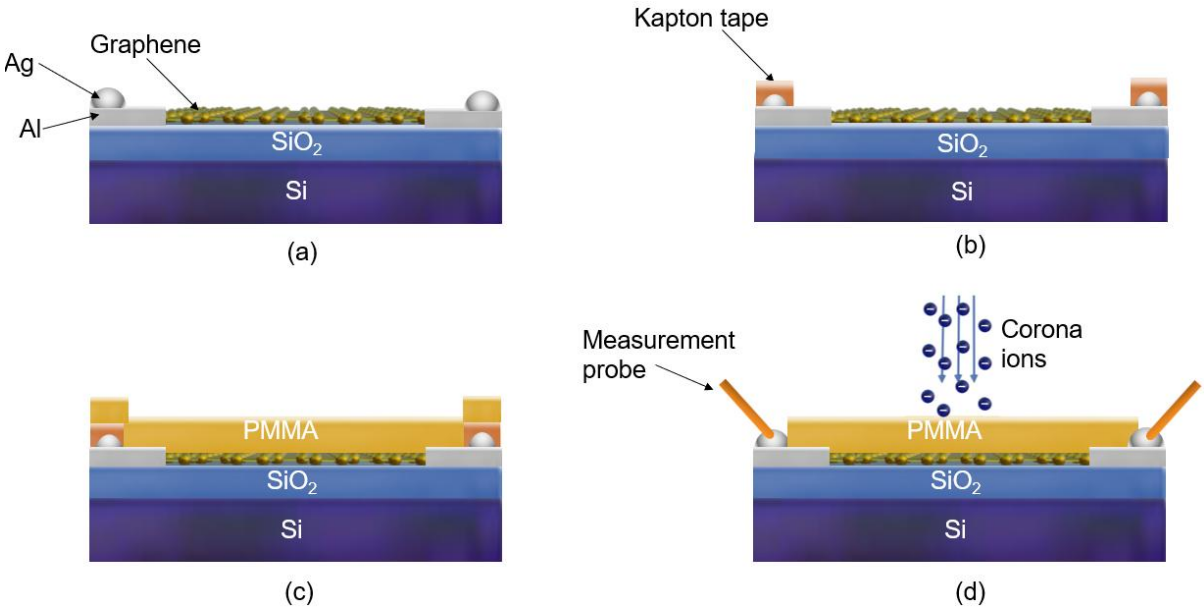

Figure 7.4: PMMA encapsulation process for graphene used in this work. (a) Graphene is transferred to a substrate and fabricated into a vdP structure with Al and Ag metallisation. (b) The Ag contact is covered using Kapton tape. (c) PMMA is spin-coated on the graphene surface. (d) The Kapton tape is removed, enabling the measurement of the graphene encapsulated with PMMA as it is subjected to corona charge deposition.

7.6 Electrical Characterisation of Graphene on Charged PMMA

Figure 7.5 (a) presents the change in R_{sheet} of a PMMA/graphene device with respect to negative charging time. The initial R_{sheet} was ~600 Ω/□, reducing to 553 Ω/□ after PMMA deposition,

likely due to reduced air exposure. As the concentration of corona charge on the PMMA increased, the R_{sheet} of the graphene decreased, appearing to saturate after 3 minutes, similar to the saturation in charge concentration observed when measuring in CPD measurement. After 10 minutes of total charging, the R_{sheet} reached a minimum of 350 Ω/□. This provides strong evidence that the charge on the PMMA is inducing doping in the graphene layer.

Figure 7.5 (b) depicts the R_{sheet} of the same sample, subject to further corona charging processes after allowing the charge to decay. After leaving the sample for 1 day in air, the R_{sheet} increased by 100 Ω/□, from ~350 Ω/□ to 450 Ω/□, likely due to the instability of the negative charge on the film. After another day, it increased by a further 25 Ω/□ to ~475 Ω/□. The smaller change in R_{sheet} on the second day is likely due to the plateau in charge decay rate over time observed in Figure 7.3 (a). On subsequently charging over several hours, the R_{sheet} of the graphene reduced to a minimum of 328 Ω/□, a >45% reduction from its initial value.

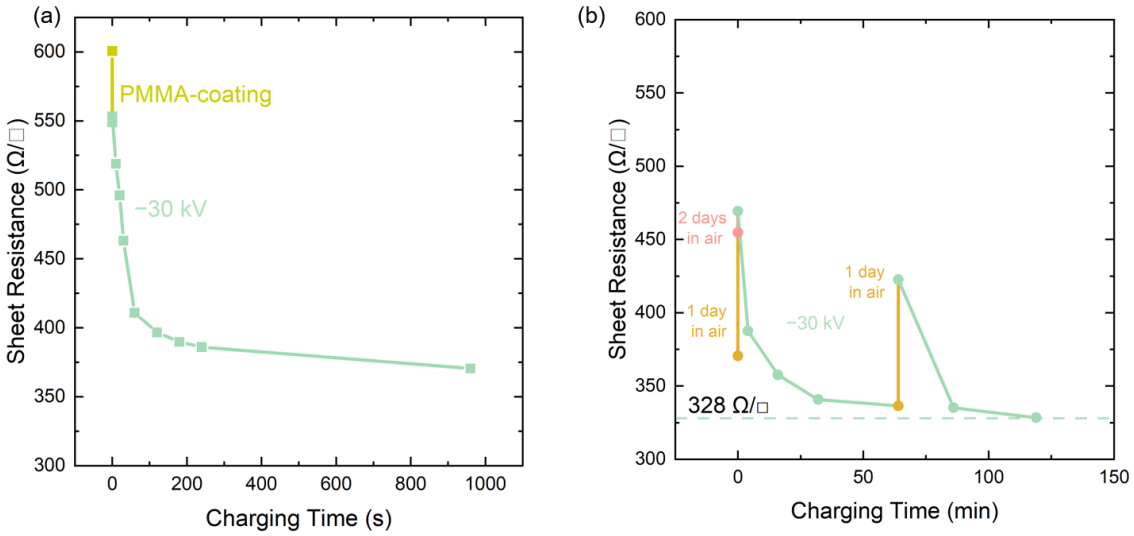

Figure 7.5: Sheet resistance of a PMMA/graphene sample as it is subject to negative corona charge over time. (a) Initial charging. (b) Charging, allowing for the charge in the PMMA to decay over different time intervals.

Figure 7.6 (a) and (b) depict how the carrier concentration and mobility of the same device as depicted in Figure 7.5 under negative bias. Adding the PMMA layer reduced carrier concentration and increased mobility, suggesting that PMMA encapsulation mitigated

atmospheric contamination and reduced scattering. There is a clear trend of increasing carrier concentration with negative charging over time, with a peak around $5\times10^{13}/cm^2$ measured after ~2 hours of charging. The carrier concentration achieved is greater than predictions from CPD measurements, indicating that changes in PMMA morphological or molecular changes may have occurred due to prolonged exposure to high negative charge concentrations. Over the same period of charging, the device mobility declined significantly from ~910 cm^2/Vs to ~380 cm^2/Vs, a reduction of over 50%. This decrease could likely be mitigated through the reduction in PMMA roughness, which would lower reduce scattering. However, as roughness provides additional localised states for charge trapping, the surface structure must be optimised for a balance of charge concentration with scattering effects [376].

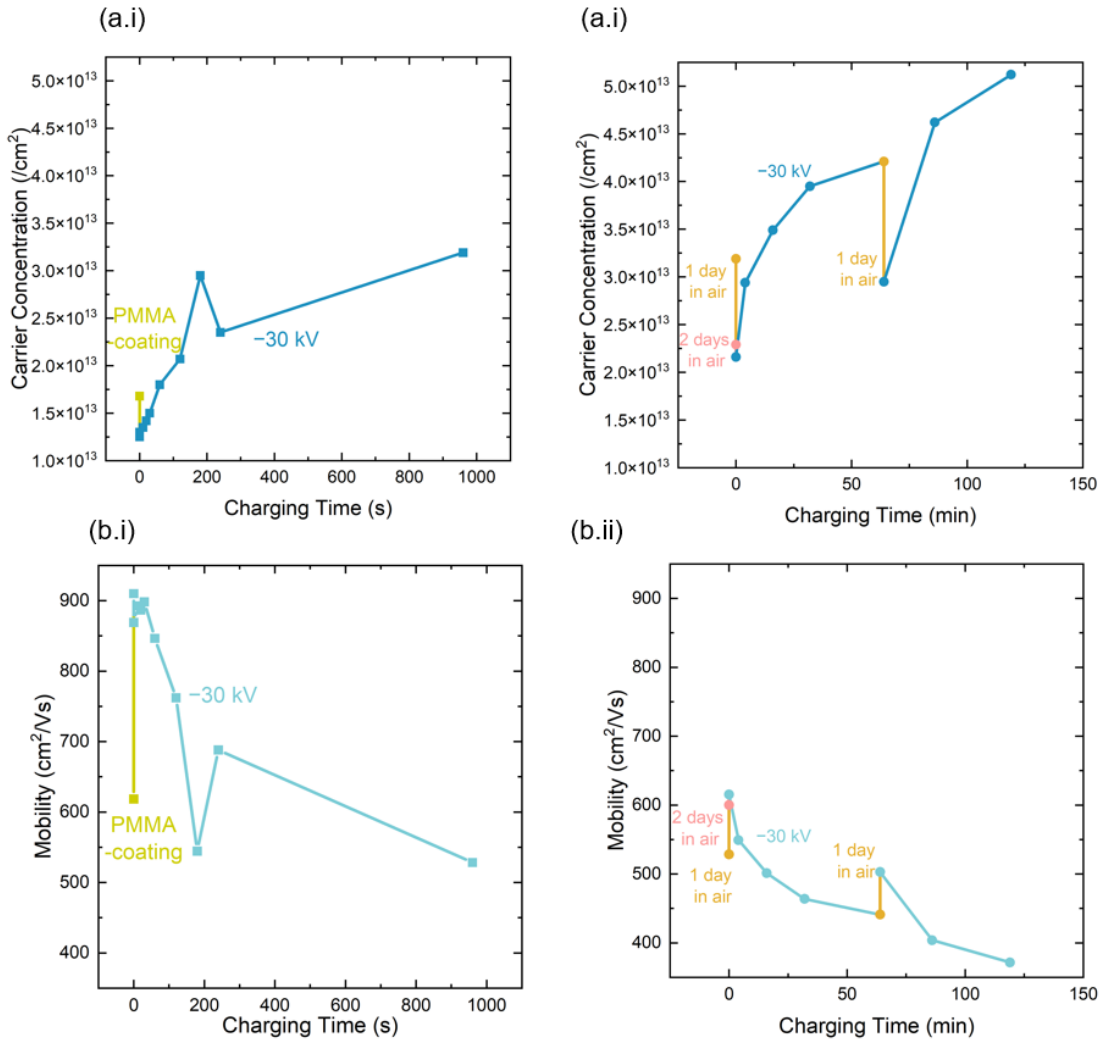

Figure 7.6:(a.i), (a.ii) Carrier concentration and mobility (b.i), (b.ii) of a PMMA/graphene device as it is subject to negative corona charge over time.

The impact of positive charge on the R_{sheet} of a PMMA/graphene device was then investigated. Figure 7.7 depicts the variations in R_{sheet}, carrier concentration and mobility of a PMMA/graphene subjected to positive charge, plotted with the same y-axis scale as that of Figure 7.6 for ease of comparison. Positive charge had a much weaker effect on the R_{sheet}. As the graphene is initially p-doped from atmospheric contaminants, the slight reduction in carrier concentration implies that the deposited positive charge induced additional negative carriers to neutralise the surface, but not sufficiently to induce n-type behaviour.

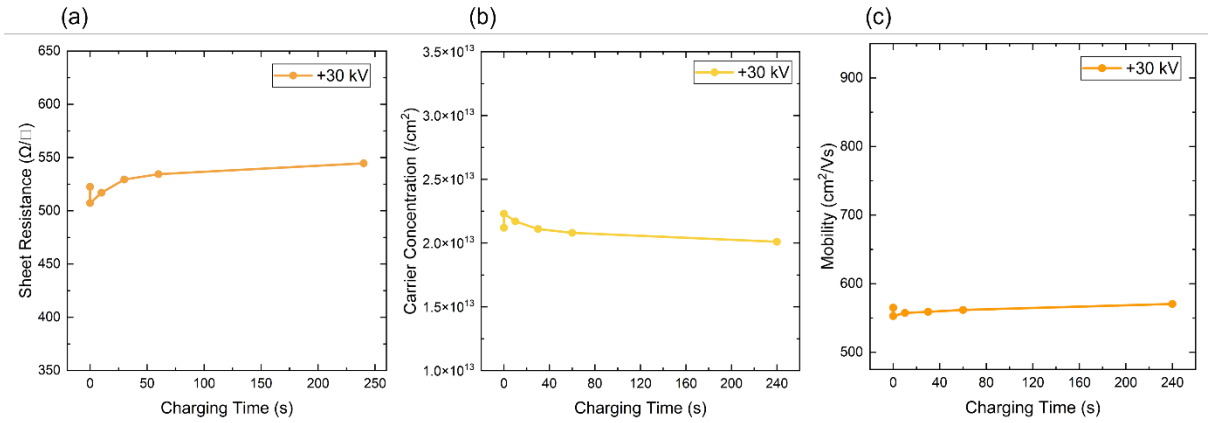

Figure 7.7: Sheet resistance (a), carrier concentration (b) and mobility (c) versus positive charging time for a PMMA/graphene device.

Identifying this slight reduction in carrier concentration, it was proposed that positive charge deposition may be sufficient to reverse the impact of negative charge, by neutralising the deposited negative corona ions on the surface of the graphene. Figure 7.8 (a) and (b) depict the variation in R_{sheet} and carrier concentration as a PMMA/graphene device is subjected first to negative, and then positive corona charge. Within 5 minutes of applying positive corona charge, both the R_{sheet} and carrier concentration return to their initial values of ~580 Ω/□ and 1.2×10^{13} /cm^2, respectively. This indicates that the charge induced by the positive ions effectively neutralised the charge induced by negative ions. After ~50 minutes of positive corona time, the R_{sheet} increases to ~1500 Ω/□, while the carrier concentration approaches 10^{11} /cm^2. This indicates depletion of the positive carriers, as the device approaches n-type behaviour. However, further charging was insufficient to activate n-type behaviour, likely due to the instability of the positive charge as discussed previously. Additionally, as the device is left in air after positive charging it quickly returns to its initial state, likely due to the adsorption of p-type atmospheric contaminants.

The ability to reverse the n- doping induced by the positive ions uncovers new functionality for device application, where the switching between n-type and p-type graphene without using an externally applied dielectric field can be applied.

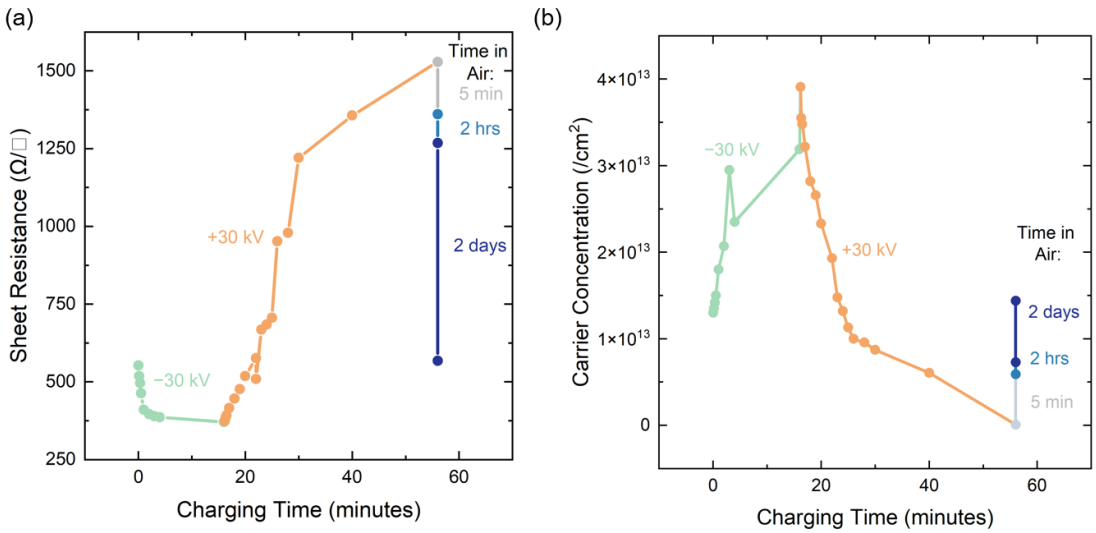

Figure 7.8: The sheet resistance (a) and carrier concentration (b) of PMMA/graphene samples subject to corona charge of different polarities

7.7 Raman Spectroscopy of Graphene on Charged PMMA

The Raman spectra of the graphene encapsulated with charged PMMA were then investigated. Devices were first measured prior to charging. After being subject to negative corona charge for 10 minutes, the Raman spectra were measured within 40 minutes. This interval was deemed appropriate for measurement without significant charge decay due to the relatively good stability of negative corona charge on PMMA on the timescale of hours. Devices were measured at different spots on the surface, using short acquisition times and very low laser power to minimise charge degradation at the surface that may be caused by the local heating of the PMMA during measurement. Figure 7.9 (a) and (b) depict the G and D peaks of the devices, before and after negative charging of the PMMA layer. There is a clear blue-shift of both the G and D peaks of the charged devices, indicating that the charged layers were p-doped by the addition of negative charge on the surface of the PMMA [301].

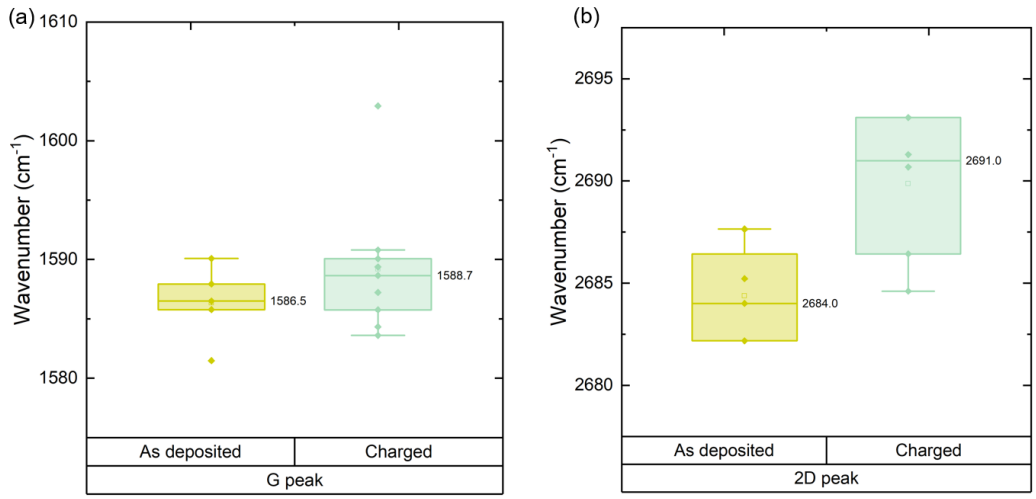

Figure 7.9: Raman G (a) and 2D (b) peak positions of a PMMA/graphene sample before and after negative corona ion deposition.

7.8 **Transmittance of Graphene on Charged PMMA**

After confirming that p-doping was induced by the negatively charged PMMA layer, the impact of the charge on transmittance was investigated. Figure 7.10 depicts the transmittance of PMMA/graphene on BSG substrates from 400-800 nm, before and after charging, with an uncoated area of the BSG glass slide used as the background reference. The transmittance profile appears slightly different from that of typical graphene samples, with a peak ~450 nm likely due to interference from the PMMA layer. There is no significant change in the spectra before or after charging, indicating that this ICD-doping process does not impact the optical transmittance of graphene.

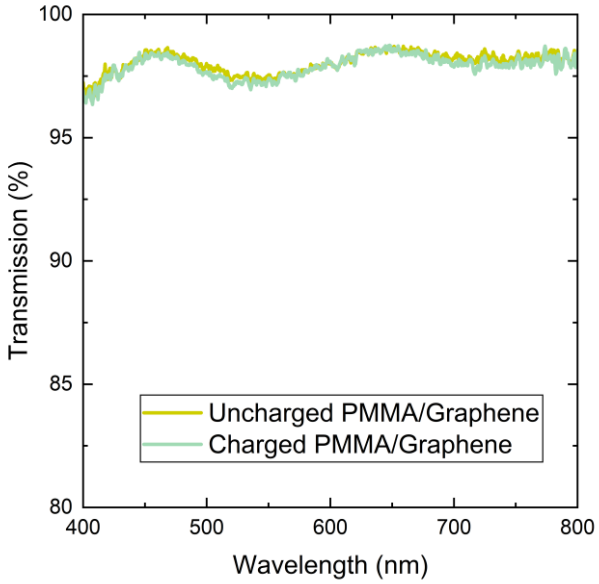

Figure 7.10: Transmittance of a PMMA/graphene layer before and after negative charging.

These results confirm the potential of charged polymers to induce strong doping in an interfacing graphene layer without impacting transmittance. However, due to the relative instability of the charge on the PMMA over time, it does not yet provide reliable device-relevant doping functionality. Improvement in charge stability may be achievable through oxygen plasma treatment of the PMMA layer before corona deposition. This could help to form oxygen functional groups on the surface which could more effectively store charge. If achieved, a polymer-based ICD-doping approach could be of significant relevance to device architectures where flexibility is desired.

To integrate ICD-doping in photovoltaic cells, stability over commercial timescales is essential. It is therefore necessary to investigate the use of more stable inorganic dielectrics for ICD-doping and encapsulation of graphene.

7.9 Charged AlO_x as an ICD for Graphene Doping

AlO_x is an inorganic dielectric with a strong potential for stable ICD-doping and encapsulation of graphene. AlO_x has a high density of traps that can store charge carriers, such as corona ions [372], [379], [380]. The deposition of corona charge on AlO_x is conventionally used to measure

its level of negative fixed charge for surface passivation in silicon solar cells [372], [380]. In this work, it is proposed that corona charge deposited and stored in these surface and trapped states in AlO_x can be used to dope an interfacing graphene layer which it encapsulates.

The encapsulation of graphene with AlO_x via ALD has become a well-established technique in research environments over the last 10-15 years [365], [368], [381], [382]. However, the deposition of high-quality dielectrics on graphene remains challenging. The lack of out-of-plane bonds in graphene makes it so that ALD-deposited layers on CVD graphene tend to aggregate at defect sites, grain boundaries and wrinkles, making it difficult to achieve uniform, thin dielectrics with few pinholes [365]. ALD AlO_x deposition on graphene often requires surface functionalisation and carefully controlled conditions of temperature and water pulsing, which require extensive optimisation to achieve good uniformity and a high dielectric constant [365].

Due to the relative complexity of developing a recipe to deposit ALD AlO_x on graphene in-house, an AlO_x fabrication technique based on the thermal evaporation of an ultrathin layer of aluminium was used in this work, similar to that developed in refs. [383], [384]. Such layers can be used as thin seed layers on which higher-quality AlO_x can be grown via ALD. The remainder of this Chapter discusses the fabrication of such a thermally-evaporated AlO_x layer on graphene without inducing damage, and the use of corona ions to build up a strong charge concentration in the AlO_x and induce doping in the graphene.

7.10 Fabrication of Thermally-Evaporated AlO_x layer

The conditions necessary for thermally-evaporated AlO_x formation were first investigated on silicon substrates. A bare silicon substrate was prepared by HF-etching, such that all surface oxides were removed. The substrate was then immediately placed in vacuum, where a 1.0-1.5 nm layer as measured using a calibrated crystal monitor was deposited at $<10^{-6}$ mbar. The

deposition rate was finely controlled at ~2-3 Å/s to ensure uniform deposition. Following deposition, the R_{sheet} of the surface was measured using the four-point probe. The layer was subsequently annealed at different temperatures and intervals over time. Figure 7.11 depicts the variation in measured 4PP resistance with annealing conditions. In the case of the "1.5 nm" Al, the R_{sheet} remained constant from ~250 Ω/□ under annealing up to 350℃. When the temperature was increased to 400℃, the resistance increased to ~800 Ω/□, indicative of partial surface oxidation being activated at this temperature. For "1 nm" Al, a 400℃ anneal over 30 minutes increased the R_{sheet} from ~300 Ω/□ to >1 GΩ/□. As this value is beyond the measurement limit of the device, it can be assumed that 400℃ anneal process was sufficient for complete oxidation of the Al surface. For the 1.5 nm layers, oxidation took over 90 minutes at 400 ˚C. This increased temperature-stress may degrade an underlying graphene layer, so the "1 nm" recipe was used henceforth.

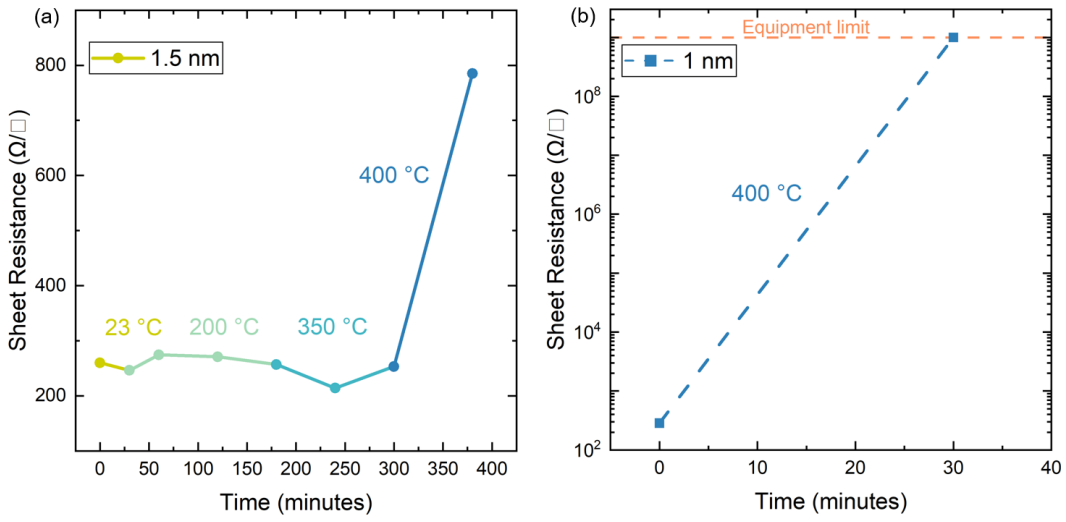

Figure 7.11: 4PP sheet resistance of Al layer as it was annealed under different temperatures over time. (a) 1.5 nm and (b) 1 nm layer as measured by the thermal evaporated crystal monitor.

To confirm that the entire Al layer had oxidised, vdP devices were fabricated on insulating substrates. Initially, Ag electrodes were deposited on four corners of a SiO_2/Si substrate. A brass mask was used to cover the Ag contact pads, allowing an ultrathin Al layer to be deposited between the contacts. The initial R_{sheet} of a "1 nm" Al layer measured using vdP was 165.7±5.5

Ω/□. After a 10-minute anneal at 400 ℃, all devices exhibited resistivity beyond the measurement range (>1 GΩ/□). This provides strong evidence that 10 minutes at 400 ˚C in air is sufficient for complete oxidation of a "1 nm" Al layer.

The transmittance of the thermally evaporated layer was then measured to determine whether the AlO_x had formed, which can be indicated by an increase in transmittance to close to 100%. Figure 7.12 depicts the transmittance of the thin Al layer on a BSG substrate, before and after annealing at 400 ℃. Also indicated is the BSG transmittance, ~90% between 350 nm and 800 nm. Unlike previous measurements in this thesis, the background is air, rather than an uncharged dielectric. Before annealing, the transmittance of the Al transmittance remained relatively low, around 60% from 350-800 nm. After annealing at 400 ℃ for 5 minutes, the transmittance increased to 80-88%, within ~5-2% absolute of the BSG. Subsequent annealing did not further increase the transmittance. This high transmittance close to that of the borosilicate glass provides further evidence that a dielectric layer has been formed through the complete oxidation of aluminium and indicates its suitability as an ICD for TCE applications.

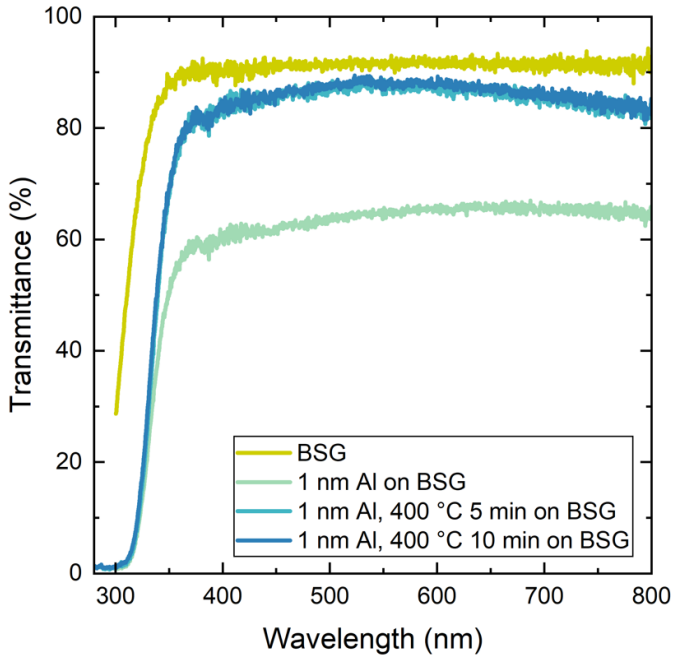

Figure 7.12: Transmittance of BSG with thin Al layer evaporated on the surface, then subject to various annealing conditions

Ellipsometry was used to measure the thickness of the oxidised films following a high-temperature anneal. Figure 7.13 depicts the oxidised thickness of films with initial Al thickness 1 nm. The mean thickness of the "1 nm" Al when oxidised increased to ~11.04±0.59 nm. This increase is expected as the initial Al seed layer incorporates additional oxygen molecules from the atmosphere to form the AlO_x, increasing its volume on the surface of the silicon. The spread of thicknesses from ~7 to 15 nm is indicative of poor thickness control when using a shutter in a thermal evaporator system. These results confirm the formation of a thick AlO_x layer on silicon following a 400℃ anneal for 10 minutes of a "1 nm" thermally evaporated Al layer.

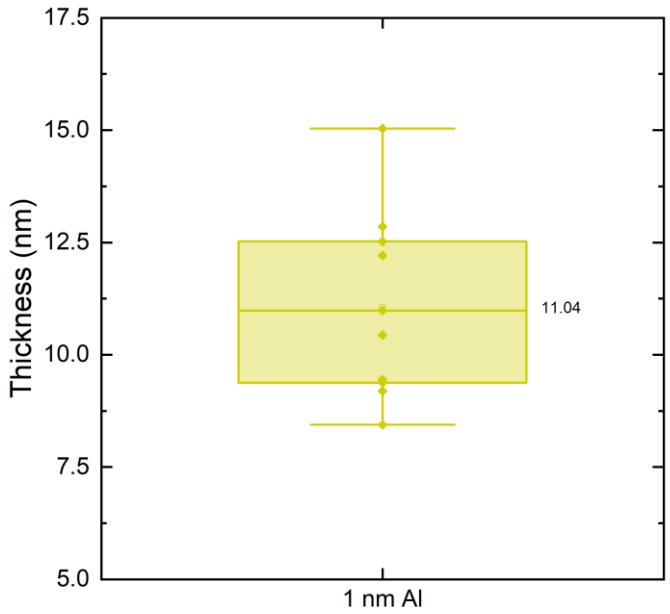

Figure 7.13: Ellipsometry-measured thickness of thermally-evaporated Al films after annealing to form AlO_x. The "1 nm" indicates the initial thickness measured using a piezoelectric crystal monitor, y-axis indicates thickness after annealing.

7.11 Charge Storage in Thermally-Evaporated AlO_x

KP was used to measure the ability of the thermally evaporated AlO_x layer to store charge. A bare silicon substrate was first prepared by HF-etching. A thin Al layer was deposited on the silicon in vacuum, and oxidised using a 400℃ anneal for 10 minutes. Figure 7.14 (a) depicts the measured CPD of a layer subject to positive and negative corona charge over time. After 4 minutes of negative charging, the CPD increases in magnitude to ~400 mV. Using an assumed

dielectric constant of AlO_x of 8-10 based on literature values [385], [386], and the ellipsometry thickness of 11.04 nm, this CPD corresponds to a charge concentration of ~4-5×10^{12} /cm^2. On application of positive charge, this can be reversed until a CPD of ~-455 mV is achieved, also corresponding to 4-5×10^{12} /cm^2. This value is relatively low, and may not be sufficient to induce doping in graphene. Additionally, as Figure 7.14 (b) demonstrates, charge stability on the AlO_x can be relatively poor, with the CPD reducing in magnitude by >100 mV in 20 minutes in both cases of positively and negatively charged devices. This makes it difficult to use such a film to dope graphene reliably.

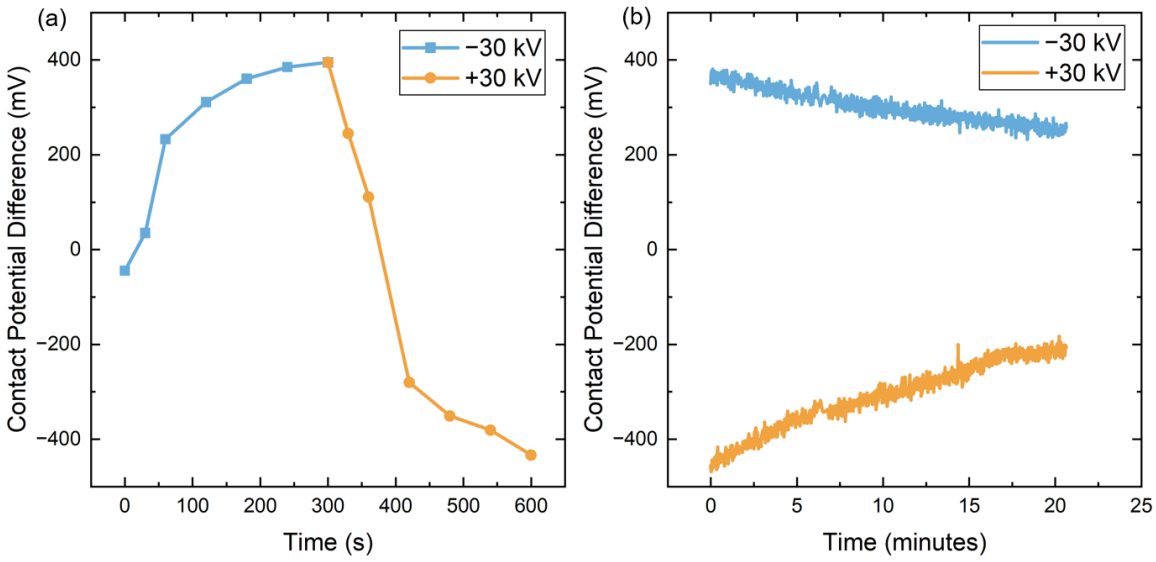

Figure 7.14: (a) Contact potential difference with respect to time as a device is held under positive or negative corona charge.(b) Decay in contact potential difference as a device is left in air after positive or negative charging.

There was significant variability in the maximum charge that could be deposited between individual films. This variation is related to differences Al deposition conditions, with its oxidation highly dependent on the variable conditions of the thermally evaporated Al layer. Variations in surface moisture, humidity and vacuum conditions during deposition can alter the surface chemistry and roughness and produce a surface more or less favourable to charge storage.

Figure 7.15 (a) and (b) depict a CPD map of the champion AlO_x sample, after positive or negative charging for 5 minutes. The gradient tracking function was used to ensure a constant tip-sample distance and control for variabilities in surface height. The peak CPD measured in the negative case was 0.984 V, corresponding to 7×10^{12} /cm^2. In the positive case the peak CPD was −1.5 V, corresponding to 6.7×10^{12} /cm2. These values of charge are sufficient to achieve doping in graphene.

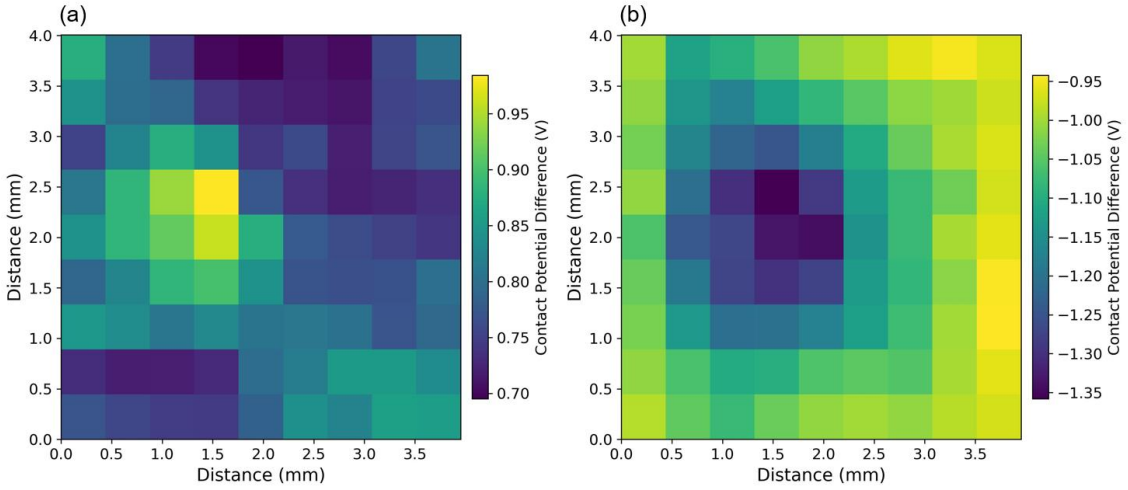

Figure 7.15: Contact potential difference maps of an AlO_x layer grown on silicon and subject to (a) Negative corona charge for x minutes, and (b) positive corona charge for 5 minutes.

There is significant variability in the surface, which may relate to charge decay during measurement, and/or differences in surface roughness contributing to differences in charge. To verify and determine the degree of surface differences such as variations in oxidation of the AlO_x surface, further characterisation is likely needed, such as via atomic force microscopy and x-ray photoelectron spectroscopy.

7.12 **Thermally-Evaporated AlO_x Formation on Graphene**

After determining the sufficient conditions to develop a highly-charged AlO_x layer on silicon, these layers were formed on graphene devices. Figure 7.16 depicts the AlO_x/graphene device fabrication process. First, a graphene device was fabricated in the vdP structure with Al contacts. A brass mask was placed to cover the Al contacts but leave the graphene layer

exposed for Al deposition. An ultrathin Al layer of ~1 nm was deposited on the graphene layer via thermal evaporation at $<10^{-6}$ mbar. Subsequently, silver electrodag contacts were painted over the original Al electrodes to ensure good contact to graphene after annealing. The device was held at 400℃ for ~10 minutes and its R_{sheet} measured at intervals until the R_{sheet} returned close to its original value before Al deposition.

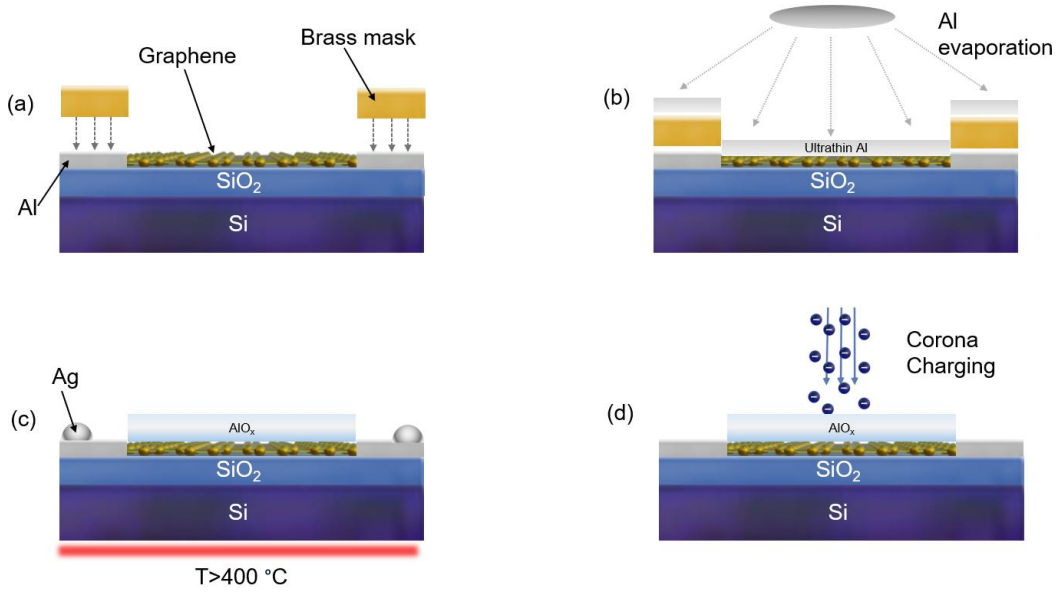

Figure 7.16: Thermally-evaporated AlO_x layer fabrication and charging. (a) Brass mask affixed to a graphene device. (b) Al evaporation. (c) High-temperature annealing in air. (d) Corona charge deposition.

To verify oxide formation on graphene, its R_{sheet} was recorded before and after deposition, and annealing. Figure 7.17 depicts the variation in vdP R_{sheet} as the Al layer is deposited and annealed. 1 Al deposition reduces the R_{sheet} from an initial ~1300 Ω/□ to ~50 Ω/□. After ~6 minutes of annealing at 400℃, the R_{sheet} returns to close to its initial value at ~1000 Ω/□. The plateau in R_{sheet} after subsequent annealing up to 10 minutes suggests that the Al has oxidised to form AlO_x. Ellipsometry measurements were used to verify that the AlO_x grown on graphene also had a thickness of ~10 nm after annealing.

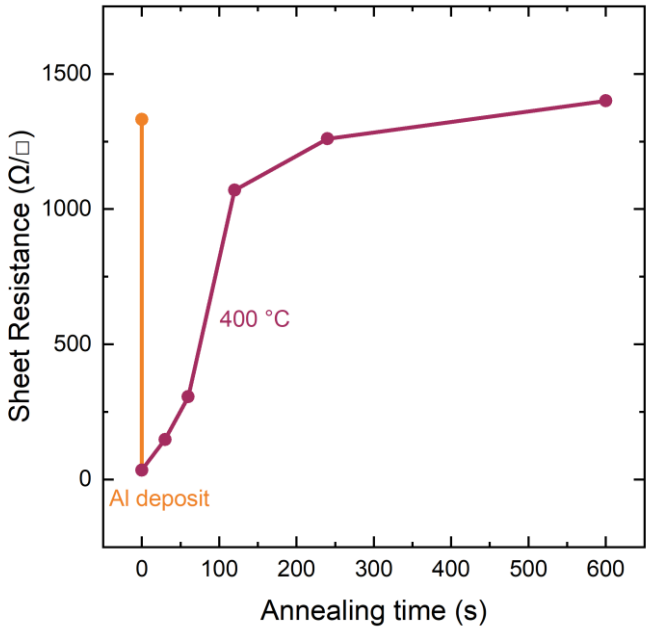

Figure 7.17: Al/Graphene sheet resistance over annealing time at 400°C. The initial aluminium thickness was recorded as 1 nm, measured using a piezoelectric crystal monitor during thermal evaporation. The final thickness after annealing was measured by ellipsometry to be ~10 nm.

7.13 Electrical Characterisation of Graphene Doped using Charged AlO_x

After the formation of an AlO_x dielectric layer on graphene, its electrical properties were measured as it was subjected to corona charge. Figure 7.18 (a) depicts the measurement set-up, and (b), (c) and (d) show the change in R_{sheet}, carrier concentration and mobility, respectively, as a device is held under negative charge. There is a clear reduction in R_{sheet} on application of negative charge, from ~1400 Ω/□ to ~860 Ω/□, a reduction by~40%. The carrier concentration increases significantly, from 3×10^{12} q/cm^2 to 4×10^{13} q/cm^2, significantly greater than predictions from KP measurement. This increase may be a non-physical artefact of the assumptions of the van der Pauw calculation breaking down in this circumstance. Precise measurement of carrier properties via other techniques such as field effect transistor devices is necessary to validate this result. Nevertheless, this will not impact the general trend, which is of significantly increased carrier concentration due to the negative bias.

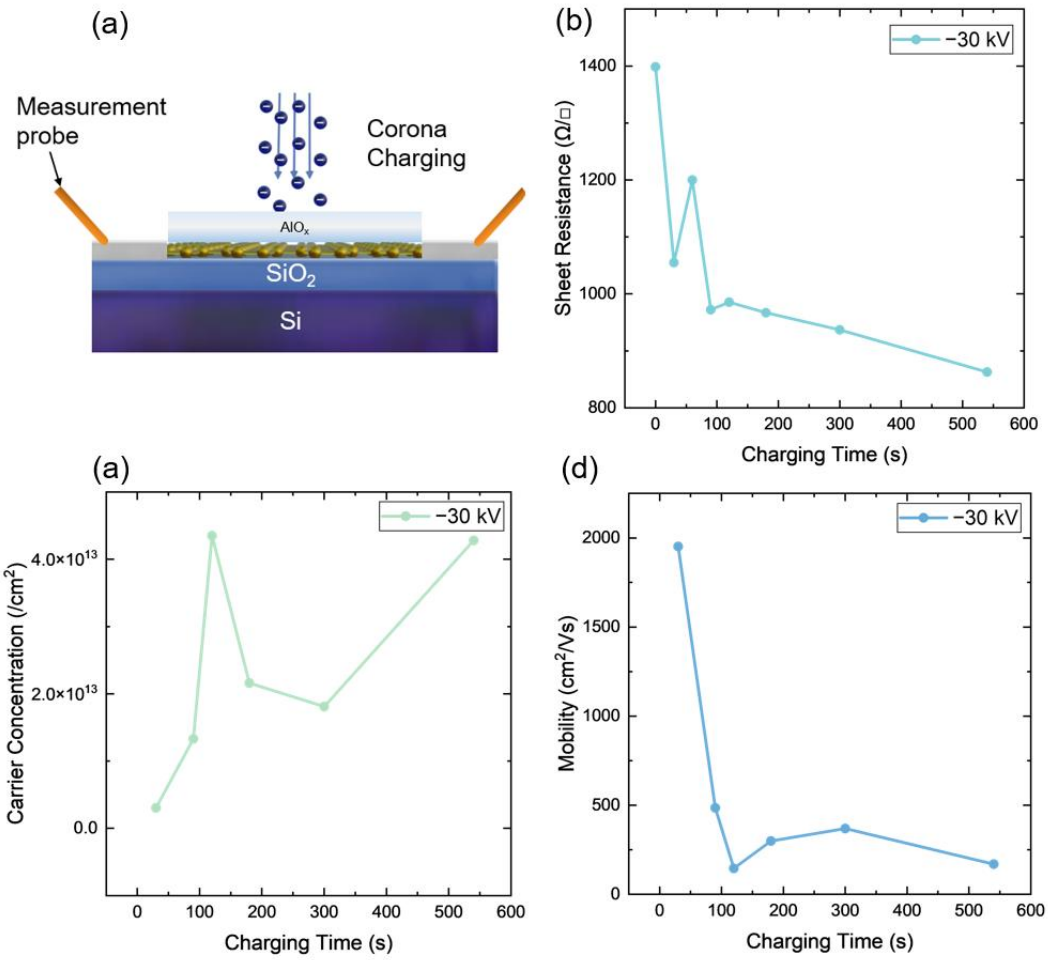

Figure 7.18: (a) Measurement set-up for electrical characterisation. (b) Sheet resistance, (c) carrier concentration, and (d) mobility of an AlO_x/graphene device as it is subject to negative charge.

Figure 7.19 depicts the variation in R_{sheet} as a device is positively charged. When subjected to positive charge, the R_{sheet} increased slightly, which may relate to a reduction in the p-type doping effect. However, subsequent charging over time did not induce n-doping.

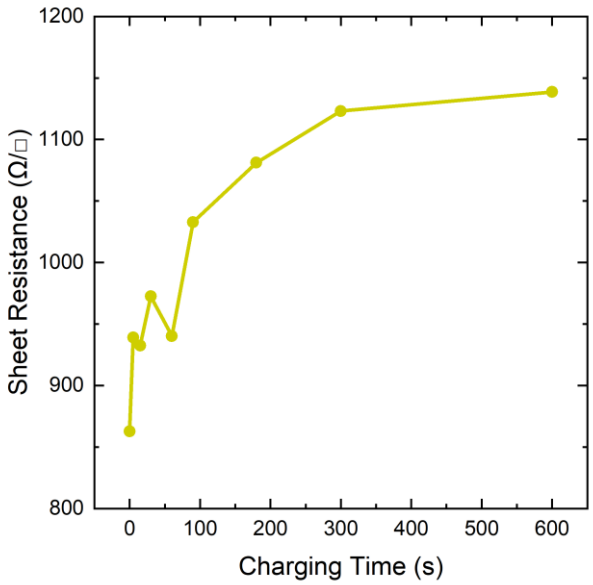

Figure 7.19: Sheet resistance versus time as a AlO_x/graphene device is subject to positive corona charge.

As in the case of PMMA, positive charging of the AlO_x failed to substantially impact the carrier properties of the graphene, while negative charging facilitated a 50% reduction in R_{sheet} and a 4× increase in carrier concentration. In this case, it is possible that bulk negative intrinsic charges in the AlO_x layer are shielding the surface corona charge from impacting the graphene. In the negative case, these charges might work in tandem to contribute to p-doping of the graphene. Further analysis of the surface and oxidation states of the thermally evaporated AlO_x layer is recommended. The insights from such an analysis could reveal whether, with improved dielectric deposition, such as via ALD, the charge screening could be prevented and n-doping induced using this method.

7.14 **Raman Spectroscopy**

Finally, the doping induced via the negatively charged AlO_x on graphene was measured via Raman spectroscopy. Figure 7.20 (a) and (b) depict the G and 2D peaks of a negatively charged AlO_x/graphene device measured within 30 minutes of charging. As in the case of PMMA, a low acquisition time measurement, with low power was used to minimise the impact of the

laser on the stability of the corona charge on the surface of the device. The subtle blueshift of both G and D peaks indicate that p-doping has been achieved using this technique.

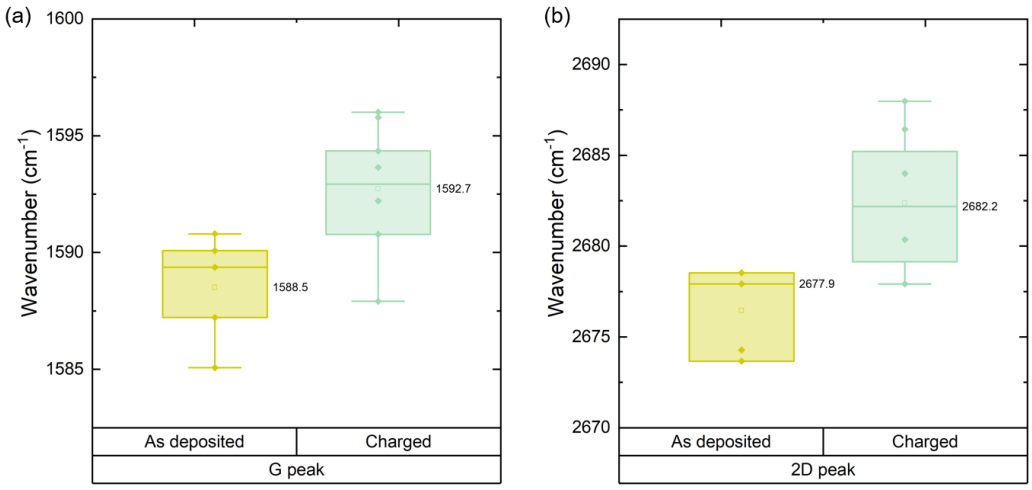

Figure 7.20: Raman G (a) and 2D (b) peak of graphene encapsulated with a negatively charged AlO_x layer deposited via thermal evaporation.

7.15 **Discussion and Conclusions**

The development of charged PMMA, and a thermally evaporated AlO_x layer, for ICD-doping of graphene were explored in this Chapter. The electrical and optical properties of graphene before and after corona charge deposition on an interfacing encapsulant dielectric were studied, providing new insights into the stability of charge on these dielectrics.

Successful p-doping was demonstrated through the deposition of corona charge on PMMA interfaced with graphene. In this case, R_{sheet} values as low as 328 Ω/□ were achieved, with the capability of reversal through the deposition of positive charge. Due to PMMA's widespread use in graphene wet transfer, charge deposition on PMMA is a low-cost, rapid method to manipulate the carrier concentration in graphene without using an external field. However, the stability of positive corona charge on this layer is relatively poor, limiting this method to p-doping of graphene. Advances in an understanding of PMMA polymer chemistry after charge deposition and the development of approaches to induce surface functionalisation are expected

to increase charge stability, which may prove beneficial to applications such as flexible electronics.

A facile method to encapsulate ultrathin AlO_x layers on graphene was also developed in this work. By depositing negative charge on the AlO_x, n-doping was achieved in graphene, with R_{sheet} reductions of >40%. AlO_x-doped graphene likely shows the most applicability to PV devices. At present, the high-temperature annealing process to form the AlO_x layer is prohibitive, but this can be overcome through the use of optimised ALD deposition which has been developed elsewhere [365]. It is expected that an even higher, more uniform concentration of charge with better stability can be achieved on such an ALD-deposited dielectric. This would provide the conditions necessary to approach R_{sheet} <150 Ω/□, to match those achieved in vacuum in Chapter 4.

Beyond optoelectronics, the encapsulation of graphene using ICDs in this way, with the capability to be reversed and precisely tailored also offers opportunities to develop a "dual-gated" ICD [354], [387], [388]. A dual-gated ICD could involve a BSG or K^+:SiO_2/Si substrate, and AlO_x or PMMA top-gate. Such a configuration would facilitate the study of materials properties in extremely high carrier density environments >10^{14}/cm^2 [389].

A primary focus of this thesis has been the exploration of ICD-doping approaches with potential processing compatibility for photovoltaic cells. However, as of yet, the specific property targets required to achieve high efficiency in tandems have been left out of the discussion. In other words, how low must the target R_{sheet} be to be competitive with, or even surpass the performance of state-of-art TCOs in tandems? Calculating these values will allow a benchmark to be set for what charge concentrations are needed in ICDs for a doped graphene layer interfacing with it to compete with conventional TCOs in photovoltaic devices.

Chapter 8

Modelling and Feasibility of Graphene as a TCE for Perovskite/Silicon Tandem Solar Cells

8.1 **Introduction**

In this thesis, several novel graphene doping techniques were demonstrated using ICDs, and their processing compatibility for tandem cells was discussed. The lowest R_{sheet} demonstrated in this work was achieved via K^+ migration in SiO_2, at ~117.9 Ω/□. This is among the lowest achieved R_{sheet} values demonstrated in large-area CVD-grown graphene monolayers reported in the literature [121], [175], [269], [298], [302]. But this value still falls short of the R_{sheet} of conventional TCO layers such as ITO, IZO and FTO, which can be ~10 Ω/□ [98], [390], [391], [392], [393], [394], [395]. However, the transmittance of graphene is uniquely broadband, offering potential optical advantages over TCOs. In Chapters 4, 6, and 7, it was shown that ICD-doping of graphene does not impact its transmittance. As the doping is induced by a uniform electric field rather than by a chemical species adsorbed on the surface, there is no significant photon scattering. Additionally, its high mobility ensures that the increased carriers induced in it do not contribute substantially to plasmonic scattering. Therefore, it is not expected that ICD-doped graphene requires an R_{sheet} as low as that of typical TCOs to be competitive for TCEs in tandem cells.

Yet, it is not clear how low the R_{sheet} of a graphene layer will need to be to minimise losses. To evaluate the R_{sheet} required for an ICD-doped graphene TCE to match the performance of TCO film in devices, the trade-off between transmittance (T%) and R_{sheet} must be considered.

The trade-off between T% and R_{sheet} is often described in terms of figures of merit (FOM). Commonly cited FOMs include Gordon et al.'s electrical conductivity to absorption coefficient ratio, σ/α [54], [396], De et al.'s electrical to optical conductivity ratio, $\frac{\sigma}{\sigma_{op}}$ [98], and Haacke's

exponentiated transmittance to R_{sheet} ratio, $\frac{T^x}{R_{sheet}}$ [397]. Although convenient for approximate comparisons, these FOMs have limitations for evaluating high-performing photovoltaic devices. De et al.'s $\frac{\sigma}{\sigma_{op}}$ FOM suffers from unphysical biases for R_{sheet} < 100 Ω/□, as small variations in R_{sheet} can disproportionately inflate the FOM, leading to unrealistic performance expectations [49]. Haacke's $\frac{T^x}{R_{sheet}}$ requires the choice of arbitrary exponents for *x* to determine the preferred transmittance % [49]. Moreover, the thickness dependence of Haacke's $\frac{T^x}{R_{sheet}}$ often favours thicker, conductive films at the expense of transparency, making comparisons difficult [54]. For this reason, a conductive, yet relatively opaque TCE might have a high FOM.

Existing FOMs also do not account for several relevant properties, including mechanical stability, thermal and chemical stability, band gap and mobility [54], [98], [396]. Over ten alternative FOMs have been proposed to incorporate several of these additional properties [94], [396], yet are limited in providing a meaningful comparison for TCE application in tandem cells. This Chapter explores a method to model TCE performance in two-terminal tandem cells, emphasising efficiency potential to compare the benefits of ICD-doped graphene vs conventional TCOs.

8.2 Modelling TCEs for Perovskite/Silicon Tandem Cells

I propose a model of TCE-dependent tandem cell performance that follows the approach published by Anand et al [398]. In this model, the theoretical performance of the cell is calculated for variations in the transmittance and R_{sheet} of the TCE. This allows a comparison between the theoretical efficiency achieved in tandem cells when incorporating different TCEs. Anand et al's model uses a detailed balance calculation to obtain the maximum power conversion efficiency of a single-junction solar cell with a given band gap, designed to absorb the AM1.5G spectrum. In this work, the detailed balance calculation is extended to account for

the absorption and collection in a two-terminal monolithic tandem device with silicon as the bottom cell.

Figure 8.1 illustrates the unit domain used for the calculation, where two possible architectures are proposed: Figure 8.1 (a) and (b) depict the side views of the two configurations, while Figure 8.1 (c) presents the top view common to both structures. In the first architecture, Figure 8.1 (a), a front TCE is placed on the surface of the perovskite absorber, collecting current and driving it to localised front metal contacts. The current flow is assumed to be entirely vertical due to the presence of a suitable optoelectronic link or an interconnection layer. This is often referred to as the recombination layer, but here, it is generalised to a layer fulfilling both conduction and optical coupling functions. For vertical current flow in the silicon absorber, a second TCE must be present at the rear surface as is typical in SHJ technology. In the second architecture, Figure 8.1 (b), surface doping in the silicon sub-cell enables charge carriers to flow to local contacts positioned at both the front and rear surfaces. This design reflects the use of silicon bottom cells such as a passivated emitter and rear cell (PERC) or a tunnelling oxide passivating contact (TOPCon) cell. Here, the rear TCE is positioned on top of the optoelectronic link, ensuring that current collected in the perovskite sub-cell is conducted to the local contact at the front of the silicon sub-cell. Such a design was originally used to produce perovskite/silicon tandem cells [52], making it highly relevant to the current large-scale production of solar PV.

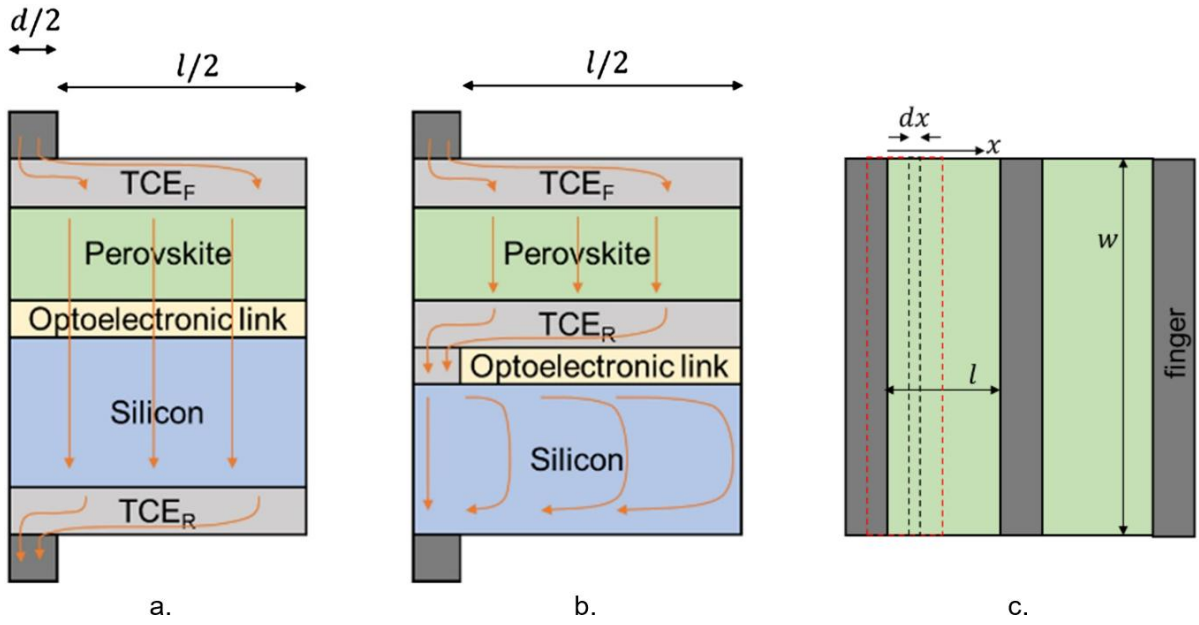

Figure 8.1: Unit domains of two-terminal tandem solar cells with d representing the finger width and l the finger pitch. (a) Lateral view of two-terminal tandem with front and rear transparent conducting electrode (TCE) for bifacial configuration. (b) Lateral view of two-terminal tandem solar cell with front TCE and TCE between sub-cells. (c) Top view of a two-terminal tandem, with w representing the cell width and dx an infinitesimal change in the x direction (perpendicular to the cell width w).

8.3 Modelling Series Resistance Losses in TCEs in Tandem Cells

In both cases of Figure 8.1 (a) and Figure 8.1 (b), each TCE accounts for one additional series resistance such that the effective series resistance must include two contributions. This can be assumed as the resistive power loss due to the lateral current flow through the TCE at one side of the cell is given by:

$$dP = I^2 dR \quad (8.1)$$

Where *dR* is the resistance contributed by an infinitesimal *dx* section of the TCE, as indicated in Figure 8.1 (c), and given by:

$$dR = R_{sheet}^{TCE} \cdot \frac{dx}{w} \quad (8.2)$$

The lateral current flow I is maximum at the midpoint between two fingers, $x = l/2$, and increases linearly to zero just underneath the contact finger, where only the contact resistance contributes towards the total series resistance. It is calculated as:

$$I = J \cdot w \cdot x \ (8.3)$$

Where J is the current density of the area of interest in the device, labelled with a red dotted-line box in Figure 8.1 (c), and equivalent to an area = $w \cdot l/2$.

The total power loss can be found by integrating the incremental resistance losses from $x = 0$ to $x = l/2$, following:

$$P_{loss} = \int I^2 dR = \int_0^{\frac{l}{2}} (J \cdot w \cdot x)^2 R_{sheet}^{TCE} \cdot \frac{dx}{w}$$

$$= \frac{l^3}{24} J^2 w R_{sheet}^{TCE} = \frac{l^3}{24} \left(\frac{I}{w \cdot l/2}\right)^2 w R_{sheet}^{TCE} = \frac{I^2 l}{6w} R_{sheet}^{TCE} = I^2 \left(\frac{R_{sheet}^{TCE} l}{6w}\right) \ (8.4)$$

The effective series resistance loss contributed by the TCE resistivity is hence:

$$R_{s0} = \frac{R_{sheet}^{TCE} l}{6w} \ (8.5)$$

The TCE is present at the front and rear and hence it will contribute twice as much series resistance:

$$R_s = 2 \frac{R_{sheet}^{TCE} l}{6w} \ (8.6)$$

Following Anand's procedure, it is possible to lump the Rs originating from the TCE to the ideal diode model, describing the operation of the entire solar cell [398]. In this case, this is a two-diode system as illustrated in Figure 8.2, and leads to a system of three equations describing both top and bottom cells as follows:

$$I = I_{0P}\left(e^{V_p/V_t} - 1\right) - I_{scP} \ (8.7)$$

$$I = I_{0Si}\left(e^{V_{Si}/V_t} - 1\right) - I_{scSi} \quad (8.8)$$

$$V_{Cell} = V_{Si} + V_P + R_s I \quad (8.9)$$

With the thermal voltage given by $V_t = kT/q$, q is the elementary charge, I_0 is the saturation current of each sub-cell, and I_{sc} is the short circuit current of each sub-cell.

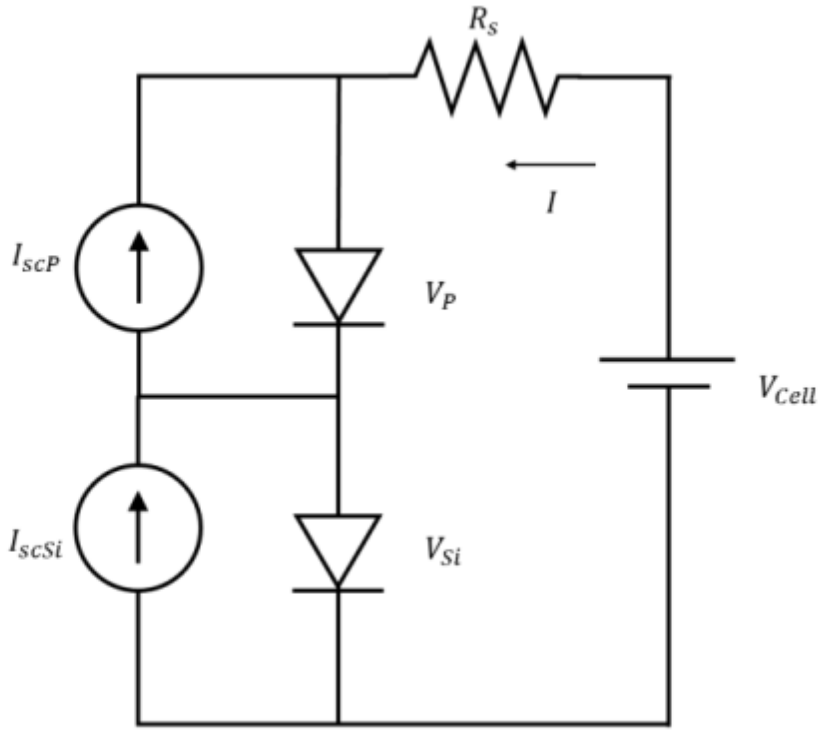

Figure 8.2: Ideal diode model of a 2-terminal tandem solar cell, with perovskite and silicon subcells connected in series. V_P and V_{Si} account for the voltage of the perovskite and silicon cells respectively, while I_{scP} and I_{scSi} account for the short-circuit current of the perovskite and silicon cells respectively.

To evaluate the maximum power output of the modelled tandem cells, the system of equations describing its operation is solved iteratively using a nonlinear system solver. In this work, a MATLAB code was developed and used to implement the trust-region dogleg algorithm to solve this system of equations [399]. The MATLAB code developed can be found in the Appendix, Section a.i. The iterative solutions are calculated for over range of cell voltages (V_{Cell}) and the maximum power point (V_m, I_m) is identified, where $P_{max} = V_m \times I_m$.

The short circuit and dark saturation currents from each cell are obtained by using the detailed balance limit as proposed by Shockley and Queisser, which relies on four assumptions [400], [401].:

1. Only the photons with energy greater than the bandgap are absorbed.
2. Each photon with energy greater than the band gap generates only one electron-hole pair.
3. The system is thermal equilibration with the surroundings and only radiative recombination takes place.
4. No losses occur from ohmic transport inside of the cell and contacts, with the contacts being perfectly selective.

The short circuit I_{sc} for each sub- currents cell are given by the proportion of photons that they absorb. For the perovskite top cell:

$$I_{scP} = w \cdot l/2.q. \int_0^{\lambda_P} AM1.5G(\lambda) \times T_{TCEf}(\lambda) d\lambda \quad (8.10)$$

Here, λ_P is the largest wavelength that can be absorbed by the perovskite cell, and T_{TCEf} is the spectral transmittance of the front TCE. AM1.5G(λ) is the wavelength-dependent Air Mass 1.5G spectral photon flux density, calculated from the spectral irradiance reported on standard ASTM G173-03 [402], divided by the energy of photons at each wavelength. Similarly, for the silicon bottom cell:

$$I_{scSi} = w.l/2.q. \int_{\lambda_P}^{\lambda_{Si}} AM1.5G(\lambda) \times T_{TCEf+Pero}(\lambda) d\lambda \quad (8.11)$$

where λ_{Si} is the largest wavelength that can be absorbed by the silicon sub-cell, and $T_{TCEf+Pero}$ is the spectral transmittance of the combined front TCE and perovskite top cell.

The dark saturation current is obtained from the blackbody radiation photon flux density at T = 300 K (BB300K). For the perovskite sub-cell, it is calculated as:

$$I_{0P} = w.l/2.q.\int_0^{\lambda_P} \mathrm{BB300K}(\lambda) * T_{TCEf}(\lambda)d\lambda \quad (8.12)$$

The blackbody radiation photon flux density at T = 300 K is given by Planck's law as:

$$\mathrm{BB300K}(\lambda) = \frac{2\pi c}{\lambda^4}\frac{1}{e^{\frac{hc}{\lambda kT}} - 1} \quad (8.13)$$

And finally, for the silicon bottom cell, the dark saturation current is similarly calculated as:

$$I_{0Si} = w.\frac{l}{2}.q.\int_0^{\lambda_{Si}} \mathrm{BB300K}(\lambda) * T_{TCEf+Pero}(\lambda)d\lambda \quad (8.14)$$

This approach provides a detailed understanding of how both short circuit currents and dark saturation currents depend on the spectral properties of the TCE and the sub-cell layers.

The current corresponding to each voltage is solved using the coupled nonlinear equations (8.7), (8.8) and (8.9). The output power density P(V) (in W/cm^2) at each voltage point can then be determined iteratively using:

$$P(V) = \frac{V_{cell} \cdot I(V)}{w \cdot \frac{l}{2}} \quad (8.15)$$

To determine the maximum power point, the voltage is swept more finely around the initially detected power peak. The calculated maximum output power is then stored as P_{max} and is used to calculate the efficiency (η) following:

$$\eta = \frac{P_{max}}{P_{in}} \quad (8.16)$$

where P_{in} = 0.1 W/cm^2 is the incident light on the cell. This calculation is looped across a range of TCE R_{sheet} and transmittance values to produce a colourmap which is used to visualise the target TCE properties to maximise efficiency (η).

8.4 Modelling TCE Weighted Average Transmittance

Optically, the architecture in Figure 8.1 (a) is more favourable as front light only passes through one TCE, minimising optical losses. Accordingly, here, the ultimate theoretical efficiency has been modelled assuming the case of Figure 8.1 (a). This is used to determine the R_{sheet} required for a graphene TCE with broadband transmittance to negligibly contribute to electrical losses when implemented in such tandem cell architectures.

The transmittance for each TCE was calculated using *OPAL2,* an optical simulation software [403], [404]. In this work, the optical path was calculated assuming normal incidence of light from the AM1.5G spectrum impinging onto a planar, multilayer stack. *OPAL2* uses an incoherent optical model: at each interface it applies the intensity Fresnel equations to calculate reflection and transmission (no phase is tracked), and within each layer it uses the Beer–Lambert law to calculate absorption. Data for *n* and *k* values were obtained from the literature. Light propagation is treated via efficient ray-tracing that decouples Fresnel losses from the path calculation. The modelled stack used a caesium–formamidinium-based mixed-halide perovskite with band gap 1.73 eV [405]. It was assumed that any charge-transport or buffer layers in the cell contributed negligibly to overall optical loss.

Figure 8.3 (a) and (b) depict the optical paths modelled in this Chapter. To better improve light coupling with the perovskite, a MgF_x layer (*n*~1.38) was placed at the front of the device stack, data ref. [406]. An optimal MgF_x thickness of 80 nm for both structures were calculated using *OPAL2*. For TCO-based devices, the TCO (*n*~1.8-2.0) offers good refractive index matching to the perovskite (*n~2.4*). To prevent strong reflection at the graphene/perovskite interface, a

SiN_x layer (n~2) was inserted at the graphene and MgF_x interface. An optimal SiN_x thickness of 30 nm was calculated using *OPAL2*. The effect on total transmittance on the stack without these anti-reflective coatings, and the effect of a glass encapsulant layer is included is discussed and modelled in the Appendix, Section a.iii.

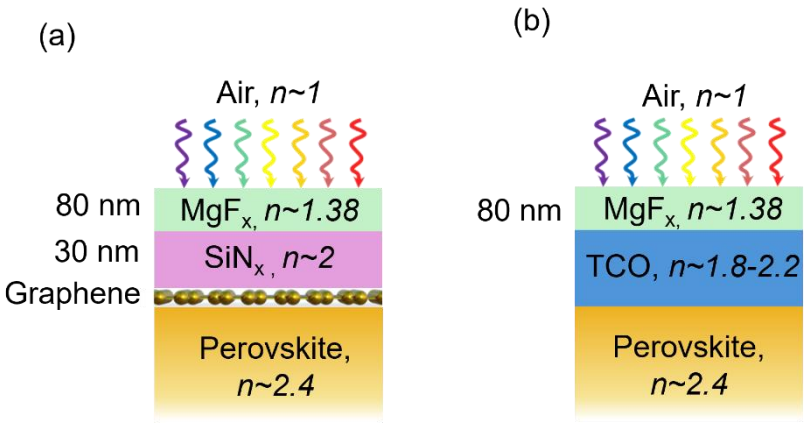

Figure 8.3: (a) Schematic of the modelled MgF_x/SiN_x/graphene/perovskite optical stack. (b) Schematic of the modelled MgF_x/TCO/perovskite stack.

TCO transmittance was calculated using refractive index n and extinction coefficient k data obtained from the literature for heavily and lightly-doped ITO [407], IZO [72], tungsten-doped indium oxide (IWO) [408], IO:H [409] and IZrO [55]. The n and k data were then fed into *OPAL2* to generate the transmittance data from 280 to 1100 nm for thicknesses 20 nm, 40 nm, 80 nm, 100 nm, and 150 nm. The use of n and k data only ensures that the additional contribution from the glass substrate, usually present in "TCO transmittance" measurements is not included in the calculations.

As graphene has atomic thickness, determining its n and k values is non-trivial, and it is difficult to obtain accurately using conventional ellipsometry, instead usually requiring spectroscopic ellipsometry [273]. For simulation, the n and k values of undoped CVD graphene were obtained from the literature [273]. In the ICD-doping techniques demonstrated in this thesis, the measured transmittance of the graphene did not change significantly. It is therefore assumed

that the literature values for undoped CVD graphene are a good representation of the *n* and *k* values of the graphene measured in this work.

Finally, the weighted averaged transmittance (WAT) was calculated using the spectral light intensity transmitted (T_x) through the simulated device stack as:

$$WAT = \frac{\int_0^{\lambda_{Si}} T_x(\lambda) \times AM1.5G(\lambda) d\lambda}{\int_0^{\lambda_{Si}} AM1.5G(\lambda) d\lambda} \quad (8.15)$$

where $T_x(\lambda)$ is the spectral light intensity transmitted through the stack, with AM1.5G data extracted from reference [29]. This enabled the definition of a single numerical "weighted average transmittance" value to describe the transmittance through the TCE that is relevant to the entire solar spectrum captured in a perovskite/silicon tandem. The code used to calculate the WAT from the spectral light intensity transmitted through the simulated device stack is given in the Appendix, Section a.ii.

8.5 TCE Weighted-Average Transmittance vs Sheet Resistance for Optimised Tandem Cell Performance

Figure 8.4Figure 8.4 shows the results of the model when applied to several TCE materials. Here, a contour map of the upper-efficiency limit for a two-terminal perovskite/silicon tandem is illustrated as a function of uniform spectral transmittance (280–1100 nm), using a 1 Sun weighted averaging to account for wavelength dependence. The y-axis of Figure 8.4 is the 'Weighted Average Transmittance' (WAT) from 85%–100%, calculated using Equation 8.15.

Based on the model, the optimum thickness for films of ITO, IZO and IO:H is ≈40 nm. Although the R_{sheet} is higher relative to a typical 100 nm case, the WAT increases significantly at this thickness, resulting in an optimised balance of properties for high efficiency. In the modelled stack, the 40 nm IO:H and heavily-doped ITO result in efficiencies >41.5%, while

the 40 nm IZO and lightly-doped ITO both result in efficiencies ~41%. For ITO, IZO and IO:H thickness beyond 40 nm, the WAT decreases sharply, resulting in a reduction in efficiency.

IWO and IZrO films offer highest tandem efficiencies at ~80 nm, likely owing to their high mobility and wide band gap. For 80 nm IZrO films of 80 nm are the most promising TCO considered here, offering efficiencies ~42.5%.

Integrating graphene as a TCE with well-optimised SiN_x and MgF_x anti-reflective coatings enables a weighted average transmittance as high as 96.90%. This is achieved as reflection at the perovskite is minimised, and the main transmittance loss arises from graphene's fundamental 2.3% broadband absorption [98], [99], [123]. This results in a maximum efficiency potential of ~43.5% for $R_{sheet} \approx 118\ \Omega/\square$, as in the case of graphene/SiO_2:K^+/Si. The potential of other ICD-doping approaches presented in this work is also indicated in Figure 8.4, with BSG-doped graphene, and graphene doped with charged SiN_x/SiO_x or PMMA all exhibiting efficiency potential of >42%. Optimising the performance of ICD-doped graphene to achieve a predicted target $R_{sheet} \approx 50\ \Omega/\square$ could facilitate maximum power conversion efficiencies >45%, >1% higher than with state-of-the-art IZrO. Thus, if graphene could be harnessed as a TCE for two-terminal perovskite/silicon tandem cells, the strict requirement on R_{sheet} could be significantly relaxed to achieve enhanced efficiencies while also improving sustainability by eliminating indium-based TCOs from the cell.

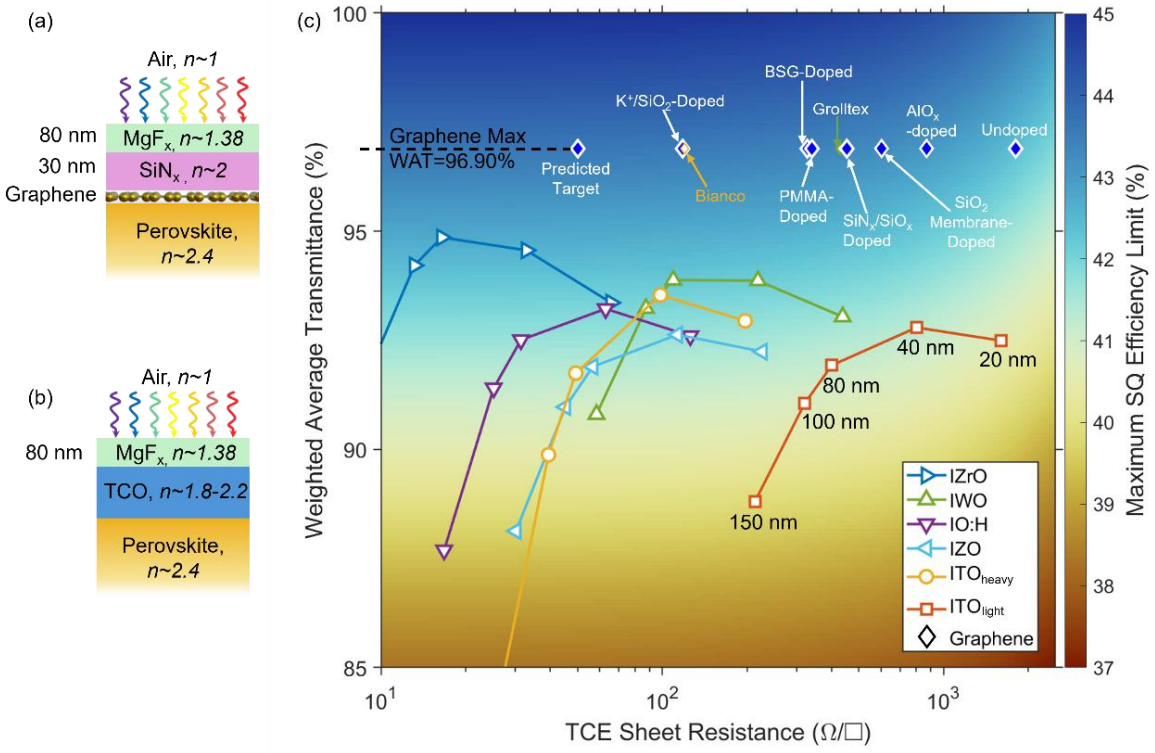

Figure 8.4: Modelling transparent conducting electrode (TCE) performance in a perovskite/silicon tandem cell structure. (a) Modelled front surface optical path for graphene and (b) transparent conducting oxide (TCO) based structures. (c) Simulated colour plot to visualise the maximum potential Shockley-Queisser (SQ) efficiency of a two-terminal perovskite/silicon tandem solar cell, assuming the only other source of loss beyond the SQ conditions arises from the TCEs used. The cell configuration consists of a perovskite cell of E_g = 1.73 eV on a silicon cell, with two TCEs, one front and one rear. The x-axis represents the TCE sheet resistance from 10 to 2500 Ω/□. The y-axis represents the weighted-average transmittance across the air-mass 1.5 global (AM1.5G) spectrum.

Several transparent conducting electrode materials are overlayed on the colour plot. In all cases, the transmittance data used excluded any glass substrate used, which might otherwise contribute a broadband ~10% loss due to reflection. MgF_x, SiN_x and perovskite n, k data was obtained from references: [405], [406], [410].

The diamonds represent chemical vapour deposition (CVD) fabricated graphene, with R_{sheet} values as reported in the literature and from this thesis. In these cases, the weight average transmittance was calculated using n, k data obtained from ref. [273]. In a real device, the thickness of the charge dielectric layer should also be optimised to minimise reflection at interfaces, but this contribution is not included here.

1. *"Grolltex" refers to the properties of an industrial supplier of large-area CVD graphene [411].*

2. *"Bianco" refers to one of the lowest R_{sheet} CVD graphene layers reported in the literature as of January 2025, with R_{sheet} = 120 Ω/□ [121].*

3. *The blue diamonds correspond to the champion samples of graphene doped using various ion-charged dielectrics in this thesis: SiO_2-membrane doped (Chapter 4), K^+/SiO_2-doped (Chapter 5), Borosilicate Glass (BSG) doped (Chapter 6), SiO_2/SiN_x-membrane doped (Chapter 6), PMMA-doped (Chapter 7) and AlO_x-doped graphene (Chapter 7). In the case of the K^+/SiO_2-doped graphene, transmittance was not measured as the doping was measured on an opaque Si substrate. However, as the doping mechanism is expected to be the equivalent as that of BSG-glass doped, it is assumed the change in optical properties are approximately equivalent.*

The white markers correspond to transparent conducting oxides (TCOs) reported in the literature. The transmittance was calculated from the n and k values of the TCOs themselves, and so the effect of glass substrate absorption/reflection measurement is not included in the calculation. As transmittance can vary with TCO thickness, the n, and k values are used to calculate the expected transmittance at 20 nm, 40 nm, 80 nm, 100 nm, and 150 nm. For each TCO, at greater thicknesses, the

sheet resistance reduces. It is assumed the mobility and carrier concentration remain constant with thickness changes. The thicknesses are explicitly labelled for lightly-doped tin-doped indium oxide (ITO_{light}) only, but the same trend of increasing thickness and sheet resistance reduction occurs for the other TCOs. The TCOs included are:

1. *Tin-doped indium oxide light (ITO_{light}) corresponds to lightly doped ITO, $N = 6.5 \times 10^{19}\ cm^{-3}$ [407].*
2. *ITO_{heavy} corresponds to heavily doped ITO, $N = 6.1 \times 10^{20}\ cm^{-3}$ [407].*
3. *Hydrogen-doped indium oxide (IO:H), $N = 1.8 \times 10^{20}\ cm^{-3}$ [409].*
4. *Tungsten-doped indium oxide (IWO), $N = 2.1 \times 10^{20}\ cm^{-3}$ [408].*
5. *Indium-doped zinc oxide (IZO), $N = 2.3 \times 10^{20}\ cm^{-3}$ [72].*
6. *Zirconium-oxide doped indium oxide (IZrO), $N = 6.2 \times 10^{20}\ cm^{-3}$ [55].*

It is necessary to qualify several limitations of the model. Assuming the only sources of electrical loss are from the TCE can lead to misleading conclusions. Not accounted for in this model is the role of metal finger shading, which is closely linked to the optimisation of TCE electrical and optical properties [45], [412]. In practical devices, metal fingers are essential for the collection of charge carriers that have been transported to them via the TCE. As metal contacts are opaque, they contribute shading losses, reflecting light away that would otherwise be absorbed in the cell. The extent of these shading losses depends on the finger width, pitch and the pattern coverage, which is directly related to the length of the unit cell *l*, as defined in the model set-up. Reducing metal grid coverage can allow for an increase in J_{sc} as more light can be absorbed in the cell [412]. However, the increased resistance of the metal grid would then necessitate a reduced R_{sheet} TCE to counterbalance the fill factor losses incurred [413]. But reducing TCE R_{sheet} typically involves increasing thickness, thereby reducing J_{sc}. Balancing these properties can become more challenging in large area devices, where there is an increased demand on the TCE, as the power loss due to TCE has been shown to increase quadratically with device dimension [413]. This fine-balance between TCE and metal grid properties should be considered for a more robust comparison between TCEs in working PV devices.

This model also assumes that the optical and electrical properties of the TCEs can be maintained when integrated in a solar cell device. The electrical and optical properties of the

graphene reported in this thesis and in the literature cited involve graphene deposition on a planar SiO_2, or a glass substrate. However, the mobility of graphene is known to be highly dependent on the properties of the substrate [111], [414]. The textured surface of a typical high-efficiency perovskite/silicon tandem device would likely be a significant impediment to achieving low R_{sheet} graphene in practical devices. Similarly, the TCO literature data used includes electrical and optical properties obtained when these films were deposited on glass. TCOs deposited directly on cells tend to have inferior optoelectronic properties due to the suboptimal, textured growth surface as compared to glass. The non-planar nature of high efficiency designs can contribute to increased carrier scattering, as well as changing the optimum thickness required to maximise light coupling in the absorber.

Crucially, in a practical device, the cell is usually encapsulated with a thick glass layer. The refractive index of this glass layer significantly alters the optics to achieve high efficiency, and can contribute to ~10% due to reflection loss. The contribution of such a layer to the overall tandem performance, is discussed in the Appendix, Section a.iii. In the case of a glass/SiN_x/graphene/perovskite stack, the WAT reduces to 91.55%. Despite this reduction, its performance remains competitive with state-of-the-art IZrO and IWO TCOs, demonstrating its promise to enable high-efficiency indium-free tandem solar cells across a range of device structures.

8.6 **Discussion and Conclusions**

This chapter provided a model to compare the performance of ICD-doped graphene with conventional TCOs in terms of performance in two-terminal perovskite/silicon tandem solar cells. Due to graphene's broadband transmittance >95%, the ICD-doped layers offered a greater efficiency potential compared to conventional TCOs. If the 117.9 Ω/□ achieved using K^+:SiO_2/Si substrates can be maintained in a tandem device, it may provide an efficiency potential >1%$_{abs}$ than the best performing conventional TCOs. Further reductions in R_{sheet}

resistance and efforts to maintain its high transmittance may yield efficiencies approaching the two-terminal limit of ~45%.

As described in Chapters 6 and 7, this work envisions the integration of such an ICD-graphene layer in a tandem cell, which involves replacing a conventional TCO, ARC, and/or protective buffer layer in a tandem cell stack with an ARC/ICD layer placed adjacent to a monolayer graphene sheet. Figure 8.5 (a) and Figure 8.5 (b) depict such potential tandem cell structures integrating ICD/graphene as all potential front and rear TCEs in the four-terminal and two-terminal configurations. In a four-terminal mechanically-stacked perovskite/silicon tandem, such an ICD-doped graphene layer could be positioned on the glass layer using corona-charged SiN_x ICDs, or migrating the ions in glass. On the rear of the perovskite or on either side of the silicon bottom cell, a charged AlO_x or PMMA-encapsulated graphene could be deposited. In a two-terminal monolithic perovskite/silicon tandem, the ICD-doped graphene layer could be placed at the top of the perovskite sub-cell and at the rear of the silicon bottom cell using charged encapsulating ICDs, with potential additional layer deposition to provide an anti-reflective benefit. In all cases, the graphene layer would be oriented to the absorber to collect charge carriers. Note that such a TCE could not replace the recombination layer in a two-terminal tandem, as the charged dielectric would impede vertical charge transport. Due to the compatibility of graphene with several HTL and ETL materials and the ambipolarity of the doping technique, ICD-doped graphene could be integrated into either p-i-n or n-i-p perovskite cell configuration, offering wide adaptability for different device processing constraints [180].

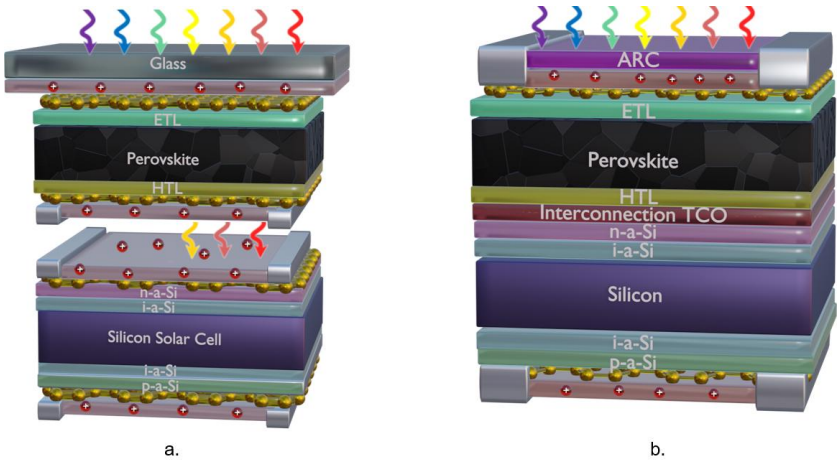

Figure 8.5: ICD-doped graphene integration in a. a four-terminal and b. two-terminal perovskite/silicon tandem cell structure.

Several technical limitations remain before such an electrode can be fabricated on industrial cells. This structure requires the metal electrode to contact the graphene layer through the dielectric. Penetrating the dielectric to contact the graphene layer, while maintaining a high charge concentration in the dielectric could prove challenging. Additionally, the production of CVD graphene is currently relatively slow compared with TCOs, typically requiring separate steps for production and transfer to the target device [415]. However, there has been some steady improvement: high-quality, large-area CVD graphene can now be transferred to flexible substrates via roll-to-roll techniques, at speeds up to 500 mm/min [125], [415], [416], and transferred to rigid substrates within 15 min [154]. The fabrication and charging of the dielectric layer would involve an additional step. Whereas engineering challenges remain for ICD-doped graphene TCEs to match the industrial maturity of TCOs, graphene fabrication and transfer benefits from being less energy intensive than fabricating indium-based TCOs and is inherently less expensive due to not requiring scarce materials [107]. The results from this Chapter indicate that ICD-doped graphene may offer substantial benefits to future tandem structures, providing a strong incentive to investigate further tandem-compatible ICD-layers which could provide a stable, high concentration of charge for graphene doping during device operation.

Chapter 9

Summary and Future Directions

9.1 **Overview**

Transparent conducting oxides (TCOs) used for simultaneous light transmission and lateral conduction have been a mainstay of optoelectronic devices for several decades [48], [54], [65]. However, with the recent advent of perovskite/silicon tandem solar cells, TCO performance requirements have become significantly more stringent. To minimise losses in tandem cells, TCOs must have a very wide band gap to enable efficient light absorption in both tandem sub-cells. However, it is challenging to achieve wide bandgap TCOs that maintain low sheet resistance, and also fit within the narrow processing constraints of tandem solar cell fabrication [45], [65]. As a result, high-efficiency perovskite/silicon tandem cells are currently limited to a handful of unsustainable indium-based TCOs: ITO, IZO and IZrO [45], [55], [395], [417], [418]. These layers severely restrict the scalability of perovskite/silicon tandems, motivating the search for new materials that can meet the restrictive materials properties and processing requirements for tandem cells.

Graphene offers many potential benefits as a TCE for tandem solar cells: it has a high broadband transmittance and high mobility, and it can be deposited gently on delicate perovskite layers without causing damage [99], [104], [419]. Yet, its high sheet resistance has limited its utility for commercial devices [45]. Current graphene doping techniques are typically based on the adsorption of chemical species on its surface, contributing to instability and reduced transmittance and mobility due to scattering [172], [175], [272], [420]. A key aim of this thesis was therefore to develop new techniques that can achieve stable graphene doping without significantly impacting transmittance or mobility.

This thesis developed a suite of techniques to dope graphene using ion-charged dielectrics (ICDs). In principle, such approaches can facilitate uniform doping via the electric field effect for minimised charge and photon scattering. There have been several reports exploring the use of charged ions in dielectrics to modulate the carrier properties of graphene [182], [302], [378], yet these approaches are limited, where stability over time, stability in air and the doping mechanism were insufficiently addressed.

The aim of this thesis was therefore to investigate novel approaches to fabricate ICDs for graphene doping, and to develop an improved understanding of the relationship between dielectric charge and graphene's electrical properties. These findings were then used to predict the performance of a graphene/ICD-based TCE in a tandem device. A summary of the major findings of this work is reviewed below.

9.2 Demonstrating ICD Graphene Doping Using Corona-Charged Dielectric Membranes

In Chapter 4, it was hypothesised that corona charge deposition on a free-standing dielectric substrate might be sufficient to tune the conductivity of graphene via the field effect. Corona charge was deposited on the rear of a suspended SiO_2 or SiN_x film, and the properties of an interfacing graphene layer were measured. It was observed that the R_{sheet} of graphene was reduced by >60% in just 3 minutes of electrostatic charging of the underlying dielectric film. Through Hall effect measurements, it was deduced that this reduction in R_{sheet} is due to the 3× increase in carrier concentration induced by the field effect from corona ions on the dielectric substrate. The doping was tuneable and readily reversible through the deposition of charge of the opposite polarity. Raman spectroscopy measurements confirmed that the doping induced by the negative charge was p-type, and the positive charge induced n-type doping. An in-house "micro-charger" was developed for in situ measurement of R_{sheet} as the device was subjected to corona charge. This showcased a clear trend: R_{sheet} decreased as the deposited charge

increased. This validated the hypothesis that corona-charge on a dielectric material induced mirror charge carriers in an interfacing graphene layer, facilitating p- and n-doping depending on the polarity of the deposited charge.

9.3 Utilising K^+ Ions inside SiO_2 for Record Low R_{sheet} Graphene

Chapter 5 investigated the use of K^+ ions migrated inside of SiO_2 to permanently dope a graphene layer interfacing with it. K^+ ions were introduced to a stable Si/SiO_2 interface via corona annealing as described in ref. [215]. The K^+ ions at a concentration $>10^{13}/cm^2$ were shown to be stable to the conditions of a graphene transfer, after which an applied electric field was used to migrate them towards a graphene electrode.

When the ions were migrated to the graphene after annealing in a vacuum, the R_{sheet} reduced significantly, from ~700 Ω/□, to 117.9 Ω/□ in the champion sample, with a clear linear relationship between applied bias and R_{sheet} observed. This is among the lowest R_{sheet} reported for >1 cm^2 CVD-transferred monolayer graphene on SiO_2 at room temperature [121], [175], [269], [298], [302], [421]. This approach was reproduced with samples with minimum R_{sheet} 129, 125.9, 134.5, and 145.0 Ω/□. FET measurements in a vacuum confirmed the n-doping of the graphene. However, when removed from the vacuum, the devices rapidly became p-doped due to atmospheric contamination. Measurements of devices re-annealed in vacuum after several days indicated that the K^+ remained highly stable at the graphene interface over time and at elevated temperatures.

It was noted that the energy required to migrate the ions to the graphene was significantly greater than the energy to migrate the ions to an Al electrode, with voltages an order of magnitude higher necessary to migrate a large concentration of ions to the graphene. This was postulated to result from a dipole-limiting effect induced by the high mobility of the carriers in graphene, which redistributes the charges at the graphene/SiO_2 interface. This electrostatic

environment may have contributed to the strong stability of the K^+ ions at the graphene/SiO_2 interface.

9.4 Investigating Dielectric Charging Methods on Transparent Glass Substrates

Chapter 6 involved the investigation of ICD generation on glass substrates, with the aim of developing a graphene/ICD/glass substrate for thin-film solar cell deposition. Building on the observed high stability of K^+ ions at the graphene/SiO_2 interface measured in Chapter 5, it was hypothesised that even highly mobile Na^+ ions in borosilicate glass could be stabilised at the graphene/dielectric interface. When an electric field was applied between the graphene and the rear electrode at an elevated temperature in a vacuum, ions could be migrated to and from the graphene/glass interface to induce n- and p-doping, respectively, as demonstrated previously in ref. [182]. However, this work, it was revealed that the Na^+ ions exhibit high stability at elevated temperatures when migrated to the graphene/glass interface. In contrast, when migrated to the rear Al, the doping effect quickly dissipated at high temperatures. This reveals a new insight into the electrostatics of the graphene/SiO_x interface when in the presence of mobile alkali ions. A minimum R_{sheet} of ~299 Ω/□ was achieved after Na^+ migration to the graphene layer, representing a reduction in R_{sheet} of ~50% compared to its initial value after annealing in vacuum. A more significant R_{sheet} reduction of >75% was enabled using a 57 nm PECVD SiO_x buffer layer between the graphene and the BSG. The presence of the SiO_x buffer layer was believed to improve doping uniformity and thus reduce scattering, enabling further reductions in R_{sheet}.

PECVD was then used to grow SiN_x and SiO_x/SiN_x layers, which are known to store charge stably in the dielectric bulk and at the SiO_x/SiN_x interfaces [332], [333], [334], [337], [338]. A high positive charge concentration $>10^{13}$ q/cm^2 in the bulk was measured using Kelvin Probe. Graphene on the charged substrates was moderately n-doped relative to graphene on an uncharged substrate, confirmed by four-point probe and Raman spectroscopy measurements.

However, the full effect of the charged substrate was likely masked as the electrical measurements were taken in air.

9.5 Demonstrating Top-Gated ICD-Doping on Graphene Encapsulated using Charged PMMA and AlO_x

Noticing that atmospheric contamination reduced the achievable R_{sheet} in air-exposed devices, Chapter 7 explored graphene doping using ICD encapsulant materials. A layer of either PMMA or AlO_x was used to encapsulate graphene and was then subjected to corona charge.

PMMA-coated graphene became p-doped on the application of negative charge. While the apparent poor stability of the positive charge prevented n-type behaviour, it effectively neutralised the negative corona charge previously deposited on its surface to reverse the p-type doping effect. This difference in doping stability was explained by the polar ester groups on the PMMA chain, which can more stably hold negative trapped charges [376].

A thermally evaporated Al layer was deposited on graphene and subjected to annealing at high temperatures to form an AlO_x layer. When the AlO_x capping layer was subjected to corona charge, the R_{sheet} was reduced by ~40% over 9 minutes. This doping process contributed to a significant reduction in carrier mobility, possibly related to the surface roughness of the AlO_x layer.

9.6 Modelling the Performance of an ICD-Doped Graphene layer

In Chapter 8, theoretical modelling was used to compare the potential TCE performance of the ICD-doped graphene layers demonstrated in Chapters 4-7. Following the method for TCE modelling developed by Anand et al. for single junction cells [398], the series resistance contributions of each TCE were lumped into the ideal diode model describing the operation of the entire tandem solar cell. The weighted averaged transmittance (WAT%) across the

spectrum was calculated so that the transmittance of various TCEs could be compared for tandem performance.

The best-performing TCOs in the model were IWO and IZrO, with optimum thicknesses at ~80 nm for improved balance of transmittance to R_{sheet}. These materials likely performed well due to their wide band gaps and high mobility. In these TCOs, the maximum efficiency potential was >42%, with IZrO achieving ~42.5%. Due to the broadband transmittance of ICD-doped graphene, the fabricated ICD/graphene layers performed well in the model demonstrated in this work. The sample with an R_{sheet} of 117.9 Ω/□ enabled a theoretical maximum efficiency ~43.5%, $1\%_{abs}$ greater than that of state-of-the-art TCOs.

It was determined that high-quality, ICD-doped graphene could enable efficiencies up to 44% if R_{sheet} <50 Ω/□. This is a significant increase in efficiency potential as compared with current alternatives while also offering the potential to reduce the use of unsustainable indium-based TCEs in high-efficiency tandem cells.

9.7 **Future work**

This thesis has demonstrated that an R_{sheet} as low as 117.9 Ω/□ can be achieved in graphene using ICD doping. It is apparent that this method causes minimal scattering and does not impact the transmittance of the graphene. However, the mechanism of these doping techniques and their long-term stability for device operation requires further investigation before such record R_{sheet} values can be achieved in practical solar cell devices. Based on the findings presented in the thesis, the following areas of future work are proposed:

1. In Chapter 4, it was observed that the R_{sheet} of graphene on corona-charged SiO_2 membranes reduced further when left in the air over time. This is similar to the reduction in R_{sheet} of corona-charged oxide layers observed in ref. [215], but its mechanism remains unclear. Investing the cause for R_{sheet} variation is recommended,

particularly through controlled measurement and storage of samples in air-free environments to minimise the impact of atmospheric contamination.

2. R_{sheet} measurements in vacuum in Chapters 5 and 6 indicated that the dipole of graphene-Na^+ or graphene-K^+ ions is highly stable at elevated temperatures. Yet the precise kinetics of this process, such as activation energies necessary to migrate ions to and from the graphene electrode were not quantified. To enable more effective doping, and gain a better understanding of stability, these properties should be measured and quantified in detail. This may explain why significantly greater energy was required to migrate ions to the graphene/SiO_2 interfaced compared to the Al/SiO_2 interface.
3. The migration of alkali ions in SiO_2 as demonstrated here offers potential for applications in memory devices, where the change in resistance facilitated by the field-assisted ion migration could be used to store information. A detailed assessment of Na^+ and K^+ ion migration in SiO_2 interfaces with 2D material electrodes is of significant interest for memristor applications. This also requires a more thorough understanding of alkali ion kinetics at the graphene/SiO_2 interface to enable precise switching with minimum power loss.
4. After identifying a common stability of Na^+ and K^+ ions at the graphene/SiO_2 interface, it is plausible that even Li^+ may be stable at this interface by a similar mechanism. This would enable lower energy switching in memory devices, as Li^+ ion drift activation is expected at reduced temperatures and biases due to its smaller ionic radius [422].
5. Surface measurements should be used to confirm the presence of and position of Na^+ and K^+ ions at the graphene/oxide interface after migration, such as via x-ray photoelectron spectroscopy or secondary ion-mass spectroscopy. This would enable a more precise quantification of dipole length.

6. In Chapter 6, the introduction of a SiO_x buffer layer between the BSG surface and the graphene appeared to enable greater reductions in R_{sheet} as Na^+ compared to a graphene device on BSG. This was proposed to occur due to a lack of scattering. However, this was not quantified directly, and therefore, a study of the differences in carrier mobility under vacuum is recommended. Approaches to distribute the charges more uniformly in this way could help to minimise reductions in mobility experienced by ICD-doped films.
7. The doping induced using a thin PECVD SiN_x/SiO_x appeared to be reduced due to atmospheric contamination. More extensive characterisation in an air-free environment is required to confirm this effect.
8. It is proposed that the stability of graphene doping using corona-charged PMMA could be improved through surface functionalisation or oxygen plasma, which may provide more localised trap states to store charge more effectively [423].
9. Corona deposition and migration into high-quality ALD AlO_x on graphene is expected to enable improved charged stability and thus, doping stability relative to the thermally evaporated AlO_x fabricated in this work.
10. The combination of an ICD substrate and ICD-encapsulating layer to permanently induce high carrier concentrations in 2D materials is proposed as a method to reveal new insight into 2D materials carrier properties and scattering [354], [387], [389].
11. There are several risks in introducing such a large concentration of ionic charge in a PV device, such as potential-induced degradation, which was not discussed in detail in this work [322]. Additionally, charges from the PV cell may effectively screen the mirror charge induced in the graphene via the ICD, reducing its doping effect. After confirmation that a low R_{sheet} can be stably preserved in the air using ICDs, a practical

demonstration of ICD-doping of graphene in a functioning PV cell should be investigated.

12. The model of TCE performance in Chapter 8 included several non-physical assumptions including assuming that the resistivity of TCEs scales linearly with thickness. In reality, current-crowding effects and discontinuities can occur as TCO thickness reduces, and differences in thickness can impact grain structure, significantly impacting mobility [424], [425], [426]. A more complete model to account for these morphological variations in TCOs is recommended for a more accurate comparison of different TCO materials for tandem cells.
13. The model of TCE performance in Chapter 8 did not account for the contribution of the metal grid in obtaining optimum properties. As the effect of the metal grid becomes more pronounced when scaling, the model should be extended to account for cells of different areas with different metal grid configurations.
14. The model of TCE performance in Chapter 8 assumed an optimised anti-reflective structure where the light impinges on a MgF_x/SiN_x/graphene/perovskite surface from air. In practical solar modules, glass encapsulates the module, contributing ~10% losses due to reflection. While this is discussed in the Appendix briefly, an improved model should incorporate these losses robustly for glass of various thickness, composition and ARC coatings to provide a better indication of the realistic performance limits of tandem solar cells using different TCE materials.

References

[1] R. F. Keeling and C. D. Keeling, " Atmospheric Monthly In Situ CO2 Data - Mauna Loa Observatory," Jan. 2024. Accessed: Sep. 25, 2024. [Online]. Available: https://library.ucsd.edu/dc/object/bb3859642r

[2] C. D. Keeling *et al.*, "Atmospheric CO2 and 13CO2 Exchange with the Terrestrial Biosphere and Oceans from 1978 to 2000: Observations and Carbon Cycle Implications," *A History of Atmospheric CO2 and Its Effects on Plants, Animals, and Ecosystems*, pp. 83–113, Jul. 2005, doi: 10.1007/0-387-27048-5_5.

[3] C. D. Keeling *et al.*, "Exchanges of Atmospheric CO2 and 13CO2 with the Terrestrial Biosphere and Oceans from 1978 to 2000. I. Global Aspects Publication Date Exchanges of Atmospheric CO 2 and 13 CO 2 with the Terrestrial Biosphere and Oceans from 1978 to 2000. I. Global Aspects," Jun. 01, 2001, *UC San Diego SIO*.

[4] X. Lan, P. Tans, and K. W. Thoning, "Trends in globally-averaged CO2 determined from NOAA Global Monitoring Laboratory measurements." Accessed: Oct. 02, 2024. [Online]. Available: https://doi.org/10.15138/9N0H-ZH07

[5] R. T. Pierrehumbert, *Principles of Planetary Climate*. 2010. doi: 10.1017/cbo9780511780783.

[6] K. Calvin *et al.*, "IPCC, 2023: Climate Change 2023: Synthesis Report. Contribution of Working Groups I, II and III to the Sixth Assessment Report of the Intergovernmental Panel on Climate Change [Core Writing Team, H. Lee and J. Romero (eds.)]. IPCC, Geneva, Switzerland.," Jul. 2023. doi: 10.59327/IPCC/AR6-9789291691647.

[7] M. R. Allen *et al.*, "Global Warming of 1.5°C. An IPCC Special Report on the impacts of global warming of 1.5°C above pre-industrial levels and related global greenhouse

gas emission pathways, in the context of strengthening the global response to the threat of climate change, sustainable development, and efforts to eradicate poverty ," Jun. 2018. doi: 10.1017/9781009157940.002.

[8] World Meteorological Organization, "State of the Global Climate 2023," Geneva, 2024.

[9] H. F. Goessling, T. Rackow, and T. Jung, "Recent global temperature surge intensified by record-low planetary albedo," *Science (1979)*, vol. 387, no. 6729, pp. 68–73, Jan. 2025, doi: 10.1126/SCIENCE.ADQ7280.

[10] "Earth's surface temperature and atmospheric carbon dioxide (1850-2023) | NOAA Climate.gov." Accessed: Jan. 18, 2025. [Online]. Available: https://www.climate.gov/media/13840

[11] N. M. Haegel *et al.*, "Terawatt-scale photovoltaics: Transform global energy Improving costs and scale reflect looming opportunities," *Science (1979)*, vol. 364, no. 6443, pp. 836–838, May 2019, doi: 10.1126/SCIENCE.AAW1845/SUPPL_FILE/AAW1845-HAEGEL-SM.PDF.

[12] N. M. Haegel *et al.*, "Photovoltaics at multi-terawatt scale: Waiting is not an option," *Science (1979)*, vol. 380, no. 6640, pp. 39–42, Apr. 2023, doi: 10.1126/SCIENCE.ADF6957/SUPPL_FILE/SCIENCE.ADF6957_SM.PDF.

[13] N. M. Haegel and S. R. Kurtz, "Global Progress Toward Renewable Electricity: Tracking the Role of Solar (Version 4)," *IEEE J Photovolt*, pp. 1–9, Sep. 2024, doi: 10.1109/JPHOTOV.2024.3450020.

[14] International Renewable Energy Agency, "Renewable power generation costs in 2023," 2024.

[15] X. Wang and A. Barnett, “The evolving value of photovoltaic module efficiency,” *Applied Sciences (Switzerland)*, vol. 9, no. 6, p. 1227, Mar. 2019, doi: 10.3390/app9061227.

[16] M. A. Green, “Commercial progress and challenges for photovoltaics,” Jan. 11, 2016, *Nature Publishing Group*. doi: 10.1038/nenergy.2015.15.

[17] S. M. Sze and K. K. Ng, *Physics of Semiconductor Devices*. John Wiley & Sons, Inc., 2006. doi: 10.1002/0470068329.

[18] T. Niewelt *et al.*, “Reassessment of the intrinsic bulk recombination in crystalline silicon,” *Solar Energy Materials and Solar Cells*, vol. 235, 2022, doi: 10.1016/j.solmat.2021.111467.

[19] H. Lin *et al.*, “Silicon heterojunction solar cells with up to 26.81% efficiency achieved by electrically optimized nanocrystalline-silicon hole contact layers,” *Nature Energy 2023*, pp. 1–11, May 2023, doi: 10.1038/s41560-023-01255-2.

[20] “LONGi Sets New World-Record for Silicon Solar Cell Efficiency, Launching 2nd Generation Ultra-Efficient BC-Based Module -LONGi.” Accessed: Sep. 24, 2024. [Online]. Available: https://www.longi.com/en/news/longi-hi-mo9-bc-world-record/

[21] H. Wu *et al.*, “Silicon heterojunction back contact solar cells by laser patterning,” *Nature 2024*, pp. 1–3, Oct. 2024, doi: 10.1038/s41586-024-08110-8.

[22] “Best Research-Cell Efficiency Chart | Photovoltaic Research | NREL.” Accessed: Oct. 18, 2024. [Online]. Available: https://www.nrel.gov/pv/cell-efficiency.html

[23] H. Shen *et al.*, “Monolithic Perovskite/Si Tandem Solar Cells: Pathways to Over 30% Efficiency,” *Adv Energy Mater*, vol. 10, no. 13, p. 1902840, Apr. 2020, doi: 10.1002/AENM.201902840.

[24] A. Al-Ashouri *et al.*, “Monolithic perovskite/silicon tandem solar cell with >29% efficiency by enhanced hole extraction,” *Science (1979)*, vol. 370, no. 6522, pp. 1300–1309, Dec. 2020, doi: 10.1126/SCIENCE.ABD4016/SUPPL_FILE/ABD4016_AL-ASHOURI_SM.PDF.

[25] J. Liu *et al.*, “Perovskite-silicon tandem solar cells with bilayer interface passivation,” *Nature*, Sep. 2024, doi: 10.1038/s41586-024-07997-7.

[26] S. P. Bremner, M. Y. Levy, and C. B. Honsberg, “Analysis of tandem solar cell efficiencies under AM1.5G spectrum using a rapid flux calculation method,” *Progress in Photovoltaics: Research and Applications*, vol. 16, no. 3, pp. 225–233, May 2008, doi: 10.1002/PIP.799.

[27] J. F. Geisz *et al.*, “Six-junction III–V solar cells with 47.1% conversion efficiency under 143 Suns concentration,” *Nature Energy 2020 5:4*, vol. 5, no. 4, pp. 326–335, Apr. 2020, doi: 10.1038/s41560-020-0598-5.

[28] J. Li *et al.*, “A Brief Review of High Efficiency III-V Solar Cells for Space Application,” *Front Phys*, vol. 8, p. 631925, Feb. 2021, doi: 10.3389/FPHY.2020.631925/BIBTEX.

[29] C. Gueymard, “SMARTS2, A Simple Model of the Atmospheric Radiative Transfer of Sunshine: Algorithms and performance assessment Simple Model for the Atmospheric Radiative Transfer of Sunshine (SMARTS2) Algorithms and performance assessment,” *Florida Solar Energy Center*, 1995.

[30] J. Liu *et al.*, “Perovskite-silicon tandem solar cells with bilayer interface passivation,” *Nature 2024*, pp. 1–3, Sep. 2024, doi: 10.1038/s41586-024-07997-7.

[31] “34.6%! Record-breaker LONGi Once Again Sets a New World Efficiency for Silicon-perovskite Tandem Solar Cells.” Accessed: Jul. 18, 2024. [Online]. Available:

https://www.longi.com/en/news/2024-snec-silicon-perovskite-tandem-solar-cells-new-world-efficiency/

[32] "34.85%! LONGi Breaks World Record for Crystalline Silicon-Perovskite Tandem Solar Cell Efficiency Again -LONGi." Accessed: Apr. 24, 2025. [Online]. Available: https://www.longi.com/en/news/silicon-perovskite-tandem-solar-cells-new-world-efficiency/

[33] Z. Yu, M. Leilaeioun, and Z. Holman, "Selecting tandem partners for silicon solar cells," 2016. doi: 10.1038/nenergy.2016.137.

[34] M. H. Futscher and B. Ehrler, "Modeling the Performance Limitations and Prospects of Perovskite/Si Tandem Solar Cells under Realistic Operating Conditions," *ACS Energy Lett*, vol. 2, no. 9, pp. 2089–2095, Sep. 2017, doi: 10.1021/ACSENERGYLETT.7B00596/ASSET/IMAGES/LARGE/NZ-2017-00596U_0004.JPEG.

[35] M. H. Futscher and B. Ehrler, "Efficiency Limit of Perovskite/Si Tandem Solar Cells," *ACS Energy Lett*, vol. 1, no. 4, pp. 863–868, Oct. 2016, doi: 10.1021/ACSENERGYLETT.6B00405/ASSET/IMAGES/LARGE/NZ-2016-004056_0005.JPEG.

[36] S. De Wolf *et al.*, "Organometallic halide perovskites: Sharp optical absorption edge and its relation to photovoltaic performance," *Journal of Physical Chemistry Letters*, vol. 5, no. 6, 2014, doi: 10.1021/jz500279b.

[37] H. Zhao *et al.*, "A Novel Anion Doping for Stable CsPbI2Br Perovskite Solar Cells with an Efficiency of 15.56% and an Open Circuit Voltage of 1.30 V," *Adv Energy Mater*, vol. 9, no. 40, 2019, doi: 10.1002/aenm.201902279.

[38] S. Manzoor, J. Häusele, K. A. Bush, Z. J. Yu, M. D. McGehee, and Z. C. Holman, "Current-matching in two-terminal perovskite/silicon tandems employing wide-bandgap perovskites and varying light-management schemes," *2018 IEEE 7th World Conference on Photovoltaic Energy Conversion, WCPEC 2018 - A Joint Conference of 45th IEEE PVSC, 28th PVSEC and 34th EU PVSEC*, pp. 220–223, Nov. 2018, doi: 10.1109/PVSC.2018.8547757.

[39] J. Cheng, I. Choi, W. Kim, H. Li, B. Koo, and M. J. Ko, "Wide-Band-Gap (2.0 eV) Perovskite Solar Cells with a VOC of 1.325 V Fabricated by a Green-Solvent Strategy," *ACS Appl Mater Interfaces*, vol. 15, no. 19, pp. 23077–23084, May 2023, doi: 10.1021/ACSAMI.3C00895/ASSET/IMAGES/LARGE/AM3C00895_0004.JPEG.

[40] M. H. Miah, M. U. Khandaker, M. B. Rahman, M. Nur-E-Alam, and M. A. Islam, "Band gap tuning of perovskite solar cells for enhancing the efficiency and stability: issues and prospects," *RSC Adv*, vol. 14, no. 23, pp. 15876–15906, May 2024, doi: 10.1039/D4RA01640H.

[41] C. Li *et al.*, "Low-bandgap mixed tin–lead iodide perovskites with reduced methylammonium for simultaneous enhancement of solar cell efficiency and stability," *Nature Energy 2020 5:10*, vol. 5, no. 10, pp. 768–776, Oct. 2020, doi: 10.1038/s41560-020-00692-7.

[42] K. Yoshikawa *et al.*, "Silicon heterojunction solar cell with interdigitated back contacts for a photoconversion efficiency over 26%," *Nat Energy*, vol. 2, no. 5, pp. 1–8, Mar. 2017, doi: 10.1038/nenergy.2017.32.

[43] M. Wright *et al.*, "Design considerations for the bottom cell in perovskite/silicon tandems: a terawatt scalability perspective," *Energy Environ Sci*, vol. 16, no. 10, pp. 4164–4190, Oct. 2023, doi: 10.1039/D3EE00952A.

[44] W. Duan *et al.*, “A route towards high-efficiency silicon heterojunction solar cells,” *Progress in Photovoltaics: Research and Applications*, vol. 30, no. 4, pp. 384–392, Apr. 2022, doi: 10.1002/PIP.3493.

[45] M. Morales-Masis, S. De Wolf, R. Woods-Robinson, J. W. Ager, and C. Ballif, “Transparent Electrodes for Efficient Optoelectronics,” *Adv Electron Mater*, vol. 3, no. 5, p. 1600529, May 2017, doi: 10.1002/AELM.201600529.

[46] M. W. Rowell and M. D. McGehee, “Transparent electrode requirements for thin film solar cell modules,” *Energy Environ Sci*, vol. 4, no. 1, pp. 131–134, Jan. 2011, doi: 10.1039/c0ee00373e.

[47] C. G. Granqvist, “Transparent conductors as solar energy materials: A panoramic review,” Oct. 15, 2007, *North-Holland*. doi: 10.1016/j.solmat.2007.04.031.

[48] K. L. Chopra, S. Major, and D. K. Pandya, “Transparent conductors-A status review,” Apr. 08, 1983, *Elsevier*. doi: 10.1016/0040-6090(83)90256-0.

[49] D. A. Jacobs, K. R. Catchpole, F. J. Beck, and T. P. White, “A re-evaluation of transparent conductor requirements for thin-film solar cells,” *J Mater Chem A Mater*, vol. 4, no. 12, pp. 4490–4496, Mar. 2016, doi: 10.1039/c6ta01670g.

[50] T. Todorov, O. Gunawan, and S. Guha, “A road towards 25% efficiency and beyond: perovskite tandem solar cells,” *Mol Syst Des Eng*, vol. 1, no. 4, pp. 370–376, Nov. 2016, doi: 10.1039/C6ME00041J.

[51] D. A. Jacobs *et al.*, “Light Management: A Key Concept in High-Efficiency Perovskite/Silicon Tandem Photovoltaics,” *Journal of Physical Chemistry Letters*, vol. 10, no. 11, pp. 3159–3170, 2019, doi: 10.1021/acs.jpclett.8b03721.

[52] Y. Wu *et al.*, “Monolithic perovskite/silicon-homojunction tandem solar cell with over 22% efficiency,” *Energy Environ Sci*, vol. 10, no. 11, pp. 2472–2479, Nov. 2017, doi: 10.1039/C7EE02288C.

[53] F. Fu *et al.*, “Monolithic Perovskite-Silicon Tandem Solar Cells: From the Lab to Fab?,” *Advanced Materials*, p. 2106540, 2022, doi: 10.1002/ADMA.202106540.

[54] R. G. Gordon, “Criteria for choosing transparent conductors,” *MRS Bull*, vol. 25, no. 8, pp. 52–57, 2000, doi: 10.1557/mrs2000.151.

[55] E. Aydin *et al.*, “Zr-Doped Indium Oxide (IZRO) Transparent Electrodes for Perovskite-Based Tandem Solar Cells,” *Adv Funct Mater*, vol. 29, no. 25, p. 1901741, Jun. 2019, doi: 10.1002/ADFM.201901741.

[56] M. Rudiger, J. Greulich, A. Richter, and M. Hermle, “Parameterization of free carrier absorption in highly doped silicon for solar cells,” *IEEE Trans Electron Devices*, vol. 60, no. 7, pp. 2156–2163, 2013, doi: 10.1109/TED.2013.2262526.

[57] S. Kim *et al.*, “Free-carrier absorption and Burstein–Moss shift effect on quantum efficiency in heterojunction silicon solar cells,” *Vacuum*, vol. 108, pp. 39–44, Oct. 2014, doi: 10.1016/J.VACUUM.2014.05.015.

[58] E. Köhnen *et al.*, “Highly efficient monolithic perovskite silicon tandem solar cells: analyzing the influence of current mismatch on device performance,” *Sustain Energy Fuels*, vol. 3, no. 8, pp. 1995–2005, Jul. 2019, doi: 10.1039/C9SE00120D.

[59] D. Zhang, W. Soppe, and R. E. I. Schropp, “Design of 4-terminal Solar Modules Combining Thin-film Wide-Bandgap Top Cells and c-Si Bottom Cells,” *Energy Procedia*, vol. 77, pp. 500–507, Aug. 2015, doi: 10.1016/J.EGYPRO.2015.07.071.

[60] M. De Bastiani *et al.*, “Efficient bifacial monolithic perovskite/silicon tandem solar cells via bandgap engineering,” *Nature Energy 2021 6:2*, vol. 6, no. 2, pp. 167–175, Jan. 2021, doi: 10.1038/s41560-020-00756-8.

[61] T. Kim *et al.*, “Megahertz-wave-transmitting conducting polymer electrode for device-to-device integration,” *Nature Communications 2019 10:1*, vol. 10, no. 1, pp. 1–11, Feb. 2019, doi: 10.1038/s41467-019-08552-z.

[62] G. Brunin, F. Ricci, V. A. Ha, G. M. Rignanese, and G. Hautier, “Transparent conducting materials discovery using high-throughput computing,” Dec. 01, 2019, *Nature Publishing Group*. doi: 10.1038/s41524-019-0200-5.

[63] S. R. Das, S. Sadeque, C. Jeong, R. Chen, M. A. Alam, and D. B. Janes, “Copercolating Networks: An Approach for Realizing High-Performance Transparent Conductors using Multicomponent Nanostructured Networks,” *Nanophotonics*, vol. 5, no. 1, pp. 180–195, Jun. 2016, doi: 10.1515/NANOPH-2016-0036/MACHINEREADABLECITATION/RIS.

[64] J. Wang, F. Ma, W. Liang, R. Wang, and M. Sun, “Optical, photonic and optoelectronic properties of graphene, h-NB and their hybrid materials,” Aug. 28, 2017, *Walter de Gruyter GmbH*. doi: 10.1515/nanoph-2017-0015.

[65] S. C. Dixon, D. O. Scanlon, C. J. Carmalt, and I. P. Parkin, “n-Type doped transparent conducting binary oxides: an overview,” *J Mater Chem C Mater*, vol. 4, no. 29, pp. 6946–6961, Jul. 2016, doi: 10.1039/C6TC01881E.

[66] V. I. Kaydanov, T. J. Coutts, and D. L. Young, “Studies of Band Structure and Free-Carrier Scattering in Transparent Conducting Oxides Based on Combined Measurements of Electron Transport Phenomena,” 2000, Accessed: Aug. 09, 2024.

[Online]. Available: http://www.doe.gov/bridgeonlineordering:http://www.ntis.gov/ordering.htm

[67] R. K. Kothandaraman, Y. Jiang, T. Feurer, A. N. Tiwari, and F. Fu, "Near-Infrared-Transparent Perovskite Solar Cells and Perovskite-Based Tandem Photovoltaics," *Small Methods*, vol. 4, no. 10, p. 2000395, Oct. 2020, doi: 10.1002/SMTD.202000395.

[68] Antonio. Facchetti and T. J. Marks, "Transparent electronics : from synthesis to applications," p. 448, 2010.

[69] A. Walsh, J. L. F. Da Silva, and S. H. Wei, "Origins of band-gap renormalization in degenerately doped semiconductors," *Phys Rev B Condens Matter Mater Phys*, vol. 78, no. 7, p. 075211, Aug. 2008, doi: 10.1103/PHYSREVB.78.075211/FIGURES/5/MEDIUM.

[70] H. Jung *et al.*, "Transparent Electrodes with Enhanced Infrared Transmittance for Semitransparent and Four-Terminal Tandem Perovskite Solar Cells," *ACS Appl Mater Interfaces*, vol. 13, no. 26, pp. 30497–30503, Jul. 2021, doi: 10.1021/ACSAMI.1C02824/ASSET/IMAGES/LARGE/AM1C02824_0006.JPEG.

[71] Y. C. Kim *et al.*, "Luminescent down-shifting CsPbBr 3 perovskite nanocrystals for flexible Cu(In,Ga)Se 2 solar cells," *Nanoscale*, vol. 12, no. 2, pp. 558–562, Jan. 2020, doi: 10.1039/C9NR06041C.

[72] M. Morales-Masis, S. Martin De Nicolas, J. Holovsky, S. De Wolf, and C. Ballif, "Low-Temperature High-Mobility Amorphous IZO for Silicon Heterojunction Solar Cells," *IEEE J Photovolt*, vol. 5, no. 5, pp. 1340–1347, Sep. 2015, doi: 10.1109/JPHOTOV.2015.2450993.

[73] B. Chen *et al.*, “Enhanced optical path and electron diffusion length enable high-efficiency perovskite tandems,” *Nature Communications 2020 11:1*, vol. 11, no. 1, pp. 1–9, Mar. 2020, doi: 10.1038/s41467-020-15077-3.

[74] E. Kobayashi, Y. Watabe, T. Yamamoto, and Y. Yamada, “Cerium oxide and hydrogen co-doped indium oxide films for high-efficiency silicon heterojunction solar cells,” *Solar Energy Materials and Solar Cells*, vol. 149, pp. 75–80, May 2016, doi: 10.1016/J.SOLMAT.2016.01.005.

[75] Y. Zhang, M. Kim, L. Wang, P. Verlinden, and B. Hallam, “Design considerations for multi-terawatt scale manufacturing of existing and future photovoltaic technologies: challenges and opportunities related to silver, indium and bismuth consumption,” *Energy Environ Sci*, vol. 14, no. 11, pp. 5587–5610, Nov. 2021, doi: 10.1039/D1EE01814K.

[76] L. Wang *et al.*, “Sustainability evaluations on material consumption for terawatt-scale manufacturing of silicon-based tandem solar cells,” *Progress in Photovoltaics: Research and Applications*, 2023, doi: 10.1002/PIP.3687.

[77] T. Minami, “Transparent conducting oxide semiconductors for transparent electrodes,” *Semicond Sci Technol*, vol. 20, no. 4, p. S35, Apr. 2005, doi: 10.1088/0268-1242/20/4/004.

[78] M. Filipič *et al.*, “CH_3NH_3PbI_3 perovskite / silicon tandem solar cells: characterization based optical simulations,” *Opt Express*, vol. 23, no. 7, p. A263, Apr. 2015, doi: 10.1364/oe.23.00a263.

[79] A. J. Bett *et al.*, “Semi-Transparent Perovskite Solar Cells with ITO Directly Sputtered on Spiro-OMeTAD for Tandem Applications,” *ACS Appl Mater Interfaces*, vol. 11, no.

49, pp. 45796–45804, Dec. 2019, doi: 10.1021/ACSAMI.9B17241/ASSET/IMAGES/LARGE/AM9B17241_0005.JPEG.

[80] Y. Smirnov *et al.*, "Wafer-scale pulsed laser deposition of ITO for solar cells: reduced damage vs. interfacial resistance," *Mater Adv*, vol. 3, no. 8, pp. 3469–3478, Apr. 2022, doi: 10.1039/D1MA01225H.

[81] E. Aydin *et al.*, "Sputtered transparent electrodes for optoelectronic devices: Induced damage and mitigation strategies," *Matter*, vol. 4, no. 11, pp. 3549–3584, Nov. 2021, doi: 10.1016/J.MATT.2021.09.021.

[82] J. Werner *et al.*, "Sputtered rear electrode with broadband transparency for perovskite solar cells," *Solar Energy Materials and Solar Cells*, vol. 141, pp. 407–413, Oct. 2015, doi: 10.1016/J.SOLMAT.2015.06.024.

[83] Z. Szabó *et al.*, "Atomic layer deposition and annealing of Ga doped ZnO films," *Mater Sci Semicond Process*, vol. 101, pp. 95–102, Oct. 2019, doi: 10.1016/J.MSSP.2019.05.028.

[84] T. Koida, H. Fujiwara, and M. Kondo, "Hydrogen-doped in2O3 as high-mobility transparent conductive oxide," *Japanese Journal of Applied Physics, Part 2: Letters*, vol. 46, no. 25–28, p. L685, Jul. 2007, doi: 10.1143/JJAP.46.L685/XML.

[85] T. Tohsophon *et al.*, "Damp heat stability and annealing behavior of aluminum doped zinc oxide films prepared by magnetron sputtering," *Thin Solid Films*, vol. 511–512, pp. 673–677, Jul. 2006, doi: 10.1016/J.TSF.2005.12.130.

[86] Z. Fan *et al.*, "Layer-by-Layer Degradation of Methylammonium Lead Tri-iodide Perovskite Microplates," *Joule*, vol. 1, no. 3, pp. 548–562, Nov. 2017, doi: 10.1016/J.JOULE.2017.08.005.

[87] B. Conings *et al.*, “Intrinsic Thermal Instability of Methylammonium Lead Trihalide Perovskite,” *Adv Energy Mater*, vol. 5, no. 15, p. 1500477, Aug. 2015, doi: 10.1002/AENM.201500477.

[88] G. E. Eperon, S. D. Stranks, C. Menelaou, M. B. Johnston, L. M. Herz, and H. J. Snaith, “Formamidinium lead trihalide: a broadly tunable perovskite for efficient planar heterojunction solar cells,” *Energy Environ Sci*, vol. 7, no. 3, pp. 982–988, Feb. 2014, doi: 10.1039/C3EE43822H.

[89] Z. Xu *et al.*, “Efficient and stable inverted MA/Br-free 2D/3D perovskite solar cells enabled by α-to-δ phase transition inhibition and crystallization modulation,” *Energy Environ Sci*, vol. 18, no. 3, pp. 1354–1365, Feb. 2025, doi: 10.1039/D4EE04136D.

[90] S. Kim *et al.*, “Recent advancements and challenges in highly stable all-inorganic perovskite solar cells,” *Materials Today Electronics*, vol. 10, p. 100127, Dec. 2024, doi: 10.1016/J.MTELEC.2024.100127.

[91] S. S. Mali, J. V. Patil, J. A. Steele, M. K. Nazeeruddin, J. H. Kim, and C. K. Hong, “All-inorganic halide perovskites for air-processed ‘n–i–p’ monolithic perovskite/organic hybrid tandem solar cells exceeding 23% efficiency,” *Energy Environ Sci*, vol. 17, no. 3, pp. 1046–1060, Feb. 2024, doi: 10.1039/D3EE02763E.

[92] A. De Rose *et al.*, “Low-temperature metallization & interconnection for silicon heterojunction and perovskite silicon tandem solar cells,” *Solar Energy Materials and Solar Cells*, vol. 261, p. 112515, Oct. 2023, doi: 10.1016/J.SOLMAT.2023.112515.

[93] C. Luderer, C. Messmer, M. Hermle, and M. Bivour, “Transport Losses at the TCO/a-Si:H/c-Si Heterojunction: Influence of Different Layers and Annealing,” *IEEE J Photovolt*, vol. 10, no. 4, pp. 952–958, Jul. 2020, doi: 10.1109/JPHOTOV.2020.2983989.

[94] N. N. Rosli, M. A. Ibrahim, N. Ahmad Ludin, M. A. Mat Teridi, and K. Sopian, “A review of graphene based transparent conducting films for use in solar photovoltaic applications,” Jan. 01, 2019, *Elsevier Ltd*. doi: 10.1016/j.rser.2018.09.011.

[95] M. R. Azani, A. Hassanpour, and T. Torres, “Benefits, Problems, and Solutions of Silver Nanowire Transparent Conductive Electrodes in Indium Tin Oxide (ITO)-Free Flexible Solar Cells,” *Adv Energy Mater*, vol. 10, no. 48, p. 2002536, Dec. 2020, doi: 10.1002/AENM.202002536;PAGE:STRING:ARTICLE/CHAPTER.

[96] A. Kim *et al.*, “Fully solution-processed transparent electrodes based on silver nanowire composites for perovskite solar cells,” *Nanoscale*, vol. 8, no. 12, pp. 6308–6316, 2016, doi: 10.1039/C5NR04585A.

[97] E. Lee *et al.*, “All-Solution-Processed Silver Nanowire Window Electrode-Based Flexible Perovskite Solar Cells Enabled with Amorphous Metal Oxide Protection,” *Adv Energy Mater*, vol. 8, no. 9, Mar. 2018, doi: 10.1002/aenm.201702182.

[98] S. De and J. N. Coleman, “Are there fundamental limitations on the sheet resistance and transmittance of thin graphene films?,” *ACS Nano*, vol. 4, no. 5, pp. 2713–2720, May 2010, doi: 10.1021/nn100343f.

[99] S. E. Zhu, S. Yuan, and G. C. A. M. Janssen, “Optical transmittance of multilayer graphene,” *EPL*, vol. 108, no. 1, p. 17007, Oct. 2014, doi: 10.1209/0295-5075/108/17007.

[100] J. W. Weber, A. A. Bol, and M. C. M. Van De Sanden, “An improved thin film approximation to accurately determine the optical conductivity of graphene from infrared transmittance,” *Appl Phys Lett*, vol. 105, no. 1, p. 013105, Jul. 2014, doi: 10.1063/1.4889852.

[101] J. K. Wassei and R. B. Kaner, “Graphene, a promising transparent conductor,” Mar. 01, 2010, *Elsevier*. doi: 10.1016/S1369-7021(10)70034-1.

[102] “The Price Of Graphene – Graphenea.” Accessed: Jun. 01, 2021. [Online]. Available: https://www.graphenea.com/pages/graphene-price#.YLV0cahKjid

[103] “Article – Graphenea EU.” Accessed: Oct. 08, 2024. [Online]. Available: https://eu.graphenea.com/pages/the-price-of-graphene

[104] P. You, Z. Liu, Q. Tai, S. Liu, and F. Yan, “Efficient Semitransparent Perovskite Solar Cells with Graphene Electrodes,” *Advanced Materials*, vol. 27, no. 24, pp. 3632–3638, Jun. 2015, doi: 10.1002/ADMA.201501145.

[105] F. Lang *et al.*, “In situ graphene doping as a route toward efficient perovskite tandem solar cells,” *physica status solidi (a)*, vol. 213, no. 7, pp. 1989–1996, Jul. 2016, doi: 10.1002/PSSA.201532944.

[106] F. Lang *et al.*, “Perovskite solar cells with large-area CVD-graphene for tandem solar cells,” *Journal of Physical Chemistry Letters*, vol. 6, no. 14, pp. 2745–2750, Jul. 2015, doi: 10.1021/ACS.JPCLETT.5B01177/SUPPL_FILE/JZ5B01177_SI_001.PDF.

[107] R. Arvidsson, D. Kushnir, S. Molander, and B. A. Sandén, “Energy and resource use assessment of graphene as a substitute for indium tin oxide in transparent electrodes,” *J Clean Prod*, vol. 132, pp. 289–297, Sep. 2016, doi: 10.1016/j.jclepro.2015.04.076.

[108] Y. Song, W. Fang, R. Brenes, and J. Kong, “Challenges and opportunities for graphene as transparent conductors in optoelectronics,” *Nano Today*, vol. 10, no. 6, pp. 681–700, Dec. 2015, doi: 10.1016/J.NANTOD.2015.11.005.

[109] A. K. Geim and K. S. Novoselov, “The rise of graphene,” *Nat Mater*, vol. 6, no. 3, pp. 183–191, Mar. 2007, doi: 10.1038/nmat1849.

[110] K. S. Novoselov *et al.*, “Two-dimensional gas of massless Dirac fermions in graphene,” *Nature*, vol. 438, no. 7065, pp. 197–200, Nov. 2005, doi: 10.1038/nature04233.

[111] J. H. Chen, C. Jang, S. Xiao, M. Ishigami, and M. S. Fuhrer, “Intrinsic and extrinsic performance limits of graphene devices on SiO 2,” *Nat Nanotechnol*, vol. 3, no. 4, pp. 206–209, Apr. 2008, doi: 10.1038/nnano.2008.58.

[112] A. H. Castro Neto, F. Guinea, N. M. R. Peres, K. S. Novoselov, and A. K. Geim, “The electronic properties of graphene,” *Rev Mod Phys*, vol. 81, no. 1, pp. 109–162, Jan. 2009, doi: 10.1103/RevModPhys.81.109.

[113] A. K. Geim, “Graphene: Status and prospects,” Jun. 19, 2009, *American Association for the Advancement of Science*. doi: 10.1126/science.1158877.

[114] S. Sarkar and S. Sarkar, “Tunneling in Graphene SymFETs,” May 2018, Accessed: Oct. 18, 2024. [Online]. Available: https://arxiv.org/abs/1805.09659v1

[115] L. Cui, J. Wang, and M. Sun, “Graphene plasmon for optoelectronics,” *Reviews in Physics*, vol. 6, p. 100054, Jun. 2021, doi: 10.1016/J.REVIP.2021.100054.

[116] K. S. Novoselov *et al.*, “Electric field effect in atomically thin carbon films,” *Science (1979)*, vol. 306, no. 5696, pp. 666–669, Oct. 2004, doi: 10.1126/science.1102896.

[117] Y. Yin, Z. Cheng, L. Wang, K. Jin, and W. Wang, “Graphene, a material for high temperature devices - Intrinsic carrier density, carrier drift velocity, and lattice energy,” *Sci Rep*, vol. 4, no. 1, pp. 1–6, Jul. 2014, doi: 10.1038/srep05758.

[118] F. J. Nelson, V. K. Kamineni, T. Zhang, E. S. Comfort, J. U. Lee, and A. C. Diebold, “Optical properties of large-area polycrystalline chemical vapor deposited graphene by spectroscopic ellipsometry,” *Appl Phys Lett*, vol. 97, no. 25, p. 253110, Dec. 2010, doi: 10.1063/1.3525940.

[119] K. I. Bolotin *et al.*, “Ultrahigh electron mobility in suspended graphene,” *Solid State Commun*, vol. 146, no. 9–10, pp. 351–355, Jun. 2008, doi: 10.1016/j.ssc.2008.02.024.

[120] J. H. Seol *et al.*, “Two-dimensional phonon transport in supported graphene,” *Science (1979)*, vol. 328, no. 5975, pp. 213–216, Apr. 2010, doi: 10.1126/science.1184014.

[121] G. V. Bianco *et al.*, “Extraordinary low sheet resistance of CVD graphene by thionyl chloride chemical doping,” *Carbon N Y*, vol. 170, pp. 75–84, Dec. 2020.

[122] C. J. Shearer, A. D. Slattery, A. J. Stapleton, J. G. Shapter, and C. T. Gibson, “Accurate thickness measurement of graphene,” *Nanotechnology*, vol. 27, no. 12, p. 125704, Feb. 2016, doi: 10.1088/0957-4484/27/12/125704.

[123] R. R. Nair *et al.*, “Fine structure constant defines visual transparency of graphene,” *Science (1979)*, vol. 320, no. 5881, p. 1308, Jun. 2008, doi: 10.1126/science.1156965.

[124] D. Akinwande, L. Tao, Q. Yu, X. Lou, P. Peng, and D. Kuzum, “Large-Area Graphene Electrodes: Using CVD to facilitate applications in commercial touchscreens, flexible nanoelectronics, and neural interfaces.,” *IEEE Nanotechnol Mag*, vol. 9, no. 3, pp. 6–14, Sep. 2015, doi: 10.1109/MNANO.2015.2441105.

[125] S. Bae *et al.*, “Roll-to-roll production of 30-inch graphene films for transparent electrodes,” *Nat Nanotechnol*, vol. 5, no. 8, pp. 574–578, Aug. 2010, doi: 10.1038/nnano.2010.132.

[126] V. B. Mbayachi, E. Ndayiragije, T. Sammani, S. Taj, E. R. Mbuta, and A. ullah khan, “Graphene synthesis, characterization and its applications: A review,” *Results Chem*, vol. 3, p. 100163, Jan. 2021, doi: 10.1016/J.RECHEM.2021.100163.

[127] Z. Liu, S. P. Lau, and F. Yan, “Functionalized graphene and other two-dimensional materials for photovoltaic devices: device design and processing,” *Chem Soc Rev*, vol. 44, no. 15, pp. 5638–5679, Jul. 2015, doi: 10.1039/C4CS00455H.

[128] S. Zhu *et al.*, “Transparent electrode for monolithic perovskite/silicon-heterojunction two-terminal tandem solar cells,” *Nano Energy*, vol. 45, pp. 280–286, Mar. 2018, doi: 10.1016/J.NANOEN.2017.12.043.

[129] Z. H. Ni *et al.*, “Graphene thickness determination using reflection and contrast spectroscopy,” *Nano Lett*, vol. 7, no. 9, pp. 2758–2763, Sep. 2007, doi: 10.1021/nl071254m.

[130] H. Jussila, H. Yang, N. Granqvist, and Z. Sun, “Surface plasmon resonance for characterization of large-area atomic-layer graphene film,” *Optica*, vol. 3, no. 2, p. 151, Feb. 2016, doi: 10.1364/optica.3.000151.

[131] S. Cheon and K. D. Kihm, “Complex Refractive Index (RI) of Graphene,” in *Handbook of Graphene*, Wiley, 2019, pp. 389–412. doi: 10.1002/9781119468455.ch31.

[132] M. Bruna and S. Borini, “Optical constants of graphene layers in the visible range,” *Appl Phys Lett*, vol. 94, no. 3, p. 31901, Jan. 2009, doi: 10.1063/1.3073717.

[133] X. Wang, Y. P. Chen, and D. D. Nolte, “Strong anomalous optical dispersion of graphene: complex refractive index measured by Picometrology,” *Opt Express*, vol. 16, no. 26, p. 22105, Dec. 2008, doi: 10.1364/oe.16.022105.

[134] D. Wang, M. Wright, N. K. Elumalai, and A. Uddin, “Stability of perovskite solar cells,” *Solar Energy Materials and Solar Cells*, vol. 147, pp. 255–275, Apr. 2016, doi: 10.1016/J.SOLMAT.2015.12.025.

[135] J. J. Shen, “Recently-explored top electrode materials for transparent organic solar cells,” *Synth Met*, vol. 271, p. 116582, Jan. 2021, doi: 10.1016/J.SYNTHMET.2020.116582.

[136] Y. Huang *et al.*, “Reliable Exfoliation of Large-Area High-Quality Flakes of Graphene and Other Two-Dimensional Materials,” *ACS Nano*, vol. 9, no. 11, pp. 10612–10620, Nov. 2015, doi: 10.1021/acsnano.5b04258.

[137] Y. Huang *et al.*, “Universal mechanical exfoliation of large-area 2D crystals,” *Nat Commun*, vol. 11, no. 1, pp. 1–9, Dec. 2020, doi: 10.1038/s41467-020-16266-w.

[138] K.-Y. Shin and J. Jang, “Highly conductive, flexible and scalable graphene hybrid thin films with controlled domain size as transparent electrodes,” *Chem. Commun.*, vol. 50, no. 50, pp. 6645–6648, 2014, doi: 10.1039/C4CC01302F.

[139] W. Zhao, M. Fang, F. Wu, H. Wu, L. Wang, and G. Chen, “Preparation of graphene by exfoliation of graphite using wet ball milling,” *J Mater Chem*, vol. 20, no. 28, pp. 5817–5819, Jul. 2010, doi: 10.1039/c0jm01354d.

[140] Q. Yang *et al.*, “High-Yield Production of Few-Layer Graphene via New-fashioned Strategy Combining Resonance Ball Milling and Hydrothermal Exfoliation,” *Nanomaterials 2020, Vol. 10, Page 667*, vol. 10, no. 4, p. 667, Apr. 2020, doi: 10.3390/NANO10040667.

[141] X. Li, J. Shen, C. Wu, and K. Wu, “Ball-Mill-Exfoliated Graphene: Tunable Electrochemistry and Phenol Sensing,” *Small*, vol. 15, no. 48, Nov. 2019, doi: 10.1002/smll.201805567.

[142] G. Huang *et al.*, “Efficient preparation and characterization of graphene based on ball milling,” *Diam Relat Mater*, vol. 130, p. 109438, Dec. 2022, doi: 10.1016/J.DIAMOND.2022.109438.

[143] Y. Xue, H. Chen, J. Qu, and L. Dai, “Nitrogen-doped graphene by ball-milling graphite with melamine for energy conversion and storage,” *2d Mater*, vol. 2, no. 4, p. 044001, Oct. 2015, doi: 10.1088/2053-1583/2/4/044001.

[144] P. L. Cullen *et al.*, “Ionic solutions of two-dimensional materials,” *Nature Chemistry 2016 9:3*, vol. 9, no. 3, pp. 244–249, Nov. 2016, doi: 10.1038/nchem.2650.

[145] Y. Hernandez *et al.*, “High-yield production of graphene by liquid-phase exfoliation of graphite,” *Nat Nanotechnol*, vol. 3, no. 9, pp. 563–568, Sep. 2008, doi: 10.1038/nnano.2008.215.

[146] A. P. Kauling *et al.*, “The Worldwide Graphene Flake Production,” *Advanced Materials*, vol. 30, no. 44, p. 1803784, Nov. 2018, doi: 10.1002/adma.201803784.

[147] Q. Zheng, Z. Li, J. Yang, and J. K. Kim, “Graphene oxide-based transparent conductive films,” Jul. 01, 2014, *Elsevier Ltd*. doi: 10.1016/j.pmatsci.2014.03.004.

[148] X. Li *et al.*, “Large-area synthesis of high-quality and uniform graphene films on copper foils,” *Science (1979)*, vol. 324, no. 5932, pp. 1312–1314, Jun. 2009, doi: 10.1126/science.1171245.

[149] R. Vishwakarma *et al.*, “Direct Synthesis of Large-Area Graphene on Insulating Substrates at Low Temperature using Microwave Plasma CVD,” *ACS Omega*, vol. 4, no. 6, pp. 11263–11270, Jun. 2019, doi: 10.1021/acsomega.9b00988.

[150] K. S. Kim *et al.*, “Large-scale pattern growth of graphene films for stretchable transparent electrodes,” *Nature*, vol. 457, no. 7230, pp. 706–710, Feb. 2009, doi: 10.1038/nature07719.

[151] K. Balasubramanian *et al.*, “Reversible defect engineering in graphene grain boundaries,” *Nat Commun*, vol. 10, no. 1, pp. 1–9, Dec. 2019, doi: 10.1038/s41467-019-09000-8.

[152] P. Vinchon, X. Glad, G. Robert Bigras, R. Martel, and L. Stafford, “Preferential self-healing at grain boundaries in plasma-treated graphene,” *Nat Mater*, vol. 20, no. 1, pp. 49–54, Jan. 2021, doi: 10.1038/s41563-020-0738-0.

[153] J. Lee, X. Zheng, R. C. Roberts, and P. X. L. Feng, “Scanning electron microscopy characterization of structural features in suspended and non-suspended graphene by customized CVD growth,” *Diam Relat Mater*, vol. 54, no. 1, pp. 64–73, Apr. 2015, doi: 10.1016/j.diamond.2014.11.012.

[154] Z. Hu *et al.*, “Rapid and Scalable Transfer of Large-Area Graphene Wafers,” *Advanced Materials*, p. 2300621, 2023, doi: 10.1002/ADMA.202300621.

[155] M. R. Anisur, R. K. S. Raman, P. C. Banerjee, S. Al-Saadi, and A. K. Arya, “Review of the role of CVD growth parameters on graphene coating characteristics and the resulting corrosion resistance,” *Surf Coat Technol*, vol. 487, p. 130934, Jul. 2024, doi: 10.1016/J.SURFCOAT.2024.130934.

[156] X. Li *et al.*, “Transfer of large-area graphene films for high-performance transparent conductive electrodes,” *Nano Lett*, vol. 9, no. 12, pp. 4359–4363, Dec. 2009, doi: 10.1021/nl902623y.

[157] P. Blake *et al.*, “Making graphene visible,” *Appl Phys Lett*, vol. 91, no. 6, p. 063124, Aug. 2007, doi: 10.1063/1.2768624.

[158] S. Wagner, C. Weisenstein, A. D. Smith, M. Östling, S. Kataria, and M. C. Lemme, “Graphene transfer methods for the fabrication of membrane-based NEMS devices,” *Microelectron Eng*, vol. 159, pp. 108–113, Jun. 2016, doi: 10.1016/j.mee.2016.02.065.

[159] J. D. Caldwell *et al.*, “Technique for the dry transfer of epitaxial graphene onto arbitrary substrates,” in *ACS Nano*, American Chemical Society, Feb. 2010, pp. 1108–1114. doi: 10.1021/nn901585p.

[160] J. W. Suk *et al.*, “Transfer of CVD-Grown Monolayer Graphene onto Arbitrary Substrates,” *ACS Nano*, vol. 5, no. 9, pp. 6916–6924, Sep. 2011, doi: 10.1021/NN201207C.

[161] A. Pirkle *et al.*, “The effect of chemical residues on the physical and electrical properties of chemical vapor deposited graphene transferred to SiO2,” *Appl Phys Lett*, vol. 99, no. 12, p. 122108, Sep. 2011, doi: 10.1063/1.3643444.

[162] W. Choi, M. A. Shehzad, S. Park, and Y. Seo, “Influence of removing PMMA residues on surface of CVD graphene using a contact-mode atomic force microscope,” *RSC Adv*, vol. 7, no. 12, pp. 6943–6949, Jan. 2017, doi: 10.1039/c6ra27436f.

[163] J. Kang, D. Shin, S. Bae, and B. H. Hong, “Graphene transfer: Key for applications,” Sep. 21, 2012, *Royal Society of Chemistry*. doi: 10.1039/c2nr31317k.

[164] Z. Liu, P. You, C. Xie, G. Tang, and F. Yan, “Ultrathin and flexible perovskite solar cells with graphene transparent electrodes,” *Nano Energy*, vol. 28, pp. 151–157, Oct. 2016, doi: 10.1016/j.nanoen.2016.08.038.

[165] H. Sung *et al.*, “Transparent Conductive Oxide-Free Graphene-Based Perovskite Solar Cells with over 17% Efficiency,” *Adv Energy Mater*, vol. 6, no. 3, p. 1501873, Feb. 2016, doi: 10.1002/AENM.201501873.

[166] V. D. Tran, S. V. N. Pammi, B. J. Park, Y. Han, C. Jeon, and S. G. Yoon, “Transfer-free graphene electrodes for super-flexible and semi-transparent perovskite solar cells fabricated under ambient air,” *Nano Energy*, vol. 65, p. 104018, Nov. 2019, doi: 10.1016/J.NANOEN.2019.104018.

[167] J. Yoon *et al.*, “Superflexible, high-efficiency perovskite solar cells utilizing graphene electrodes: towards future foldable power sources,” *Energy Environ Sci*, vol. 10, no. 1, pp. 337–345, Jan. 2017, doi: 10.1039/C6EE02650H.

[168] J. H. Heo, D. H. Shin, M. H. Jang, M. L. Lee, M. G. Kang, and S. H. Im, “Highly flexible, high-performance perovskite solar cells with adhesion promoted AuCl3-doped graphene electrodes,” *J Mater Chem A Mater*, vol. 5, no. 40, pp. 21146–21152, Oct. 2017, doi: 10.1039/C7TA06465A.

[169] S. Fernández *et al.*, “Advanced Graphene-Based Transparent Conductive Electrodes for Photovoltaic Applications,” *Micromachines (Basel)*, vol. 10, no. 6, p. 402, Jun. 2019, doi: 10.3390/MI10060402.

[170] L. Lancellotti *et al.*, “Graphene as non conventional transparent conductive electrode in silicon heterojunction solar cells,” *Appl Surf Sci*, vol. 525, p. 146443, Sep. 2020, doi: 10.1016/J.APSUSC.2020.146443.

[171] I. Torres, S. Fernández, M. Fernández-Vallejo, I. Arnedo, and J. J. Gandía, “Graphene-Based Electrodes for Silicon Heterojunction Solar Cell Technology,” *Materials 2021, Vol. 14, Page 4833*, vol. 14, no. 17, p. 4833, Aug. 2021, doi: 10.3390/MA14174833.

[172] B. Guo, L. Fang, B. Zhang, and J. R. Gong, “Graphene Doping: A Review,” *Insciences Journal | Nanotechnology ISSN 1664-171X Insciences Journal*, vol. 1, no. 2, pp. 80–89, 2011, doi: 10.5640/insc.010280.

[173] C. Zhang, L. Fu, N. Liu, M. Liu, Y. Wang, and Z. Liu, “Synthesis of nitrogen-doped graphene using embedded carbon and nitrogen sources,” *Advanced Materials*, vol. 23, no. 8, pp. 1020–1024, Feb. 2011, doi: 10.1002/adma.201004110.

[174] Y. F. Lu *et al.*, “Nitrogen-doped graphene sheets grown by chemical vapor deposition: Synthesis and influence of nitrogen impurities on carrier transport,” *ACS Nano*, vol. 7, no. 8, pp. 6522–6532, Aug. 2013, doi: 10.1021/NN402102Y/SUPPL_FILE/NN402102Y_SI_001.PDF.

[175] J. Narayan and K. Bezborah, “Recent advances in the functionalization, substitutional doping and applications of graphene/graphene composite nanomaterials,” *RSC Adv*, vol. 14, no. 19, pp. 13413–13444, Apr. 2024, doi: 10.1039/D3RA07072G.

[176] A. Capasso *et al.*, “Nitrogen-doped graphene films from chemical vapor deposition of pyridine: Influence of process parameters on the electrical and optical properties,” *Beilstein Journal of Nanotechnology*, vol. 6, no. 1, pp. 2028–2038, Oct. 2015, doi: 10.3762/bjnano.6.206.

[177] S. Shin *et al.*, “Highly stable self-passivated MoO3-doped graphene film with nonvolatile MoOx layer,” *Mater Today Commun*, vol. 33, p. 104432, Dec. 2022, doi: 10.1016/J.MTCOMM.2022.104432.

[178] S. L. Hellstrom *et al.*, “Strong and stable doping of carbon nanotubes and graphene by MoO x for transparent electrodes,” *Nano Lett*, vol. 12, no. 7, pp. 3574–3580, Jul. 2012, doi: 10.1021/NL301207E/SUPPL_FILE/NL301207E_SI_001.PDF.

[179] S. Li *et al.*, “Transparent-conductive-oxide-free front contacts for high-efficiency silicon heterojunction solar cells,” *Joule*, vol. 5, no. 6, pp. 1535–1547, Jun. 2021, doi: 10.1016/J.JOULE.2021.04.004.

[180] J.-M. Choi *et al.*, “Overview and Outlook on Graphene and Carbon Nanotubes in Perovskite Photovoltaics from Single-Junction to Tandem Applications,” *Adv Funct Mater*, vol. 32, no. 42, p. 2204594, Oct. 2022, doi: 10.1002/ADFM.202204594.

[181] A. V. Klekachev, A. Nourbakhsh, I. Asselberghs, A. L. Stesmans, M. M. Heyns, and S. De Gendt, “Graphene Transistors and Photodetectors,” *Electrochem Soc Interface*, vol. 22, no. 1, p. 63, Jan. 2013, doi: 10.1149/2.F07131IF.

[182] A. Paradisi, J. Biscaras, and A. Shukla, “Space charge induced electrostatic doping of two-dimensional materials: Graphene as a case study,” *Appl Phys Lett*, vol. 107, no. 14, p. 143103, Oct. 2015, doi: 10.1063/1.4932572.

[183] R. S. Bonilla and P. R. Wilshaw, “A technique for field effect surface passivation for silicon solar cells,” *Appl Phys Lett*, vol. 104, no. 23, p. 232903, Jun. 2014, doi: 10.1063/1.4882161.

[184] R. S. Bonilla and P. R. Wilshaw, “Potassium ions in SiO2: electrets for silicon surface passivation,” *J Phys D Appl Phys*, vol. 51, no. 2, p. 025101, Dec. 2017, doi: 10.1088/1361-6463/AA9B1B.

[185] R. S. Bonilla, C. Reichel, M. Hermle, P. Hamer, and P. R. Wilshaw, “Long term stability of c-Si surface passivation using corona charged SiO 2,” *Appl Surf Sci*, vol. 412, pp. 657–667, Aug. 2017, doi: 10.1016/j.apsusc.2017.03.204.

[186] K. Misawa, T. Sugiyama, G. Hashiguchi, and H. Toshiyoshi, “Reliability of potassium ion electret in silicon oxide for vibrational energy harvester applications,” *Jpn J Appl Phys*, vol. 54, no. 6, p. 067201, Jun. 2015, doi: 10.7567/JJAP.54.067201.

[187] K. Misawa *et al.*, “SiO 2 Electret Generated by Potassium Ions on a Comb-Drive Actuator Related content Reliability of potassium ion electret in silicon oxide for vibrational energy harvester applications Mechanical Vibration Characteristics for the Driving Part in Array of ,” *Appl. Phys. Express*, vol. 4, p. 114103, 2011, doi: 10.1143/APEX.4.114103.

[188] R. Woods-Robinson, M. Morales-Masis, G. Hautier, and A. Crovetto, “ From Design to Device: Challenges and Opportunities in Computational Discovery of p -Type Transparent Conductors ,” *PRX Energy*, vol. 3, no. 3, p. 031001, Aug. 2024, doi: 10.1103/PRXENERGY.3.031001/FIGURES/6/MEDIUM.

[189] M. F. Pantano *et al.*, “Investigation of charges-driven interaction between graphene and different SiO 2 surfaces,” *Carbon N Y*, vol. 148, pp. 336–343, Jul. 2019, doi: 10.1016/j.carbon.2019.03.071.

[190] “Floated Borosilicate Glass from SCHOTT, UCQ Optics.” Accessed: Jan. 07, 2025. [Online]. Available: https://www.uqgoptics.com/wp-content/uploads/2019/07/Schott-Borofloat-33.pdf

[191] “Fused Quartz - Fused Quartz Glass - UQG Optics.” Accessed: Jan. 12, 2025. [Online]. Available: https://www.uqgoptics.com/materials/fused-quartz/

[192] X. Xu *et al.*, “A comparison of structures and properties of SiNx and SiOx films prepared by PECVD,” *J Non Cryst Solids*, vol. 358, no. 1, pp. 99–106, Jan. 2012, doi: 10.1016/J.JNONCRYSOL.2011.08.029.

[193] “Monolayer Graphene on Cu with PMMA Coating – Graphenea.” Accessed: Oct. 21, 2024. [Online]. Available: https://www.graphenea.com/collections/buy-graphene-films/products/monolayer-graphene-on-cu-with-pmma-coating-4-inches

[194] J. Moreira, A. C. Vale, and N. M. Alves, “Spin-coated freestanding films for biomedical applications,” *J Mater Chem B*, vol. 9, no. 18, pp. 3778–3799, May 2021, doi: 10.1039/D1TB00233C.

[195] N. G. Semaltianos, “Spin-coated PMMA films,” *Microelectronics J*, vol. 38, no. 6–7, pp. 754–761, Jun. 2007, doi: 10.1016/J.MEJO.2007.04.019.

[196] Y. Mouhamad, P. Mokarian-Tabari, N. Clarke, R. A. L. Jones, and M. Geoghegan, “Dynamics of polymer film formation during spin coating,” *J Appl Phys*, vol. 116, no. 12, p. 30, Sep. 2014, doi: 10.1063/1.4896674/982309.

[197] MicroChem Corp, “ Nano PMMA and Copolymer Processing Guidelines.” Accessed: Oct. 22, 2024. [Online]. Available: https://kayakuam.com/wp-content/uploads/2019/09/PMMA_Data_Sheet.pdf

[198] T. Wei, F. Hauke, A. Hirsch, T. Wei, F. Hauke, and A. Hirsch, “Evolution of Graphene Patterning: From Dimension Regulation to Molecular Engineering,” *Advanced Materials*, vol. 33, no. 45, p. 2104060, Nov. 2021, doi: 10.1002/ADMA.202104060.

[199] T. Wei, L. Bao, F. Hauke, and A. Hirsch, “Recent Advances in Graphene Patterning,” *Chempluschem*, vol. 85, no. 8, pp. 1655–1668, Aug. 2020, doi: 10.1002/CPLU.202000419.

[200] M. Zhang *et al.*, “Patterning of graphene using wet etching with hypochlorite and UV light,” *Scientific Reports 2022 12:1*, vol. 12, no. 1, pp. 1–8, Mar. 2022, doi: 10.1038/s41598-022-08674-3.

[201] A. M. Pérez-Mas, P. Álvarez, N. Campos, D. Gómez, and R. Menéndez, “Graphene patterning by nanosecond laser ablation Graphene patterning by nanosecond laser ablation: The effect of the substrate interaction with graphene”.

[202] Y. Yan, S. Peng, Z. Jin, D. Zhang, and J. Shi, “Recovering the Intrinsic Electrical Property of a Graphene Field-Effect Transistor by Interface Cleaning Technology,” *ACS Appl Electron Mater*, vol. 5, no. 6, pp. 3113–3119, Jun. 2023, doi: 10.1021/ACSAELM.3C00187/ASSET/IMAGES/LARGE/EL3C00187_0005.JPEG.

[203] H. Yun *et al.*, “Removal of photoresist residues and healing of defects on graphene using H2 and CH4 plasma,” *Appl Surf Sci*, vol. 463, pp. 802–808, Jan. 2019, doi: 10.1016/J.APSUSC.2018.08.202.

[204] B. Zhuang, S. Li, S. Li, and J. Yin, “Ways to eliminate PMMA residues on graphene —— superclean graphene,” *Carbon N Y*, vol. 173, pp. 609–636, Mar. 2021, doi: 10.1016/J.CARBON.2020.11.047.

[205] T. Dong, M. Sparkes, C. Durkan, and W. O’Neill, “Evaluating femtosecond laser ablation of graphene on SiO2/Si substrate,” *J Laser Appl*, vol. 28, no. 2, p. 022202, Mar. 2016, doi: 10.2351/1.4944510.

[206] I. I. Bobrinetskiy, A. V. Emelianov, C.-L. Lin, N. Otero, and P. M. Romero, “Ultrafast laser patterning of graphene,” *Nanotechnology VIII*, vol. 10248, p. 1024812, May 2017, doi: 10.1117/12.2265430.

[207] R. Sahin, E. Simsek, and S. Akturk, “Nanoscale patterning of graphene through femtosecond laser ablation,” *Appl Phys Lett*, vol. 104, no. 5, p. 053118, Feb. 2014, doi: 10.1063/1.4864616.

[208] HAG KE, BEHRNDT KH, and KOBIN I, “Adhesion Mechanism of Gold-Underlayer Film Combinations to Oxide Substrates,” *Journal of Vacuum Science and Technology*, vol. 6, no. 1, pp. 148–152, Jan. 1969, doi: 10.1116/1.1492648.

[209] M. M. Shahin, “Mass-spectrometric studies of corona discharges in air at atmospheric pressures,” *J Chem Phys*, vol. 45, no. 7, pp. 2600–2605, May 1966, doi: 10.1063/1.1727980.

[210] M. M. Shahin, “Nature of Charge Carriers in Negative Coronas,” *Applied Optics, Vol. 8, Issue S1, pp. 106-110*, vol. 8, no. 101, pp. 106–110, Jan. 1969, doi: 10.1364/AO.8.S1.000106.

[211] B. L. Henson, “A derivation of Warburg’s law for point to plane coronas,” *J Appl Phys*, vol. 52, no. 6, pp. 3921–3923, Jun. 1981, doi: 10.1063/1.329241.

[212] E. Warburg, “Ueber die Spitzenentladung,” *Ann Phys*, vol. 303, no. 1, pp. 69–83, Jan. 1899, doi: 10.1002/ANDP.18993030104.

[213] K. A. Collett *et al.*, “Scalable Techniques for Producing Field-Effect Passivation in High-Efficiency Silicon Solar Cells,” *IEEE J Photovolt*, vol. 9, no. 1, pp. 26–33, Jan. 2019, doi: 10.1109/JPHOTOV.2018.2872032.

[214] I. R. Al-Dhahir, “Exploiting Extrinsic Passivation on Thin Film Dielectrics for High Efficiency Solar Cells,” PhD thesis, University of Oxford, 2021.

[215] M. Yu *et al.*, “Assessing the Potential of Inversion Layer Solar Cells Based on Highly Charged Dielectric Nanolayers,” *Physica Status Solidi - Rapid Research Letters*, 2021, doi: 10.1002/pssr.202100129.

[216] M. Y. Yu, “Exploiting Ion-Charged Dielectrics for High Efficiency Solar Cell Architectures,” PhD thesis, University of Oxford, 2023.

[217] F. Qing *et al.*, “A general and simple method for evaluating the electrical transport performance of graphene by the van der Pauw–Hall measurement,” *Sci Bull (Beijing)*, vol. 63, no. 22, pp. 1521–1526, Nov. 2018, doi: 10.1016/J.SCIB.2018.10.007.

[218] L. J. van der Pauw, “A method of measuring specific resistivity and hall effect of discs of arbitrary shape,” *Philips Research Reports*, no. 13, pp. 1–9, Jan. 1958, doi: 10.1142/9789814503464_0017.

[219] L. . J. Van der Pauw, “A Method of Measuring the Resistivity and Hall Coefficient on Lamellae of Arbitrary Shape,” *Philips Research Reports*, no. 20, pp. 220–224, 1958, Accessed: Oct. 24, 2024. [Online]. Available: https://www.scirp.org/reference/referencespapers?referenceid=1320944

[220] D. W. Koon, M. Heřmanová, and J. Náhlík, “Electrical conductance sensitivity functions for square and circular cloverleaf van der Pauw geometries,” *Meas Sci Technol*, vol. 26, no. 11, p. 115004, Sep. 2015, doi: 10.1088/0957-0233/26/11/115004.

[221] R. Chwang, B. J. Smith, and C. R. Crowell, “Contact size effects on the van der Pauw method for resistivity and Hall coefficient measurement,” *Solid State Electron*, vol. 17, no. 12, pp. 1217–1227, Dec. 1974, doi: 10.1016/0038-1101(74)90001-X.

[222] G. González-Díaz *et al.*, “A robust method to determine the contact resistance using the van der Pauw set up,” *Measurement*, vol. 98, pp. 151–158, Feb. 2017, doi: 10.1016/J.MEASUREMENT.2016.11.040.

[223] L. B. Valdes, “Resistivity Measurements on Germanium for Transistors,” *Proceedings of the IRE*, vol. 42, no. 2, pp. 420–427, 1954, doi: 10.1109/JRPROC.1954.274680.

[224] D. M. A. MacKenzie *et al.*, “Wafer-scale graphene quality assessment using micro four-point probe mapping,” *Nanotechnology*, vol. 31, no. 22, p. 225709, Mar. 2020, doi: 10.1088/1361-6528/AB7677.

[225] J. Ding, F. T. Fisher, and E.-H. Yang, “Direct transfer of corrugated graphene sheets as stretchable electrodes,” *Journal of Vacuum Science & Technology B, Nanotechnology and Microelectronics: Materials, Processing, Measurement, and Phenomena*, vol. 34, no. 5, Sep. 2016, doi: 10.1116/1.4961594/593410.

[226] L. J. Swartzendruber, “Four-point probe measurement of non-uniformities in semiconductor sheet resistivity,” *Solid State Electron*, vol. 7, no. 6, pp. 413–422, Jun. 1964, doi: 10.1016/0038-1101(64)90038-3.

[227] F. M. Smits, “Measurement of Sheet Resistivities with the Four-Point Probe,” *Bell System Technical Journal*, vol. 37, no. 3, pp. 711–718, 1958, doi: 10.1002/J.1538-7305.1958.TB03883.X.

[228] S. B. Mitta *et al.*, “Electrical characterization of 2D materials-based field-effect transistors,” *2d Mater*, vol. 8, no. 1, p. 012002, Nov. 2020, doi: 10.1088/2053-1583/ABC187.

[229] D. K. Schroder, “Semiconductor Material and Device Characterization: Third Edition,” *Semiconductor Material and Device Characterization: Third Edition*, pp. 1–779, Apr. 2005, doi: 10.1002/0471749095.

[230] D. A. . Neamen, “Semiconductor physics and devices : basic principles,” p. 746, 2003.

[231] B. J. Gordon, “C-V plotting: myths and methods,” *Solid State Technology*, vol. 36, no. 1, pp. 57–62, Jan. 1993, Accessed: Oct. 31, 2024. [Online]. Available:

https://go.gale.com/ps/i.do?p=AONE&sw=w&issn=0038111X&v=2.1&it=r&id=GALE%7CA13468387&sid=googleScholar&linkaccess=fulltext

[232] P. Blood, "Capacitance-voltage profiling and the characterisation of III-V semiconductors using electrolyte barriers," *Semicond Sci Technol*, vol. 1, no. 1, p. 7, Jul. 1986, doi: 10.1088/0268-1242/1/1/002.

[233] T. W. Hickmott, "Thermally stimulated ionic conductivity of sodium in thermal SiO2," *J Appl Phys*, vol. 46, no. 6, p. 2583, Sep. 2008, doi: 10.1063/1.321935.

[234] P. Willke *et al.*, "Local transport measurements in graphene on SiO2 using Kelvin probe force microscopy," *Carbon N Y*, vol. 102, pp. 470–476, Jun. 2016, doi: 10.1016/J.CARBON.2016.02.067.

[235] R. S. Bonilla, "Modelling of Kelvin probe surface voltage and photovoltage in dielectric-semiconductor interfaces," *Mater Res Express*, vol. 9, no. 8, p. 085901, Aug. 2022, doi: 10.1088/2053-1591/AC84C8.

[236] C. E. Kehayias, S. MacNaughton, S. Sonkusale, and C. Staii, "Kelvin probe microscopy and electronic transport measurements in reduced graphene oxide chemical sensors," *Nanotechnology*, vol. 24, no. 24, p. 245502, May 2013, doi: 10.1088/0957-4484/24/24/245502.

[237] I. D. Baikie, S. Mackenzie, P. J. Z. Estrup, and J. A. Meyer, "Noise and the Kelvin method," *Review of Scientific Instruments*, vol. 62, no. 5, pp. 1326–1332, May 1991, doi: 10.1063/1.1142494.

[238] R. S. Bonilla, N. Jennison, D. Clayton-Warwick, K. A. Collett, L. Rands, and P. R. Wilshaw, "Corona Charge in SiO2: Kinetics and Surface Passivation for High

Efficiency Silicon Solar Cells," *Energy Procedia*, vol. 92, pp. 326–335, Aug. 2016, doi: 10.1016/J.EGYPRO.2016.07.090.

[239] R. S. Bonilla Osorio, "Surface passivation for silicon solar cells," University of Oxford, 2015.

[240] C. V Raman, "A new radiation," *Indian J. Phys*, vol. 2, pp. 387–398, 1928.

[241] "C.V. Raman The Raman Effect - Landmark - American Chemical Society." Accessed: May 10, 2025. [Online]. Available: https://www.acs.org/education/whatischemistry/landmarks/ramaneffect.html

[242] J. R. Ferraro, K. Nakamoto, and C. W. Brown, *Introductory Raman Spectroscopy*, Second Edition. 2003. Accessed: May 10, 2025. [Online]. Available: https://www.sciencedirect.com/book/9780122541056/introductory-raman-spectroscopy

[243] A. McCreary *et al.*, "Quasi-two-dimensional magnon identification in antiferromagnetic FeP S3 via magneto-Raman spectroscopy," *Phys Rev B*, vol. 101, no. 6, p. 064416, Feb. 2020, doi: 10.1103/PHYSREVB.101.064416/FIGURES/4/MEDIUM.

[244] L. M. Malard, M. A. Pimenta, G. Dresselhaus, and M. S. Dresselhaus, "Raman spectroscopy in graphene," *Phys Rep*, vol. 473, no. 5–6, pp. 51–87, Apr. 2009, doi: 10.1016/J.PHYSREP.2009.02.003.

[245] M. S. Dresselhaus, A. Jorio, and R. Saito, "Characterizing graphene, graphite, and carbon nanotubes by Raman spectroscopy," *Annu Rev Condens Matter Phys*, vol. 1, no. Volume 1, 2010, pp. 89–108, Jul. 2010, doi: 10.1146/ANNUREV-CONMATPHYS-070909-103919/CITE/REFWORKS.

[246] A. C. Ferrari and D. M. Basko, “Raman spectroscopy as a versatile tool for studying the properties of graphene,” *Nature Nanotechnology 2013 8:4*, vol. 8, no. 4, pp. 235–246, Apr. 2013, doi: 10.1038/nnano.2013.46.

[247] A. C. Ferrari *et al.*, “Raman spectrum of graphene and graphene layers,” *Phys Rev Lett*, vol. 97, no. 18, p. 187401, Oct. 2006, doi: 10.1103/PhysRevLett.97.187401.

[248] M. A. Pimenta, G. Dresselhaus, M. S. Dresselhaus, L. G. Cançado, A. Jorio, and R. Saito, “Studying disorder in graphite-based systems by Raman spectroscopy,” *Physical Chemistry Chemical Physics*, vol. 9, no. 11, pp. 1276–1290, Mar. 2007, doi: 10.1039/B613962K.

[249] R. Fates, H. Bouridah, and J.-P. Raskin, “Probing carrier concentration in gated single, bi- and tri-layer CVD graphene using Raman spectroscopy,” *Carbon N Y*, vol. 149, pp. 390–399, Aug. 2019, doi: 10.1016/j.carbon.2019.04.078.

[250] A. Das *et al.*, “Monitoring dopants by Raman scattering in an electrochemically top-gated graphene transistor,” *Nature Nanotechnology 2008 3:4*, vol. 3, no. 4, pp. 210–215, Mar. 2008, doi: 10.1038/nnano.2008.67.

[251] M. Bruna, A. K. Ott, M. Ijäs, D. Yoon, U. Sassi, and A. C. Ferrari, “Doping dependence of the Raman spectrum of defected graphene,” *ACS Nano*, vol. 8, no. 7, pp. 7432–7441, Jul. 2014, doi: 10.1021/NN502676G/ASSET/IMAGES/MEDIUM/NN-2014-02676G_0011.GIF.

[252] D. M. Basko, S. Piscanec, and A. C. Ferrari, “Electron-electron interactions and doping dependence of the two-phonon Raman intensity in graphene,” *Phys Rev B*, vol. 80, no. 16, p. 165413, Oct. 2009, doi: 10.1103/PHYSREVB.80.165413/FIGURES/4/MEDIUM.

[253] J. Bin Wu, M. L. Lin, X. Cong, H. N. Liu, and P. H. Tan, “Raman spectroscopy of graphene-based materials and its applications in related devices,” *Chem Soc Rev*, vol. 47, no. 5, pp. 1822–1873, Mar. 2018, doi: 10.1039/C6CS00915H.

[254] C. V. Cushman, Nicholas. Smith, Massoud. Kaykhaii, N. J. Podraza, and M. R. Linford, “An Introduction to Modeling in Spectroscopic Ellipsometry, Focusing on Models for Transparent Materials: the Cauchy and Sellmeier Models,” *Vacuum Coatings and Technology*, Jun. 2016.

[255] R. Pascu and M. Dinescu, “Spectroscopic Ellipsometry,” *Rom Rep Phys*, vol. 64, no. 1, pp. 135–142, 2012.

[256] G. E. Jellison, “Optical functions of silicon determined by two-channel polarization modulation ellipsometry,” *Opt Mater (Amst)*, vol. 1, no. 1, pp. 41–47, Jan. 1992, doi: 10.1016/0925-3467(92)90015-F.

[257] M. Bass, “Handbook of Optics,” 2010.

[258] E. D. Palik, “Handbook of Optical Constants of Solids, Volumes I, II, and III,” p. 821, 1998, Accessed: Oct. 31, 2024. [Online]. Available: http://books.google.com/books?id=rxuG1kXvSqgC

[259] J. Dong, H. Wang, H. Peng, Z. Liu, K. Zhang, and F. Ding, “Formation mechanism of overlapping grain boundaries in graphene chemical vapor deposition growth,” *Chem Sci*, vol. 8, no. 3, pp. 2209–2214, Feb. 2017, doi: 10.1039/C6SC04535A.

[260] J. Y. Lee *et al.*, “Direct observation of grain boundaries in chemical vapor deposited graphene,” *Carbon N Y*, vol. 115, pp. 147–153, May 2017, doi: 10.1016/J.CARBON.2017.01.009.

[261] M. Lockett, V. Sarmiento, M. Balingit, M. T. Oropeza-Guzmán, and O. Vázquez-Mena, "Direct chemical conversion of continuous CVD graphene/graphite films to graphene oxide without exfoliation," *Carbon N Y*, vol. 158, pp. 202–209, Mar. 2020, doi: 10.1016/J.CARBON.2019.10.076.

[262] R. S. Bonilla, B. Hoex, P. Hamer, and P. R. Wilshaw, "Dielectric surface passivation for silicon solar cells: A review," *Physica Status Solidi (A) Applications and Materials Science*, vol. 214, no. 7, p. 1700293, Jul. 2017, doi: 10.1002/pssa.201700293.

[263] T. Ohmi and H. Mishima, "Static Charge Removal with IPA Solution," *IEEE Transactions on Semiconductor Manufacturing*, vol. 7, no. 4, pp. 440–446, 1994, doi: 10.1109/66.330281.

[264] H. Park *et al.*, "Evaluation of the average grain size of polycrystalline graphene using an electrical characterization method," *Solid State Electron*, vol. 186, p. 108172, Dec. 2021, doi: 10.1016/J.SSE.2021.108172.

[265] Y. Jia *et al.*, "Toward High Carrier Mobility and Low Contact Resistance: Laser Cleaning of PMMA Residues on Graphene Surfaces," *Nanomicro Lett*, vol. 8, no. 4, pp. 336–346, Oct. 2016, doi: 10.1007/S40820-016-0093-5/FIGURES/6.

[266] Y. Dan, Y. Lu, N. J. Kybert, Z. Luo, and A. T. C. Johnson, "Intrinsic response of graphene vapor sensors," *Nano Lett*, vol. 9, no. 4, pp. 1472–1475, Apr. 2009, doi: 10.1021/NL8033637/ASSET/IMAGES/LARGE/NL-2008-033637_0001.JPEG.

[267] C. Melios *et al.*, "Effects of humidity on the electronic properties of graphene prepared by chemical vapour deposition," *Carbon N Y*, vol. 103, pp. 273–280, Jul. 2016, doi: 10.1016/J.CARBON.2016.03.018.

[268] Y. Yang, K. Brenner, and R. Murali, “The influence of atmosphere on electrical transport in graphene,” *Carbon N Y*, vol. 50, no. 5, pp. 1727–1733, Apr. 2012, doi: 10.1016/J.CARBON.2011.12.008.

[269] H. Lee, K. Paeng, and I. S. Kim, “A review of doping modulation in graphene,” *Synth Met*, vol. 244, pp. 36–47, Oct. 2018, doi: 10.1016/J.SYNTHMET.2018.07.001.

[270] C. Berger *et al.*, “Electronic confinement and coherence in patterned epitaxial graphene,” *Science (1979)*, vol. 312, no. 5777, pp. 1191–1196, May 2006, doi: 10.1126/science.1125925.

[271] W. S. Leong *et al.*, “Paraffin-enabled graphene transfer,” *Nat Commun*, vol. 10, no. 1, pp. 1–8, Dec. 2019, doi: 10.1038/s41467-019-08813-x.

[272] Y. Song, W. Fang, A. L. Hsu, and J. Kong, “Iron (III) Chloride doping of CVD graphene,” *Nanotechnology*, vol. 25, no. 39, p. 395701, Oct. 2014, doi: 10.1088/0957-4484/25/39/395701.

[273] W. Li *et al.*, “Broadband optical properties of graphene by spectroscopic ellipsometry,” *Carbon N Y*, vol. 99, pp. 348–353, Apr. 2016, doi: 10.1016/J.CARBON.2015.12.007.

[274] X. Ma and H. Zhang, “Fabrication of graphene films with high transparent conducting characteristics,” *Nanoscale Res Lett*, vol. 8, no. 1, pp. 1–6, Oct. 2013, doi: 10.1186/1556-276X-8-440/FIGURES/6.

[275] T. Usui, C. A. Donnelly, M. Logar, R. Sinclair, J. Schoonman, and F. B. Prinz, “Approaching the limits of dielectric breakdown for SiO2 films deposited by plasma-enhanced atomic layer deposition,” *Acta Mater*, vol. 61, no. 20, pp. 7660–7670, Dec. 2013, doi: 10.1016/J.ACTAMAT.2013.09.003.

[276] D. R. Kerr, “Effect of Temperature and Bias on Glass-Silicon Interfaces,” *IBM J Res Dev*, vol. 8, no. 4, pp. 385–393, Apr. 2010, doi: 10.1147/RD.84.0385.

[277] D. R. Kerr, “A Review of Instability Mechanisms in Passivation Films,” pp. 1–8, Jun. 2007, doi: 10.1109/IRPS.1970.362425.

[278] E. H. Snow, A. S. Grove, B. E. Deal, and C. T. Sah, “Ion Transport Phenomena in Insulating Films,” *J Appl Phys*, vol. 36, no. 5, pp. 1664–1673, May 1965, doi: 10.1063/1.1703105.

[279] M. Yamin, “Charge Storage Effects in Silicon Dioxide Films,” *IEEE Trans Electron Devices*, vol. ED-12, no. 3, pp. 88–96, 1965, doi: 10.1109/T-ED.1965.15461.

[280] R. Saito, M. Nagatomo, N. Makino, S. Hayashi, and M. Kudo, “Characterization of ion-induced sodium migration in various kinds of silicon oxide films,” *Appl Surf Sci*, vol. 203–204, pp. 508–511, Jan. 2003, doi: 10.1016/S0169-4332(02)00723-7.

[281] B. R. Singh, S. S. Rai, and R. S. Srivastava, “Transport of sodium ions in silicon dioxide films using MOS structure,” *physica status solidi (a)*, vol. 13, no. 1, pp. 51–59, Sep. 1972, doi: 10.1002/PSSA.2210130103.

[282] G. ; Greeuw and J. F. Verwey, “The mobility of Na+, Li+, and K+ ions in thermally grown SiO2 films,” *Ion Transport Phenomena in Insulating Films Journal of Applied Physics*, vol. 56, no. 8, p. 130, 1984, doi: 10.1063/1.334256.

[283] L. Yang *et al.*, “Thermally evaporated SiO serving as gate dielectric in graphene field-effect transistors,” *IEEE Trans Electron Devices*, vol. 64, no. 4, pp. 1846–1850, 2017, doi: 10.1109/TED.2017.2665598.

[284] “Dielectric Breakdown,” vol. 22, pp. 87–106, Jan. 1990, doi: 10.1016/B978-0-12-234122-9.50011-0.

[285] J. F. Verweij and J. H. Klootwijk, “Dielectric breakdown I: A review of oxide breakdown,” *Microelectronics J*, vol. 27, pp. 611–633, 1996.

[286] N. KLEIN and H. GAFNI, “The Maximum Dielectric Strength of Thin Silicon Oxide Films,” *IEEE Trans Electron Devices*, vol. ED-13, no. 2, pp. 281–289, 1966, doi: 10.1109/T-ED.1966.15681.

[287] K. A. Collett *et al.*, “An enhanced alneal process to produce SRV < 1 cm/s in 1 Ω cm n-type Si,” *Solar Energy Materials and Solar Cells*, vol. 173, pp. 50–58, Dec. 2017, doi: 10.1016/J.SOLMAT.2017.06.022.

[288] G. Shao and G. Shao, “Work Function and Electron Affinity of Semiconductors: Doping Effect and Complication due to Fermi Level Pinning,” *Energy & Environmental Materials*, vol. 4, no. 3, pp. 273–276, Jul. 2021, doi: 10.1002/EEM2.12218.

[289] M. C. James, M. Cattelan, N. A. Fox, R. F. Silva, R. M. Silva, and P. W. May, “Experimental Studies of Electron Affinity and Work Function from Aluminium on Oxidized Diamond (100) and (111) Surfaces,” *physica status solidi (b)*, vol. 258, no. 7, p. 2100027, Jul. 2021, doi: 10.1002/PSSB.202100027.

[290] T. Yoon, Q. Wu, D. J. Yun, S. H. Kim, and Y. J. Song, “Direct tuning of graphene work function via chemical vapor deposition control,” *Scientific Reports 2020 10:1*, vol. 10, no. 1, pp. 1–6, Jun. 2020, doi: 10.1038/s41598-020-66893-y.

[291] N. Dimov, A. Staykov, M. Irfan, M. Kusdhany, and S. M. Lyth, “Tailoring the work function of graphene via defects, nitrogen-doping and hydrogenation: A first principles study,” 2023, doi: 10.1088/1361-6528/ac7ecf.

[292] G. A. Bourret-Sicotte, “Shielded Hydrogen Plasma: A Novel Hydrogenation Method for Silicon Solar Cells”.

[293] W. Xie, L. T. Weng, K. M. Ng, C. K. Chan, and C. M. Chan, “Clean graphene surface through high temperature annealing,” *Carbon N Y*, vol. 94, pp. 740–748, Nov. 2015, doi: 10.1016/J.CARBON.2015.07.046.

[294] Y. C. Lin, C. C. Lu, C. H. Yeh, C. Jin, K. Suenaga, and P. W. Chiu, “Graphene annealing: How clean can it be?,” *Nano Lett*, vol. 12, no. 1, pp. 414–419, Jan. 2012, doi: 10.1021/nl203733r.

[295] M. Tripathi *et al.*, “Cleaning graphene: Comparing heat treatments in air and in vacuum,” *physica status solidi (RRL) – Rapid Research Letters*, vol. 11, no. 8, p. 1700124, Aug. 2017, doi: 10.1002/PSSR.201700124.

[296] D. ; Liu, S. ; Wei, D. Wang, D. Liu, S. Wei, and D. Wang, “Improving the Sensing Properties of Graphene MEMS Pressure Sensor by Low-Temperature Annealing in Atmosphere,” *Sensors (Basel)*, vol. 22, no. 20, p. 8082, Oct. 2022, doi: 10.3390/S22208082.

[297] G. H. Beall, M. Comte, M. J. Dejneka, P. Marques, P. Pradeau, and C. Smith, “Ion-exchange in glass-ceramics,” *Front Mater*, vol. 3, p. 214480, Aug. 2016, doi: 10.3389/FMATS.2016.00041/BIBTEX.

[298] G. V. Bianco, A. Sacchetti, A. Milella, M. M. Giangregorio, S. Dicorato, and G. Bruno, “Defect healing and doping of CVD graphene by thermal sulfurization,” *Nanoscale Adv*, vol. 6, no. 10, pp. 2629–2635, May 2024, doi: 10.1039/D4NA00124A.

[299] D. Guo *et al.*, “Phonon scattering channel and electrical transport of graphene induced by the anharmonic phonon renormalization,” *Physica E Low Dimens Syst Nanostruct*, vol. 155, p. 115827, Jan. 2024, doi: 10.1016/J.PHYSE.2023.115827.

[300] E. A. Kolesov *et al.*, “The effect of atmospheric doping on pressure-dependent Raman scattering in supported graphene,” *Beilstein journal of nanotechnology*, vol. 9, no. 1, pp. 704–710, 2018, doi: 10.3762/BJNANO.9.65.

[301] J. H. Bong, O. Sul, A. Yoon, S. Y. Choi, and B. J. Cho, “Facile graphene n-doping by wet chemical treatment for electronic applications,” *Nanoscale*, vol. 6, no. 15, pp. 8503–8508, Jul. 2014, doi: 10.1039/C4NR01160K.

[302] C. Graham, M. Marchena, B. Paulillo, I. Bhattacharyya, P. Mazumder, and V. Pruneri, “Highly doped graphene on ion-exchanged glass,” *2d Mater*, vol. 10, no. 3, p. 035037, Jun. 2023, doi: 10.1088/2053-1583/ACDBDA.

[303] A. K. Varshneya, “Fundamentals of Inorganic Glasses,” 1994.

[304] M. M. Smedskjaer, J. C. Mauro, R. E. Youngman, C. L. Hogue, M. Potuzak, and Y. Yue, “Topological principles of borosilicate glass chemistry,” *Journal of Physical Chemistry B*, vol. 115, no. 44, pp. 12930–12946, Nov. 2011, doi: 10.1021/JP208796B/ASSET/IMAGES/LARGE/JP-2011-08796B_0005.JPEG.

[305] M. Wang *et al.*, “Ion exchange strengthening and thermal expansion of glasses: Common origin and critical role of network connectivity,” *J Non Cryst Solids*, vol. 455, pp. 70–74, Jan. 2017, doi: 10.1016/J.JNONCRYSOL.2016.10.027.

[306] J. Luo, H. He, N. J. Podraza, L. Qian, C. G. Pantano, and S. H. Kim, “Thermal Poling of Soda-Lime Silica Glass with Nonblocking Electrodes—Part 1: Effects of Sodium Ion Migration and Water Ingress on Glass Surface Structure,” *Journal of the American Ceramic Society*, vol. 99, no. 4, pp. 1221–1230, Apr. 2016, doi: 10.1111/JACE.14081.

[307] G. Y. Odo, L. N. Nogueira, and C. M. Lepienski, “Ionic migration effects on the mechanical properties of glass surfaces,” *J Non Cryst Solids*, vol. 247, no. 1–3, pp. 232–236, Jun. 1999, doi: 10.1016/S0022-3093(99)00076-9.

[308] G. Wallis and D. I. Pomerantz, “Field Assisted Glass-Metal Sealing,” *J Appl Phys*, vol. 40, no. 10, pp. 3946–3949, Sep. 1969, doi: 10.1063/1.1657121.

[309] J. Leib *et al.*, “Anodic bonding at low voltage using microstructured borosilicate glass thin-films,” *Electronics System Integration Technology Conference, ESTC 2010 - Proceedings*, 2010, doi: 10.1109/ESTC.2010.5642923.

[310] F. De Lucia and P. J. A. Sazio, “Thermal Poling of Optical Fibers: A Numerical History,” *Micromachines (Basel)*, vol. 11, no. 2, p. 139, Feb. 2020, doi: 10.3390/MI11020139.

[311] A. Paradisi, J. Biscaras, and A. Shukla, “Inducing conductivity in polycrystalline ZnO1-x thin films through space charge doping,” *J Appl Phys*, vol. 122, no. 9, p. 095301, Sep. 2017, doi: 10.1063/1.5001127.

[312] E. Sterpetti, J. Biscaras, A. Erb, and A. Shukla, “Comprehensive phase diagram of two-dimensional space charge doped Bi2Sr2CaCu2O8+x,” *Nature Communications 2017 8:1*, vol. 8, no. 1, pp. 1–8, Dec. 2017, doi: 10.1038/s41467-017-02104-z.

[313] J. Biscaras, Z. Chen, A. Paradisi, and A. Shukla, “Onset of two-dimensional superconductivity in space charge doped few-layer molybdenum disulfide,” *Nature Communications 2015 6:1*, vol. 6, no. 1, pp. 1–8, Nov. 2015, doi: 10.1038/ncomms9826.

[314] F. Wang, J. Biscaras, A. Erb, and A. Shukla, “Superconductor-insulator transition in space charge doped one unit cell Bi2.1Sr1.9CaCu2O8+x,” *Nature Communications 2021 12:1*, vol. 12, no. 1, pp. 1–6, May 2021, doi: 10.1038/s41467-021-23183-z.

[315] H. Kowalczyk, J. Biscaras, N. Pistawala, L. Harnagea, S. Singh, and A. Shukla, “Gate and Temperature Driven Phase Transitions in Few-Layer MoTe2,” *ACS Nano*, vol. 17, no. 7, pp. 6708–6718, Apr. 2023, doi: 10.1021/ACSNANO.2C12610/ASSET/IMAGES/LARGE/NN2C12610_0007.JPEG.

[316] M. Philippi, I. Gutiérrez-Lezama, N. Ubrig, and A. F. Morpurgo, “Lithium-ion conducting glass ceramics for electrostatic gating,” *Appl Phys Lett*, vol. 113, no. 3, p. 33502, Jul. 2018, doi: 10.1063/1.5038407/37020.

[317] E. Raoult *et al.*, “Iterative method for optical modelling of perovskite-based tandem solar cells,” *Optics Express, Vol. 30, Issue 6, pp. 9604-9622*, vol. 30, no. 6, pp. 9604–9622, Mar. 2022, doi: 10.1364/OE.444698.

[318] Y. Jiang *et al.*, “Optical analysis of perovskite/silicon tandem solar cells,” *J Mater Chem C Mater*, vol. 4, no. 24, pp. 5679–5689, Jun. 2016, doi: 10.1039/C6TC01276K.

[319] K. Brecl, M. Jošt, M. Bokalič, J. Ekar, J. Kovač, and M. Topič, “Are Perovskite Solar Cell Potential-Induced Degradation Proof?,” *Solar RRL*, vol. 6, no. 2, p. 2100815, Feb. 2022, doi: 10.1002/SOLR.202100815.

[320] J. H. Park and J. Y. Kim, “A hurdle in commercializing the perovskite/Si tandem solar cell: Potential-induced degradation,” *Matter*, vol. 5, no. 10, pp. 3091–3093, Oct. 2022, doi: 10.1016/J.MATT.2022.09.015.

[321] J. Oh, S. Bowden, and G. S. TamizhMani, “Potential-Induced Degradation (PID): Incomplete Recovery of Shunt Resistance and Quantum Efficiency Losses,” *IEEE J Photovolt*, vol. 5, no. 6, pp. 1540–1548, Aug. 2015, doi: 10.1109/JPHOTOV.2015.2459919.

[322] W. Luo *et al.*, “Potential-induced degradation in photovoltaic modules: a critical review,” *Energy Environ Sci*, vol. 10, no. 1, pp. 43–68, Jan. 2017, doi: 10.1039/C6EE02271E.

[323] A. Doi and S. Maruno, “Thermally stimulated currents in pyrex and soda-lime glasses,” *J Mater Sci*, vol. 21, no. 6, pp. 1863–1867, Jun. 1986, doi: 10.1007/BF00547920/METRICS.

[324] F. V. Natrup, H. Bracht, S. Murugavel, and B. Roling, “Cation diffusion and ionic conductivity in soda-lime silicate glasses,” *Physical Chemistry Chemical Physics*, vol. 7, no. 11, pp. 2279–2286, May 2005, doi: 10.1039/B502501J.

[325] W. Zhu and B. Lv, “Uncovering the dominant scattering mechanism in graphene system,” *Phys Lett A*, vol. 377, no. 25–27, pp. 1649–1654, Oct. 2013, doi: 10.1016/J.PHYSLETA.2013.04.048.

[326] L. Xu *et al.*, “Potential-induced degradation in perovskite/silicon tandem photovoltaic modules,” *Cell Rep Phys Sci*, vol. 3, no. 9, p. 101026, Sep. 2022, doi: 10.1016/J.XCRP.2022.101026.

[327] E. Aydin *et al.*, “Interplay between temperature and bandgap energies on the outdoor performance of perovskite/silicon tandem solar cells,” *Nature Energy 2020 5:11*, vol. 5, no. 11, pp. 851–859, Sep. 2020, doi: 10.1038/s41560-020-00687-4.

[328] K. Kumar, Y. S. Kim, and E. H. Yang, “The influence of thermal annealing to remove polymeric residue on the electronic doping and morphological characteristics of graphene,” *Carbon N Y*, vol. 65, pp. 35–45, Dec. 2013, doi: 10.1016/J.CARBON.2013.07.088.

[329] V. J. Kapoor and J. P. Delatore, “Effects of oxide thickness on charge trapping in metal-nitride-oxide- semiconductor structures,” *J Appl Phys*, vol. 53, no. 7, pp. 5079–5085, Jul. 1982, doi: 10.1063/1.331340.

[330] V. J. Kapoor and R. A. Turi, “Charge storage and distribution in the nitride layer of the metal-nitride-oxide semiconductor structures,” *J Appl Phys*, vol. 52, no. 1, pp. 311–319, Jan. 1981, doi: 10.1063/1.328495.

[331] V. Leonov and C. Van Hoof, “Multilayer Inorganic Electrets with SiO2 and Si3N4 Layers for Applications on Heated Machinery,” *Smart Materials Research*, vol. 2012, no. 1, p. 904168, Jan. 2012, doi: 10.1155/2012/904168.

[332] W. L. Warren *et al.*, “Electron paramagnetic resonance investigation of charge trapping centers in amorphous silicon nitride films,” *J Appl Phys*, vol. 74, no. 6, pp. 4034–4046, Sep. 1993, doi: 10.1063/1.355315.

[333] J. Robertson, “Defects and hydrogen in amorphous silicon nitride,” *Philosophical Magazine B*, vol. 69, no. 2, pp. 307–326, 1994, doi: 10.1080/01418639408240111.

[334] R. S. Bonilla, C. Reichel, M. Hermle, and P. R. Wilshaw, “On the location and stability of charge in SiO2/SiNx dielectric double layers used for silicon surface passivation,” *J Appl Phys*, vol. 115, no. 14, p. 144105, Apr. 2014, doi: 10.1063/1.4871075/932341.

[335] S. Duttagupta, F. Ma, B. Hoex, T. Mueller, and A. G. Aberle, “Optimised Antireflection Coatings using Silicon Nitride on Textured Silicon Surfaces based on Measurements and Multidimensional Modelling,” *Energy Procedia*, vol. 15, pp. 78–83, Jan. 2012, doi: 10.1016/J.EGYPRO.2012.02.009.

[336] G. Hashmi, M. J. Rashid, Z. H. Mahmood, M. Hoq, and M. H. Rahman, “Investigation of the impact of different ARC layers using PC1D simulation: application to crystalline

silicon solar cells," *Journal of Theoretical and Applied Physics*, vol. 12, no. 4, pp. 327–334, Dec. 2018, doi: 10.1007/S40094-018-0313-0/FIGURES/4.

[337] X. Zhang and G. M. Sessler, "Charge dynamics in silicon nitride/silicon oxide double layers," *Appl Phys Lett*, vol. 78, no. 18, pp. 2757–2759, Apr. 2001, doi: 10.1063/1.1369387.

[338] K. J. Weber and H. Jin, "Improved silicon surface passivation achieved by negatively charged silicon nitride films," *Appl Phys Lett*, vol. 94, no. 6, p. 63509, Feb. 2009, doi: 10.1063/1.3077157/120995.

[339] S. Wang, Y. Zhang, J. Liu, X. Zou, and J. Zhang, "PECVD SiO2/Si3N4 Double-layer Electrets for Application in Micro-devices," *IOP Conf Ser Mater Sci Eng*, vol. 611, no. 1, p. 012088, Oct. 2019, doi: 10.1088/1757-899X/611/1/012088.

[340] V. Sharma, C. Tracy, D. Schroder, M. Flores, B. Dauksher, and S. Bowden, "Study and manipulation of charges present in silicon nitride films," *Conference Record of the IEEE Photovoltaic Specialists Conference*, pp. 1288–1293, 2013, doi: 10.1109/PVSC.2013.6744377.

[341] C. Petridis, G. Kakavelakis, and E. Kymakis, "Renaissance of graphene-related materials in photovoltaics due to the emergence of metal halide perovskite solar cells," *Energy Environ Sci*, vol. 11, no. 5, pp. 1030–1061, May 2018, doi: 10.1039/C7EE03620E.

[342] H. Zhu *et al.*, "Long-term operating stability in perovskite photovoltaics," *Nature Reviews Materials 2023 8:9*, vol. 8, no. 9, pp. 569–586, Aug. 2023, doi: 10.1038/s41578-023-00582-w.

[343] A. Kumar, U. Bansode, S. Ogale, and A. Rahman, “Understanding the thermal degradation mechanism of perovskite solar cells via dielectric and noise measurements,” *Nanotechnology*, vol. 31, no. 36, p. 365403, Jun. 2020, doi: 10.1088/1361-6528/AB97D4.

[344] L. Duan *et al.*, “Stability challenges for the commercialization of perovskite–silicon tandem solar cells,” *Nature Reviews Materials 2023 8:4*, vol. 8, no. 4, pp. 261–281, Jan. 2023, doi: 10.1038/s41578-022-00521-1.

[345] X. Wang, Y. Sun, and K. Liu, “Chemical and structural stability of 2D layered materials,” *2d Mater*, vol. 6, no. 4, p. 042001, Jul. 2019, doi: 10.1088/2053-1583/AB20D6.

[346] A. A. Sagade *et al.*, “Highly air stable passivation of graphene based field effect devices,” *Nanoscale*, vol. 7, no. 8, pp. 3558–3564, Feb. 2015, doi: 10.1039/C4NR07457B.

[347] K. Zhang, Y. Feng, F. Wang, Z. Yang, and J. Wang, “Two dimensional hexagonal boron nitride (2D-hBN): Synthesis, properties and applications,” Nov. 30, 2017, *Royal Society of Chemistry*. doi: 10.1039/c7tc04300g.

[348] J. D. Thomsen *et al.*, “Suppression of intrinsic roughness in encapsulated graphene,” *Phys Rev B*, vol. 96, no. 1, p. 014101, Jul. 2017, doi: 10.1103/PHYSREVB.96.014101/FIGURES/5/MEDIUM.

[349] A. S. Mayorov *et al.*, “Micrometer-Scale Ballistic Transport in Encapsulated Graphene at Room Temperature”.

[350] S. Fukamachi *et al.*, “Large-area synthesis and transfer of multilayer hexagonal boron nitride for enhanced graphene device arrays,” *Nature Electronics 2023 6:2*, vol. 6, no. 2, pp. 126–136, Feb. 2023, doi: 10.1038/s41928-022-00911-x.

[351] J. M. J. Lopes, “Synthesis of hexagonal boron nitride: From bulk crystals to atomically thin films,” *Progress in Crystal Growth and Characterization of Materials*, vol. 67, no. 2, p. 100522, May 2021, doi: 10.1016/J.PCRYSGROW.2021.100522.

[352] W. Huang *et al.*, “Encapsulation strategies on 2D materials for field effect transistors and photodetectors,” *Chinese Chemical Letters*, vol. 33, no. 5, pp. 2281–2290, May 2022, doi: 10.1016/J.CCLET.2021.08.086.

[353] H. K. Seo, M. H. Park, Y. H. Kim, S. J. Kwon, S. H. Jeong, and T. W. Lee, “Laminated Graphene Films for Flexible Transparent Thin Film Encapsulation,” *ACS Appl Mater Interfaces*, vol. 8, no. 23, pp. 14725–14731, Jun. 2016, doi: 10.1021/ACSAMI.6B01639/ASSET/IMAGES/LARGE/AM-2016-016394_0008.JPEG.

[354] N. Park, D. Suh, and H. Kang, “Feasibility of a Dual-Gate Graphene Transistor to Test Various Gate Dielectrics for Two-Dimensional Device Application,” *Journal of the Korean Physical Society*, vol. 77, no. 10, pp. 888–892, Nov. 2020, doi: 10.3938/JKPS.77.888/METRICS.

[355] V. Kedambaimoole, V. Shirhatti, N. Neella, P. Ray, K. Rajanna, and M. M. Nayak, “PDMS encapsulated graphene-nickel composite film as flexible tactile sensor,” *Proceedings of IEEE Sensors*, vol. 2017-December, pp. 1–3, Dec. 2017, doi: 10.1109/ICSENS.2017.8233967.

[356] N. Delikoukos, S. Katsiaounis, J. Parthenios, L. Sygellou, D. Tasis, and K. Papagelis, “Probing Electronic Doping in CVD Graphene Crystals Treated by HNO3 Vapors,” *ACS*

Omega, Dec. 2024, doi: 10.1021/ACSOMEGA.4C05697/ASSET/IMAGES/LARGE/AO4C05697_0003.JPEG.

[357] X. Wan *et al.*, "Graphene transport properties upon exposure to PMMA processing and heat treatments," *2d Mater*, vol. 1, no. 3, p. 035005, Nov. 2014, doi: 10.1088/2053-1583/1/3/035005.

[358] D. Hughes *et al.*, "Effectiveness of poly(methyl methacrylate) spray encapsulation for perovskite solar cells," *Journal of Physics: Energy*, vol. 6, no. 2, p. 025001, Feb. 2024, doi: 10.1088/2515-7655/AD20F5.

[359] H. Alles, J. Aarik, J. Kozlova, A. Niilisk, R. Rammula, and V. Sammelselg, "7 Atomic Layer Deposition of High-k Oxides on Graphene".

[360] A. Kumar, P. Tyagi, J. Dagar, and R. Srivastava, "Tunable field effect properties in solid state and flexible graphene electronics on composite high – low k dielectric," *Carbon N Y*, vol. 99, pp. 579–584, Apr. 2016, doi: 10.1016/J.CARBON.2015.12.073.

[361] A. Sanne, H. C. P. Movva, S. Kang, C. McClellan, C. M. Corbet, and S. K. Banerjee, "Poly(methyl methacrylate) as a self-assembled gate dielectric for graphene field-effect transistors," *Appl Phys Lett*, vol. 104, no. 8, p. 83106, Feb. 2014, doi: 10.1063/1.4866338/132700.

[362] "The optical and electrical characteristics of PMMA film prepared by spin coating method", doi: 10.1088/1757-899X/87/1/012032.

[363] T. Nam *et al.*, "A composite layer of atomic-layer-deposited Al2O3 and graphene for flexible moisture barrier," *Carbon N Y*, vol. 116, pp. 553–561, May 2017, doi: 10.1016/J.CARBON.2017.02.023.

[364] B. Dlubak, P. R. Kidambi, R. S. Weatherup, S. Hofmann, and J. Robertson, "Substrate-assisted nucleation of ultra-thin dielectric layers on graphene by atomic layer deposition," *Appl Phys Lett*, vol. 100, no. 17, p. 173113, Apr. 2012, doi: 10.1063/1.4707376/384688.

[365] R. H. J. Vervuurt, W. M. M. E. Kessels, and A. A. Bol, "Atomic Layer Deposition for Graphene Device Integration," *Adv Mater Interfaces*, vol. 4, no. 18, p. 1700232, Sep. 2017, doi: 10.1002/ADMI.201700232.

[366] B. Fallahazad, S. Kim, L. Colombo, and E. Tutuc, "Dielectric thickness dependence of carrier mobility in graphene with HfO2 top dielectric," *Appl Phys Lett*, vol. 97, no. 12, p. 123105, Sep. 2010, doi: 10.1063/1.3492843/810528.

[367] A. Alnuaimi, I. Almansouri, I. Saadat, and A. Nayfeh, "High performance graphene-silicon Schottky junction solar cells with HfO2 interfacial layer grown by atomic layer deposition," *Solar Energy*, vol. 164, pp. 174–179, Apr. 2018, doi: 10.1016/j.solener.2018.02.020.

[368] B. Canto *et al.*, "Plasma-Enhanced Atomic Layer Deposition of Al2O3 on Graphene Using Monolayer hBN as Interfacial Layer," *Adv Mater Technol*, vol. 6, no. 11, p. 2100489, Nov. 2021, doi: 10.1002/ADMT.202100489.

[369] S. U. Lee, H. Park, H. Shin, and N. G. Park, "Atomic layer deposition of SnO2 using hydrogen peroxide improves the efficiency and stability of perovskite solar cells," *Nanoscale*, vol. 15, no. 10, pp. 5044–5052, Mar. 2023, doi: 10.1039/D2NR06884B.

[370] M. Boubaya and G. Blaise, "Charging regime of PMMA studied by secondary electron emission," *The European Physical Journal Applied Physics*, vol. 37, no. 1, pp. 79–86, Jan. 2007, doi: 10.1051/EPJAP:2006128.

[371] C. Lili, J. Jian, X. Zhongfu, C. Gangjin, and W. Zhenzhong, “Charge storage and transport in polymethylmethacrylate (PMMA) film,” *J Electrostat*, vol. 44, no. 1–2, pp. 61–65, Jul. 1998, doi: 10.1016/S0304-3886(98)00023-0.

[372] N. E. Grant *et al.*, “Activation of Al2O3 surface passivation of silicon: Separating bulk and surface effects,” *Appl Surf Sci*, vol. 645, p. 158786, Feb. 2024, doi: 10.1016/J.APSUSC.2023.158786.

[373] D. Suh and W. S. Liang, “Electrical properties of atomic layer deposited Al2O3 with anneal temperature for surface passivation,” *Thin Solid Films*, vol. 539, pp. 309–316, Jul. 2013, doi: 10.1016/J.TSF.2013.05.082.

[374] R. Goseki and T. Ishizone, “Poly(methyl methacrylate) (PMMA),” *Encyclopedia of Polymeric Nanomaterials*, pp. 1702–1710, 2015, doi: 10.1007/978-3-642-29648-2_244.

[375] P. K. C. Pillai, T. C. Goel, and A. K. Tripathi, “Surface potential decay characteristics of corona charged CuPh-PMMA layers,” *J Mater Sci Lett*, vol. 4, no. 9, pp. 1131–1134, Sep. 1985, doi: 10.1007/BF00720434/METRICS.

[376] S. V. Tewari, R. Chandra, S. K. Sharma, R. Sarathi, A. Sharma, and K. C. Mittal, “Surface potential decay of PMMA and POM in air,” *Mater. Res. Express*, vol. 2, p. 45301, 2015, doi: 10.1088/2053-1591/2/4/045301.

[377] “Charge decay on both surfaces of charged stereoregular PMMA films | IEEE Conference Publication | IEEE Xplore.” Accessed: Jan. 16, 2025. [Online]. Available: https://ieeexplore.ieee.org/document/7341507

[378] A. Lartsev *et al.*, “Tuning carrier density across Dirac point in epitaxial graphene on SiC by corona discharge,” *Appl Phys Lett*, vol. 105, no. 6, p. 63106, Aug. 2014, doi: 10.1063/1.4892922/384927.

[379] M. B. González, J. M. Rafí, O. Beldarrain, M. Zabala, and F. Campabadal, “Charge trapping analysis of Al2O3 films deposited by atomic layer deposition using H2O or O3 as oxidant,” *Journal of Vacuum Science & Technology B, Nanotechnology and Microelectronics: Materials, Processing, Measurement, and Phenomena*, vol. 31, no. 1, pp. 1–101, Jan. 2013, doi: 10.1116/1.4766182/466628.

[380] Z. Xin *et al.*, “Passivation Mechanisms of Atomic Layer-deposited AlOx Films and AlOx/SiOx Stack,” *IOP Conf Ser Mater Sci Eng*, vol. 585, no. 1, p. 012026, Jul. 2019, doi: 10.1088/1757-899X/585/1/012026.

[381] R. H. J. Vervuurt, B. Karasulu, M. A. Verheijen, W. (Erwin) M. M. Kessels, and A. A. Bol, “Uniform Atomic Layer Deposition of Al $_2$ O $_3$ on Graphene by Reversible Hydrogen Plasma Functionalization,” *Chemistry of Materials*, vol. 29, no. 5, Mar. 2017, doi: 10.1021/acs.chemmater.6b04368.

[382] Z. Weng *et al.*, “Memristors with Monolayer Graphene Electrodes Grown Directly on Sapphire Wafers,” 2024, doi: 10.1021/acsaelm.4c01208.

[383] M. H. Boratto and L. V. De Andrade Scalvi, “Deposition of Al2O3 by resistive evaporation and thermal oxidation of Al to be applied as a transparent FET insulating layer,” *Ceram Int*, vol. 40, no. 2, pp. 3785–3791, Mar. 2014, doi: 10.1016/J.CERAMINT.2013.09.041.

[384] H. Yang *et al.*, “Ultrathin Al Oxide Seed Layer for Atomic Layer Deposition of High-κ Al2O3 Dielectrics on Graphene,” *Chinese Physics Letters*, vol. 37, no. 7, p. 076801, Jul. 2020, doi: 10.1088/0256-307X/37/7/076801.

[385] A. Kumar *et al.*, “Low-temperature solution-processed high-capacitance AlOx dielectrics for low-voltage carbon-based transistors,” *Org Electron*, vol. 110, p. 106636, Nov. 2022, doi: 10.1016/J.ORGEL.2022.106636.

[386] K. S. Shamala, L. C. S. Murthy, and K. N. Rao, “Studies on optical and dielectric properties of Al 2 O 3 thin films prepared by electron beam evaporation and spray pyrolysis method,” *Materials Science and Engineering B*, vol. 106, pp. 269–274, 2004, doi: 10.1016/j.mseb.2003.09.036.

[387] S. Kim *et al.*, “Realization of a high mobility dual-gated graphene field-effect transistor with Al2O3 dielectric,” *Appl Phys Lett*, vol. 94, no. 6, Feb. 2009, doi: 10.1063/1.3077021/121162.

[388] P. Solís-Fernández, S. Okada, T. Sato, M. Tsuji, and H. Ago, “Gate-Tunable Dirac Point of Molecular Doped Graphene,” *ACS Nano*, vol. 10, no. 2, pp. 2930–2939, Feb. 2016, doi: 10.1021/ACSNANO.6B00064/SUPPL_FILE/NN6B00064_SI_001.PDF.

[389] B. I. Weintrub, Y. L. Hsieh, S. Kovalchuk, J. N. Kirchhof, K. Greben, and K. I. Bolotin, “Generating intense electric fields in 2D materials by dual ionic gating,” *Nature Communications 2022 13:1*, vol. 13, no. 1, pp. 1–6, Nov. 2022, doi: 10.1038/s41467-022-34158-z.

[390] “MAM ITO Glass｜ - Luminescence technology corp.” Accessed: Jan. 13, 2025. [Online]. Available: https://www.lumtec.com.tw/products-view.php?ID=4211

[391] D. A. Keller, H. N. Barad, E. Rosh-Hodesh, A. Zaban, and D. Cahen, “Can fluorine-doped tin Oxide, FTO, be more like indium-doped tin oxide, ITO? Reducing FTO surface roughness by introducing additional SnO2 coating,” *MRS Commun*, vol. 8, no. 3, pp. 1358–1362, Sep. 2018, doi: 10.1557/MRC.2018.179.

[392] “FTO Glass Substrates, Unpatterned | TEC 8, TEC 10, TEC 15 FTO | Ossila.” Accessed: Jan. 13, 2025. [Online]. Available: https://www.ossila.com/products/fto-glass-unpatterned

[393] A. K.; Akhmedov *et al.*, "Transparent Conductive Indium Zinc Oxide Films: Temperature and Oxygen Dependences of the Electrical and Optical Properties," *Coatings 2022, Vol. 12, Page 1583*, vol. 12, no. 10, p. 1583, Oct. 2022, doi: 10.3390/COATINGS12101583.

[394] Z. Ying *et al.*, "Sputtered Indium-Zinc Oxide for Buffer Layer Free Semitransparent Perovskite Photovoltaic Devices in Perovskite/Silicon 4T-Tandem Solar Cells," *Adv Mater Interfaces*, vol. 8, no. 6, p. 2001604, Mar. 2021, doi: 10.1002/ADMI.202001604.

[395] Y. H. Chiang, C. C. Peng, Y. H. Chen, Y. L. Tung, S. Y. Tsai, and P. Chen, "The utilization of IZO transparent conductive oxide for tandem and substrate type perovskite solar cells," *J Phys D Appl Phys*, vol. 51, no. 42, p. 424002, Aug. 2018, doi: 10.1088/1361-6463/AAD71C.

[396] K. Fleischer, E. Norton, D. Mullarkey, D. Caffrey, and I. V. Shvets, "Quantifying the performance of P-type transparent conducting oxides by experimental methods," *Materials*, vol. 10, no. 9, p. 1019, Sep. 2017, doi: 10.3390/ma10091019.

[397] G. Haacke, "New figure of merit for transparent conductors," *J Appl Phys*, vol. 47, no. 9, p. 4086, Aug. 2008, doi: 10.1063/1.323240.

[398] A. Anand, M. M. Islam, R. Meitzner, U. S. Schubert, and H. Hoppe, "Introduction of a Novel Figure of Merit for the Assessment of Transparent Conductive Electrodes in Photovoltaics: Exact and Approximate Form," *Adv Energy Mater*, vol. 11, no. 26, p. 2100875, Jul. 2021, doi: 10.1002/AENM.202100875.

[399] "Equation Solving Algorithms - MATLAB & Simulink - MathWorks United Kingdom." Accessed: Jul. 29, 2022. [Online]. Available: https://uk.mathworks.com/help/optim/ug/equation-solving-algorithms.html

[400] J. F. Guillemoles, T. Kirchartz, D. Cahen, and U. Rau, “Guide for the perplexed to the Shockley–Queisser model for solar cells,” *Nature Photonics 2019 13:8*, vol. 13, no. 8, pp. 501–505, Jul. 2019, doi: 10.1038/s41566-019-0479-2.

[401] W. Shockley and H. J. Queisser, “Detailed Balance Limit of Efficiency of p-n Junction Solar Cells,” *J Appl Phys*, vol. 32, no. 3, p. 510, Jun. 2004, doi: 10.1063/1.1736034.

[402] “Standard Tables for Reference Solar Spectral Irradiances: Direct Normal and Hemispherical on 37° Tilted Surface.” Accessed: Jul. 29, 2022. [Online]. Available: https://www.astm.org/g0173-03r20.html

[403] K. R. McIntosh and S. C. Baker-Finch, “OPAL 2: Rapid optical simulation of silicon solar cells,” in *2012 38th IEEE Photovoltaic Specialists Conference*, IEEE, Jun. 2012, pp. 000265–000271. doi: 10.1109/PVSC.2012.6317616.

[404] “OPAL 2.” Accessed: May 18, 2025. [Online]. Available: https://www2.pvlighthouse.com.au/calculators/OPAL%202/OPAL%202.aspx

[405] J. Werner *et al.*, “Complex Refractive Indices of Cesium-Formamidinium-Based Mixed-Halide Perovskites with Optical Band Gaps from 1.5 to 1.8 eV,” *ACS Energy Lett*, vol. 3, no. 3, pp. 742–747, Mar. 2018, doi: 10.1021/acsenergylett.8b00089.

[406] J. M. Siqueiros, R. Machorro, and L. E. Regalado, “Determination of the optical constants of MgF_2 and ZnS from spectrophotometric measurements and the classical oscillator method,” *Applied Optics, Vol. 27, Issue 12, pp. 2549-2553*, vol. 27, no. 12, pp. 2549–2553, Jun. 1988, doi: 10.1364/AO.27.002549.

[407] Z. C. Holman *et al.*, “Infrared light management in high-efficiency silicon heterojunction and rear-passivated solar cells,” *J Appl Phys*, vol. 113, no. 1, p. 013107, Jan. 2013, doi: 10.1063/1.4772975.

[408] C. Han *et al.*, “Room-temperature sputtered tungsten-doped indium oxide for improved current in silicon heterojunction solar cells,” *Solar Energy Materials and Solar Cells*, vol. 227, p. 111082, Aug. 2021, doi: 10.1016/J.SOLMAT.2021.111082.

[409] B. Macco, Y. Wu, D. Vanhemel, and W. M. M. Kessels, “High mobility In2O3:H transparent conductive oxides prepared by atomic layer deposition and solid phase crystallization,” *physica status solidi (RRL) – Rapid Research Letters*, vol. 8, no. 12, pp. 987–990, Dec. 2014, doi: 10.1002/PSSR.201409426.

[410] S. C. Baker-Finch and K. R. McIntosh, “Reflection of normally incident light from silicon solar cells with pyramidal texture,” *Progress in Photovoltaics: Research and Applications*, vol. 19, no. 4, pp. 406–416, Jun. 2011, doi: 10.1002/PIP.1050.

[411] “Monolayer graphene on 8-inch (200mm) diameter Si/SiO2 wafer - GROLLTEX - GRAPHENE-ROLLING-TECHNOLOGIES.” Accessed: Jul. 19, 2022. [Online]. Available: https://grolltex.com/product/contiguous-monolayer-graphene-8-inch-200mm-diameter-si-sio2-wafer/

[412] C. Messmer *et al.*, “Optimized front TCO and metal grid electrode for module-integrated perovskite–silicon tandem solar cells,” *Progress in Photovoltaics: Research and Applications*, vol. 30, no. 4, pp. 374–383, Apr. 2022, doi: 10.1002/PIP.3491.

[413] A. ur Rehman, E. P. Van Kerschaver, E. Aydin, W. Raja, T. G. Allen, and S. De Wolf, “Electrode metallization for scaled perovskite/silicon tandem solar cells: Challenges and opportunities,” *Progress in Photovoltaics: Research and Applications*, vol. 31, no. 4, pp. 429–442, Apr. 2023, doi: 10.1002/PIP.3499.

[414] C. R. Dean *et al.*, “Boron nitride substrates for high-quality graphene electronics,” *Nature Nanotechnology 2010 5:10*, vol. 5, no. 10, pp. 722–726, Aug. 2010, doi: 10.1038/nnano.2010.172.

[415] H. Xin and W. Li, “A review on high throughput roll-to-roll manufacturing of chemical vapor deposition graphene,” *Appl Phys Rev*, vol. 5, no. 3, Sep. 2018, doi: 10.1063/1.5035295/14573816/031105_1_ACCEPTED_MANUSCRIPT.PDF.

[416] E. S. Polsen, D. Q. McNerny, B. Viswanath, S. W. Pattinson, and A. John Hart, “High-speed roll-to-roll manufacturing of graphene using a concentric tube CVD reactor,” *Scientific Reports 2015 5:1*, vol. 5, no. 1, pp. 1–12, May 2015, doi: 10.1038/srep10257.

[417] D. Turkay *et al.*, “Synergetic substrate and additive engineering for over 30%-efficient perovskite-Si tandem solar cells,” *Joule*, vol. 8, no. 6, pp. 1735–1753, Jun. 2024, doi: 10.1016/J.JOULE.2024.04.015.

[418] A. A. Said *et al.*, “Sublimed C60 for efficient and repeatable perovskite-based solar cells,” *Nature Communications 2024 15:1*, vol. 15, no. 1, pp. 1–10, Jan. 2024, doi: 10.1038/s41467-024-44974-0.

[419] D. De Fazio *et al.*, “High-Mobility, Wet-Transferred Graphene Grown by Chemical Vapor Deposition,” *ACS Nano*, vol. 13, no. 8, pp. 8926–8935, Aug. 2019, doi: 10.1021/ACSNANO.9B02621/ASSET/IMAGES/MEDIUM/NN-2019-02621N_0010.GIF.

[420] A. N. Mehta *et al.*, “Understanding noninvasive charge transfer doping of graphene: a comparative study,” *Journal of Materials Science: Materials in Electronics*, vol. 29, no. 7, pp. 5239–5252, Apr. 2018, doi: 10.1007/S10854-017-8443-8/TABLES/1.

[421] H. Lu, Y. Guo, and J. Robertson, “Charge transfer doping of graphene without degrading carrier mobility,” *J Appl Phys*, vol. 121, no. 22, p. 224304, Jun. 2017, doi: 10.1063/1.4985121.

[422] A. R. Kulkarni, H. S. Maiti, and A. Paul, “Fast ion conducting lithium glasses-Review,” *Bull. Mater. Sci*, vol. 6, no. 2, pp. 201–221, 1984.

[423] J. Chai, F. Lu, B. Li, and D. Y. Kwok, “Wettability interpretation of oxygen plasma modified poly(methyl methacrylate),” *Langmuir*, vol. 20, no. 25, pp. 10919–10927, Dec. 2004, doi: 10.1021/LA048947S/ASSET/IMAGES/LARGE/LA048947SF00009.JPEG.

[424] M. Topič and M.-J. Kim, “A Study on Optimal Indium Tin Oxide Thickness as Transparent Conductive Electrodes for Near-Ultraviolet Light-Emitting Diodes,” *Materials 2023, Vol. 16, Page 4718*, vol. 16, no. 13, p. 4718, Jun. 2023, doi: 10.3390/MA16134718.

[425] M. Ahmed, A. Bakry, E. R. Shaaban, and H. Dalir, “Structure, Electrical and Optical Properties of ITO Thin Films and their Influence on Performance of CdS/CdTe Thin-Film Solar Cells”.

[426] H. Jiang *et al.*, “Thickness-dependent loss-induced failure of an ideal ENZ-enhanced optical response in planar ultrathin transparent conducting oxide films,” *Optics Express, Vol. 31, Issue 2, pp. 2208-2224*, vol. 31, no. 2, pp. 2208–2224, Jan. 2023, doi: 10.1364/OE.479098.

[427] E. Raoult *et al.*, “Optical Characterizations and Modelling of Semitransparent Perovskite Solar Cells for Tandem Applications,” in *36th EU PVSEC*, 2019, pp. 757–763.

Appendix

a.i TCE Modelling Code

Attached below is the MATLAB code used to model the maximum perovskite/silicon tandem cell efficiency as described in Chapter 8. This code assumes the only losses arise from the TCE: focusing on the TCE's sheet resistance and its weighted-average transmittance (WAT) across the AM1.5G spectrum.

```
clear variables;

% This code is used to calculate the maximum SQ efficiency in a perovskite/silicon
tandem cell from variation
% in Rsheet and Transmittance of the TCE

% Physical Constants and Parameters
q=1.60e-19; %C electron charge (C)
epsrox=3.9; % silicon oxide relative permitivity
eps0=8.85e-14; % vacuum permitivity (F/cm)
epsrs=11.9; % Silicon relative permitivity
k=1.38e-23; % Boltzmann constant (J/K)
T=300; % Temperature (K)
Vt=(k*T)/q; % Thermal energy (eV)
hc=1240; % Planck constant * speed of light (eV*nm)
c=3e8; % Speed of light (m/s)
Pin=0.1; % Incident power of light (W/cm2)

% unit cell dimensions
w=1;  % width of unit cell (cm). Increase in width causes a proportional increase
in photocurrent BUT causes a reciprocal decrease in series resistance.
l=0.1; % length of unit cell (cm)

% Loading a file "AM15g.mat", containing AM1.5G spectrum data".
load('AM15g.mat'); % #/s/cm^2/nm
LambdaVar=AM15g(:,1); % Wavelength values (nm)
AM15gFlux=AM15g(:,2); % Photon flux (#/s/cm^2/nm)

% Set up band gap of silicon bottom cell
EgapSi=1.12;
LambdaSi=hc/EgapSi;

% Set up loops for variations in TCE properties
dimLoop0=150; % number of iterations of Sheet resistance
dimLoop1=150; % number of iterations of Transmittance
dimLoop2=150; % number of iterations of  I-V curve

% Loop over Rsheet and TCE Transmittance
Rsheet = logspace(log10(10), log10(2500), dimLoop0);% Log-distributed Rsheet
values
MaxEta=zeros(dimLoop0,dimLoop1); % Store Max efficiency

% Defining perovskite band gap
```

```
EgapP=1.73;

% Find wavelengths corresponding to band gaps of perovskite and silcon subcells
LambdaP=hc/EgapP;
[~,iLambdaP]=min(abs(LambdaVar-LambdaP));
[~,iLambdaSi]=min(abs(LambdaVar-LambdaSi));

% Define Blackbody at 300 K, BB300K in #/s/cm^2/nm
BB300K=(2*pi*c./((LambdaVar*1e-9).*LambdaVar.*(LambdaVar*1e-
7).^2)).*(1./(exp(hc./((LambdaVar).*Vt))-1));

% TCE transmittance, as function of the AM1.5G spectrum wavelengths
TtceF=ones(length(LambdaVar),1);

% Vary TCE transmittance axis between 85 to 100% (Plotted range)
TtceFvec=linspace(0.85,1,dimLoop1);

for ind0=1:dimLoop0

    % For each Rsheet value
    Rs=2*Rsheet(ind0)*l/(6*w); % Series resistance from TCE Rsheet (Ohm)

    % EgapPvec=linspace(1.6,1.8,dimLoop1);

    for ind1=1:dimLoop1 % loop over changes in TCE transmittance

        % Scale the TCE transmittance for each loop
        TtceF1=TtceF*TtceFvec(ind1);

        % Calculate the short-circuit current (Isc) and dark saturation current
(I0) for both perovskite and
        % silicon subcells (Equations 8.10, 8.11, 8.12 and 8.14 in Chapter 8)


IscP=q*w*(l/2)*trapz(LambdaVar(1:iLambdaP),AM15gFlux(1:iLambdaP).*TtceF1(1:iLambda
P));

I0P=q*w*(l/2)*trapz(LambdaVar(1:iLambdaP),BB300K(1:iLambdaP).*TtceF1(1:iLambdaP));


IscSi=q*w*(l/2)*trapz(LambdaVar(iLambdaP:iLambdaSi),AM15gFlux(iLambdaP:iLambdaSi).
*TtceF1(iLambdaP:iLambdaSi));

I0Si=q*w*(l/2)*trapz(LambdaVar(iLambdaP:iLambdaSi),BB300K(iLambdaP:iLambdaSi).*Ttc
eF1(iLambdaP:iLambdaSi));

        % Define a range of voltages to simulate the I-V curve
        Vcell=linspace(0.01,EgapP+EgapSi,dimLoop2)' ; % Vcell

        % Initialise arrays to store power and current data
        PowerLog=zeros(dimLoop2,1);
        PowerLog2=PowerLog;
        JcellLog=zeros(dimLoop2,1);
        JcellLog2=JcellLog;

        % Loop through each voltage point to calculate current and power
        for ind2=1:length(Vcell)

            % x= [Vp, Vsi, I]
```

```
            % Nonlinear system to solve for current at each voltage
            F2 = @(x) [x(3)- I0P.*(exp(x(1)./Vt)-1)+ IscP ;
                      x(3)- I0Si.*(exp(x(2)./Vt)-1)+ IscSi ;
                     Vcell(ind2) - x(1) - x(2) - Rs.*x(3) ];

            % Initial guess for fsolve
            x0 = [Vcell(ind2)/2;Vcell(ind2)/2;1/(1/IscP+1/IscSi)];
            % Suppress fsolve output
            options = optimoptions('fsolve','Display','none');
            % Solve the system of equations
            [Sol,fval] = fsolve(F2,x0,options);

            % Calculate the power and current at a given voltage
            PowerLog(ind2)=Vcell(ind2)*Sol(3)/(w*(l/2)); % Power in W/cm^2
            JcellLog(ind2)=Sol(3)/(w*(l/2)); % Current density in A/cm^2
        end

        % Finding the voltage corresponding to maximum power
        [~,iP1]=min(PowerLog); % Find index where power is maximum
        Vcell=linspace(Vcell(iP1-1),Vcell(iP1+1),dimLoop2)' ; % Zoom into voltage
range around maximum power

        % Now recompute the power with finer voltage steps
        for ind2=1:dimLoop2

        F2 = @(x) [x(3)- I0P.*(exp(x(1)./Vt)-1)+ IscP ;
                  x(3)- I0Si.*(exp(x(2)./Vt)-1)+ IscSi ;
                 Vcell(ind2) - x(1) - x(2) - Rs.*x(3) ];
        x0 = [Vcell(ind2)/2;Vcell(ind2)/2;1/(1/IscP+1/IscSi)];
        options = optimoptions('fsolve','Display','none');
        [Sol,fval] = fsolve(F2,x0,options);

        PowerLog2(ind2)=Vcell(ind2)*Sol(3)/(w*(l/2)); % Recalculate power
        JcellLog2(ind2)=Sol(3)/(w*(l/2)); % Recalculate current density
        end

        % Calculate and log the maximum efficiency for this combination of TCE
Rsheetand transmittance, and log it.

        MaxEta(ind0, ind1)=-min(PowerLog2)./Pin;
        % display (-min(PowerLog2)./Pin)

    end
% plot(EgapPvec,MaxEta)

end


% Create the plot to visualise the efficiency
figure;
% TCE transmittance and max efficiency multiplied by 100 to be shown in units of
%.

imagesc(Rsheet,TtceFvec*100,100*MaxEta');

set(gca, ...
    'YDir',   'normal', ...      % right-way-up y-axis
    'XScale', 'log', ...         % log x-axis
    'TickDir','out', ...         % ticks pointing outward
```

```
    'LineWidth', 1, ...          % axis & tick thickness
    'FontSize', 16);             % Tick label font size

% Colorbar: keep default tick direction, but bump its font
cb = colorbar;
set(cb, 'FontSize', 16);

% Apply colormap
colormap( crameri('roma',256) );

% Set axis labels
xlabel('TCE Sheet Resistance (\Omega/□)', 'FontSize', 18);
ylabel('Weighted Average Transmittance (%)', 'FontSize', 18);
%
% Set y-axis limits
ylim([85, 100]);
xlim([10, 2500]);
clim([37, 45]);
%
% Add and label colorbar
ylabel(colorbar, 'Maximum SQ Efficiency Limit (%)', 'FontSize', 18);
```

a.ii TCE Weighted Average Transmittance Calculator

Below is the Python code used to calculate the weighted average transmittance of each transparent conducting electrode from the spectral light intensity transmitted (T_x) through a simulated device stack, as described in Chapter 8.

```
import pandas as pd
import numpy as np
import os

def compute_WAT_from_excel(excel_path, lambda_Si=1100.0):
    """
    Compute weighted-average transmittance WAT from a 5-column Excel sheet obtained
using OPAL2:
      col1: Wavelength (nm)
      col2: Photon energy (eV)
      col3: Reflection
      col4: Absorption
      col5: Transmission (Tx)
    """
    # 1) Load data from Excel (assuming the first sheet contains the data)
    df   =   pd.read_excel(excel_path,   header=0,   usecols=['Wavelength   (nm)',
'Transmission'])

    # 2) Restrict transmission data to ≤ Si cut-off
    mask = df['Wavelength (nm)'] <= lambda_Si
    wl_Tx = df.loc[mask, 'Wavelength (nm)'].values
    Tx    = df.loc[mask, 'Transmission'].values

    # 4) Integrate to compute WAT
    numerator   = np.trapz(Tx * wl_Tx, wl_Tx)
    denominator = np.trapz(wl_Tx, wl_Tx)
```

```
    return numerator / denominator

def batch_process_WAT(input_dir, lambda_Si=1100.0):
    """
    Batch process all Excel files in a directory to compute WAT for each dataset
    and save a summary file with the results.
    """
    results = []

    for filename in os.listdir(input_dir):
        if filename.endswith('.xlsx'):  # Only process .xlsx files
            excel_path = os.path.join(input_dir, filename)

            if os.path.exists(excel_path):
                # Calculate WAT
                WAT = compute_WAT_from_excel(excel_path, lambda_Si)

                # Append the result to the list
                results.append({
                    'CSV File': filename,
                    'WAT': WAT
                })
                print(f"Processed {filename} and calculated WAT: {WAT:.4f}")
            else:
                print(f"Warning: File {excel_path} does not exist.")

    # Save all results to a single summary file
    if results:
        summary_df = pd.DataFrame(results)
        summary_file = os.path.join(input_dir, 'WAT_summary_analysed.xlsx')
        summary_df.to_excel(summary_file, index=False)
        print(f"Summary saved as {summary_file}")
    else:
        print("No files were processed.")

if __name__ == '__main__':
    # Define your directory containing the Excel files
    input_dir = r'D:\Thesis Pictures High Res\Model\GlassTCE\IZO_Glass_MgFx.fig'

    # Process the files and save the results in a summary file
    lambda_Si = 1100.0  # Si band-edge in nm
    batch_process_WAT(input_dir, lambda_Si)
```

a.iii **Incorporating in Glass in Weighted-Average Transmittance vs Sheet Resistance Model for Perovskite/Silicon Tandem Cells**

One of the limitations of the model presented in Chapter 8 is that it presented the transmittance through the device stack without considering the effect of the thick glass encapsulation layer normally present in solar modules. This approach provided a clear comparison between graphene TCEs and TCOs in situations with optimised anti-reflective layers. However,

inclusion of the glass encapsulating layer is essential for fair comparison between graphene and TCOs.

Figure A.1 depicts the results from a model similar to that depicted in Chapter 8, but including a glass encapsulant layer of semi-infinite thickness. Glass was assumed to have a pure SiO_2 composition, with *n* and *k* values obtained from reference [427]. For the schematic depicted in Figure A.1 (a), the optical path consists of consists of air/glass/graphene/perovskite. In this case, significant loss occurs due to the reflection at the glass/graphene/perovskite interface owing to poor refractive index matching. This results in a WAT for graphene ~89.02%. This compares quite poorly compared to structures involving TCOs such as glass/TCO/perovskite structure, depicted in Figure A.1 (b). One of the benefits of TCOs is their refractive indices (~1.8-2.2) are a good intermediate between glass (~1.5) and the perovskite absorber (~2.4), which reduce reflection in this system compared to the glass/graphene/perovskite stack. In this system, all but the >80 nm heavily-doped ITO (ITO_{heavy}), the 150 nm lightly-doped ITO (ITO_{light}), and >100 nm IZO perform better than the graphene TCE. Figure A.1 (c) depicts a schematic showing the introduction of a SiN_x layer (*n~2*) between the glass and the graphene to reduce the refractive index mismatch and reduce reflectance at the graphene. *OPAL2* was used to calculate the optimum SiN_x thickness as 63 nm, leading to a WAT of 91.55%. In this case, the SiN_x could act as both the ion-charged dielectric, and the anti-reflective coating, and can provide performance exceeding that of all but high mobility IZrO, with efficiency potential >41%. This demonstrates that graphene can be competitive with state-of-the-art TCOs, but consideration for the refractive indices of adjacent layers is essential.

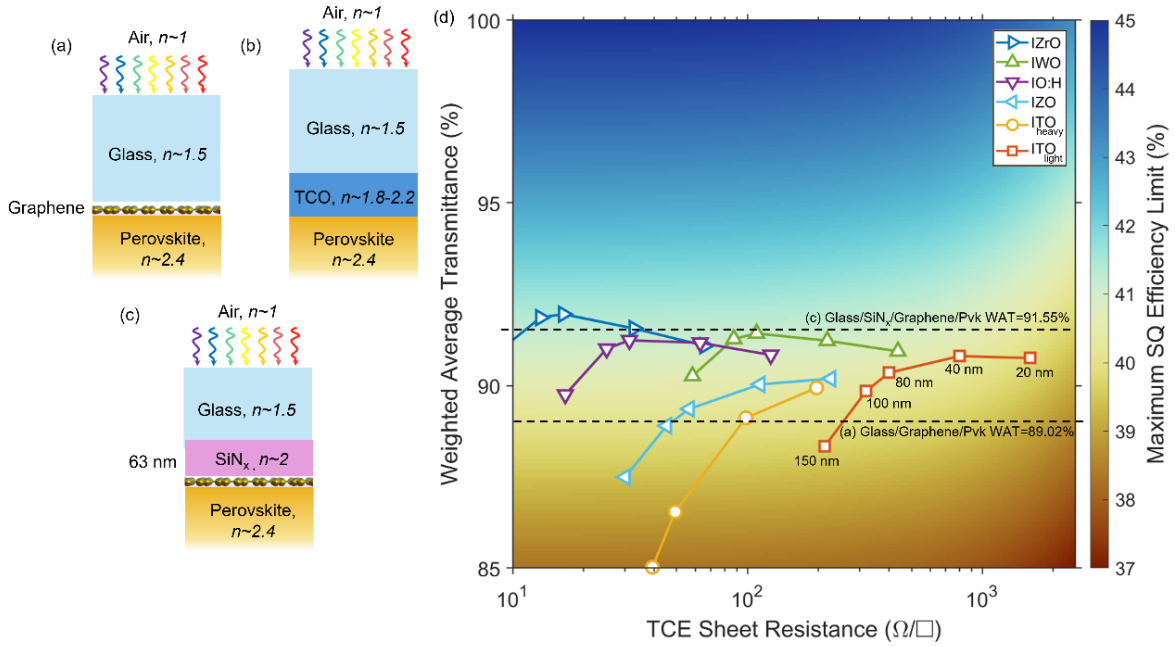

Figure A.1: Optical path through (a) a glass/graphene/perovskite cell stack, (b) a glass/SiN_x/graphene/perovskite, and (c) a glass/TCO/perovskite cell stack. (d) Simulated colour plot to visualise the maximum potential Shockley-Queisser (SQ) efficiency of a two-terminal perovskite/silicon tandem solar cell, assuming the only other source of loss beyond the SQ conditions arises from the transparent conducting electrodes used. The cell configuration consists of a perovskite cell of E_g = 1.73 eV on a silicon cell, with two transparent conducting electrodes (TCEs) (one front and one rear. The x-axis represents the TCE sheet resistance from 10 to 2500 Ω/□. The y-axis represents the weighted-average transmittance across the air-mass 1.5 global (AM1.5G) spectrum. The data points correspond to TCOs of different thickness in structure (b), while the dotted lines correspond to the calculated transmittance through the graphene-based stacks (a) and (c) respectively.

The refractive index matching of the glass/TCE/perovskite system can be further improved using an MgF_x layer (n~1.38) between the air and glass. MgF_x n and k data were obtained from reference [406], and the optical path simulated in *OPAL2* to calculate the weighted-average transmittance. Figure A.2 (a) and (b) depict schematics of such structures involving graphene/SiN_x or a TCO respectively. In these structures, the optimum MgF_x and SiN_x thickness were calculated to be 90 nm and 30 nm respectively. Figure A.2 (c) depicts the properties of these structures overlayed on the simulated colour plot describing perovskite/silicon tandem cell efficiency as in Chapter 8. As expected, the reflection is further minimised using this layer, with maximum potential efficiency approaching ~42% for both the ICD-doped graphene and the IZrO layer from 40-100 nm. This is reduced compared to the optimised stacks discussed in Chapter 8 due to the glass reflection, which is difficult to

eliminate entirely. It is expected that further optimisations of ARC layers and appropriate texturing could further increase the overall WAT to achieve higher efficiencies toward >43%.

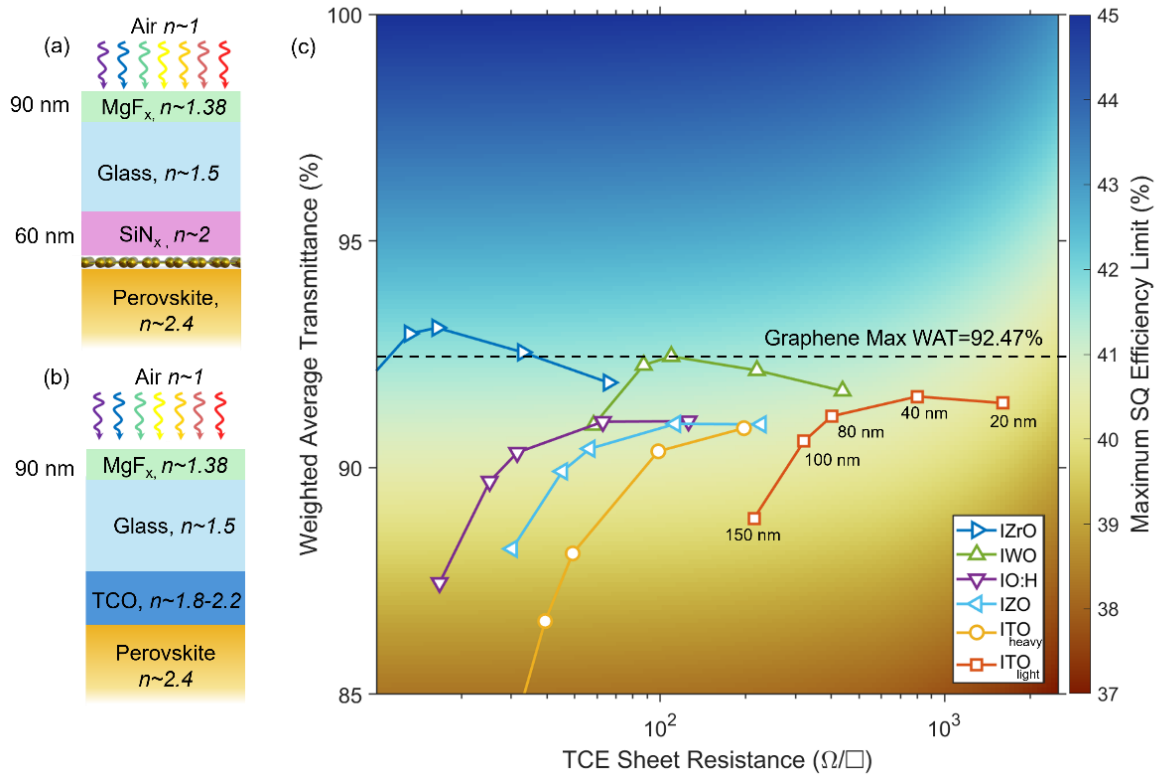

Figure A.2: Optical path through (a) a MgF_x/glass/SiN_x/graphene/perovskite cell stack, and (b) a MgF_x/glass/TCO/perovskite cell stack. (d) Simulated colour plot to visualise the maximum potential Shockley-Queisser (SQ) efficiency of a two-terminal perovskite/silicon tandem solar cell, assuming the only other source of loss beyond the SQ conditions arises from the transparent conducting electrodes (TCEs) used. The cell configuration consists of a perovskite cell of E_g = 1.73 eV on a silicon cell, with two TCEs (one front and one rear. The x-axis represents the TCE sheet resistance from 10 to 2500 Ω/□. The y-axis represents the weighted-average transmittance across the air-mass 1.5 global (AM1.5G) spectrum. The data points correspond to TCOs of different thickness in structure (b), while the dotted line corresponds to the calculated transmittance through the graphene-based stack (a).